2019

Alignment And Morphological Effects Of Nanoplates In Lamellar Diblock Copolymer Thin Films

Nadia Krook
University of Pennsylvania

Alignment And Morphological Effects Of Nanoplates In Lamellar Diblock Copolymer Thin Films

Abstract

The ability to disperse inorganic nanoparticles (NPs) of various shapes, sizes, and compositions in polymeric matrices enables researchers to continuously engineer new material combinations with different resulting properties. Polymer nanocomposites (PNCs) can be further customized for specific applications by intentionally organizing and orienting NPs within these hybrid materials. Despite significant advances in the field of PNCs, full control over the orientation of embedded anisotropic NPs, specifically nanoplates, is not well-established without employing multistep processes. Capturing either in-plane (parallel) or out-of-plane (vertical) orientation of nanoplates in thin polymer films through a scalable method would create new opportunities for developing coating technologies that benefit from orientation-dependent properties.

Within this dissertation, we accomplish, for what we believe to be the first time, both in-plane and out-of-plane alignment of nanoplates in thin film PNCs through self-assembly. Monodisperse gadolinium trifluoride rhombic nanoplates doped with ytterbium and erbium GdF3:Yb/Er (20/2 mol%) are synthesized while self-assembling lamellar-forming poly(styrene-b-methyl methacrylate) (PS-b-PMMA) block copolymers (BCPs) are formed. With microdomains oriented either parallel or perpendicular to the substrate, the lamellae serve as guides to direct the two modes of nanoplate alignment. To form PNCs, the nanoplate surfaces are functionalized with phosphoric acid functionalized polyethylene glycol (PEG-PO3H2) brush to create favorable interactions between the NPs and PMMA. In the parallel BCP nanocomposite system, three characteristic behaviors are observed as a function of nanoplate volume fraction (ϕ). At low ϕ, the nanoplates sequester to the PMMA domain and ordered lamellae successfully direct in-plane NP alignment. Here, the nanoplates further assemble into strings separated by small equilibrium interparticle distances. At intermediate ϕ, the PNCs phase separate into regions of ordered lamellae and regions of disordered BCP with unaligned nanoplates. While at the highest ϕ, the nanoplates jam in a kinetically trapped state and are isotropically dispersed throughout entirely disordered lamellae. Recognizing that chemical specificity and low ϕ are requisite conditions for not disrupting the equilibrium BCP morphology, vertical nanoplate alignment in PS-b-PMMA was also successfully established through self-assembly. Overall, the studies herein seek to understand the alignment and morphological effects of nanoplates in lamellar BCP thin films by identifying and understanding the thermodynamic contributions of the system.

Degree Type

Dissertation

Degree Name

Doctor of Philosophy (PhD)

Graduate Group

Materials Science & Engineering

First Advisor

Russell J. Composto

Second Advisor

Christopher B. Murray

ALIGNMENT AND MORPHOLOGICAL EFFECTS OF NANOPLATES IN LAMELLAR DIBLOCK COPOLYMER THIN FILMS

Nadia M. Krook

A DISSERTATION

in

Materials Science and Engineering

Presented to the Faculties of the University of Pennsylvania

in

Partial Fulfillment of the Requirements for the

Degree of Doctor of Philosophy

2019

Co-Supervisor of Dissertation

Signature _____

Russell J. Composto

Professor Materials Science and Engineering,
University of Pennsylvania

Co-Supervisor of Dissertation

Signature _____

Christopher B. Murray

Professor Materials Science and Engineering,
University of Pennsylvania

Graduate Group Chairperson

Signature _____

I-Wei Chen, Professor of Materials Science and Engineering, University of Pennsylvania

Dissertation Committee

Jeffrey S. Meth, Technical Fellow, DuPont

Robert A. Riggleman, Professor of Chemical and Biomolecular Engineering, University of Pennsylvania

ALIGNMENT AND MORPHOLOGICAL EFFECTS OF NANOPLATES IN LAMELLAR DIBLOCK COPOLYMER THIN FILMS

To my parents.

ACKNOWLEDGMENT

I would like to acknowledge the numerous people who have supported me while this work came to fruition. On my very first day of graduate school, I attended a project kickoff meeting with Russell J. Composto (co-advisor), Christopher B. Murray (co-advisor), Jeffrey S. Meth, and Robert A. Riggleman – a team that not only became my dissertation committee, but also became teachers and mentors during my thesis journey. Not long after that first meeting, Russ asked me, apart from scientific training and research progress, what I wanted to gain from the PhD experience. Among the multiple opportunities I was looking forward to, I mentioned to him that I was interested in engaging in collaborative work, pursuing a career in industry, partaking in an international experience, and growing as a mentor through teaching and outreach. Each of my advisors and committee members played an instrumental role in making all of those goals happen. My research has benefited considerably from fruitful collaborations with Rob's group and I am grateful for the insights he and his group offered to my experimental findings. Jeff has always taken an active role in my career development and offered unlimited advice and guidance when considering my next steps. I am truly thankful for his involvement and look forward to his continued mentorship as I begin my career in industry. I am indebted to my co-advisors, Russ and Chris, and their commitment to challenge and encourage me over the past five years. I have had the chance to grow personally and professionally beyond the traditional PhD experience as a result of their nominations to various awards and opportunities, their support for a three month experience in Grenoble (France), their commitment to making STEM accessible to all through outreach and teaching, and much more. I have been very lucky to have such supportive advisors and committee members dedicated to my growth and success since the first day.

I am also grateful for the interactions I had with my French sponsors, Patrice Rannou and Manuel Maréchal, during my stay at the Grenoble Innovation for Advanced New Technologies

(GIANT) campus in Grenoble, France. Thank you to Kristin Fields and the Research and Education in Active Coating Technologies (REACT) team for helping to have made my international experience possible. It is because of Pat Overend, Vicky Lee, and Irene Clements that the Department of Materials Science and Engineering (MSE) has felt like home for me. I looked forward to seeing them every day and will miss them tremendously. I am also grateful for the microscopy training and patience Doug Yates and Jamie Ford provided when I started my research. Jamie, along with Emmabeth Parrish and Sarah Seeger (my soup sisters), always made sure there was time to break for lunch and I value the sense of community this lunch group provided.

Thank you also to current and past members of the Composto group (Michael Boyle, Rob Ferrier, Martha Grady, Teddy Kurkoski, Hyun-Su Lee, Chia-Chun "Jim" Lin, Shawn Maguire, Carlos Medina, Emmabeth Parrish, Boris Rasin, Katie Rose, and Sarah Seeger) and the Murray group (Vicky Doan-Nguyen, Katie Elbert, Nick Greybush, Natalie Gogotsi, Guillaume Gouget, Davit Jishkariani, Austin Keller, Jennifer Lee, Emanuele Marino, Stan Najmr, Yaoting Wu, Chenjie Zeng, and Mingliang Zhang) who have contributed greatly to my time at Penn. I am also grateful for my collaborators in the Riggleman group (Jason Koski, Ben Lindsay, and Christian Tabedzki) and friends from Karen I. Winey's group (Eric Bailey, Francisco Buitrago, Phil Griffin, Rob Middleton, Mike O'Reilly, Ben Paren, James Pressly, Ted Trigg, Cathy Yang, and Lu Yan). I couldn't have gotten through my first year without the encouragement from and long hours of problem solving with members of my PhD cohort (Kathryn Hasz, Stephanie Malek, and James Pressly). Thank you also to all of my other friends in Penn MSE, other departments, and outside the walls of Penn who have enriched my life in countless ways including, but not limited to Rahul Agarwal, Ana Alvarez, Madeline (Dean) Fink, Seth Harper, Michael Kelly, Jackie Kovach, Kira Lauer, Neha Manohar, Gabby Mariotti, Mike Synodis, Anne Vanasse, Sydney Williams, OC7, and the Ladies of the 507.

I am so profoundly grateful for my family, immediate and extended, which has grown in the best ways over these last five years. At only two years old now, my nephew, Wyatt, undoubtedly brings out the best of our family, evoking more smiles, laughter, and life than any of us knew possible. Wyatt's dad and my brother-in-law, Michael, continues to be a calming force in the Krook clan and a source of wisdom. I appreciate his insight and, more than he knows, value the brotherly sign of approval he quietly shared after introducing someone new to my family. So, to that newest addition, my love and my best friend, Mike, thank you for your unwavering patience, empowerment, and love. You bring light to my dark days and joy to everyday. I am so grateful that your indecisiveness led you back to Philadelphia and that your decisiveness ultimately led you to me. I love you to the moon.

Finally, it is difficult to articulate the impact my sister, Melanie, and my parents have had on my life. They have been my most influential role models and my greatest pillars of strength and support. Melanie, I have always and will always look up to you. You not only taught me how to ride a bike and water ski, but you have also taught me to set goals, concur fears, and be the best I can be. Maman, merci for showing me what it means to be a courageous, compassionate, strong, independent woman. You have always fueled my creativity and have inspired your daughters to push barriers and excel in the field of science. Papa, my fishing buddy, I have spent some of my most peaceful and cherished hours casting out lines with you in our fishing hole. You have shared life advice with me, taught me what it means to be gritty, and shown me how to give a killer presentation. I once wrote to you, Papa, that I caught the *catch* of a lifetime when I was *lure*-d into this world by an outstanding set of parents. My parents, my *catch* of a lifetime, continue to be the type of *catch* I aspire to be every day. As my mom most simply and elegantly put it, "…je tiens á remercier mes parents sans lesquels rien de tout cela n'aurait été possible."[1] Je vous aime énormément. Thank you for helping me become the person I am today.

1. Debiak, T. Beta-Lactamase Inhibitors: Clavulanic Acid Analogues. University of Notre Dame, 1983.

ABSTRACT

ALIGNMENT AND MORPHOLOGICAL EFFECTS OF NANOPLATES IN LAMELLAR DIBLOCK COPOLYMER THIN FILMS

Nadia M. Krook

Russell J. Composto

Christopher B. Murray

The ability to disperse inorganic nanoparticles (NPs) of various shapes, sizes, and compositions in polymeric matrices enables researchers to continuously engineer new material combinations with different resulting properties. Polymer nanocomposites (PNCs) can be further customized for specific applications by intentionally organizing and orienting NPs within these hybrid materials. Despite significant advances in the field of PNCs, full control over the orientation of embedded anisotropic NPs, specifically nanoplates, is not well-established without employing multistep processes. Capturing either in-plane (parallel) or out-of-plane (vertical) orientation of nanoplates in thin polymer films through a scalable method would create new opportunities for developing coating technologies that benefit from orientation-dependent properties.

Within this dissertation, we accomplish, for what we believe to be the first time, both in-plane and out-of-plane alignment of nanoplates in thin film PNCs through self-assembly. Monodisperse gadolinium trifluoride rhombic nanoplates doped with ytterbium and erbium GdF_3:Yb/Er (20/2 mol%) are synthesized while self-assembling lamellar-forming poly(styrene-*b*-methyl methacrylate) (PS-*b*-PMMA) block copolymers (BCPs) are formed. With microdomains oriented either parallel or perpendicular to the substrate, the lamellae serve as guides to direct the two modes of nanoplate alignment. To form PNCs, the nanoplate surfaces are functionalized with phosphoric acid functionalized polyethylene glycol (PEG-PO_3H_2) brush to create favorable interactions between the NPs and PMMA. In the parallel BCP nanocomposite system, three

characteristic behaviors are observed as a function of nanoplate volume fraction (ϕ). At low ϕ, the nanoplates sequester to the PMMA domain and ordered lamellae successfully direct in-plane NP alignment. Here, the nanoplates further assemble into strings separated by small equilibrium interparticle distances. At intermediate ϕ, the PNCs phase separate into regions of ordered lamellae and regions of disordered BCP with unaligned nanoplates. While at the highest ϕ, the nanoplates jam in a kinetically trapped state and are isotropically dispersed throughout entirely disordered lamellae. Recognizing that chemical specificity and low ϕ are requisite conditions for not disrupting the equilibrium BCP morphology, vertical nanoplate alignment in PS-*b*-PMMA was also successfully established through self-assembly. Overall, the studies herein seek to understand the alignment and morphological effects of nanoplates in lamellar BCP thin films by identifying and understanding the thermodynamic contributions of the system.

TABLE OF CONTENTS

LIST OF TABLES

LIST OF FIGURES

CHAPTER 1: Introduction

1.1 Motivation

Polymer nanocomposites (PNCs) are created by incorporating nanoscale particles into polymer matrices. The ability to combine inorganic and organic building blocks has received significant attention since the resulting material will possess properties of each component. PNCs leverage polymers as a flexible and processable platform in which to embed a variety of nanoparticles (NPs). These fillers can then impart specific characteristics to the matrix such as mechanical strength,[1,2] electrical conductivity,[3] and optical[4-7] and magnetic properties.[8-9] Compared to conventional additives, the incorporation of nanosized particles provides certain advantages. These advantages mostly emerge from the high surface area-to-volume ratio attributed to NPs. Foremost, loadings of only 1-5 vol% of NPs, instead of 15-40 vol% for traditional particles, are required to augment matrix properties.[10] Additionally, physical phenomena emerge in nanoscale materials, which deviate from bulk properties, including quantum confinement effects that tune optical and electrical properties.[11-14] However, the properties of these heterogeneous PNC materials are ultimately determined not only by the characteristics of both the fillers and the matrix and the length scale of these components, but also by the quality of particle dispersion.[15]

Having full control over NP assemblies within PNCs is critical for creating materials with a precise structural design. To synthetically attain such sophisticated heterogeneous structures, an active area of research employs self-assembling block copolymers (BCPs). While a significant collection of research has focused on understanding the polymer physics that determine the placement of spherical NPs in BCPs, limited studies have examined the parameters that dictate the position and, importantly, the orientation of anisotropic (non-spherical) NPs in BCPs. More specifically, precise control over nanoplate alignment in self-assembling BCPs remains largely uninvestigated. This thesis work is motivated by the opportunity to harness shape and orientation

dependent properties of anisotropic NPs. By leveraging self-assembled BCP matrices, aligned NP assemblies that have been widely studied in inorganic systems for specific properties could then be self-contained in continuous, solution processable films.[16-20] Ultimately, multifunctional materials could be formed for various applications by capturing aligned particles in easy-to-process polymer coatings. By extending the polymer physics knowledge gained from the studies of isotropic NPs in BCPs, the goal is to establish a thermodynamic understanding to achieve deliberate alignment, organization, and placement of anisotropic NPs, and more specifically nanoplates, in PNCs.

1.2 Thermodynamics of Block Copolymers

The thermodynamics of a blend of two chemically disparate polymers is first considered. Assuming no change in volume upon mixing, a binary macromolecule mixture is described by its Helmholtz free energy of mixing per lattice site ($\Delta\bar{F}_{\text{mix}}$) as shown by

$$\Delta\bar{F}_{\text{mix}} = \Delta\bar{U}_{\text{mix}} - \text{T}\Delta\bar{S}_{\text{mix}} \qquad (1.1)$$

This expression includes both an entropy ($\Delta\bar{S}_{\text{mix}}$) and energy ($\Delta\bar{U}_{\text{mix}}$) of mixing term. The free energy of mixing per lattice site ($\Delta\bar{F}_{\text{mix}}$) of a binary polymer solution will either favor mixing if $\Delta\bar{F}_{\text{mix}} < 0$ or inhibit mixing if $\Delta\bar{F}_{\text{mix}} > 0$. The entropic contribution is related to the Boltzmann constant (k_{B}), the volume fraction of polymer A (ϕ_{A}), the volume fraction of polymer B (ϕ_{B}), and the degree of polymerization of each species (N_{A} and N_{B}, respectively) as given by

$$\Delta\bar{S}_{\text{mix}} = -k_{\text{B}}\left(\frac{\phi_{\text{A}}}{N_{\text{A}}}\ln\phi_{\text{A}} + \frac{\phi_{\text{B}}}{N_{\text{B}}}\ln\phi_{\text{B}}\right) \qquad (1.2)$$

This entropy term is always positive and thus favors mixing. However, since N_{A} and N_{B} tend to be much greater than unity for polymers, the entropy of mixing value is a very small contribution to the overall free energy of mixing. Polymers are described to have "stymied entropy" since the more monomers in a chain, the fewer possible conformations, and thus the lower the entropy.[21] Conversely, the energy of mixing term can either promote or oppose mixing of the polymer chains. As described by

$$\Delta\overline{U}_{\text{mix}} = kT(\chi\phi_{\text{A}}\phi_{\text{B}}) \qquad (1.3)$$

$\Delta\overline{U}_{\text{mix}}$ of a polymer blend depends on temperature (T) and the Flory−Huggins interaction parameter (χ), in addition to ϕ_{A}, ϕ_{B}, and k_{B}. This dimensionless interaction parameter considers all the possible pairwise interactions in the blend (AA, BB, AB). The sign of χ indicates whether there is a net repulsive or net attractive behavior within the blend. When $\chi > 0$, the system opposes mixing; when $\chi < 0$, it promotes mixing; and when $\chi = 0$, the blend is ideal. The temperature dependent Flory−Huggins interaction parameter is described empirically by

$$\chi \cong A + \frac{B}{T} \qquad (1.4)$$

where Term A describes the entropic contribution to χ while B/T characterizes the enthalpic contribution as a function of temperature, T. If $B < 0$, the polymer solution has an upper critical solution temperature (UCST) above which mixing is encouraged. If $B > 0$, the system has a lower critical solution temperature (LCST) and becomes more miscible as temperature decreases below this critical point. Ultimately, Equation 1.1 can be recast as

$$\Delta\overline{F}_{\text{mix}} = k_{\text{B}}T\left(\frac{\phi_{\text{A}}}{N_{\text{A}}}\ln\phi_{\text{A}} + \frac{\phi_{\text{B}}}{N_{\text{B}}}\ln\phi_{\text{B}} + \chi\phi_{\text{A}}\phi_{\text{B}}\right) \qquad (1.5)$$

Block copolymers are a class of macromolecules that join chemically disparate polymer chains (referred to as polymer blocks) by covalent bonds. Depending on the number of blocks and whether the polymers are linear or branched, a variety of molecular architectures can be achieved (details discussed elsewhere).[22] The simplest system, and the focus of this discussion and the BCPs used in the original work presented in this document, joins two linear and incompatible polymers in sequence and is termed a diblock copolymer. To satisfy the system requirement to minimize free energy, BCPs can phase separate depending on the competition between entropy and enthalpy. When considering BCPs, the fundamental difference that deviates from the thermodynamic construct above for a polymer blend is that they are unable to macrophase separate. Instead, BCPs self-assemble into intricate morphologies on the micro, meso, or nano length scales referred to

historically as microphase-separation.[22] These equilibrium structures arise from balancing the enthalpic force that drives separation (described by χ) of the blocks with the restoring entropic force. The entropic force limits chain stretching at the covalent bond since fewer chain conformations are available as polymer A extends away from polymer B.

The phase space of microphase-separating diblock copolymers is characterized by the following controllable experimental parameters: the total degree of polymerization (N), volume fraction of each segment (f), and χ. Phase diagrams for symmetric diblock copolymers have been developed through self-consistent mean-field theory (SCFT) that agree well with morphologies observed experimentally.[23,24] Matsen and Bates theoretically predicted the following six distinct equilibrium phases shown in Figure 1.1: lamellar (L), hexagonally packed cylinders (H), close-packed spheres (CPS), bicontinuous Ia$\bar{3}$d cubic or gyroid ($Q_{Ia\bar{3}d}$), body-centered cubic spheres ($Q_{Im\bar{3}m}$), and disordered (DIS).[24] The thermodynamically stable morphologies are illustrated in the schematic shown Figure 1.2.[25] The order-to-disorder transition (ODT) occurs at $f = 0.5$ and $\chi N \sim 10.4$, below which the melt is disordered. The weak segregation limit (WSL), where the microdomains are not well-defined, occurs near the ODT, but when $\chi N > 10.4$. When $\chi N \gg 10.4$, corresponding to low temperatures, the BCP is in a regime known as the strong segregation limit (SSL) where the A and B microdomains are well-defined with limited interfacial area.[26] Balancing the elastic energy of the chains and interfacial energy between A and B leads to an expression that describes the dimension of lamellar domains of a BCP centered at $f = 0.5$ in the SSL.[22] Equation 1.6 shows that domain period (λ) of lamellae scales as $N^{2/3}$ and also depends on the χ and monomer size (a).

$$\lambda = 1.03 a \chi^{\frac{1}{6}} N^{\frac{2}{3}} \qquad (1.6)$$

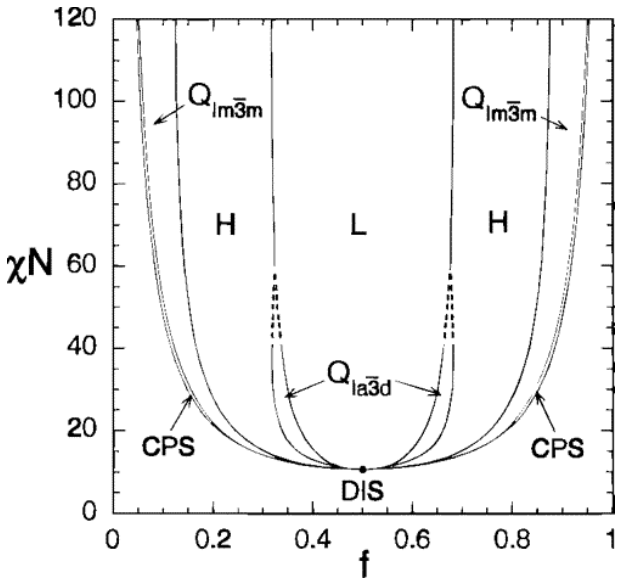

Figure 1.1. Phase diagram calculated by SCFT for a symmetric diblock copolymer systems, mapping the possible phases for different combinations of χN and f. Figure was reprinted (adapted) with permission from Matsen, M. W.; Bates, F. S. *Macromolecules* **1996**, 4, 1091-1098.[24] Copyright 1996 American Chemical Society.

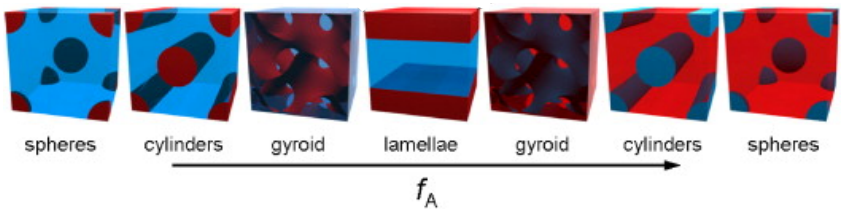

Figure 1.2. Illustration of an A-B diblock copolymer, represented simply with red and blue blocks, assembled into its thermodynamically stable phases governed by the relative volume fraction (*f*) of the polymer blocks [increasing volume fraction of A (f_A) from left to right]. Figure was reprinted (adapted) with permission from Darling, S. B. *Prog. Polym. Sci.* **2007**, 32, 1152-1204.[25] Copyright 2007, with permission from Elsevier.

1.3 Directing the Location of Isotropic Nanoparticles in Block Copolymer Domains

The various BCP morphologies attained by microphase-separation can serve as guides to direct the assembly of NPs into hierarchical structures. Controlling the microstructure of self-

assembling nanocomposites requires precise particle placement within the domains. Incorporating specifically designed and premade polymer functionalized NPs into a well understood phase space of a premade BCP, described by parameters such as χN, f, and the segregation strength, enables experimentalist to gain full control of both systems. This next section will begin to explore the portfolio of studies of isotropic (spherical) NPs dispersed in BCPs and discuss how variables in the system influence particle placement in a BCP matrix. This background aims to present the polymer physic insights gained from these seminal works so that they may later be discussed in context of anisotropic NPs in BCP nanocomposites.

1.3.1 Effect of Polymer Brush Chemistry. There is a delicate balance between the entropic and the enthalpic contributions to the free energy of a well-defined NP dispersed in a BCP matrix that will control its location within the domains. The following conversation will first discuss particle placement in relation to the interactions between the BCP and ligand chains, while ignoring entropic arguments. Then, how particle dispersion is affected by conformational and translational entropic repercussions will be introduced into the framework in the following section. More specifically, the relationship between these entropy penalties will be discussed in Section 1.3.2 as a function of particle size.

The surface chemistry of NPs placed in an A-B copolymer matrix determines particle placement and whether particles adsorb to the interface or segregate to either the A or B block. Kim *et al.* explored general ligand chemistry methods to tune the enthalpic interactions to localize gold (Au) NPs to the A/B interface.[27] Au NPs that were functionalized with a thiolated random copolymer of PS and poly(2-vinylpyridine) (PS-*r*-P2VP-SH; M_n = 3.5 kg/mol, PDI = 1.1) were embedded into a symmetric lamellar-forming poly(styrene-*b*-2 vinylpyridine) (PS-*b*-P2VP; M_n = 196.5 kg/mol, PDI = 1.11) to form bulk nanocomposites.[27] By varying PS mole fraction (F_{PS}) from F_{PS} = 0.52 to F_{PS} = 0.42, the authors observed interfacial adsorption over a narrow F_{PS} window.[27] At a nearly 50/50 composition of F_{PS} = 0.52, the NPs were bound to the PS/P2VP interface while

at F_{PS} = 0.42 the NPs were localized in the P2VP domains.[27] To maximize favorable enthalpic interactions when the ligand composition was not neutral, the system relocates NPs to the block whose chemistry was identical to the dominant moiety in the ligand. To support their results, the authors derived an expression for adsorption energy (E_a) of a NP to the diblock interface as a function of particle radius (R), interfacial tension (γ_{AB}), and mole fraction of one of the chemical constituents (F_A). Originated both from a classical study performed by Pieranski (trapping PS microspheres at the interface of water and air) and random copolymer theory, the energetic expression[27,28] is given by

$$E_a = (\pi R^2 \gamma_{AB})(1 - |1 - 2F_A|)^2 \qquad (1.7)$$

Consequently, a NP is more likely to segregate to the A/B interface the larger the value of E_a, with a maximum value when F_A = 0.5. When more of one species is introduced onto the surface, the NP would prefer to disperse within that block. Apart from ligand composition, this relationship elucidates how particle size impacts NP localization with respect to enthalpic interactions. Increasing the size of the NP will enhance the effect of NP adsorption or desorption from the A/B interface. To precisely place a NP within one of the blocks, theoretically, a large particle with mostly, if not all, of one chemical ligand species can be designed. However, maximizing preferential interactions by increasing NP size (larger surface area) and thus the favorable surface interactions has a cost when entropic arguments are considered. These repercussions will affect how NPs driven to one of the polymer blocks are distributed within the domain and will be considered next.

1.3.2 Effect of Nanoparticle Size. Congruent studies were performed theoretically by Thompson *et al.*[29,30] and experimentally by Chiu *et al.* [31,32] to predict how NP dimension affects BCP chain conformation and consequently the placement of NPs within a domain. The calculations completed by Thompson *et al*. predicted two discrete phases for A-like NPs distributed in the A block of an A-B lamellar copolymer. A “center-filled lamellar” phase, where NPs localized in well-

ordered arrays in the middle of the A domain, was realized when the particles were relatively large.[30] NP inclusions were considered large when the ratio (R/R_0) of particle radius (R, core plus brush) to the polymer's natural size (R_0, half the domain spacing) was 0.3.[30] When R/R_0 = 0.2, the comparatively small particles formed an "edge-filled lamellar" phase with NPs segregated towards the edges of the A domain.[30] Corresponding experiments were executed by Chiu *et al.*[31,32] Au NPs functionalized with PS-SH (M_n = 1.3 kg/mol, PDI = 1.1) were incorporated into bulk lamellar-forming PS-*b*-P2VP of different molecular weights, consequently varying R/R_0. Only the "center-filled lamellar" phase was observed experimentally as R/R_0 varied from 0.44 to 0.13. Instead of an "edge-filled lamellar" morphology, Chiu *et al.* identified that the NP density delocalized from the domain centers as R/R_0 decreased. The discrepancy between numerical predictions and experiments can in part be attributed to assumptions of monodisperse hard-sphere NPs in the theoretical construct whereas relatively polydisperse particles were employed experimentally.[32]

The relationship between conformational and translational entropy can explain why NPs delocalize from the center and begin to distribute evenly through a BCP domain when the average particle size decreases. Conformational entropy is reduced when polymer chains are frustrated by NP obstacles integrated into the system. Chains stretch and condense to accommodate the inclusions, decreasing the number of possible polymer conformations. Therefore, Thompson *et al*. indicates that for large NPs, conformational entropy dominates the system.[29,30] To avoid excessive chain stretching and compressing around particles, large NPs segregate to a "center-filled lamellar" phase. Ultimately, when the large NPs localize to the center of a lamellar domain, translational entropy is decreased, but not enough to offset the gain in conformational entropy.[29-32] Conversely, translational entropy dominates a BCP nanocomposite containing small NPs. Corroborated by the "edge-filled lamellar" phase shown by Thompson *et al*., the gain in translational entropy attributed to redistributing small particles outweighs the sacrifice to conformational entropy .[29,30] This explanation is congruous to the experiments by Chiu *et al.* where the density of particles is higher

at the center of the PS domains when the NP and thus R/R_0 is large (R/R_0 = 0.44 case) to maximize conformational entropy.[32] Similarly, particles are more evenly distributed throughout the domain when the NP and thus R/R_0 is small (R/R_0 = 0.32 case) to maximize translational entropy.[32]

1.3.3 Effect of Polymer Brush Areal Chain Density. Not only does the chemistry of polymer brushes (Section 1.3.1) help stabilize NPs and promote dispersion, but additional tunable ligand parameters will also contribute to precise NP placement in self-assembling BCP nanocomposites. The following discussions will present studies that have attempted to isolate the individual effects of areal chain density (σ, Section 1.3.3) and ligand molecular weight (M_n, Section 1.3.4). First, Kim *et al*. established a robust procedure to control the position of a homopolymer functionalized Au NPs in bulk lamellar-forming PS-*b*-P2VP by adjusting ligand areal chain density, also referred to as grafting density.[33] A symmetric lamellar-forming PS-*b*-P2VP (M_n = 196.5 kg/mol, PDI = 1.11) mixed with PS-SH (M_n = 3.4 kg/mol, PDI = 1.15) functionalized Au NPs at a final weight fraction of 0.15 was studied.[33] When the grafting densities of PS-SH brushes on the particle surfaces were relatively high (σ = 1.64 chains/nm^2) the NPs were located at the center of the PS domains.[33] As the areal chain density decreased to σ = 1.45 chains/nm^2, the NPs began delocalizing from the domain centers towards the PS/P2VP interfaces until they were mostly located at the PS/P2VP interfaces when σ = 1.22 chains/nm^2.[33] Finally, at a relatively low grafting density of σ = 0.83 chains/nm^2, essentially all of the PS-SH functionalized Au NPs were segregated to the PS/P2VP interfaces.[33] Kim *et al.* concluded that as the surface coverage of the polymer brush layer decreases, the NPs transition from being energetically attracted to the PS block to the PS/P2VP interface at some critical areal chain density (σ_C).

The interaction between Au and PS is relatively weak compared to the favorable interaction between Au and P2VP. Therefore, the driving force for NP relocation from the PS block to the PS/P2VP interface as the brush grafting density decreases from σ = 1.64 chains/nm^2 to σ = 1.22 chains/nm^2 is attributed to a hindered shielding effect of the Au NP core.[33] At an areal chain density

less than σ_C = 1.3 chains/nm^2, the ligands coverage is not sufficient enough to screen the enthalpically favorable interaction between the Au NP core and the P2VP block and the NPs are therefore adsorbed to the PS/P2VP interfaces. Consequently, if the NP material has a chemical affinity to either polymer blocks, varying the grafting density of the functionalized polymer brushes, thereby screening (high σ) or revealing (low σ) the NP core, provides a versatile approach to directing the location of isotropic NPs in a BCP nanocomposite.

1.3.4 Effect of Polymer Brush Molecular Weight. Because of the curved surfaces of isotropic NPs, the achievable areal chain densities on spherical Au NPs are 1.2 to 23.5 times greater than the coverage that can be attained on flat Au substrates.[34] Increasing the molecular weight, and thus the molecule length of a ligand, will enhance steric hindrance on a NP surface and more effectively shield the NP core at low surface coverages.[34] However, as discussed in Section 1.3.3, decreasing grafting density below σ_C, when the NP core material favors one of the BCP blocks, will promote NP adsorption to the BCP interface. The ensuing conversation will present another study from Kim *et al.* to demonstrate the correlation between ligand molecular weight, critical areal chain density and inevitably, NP adsorption.

The dispersion of PS-SH functionalized Au NPs, with the following brush molecular weights at various σ, in symmetric lamellar-forming PS-*b*-P2VP (M_n = 196.5 kg/mol, PDI = 1.11) bulk films was studied: M_n = 1.5 kg/mol, PDI = 1.2; M_n = 2.5 kg/mol, PDI = 1.1; M_n = 3.4 kg/mol, PDI = 1.15; M_n = 6.5 kg/mol, PDI = 1.1; and M_n = 13 kg/mol, PDI = 1.1 (denoted $PS_{1.5}$-SH, $PS_{2.5}$-SH, $PS_{3.4}$-SH, $PS_{6.5}$-SH, and PS_{13}-SH, respectively).[35] The phase diagram in Figure 1.3 relates the areal chain density threshold for transitioning NPs from the PS block to the PS/P2VP interface with polymer brush M_n.[35] For example, the critical grafting densities for when $PS_{1.5}$-SH and PS_{13}-SH functionalized Au NPs adhere to the PS/P2VP interface are σ_C = 3.1 chains/nm^2 and σ_C = 0.9 chains/nm^2, respectively.[35] The results suggest that fewer bulky PS-SH brushes, of high molecular weights, are necessary to screen the Au NP interactions and prevent interfacial adsorption.

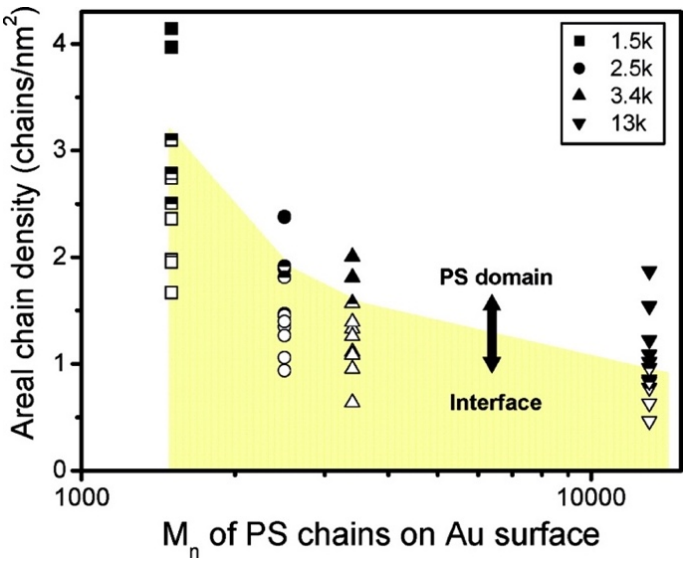

Figure 1.3. Phase diagram for PS-SH functionalized Au NP location as a function of areal chain density and M_n of PS-SH ligands. Filled symbols indicate that NPs are located in the PS domain, at the PS/P2VP interface for open symbols, and at both locations for half-filled symbols. Figure was reprinted (adapted) with permission from Kim, B. J.; Fredrickson, G. H.; Kramer, E. J. *Macromolecules* **2008**, 41, 436-447.[35] Copyright 2008 American Chemical Society.

1.4 Nanoparticle Anisotropy

The preceding conversation focused on how polymer brush chemistry (Section 1.3.1), grafting density (Section 1.3.3), and molecular weight (Section 1.3.4) as well as NP size and BCP molecular weight (Section 1.3.2) affect the dispersion and organization of isotropic NPs in lamellar-forming BCPs. However, fewer studies have explored the effects of NP anisotropy in BCPs. In order to capture their shape and orientation-dependent properties in polymer matrices, outstanding questions still remain regarding how the large BCP nanocomposite parameter space could be optimized to place and, importantly, orient nanorods or nanoplates. To achieve alignment of anisotropic NPs in polymeric systems, alternate methods have been employed. For example, flow-induced NP alignment has been observed as a result of the shear forces in polymer processing techniques including injection molding,[36] doctor blading,[37] spin-coating,[37] and nanofiber drawing.[38]

Magnetic and electric fields have also been applied to orient anisotropic NPs like hexagonal boron nitride platelets[39] and gold nanorods,[40] respectively, in PNCs. Furthermore, researchers have incorporated nanorods and nanoplates into other soft matter assemblies like micelles[41] and liquid crystals[42] to direct NP orientation. However, in contrast to these examples, self-assembling BCPs offer a versatile approach to create continuous nanocomposite films that could be applied to substrates with minimal processing steps. By leveraging the tunable parameter space of PNCs and by matching the NP shape to the assembled BCP morphology, as shown in Figure 1.4, anisotropic NP alignment has the potential to be achieved for a variety of material systems.[43] The majority of the research that combines anisotropic NPs with BCP or BCP-based supramolecules has focused predominately on nanorod inclusions. These studies either use BCP patterns to template nanorod arrays on the polymer film surfaces[44-48] or disperse the nanorods in cylindrical[49-51] or lamellar[49,52,53] domains.

While BCP nanocomposites containing nanorods have garnered increasing attention in recent years, research on BCP nanocomposites with aligned nanoplates has remained relatively uncharted. By adding only a few weight percent of either clay and silica-like or graphite-based nanoplates to polymers, the mechanical, rheological, electrical, thermal, and flame retardant performance of PNCs can be dramatically improved. Researchers have previously been successful at integrating clay[54-57] and graphitic[58-61] plates within BCPs to create composite materials, but the BCP morphology did not play a significant role in the design. These filler systems are relatively large, compared to NPs synthesized using colloidal synthesis techniques, and can be difficult to exfoliate as individual particles. BCPs have therefore been alternatively used as compatibilizers to exfoliate and intercalate the clay[62-64] or graphite-based[65] sheets. Interestingly, in some demonstrations of clay platelets[66,67] and graphene oxide[68] dispersed in BCP matrices, instead of the BCP morphology directing the alignment of these fillers, the particles are templating the direction of BCP assembly. Here, the domains emanate perpendicularly from the planar surface of the

particles. While some mixtures of silica-like or graphite-based sheets and BCPs have been explored, self-assembled BCP composites with these materials aligned by the microdomains of any of the possible morphologies were not show in these studies. Albeit platelets, the clay and graphitic filler systems pose challenges related to their large size and exfoliation procedures to initiate studies of nanoplate alignment guided by self-assembling BCPs. Therefore, a clearly defined nanoplate system is necessary to proceed.

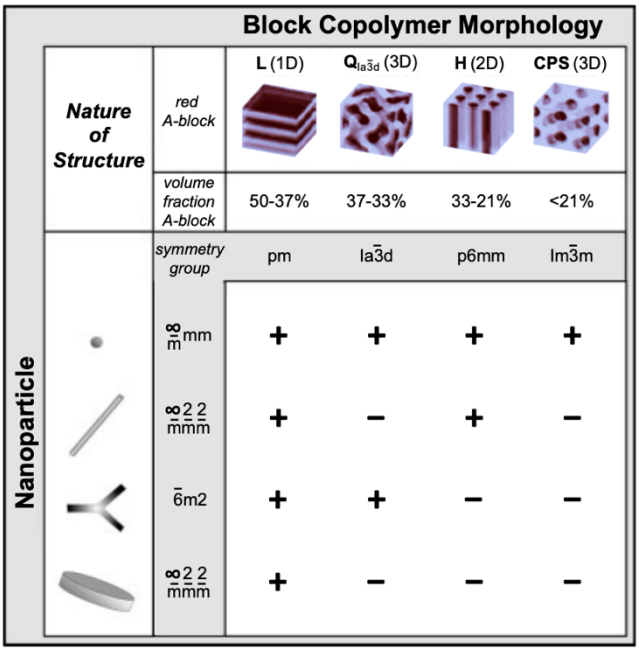

Figure 1.4. Symmetry compatibility chart between the point-groups of the represented NPs and the space-groups of traditional BCP morphologies presented in Figure 1.1. The minority and majority microdomains are represented by the red and blue blocks, respectively. Compatibility is indicated by (+) while incompatibility is indicated by (–), providing design guidelines for BCP composites. Figure was reprinted (adapted) with permission from Bockstaller, M. R.; Mickiewicz, R. A.; Thomas, E. L. *Adv. Mater.* **2005,** 17, 1331-1349.[43] Copyright 2005 John Wiley & Sons, Inc.

1.5 Outline of Thesis Chapters

Following the guidelines from Figure 1.4 for commensurate BCP morphology and NP shape, this thesis begins a systematic exploration of a model polymer functionalized nanoplate integrated into a lamellar-forming BCP. The alignment and morphological effects of nanoplates in lamellar diblock copolymer thin films is investigated by experimentally and/or theoretically studying the influence of NP loading, NP separation, and microdomain orientation with variations in BCP molecular weight. The presented work not only expands our knowledge of PNC phase behavior, but also introduces a framework to further study the parameters that affect nanoplate alignment in BCP nanocomposites. The discussions in the ensuing chapters adapt the thermodynamic insights gained from directing the location of isotropic NPs in BCP domains to understand the factors that impact nanoplate orientation. Ultimately, the goal is to establish a platform to intentionally manipulate the assembly of nanoplates to exploit their shape and orientation-dependent properties. Our ability to control anisotropic NP alignment in PNCs through self-assembling techniques lends itself to creating multifunctional materials with unique properties for various applications.

Chapter 2 establishes a well-defined system to investigate the alignment of nanoplates in a lamellar-forming poly(styrene-*b*-methyl methacrylate) (PS-*b*-PMMA) BCP with domains oriented parallel to the substrate. Monodisperse gadolinium trifluoride rhombic nanoplates doped with ytterbium and erbium [GdF_3:Yb/Er (20/2 mol%)] are synthesized and grafted with phosphoric acid functionalized polyethylene glycol (PEG-PO_3H_2). Designed with chemical specificity to one block, the nanoplates align in the PMMA domain at low volume fractions (ϕ = 0.0083 and ϕ = 0.017). At these low NP loadings, the BCP lamellae are ordered and induce preferential alignment of the GdF_3:Yb/Er nanoplates. However, at high volume fractions (ϕ = 0.050 and ϕ = 0.064), the BCP lamellae are disordered with isotropically dispersed nanoplates. The transition from an ordered BCP system with aligned nanoplates to a disordered BCP with unaligned nanoplates coincides with

the calculated overlap volume fraction, $\phi^* = 0.051$, where the pervaded space of the NPs begin to overlap. Two phenomena are observed in the results: the effect of lamellar formation on nanoplate orientation and the overall phase behavior of the PNCs.

Chapter 3. Within the ordered PS-*b*-PMMA BCP lamellae in Chapter 2, the oriented GdF_3:Yb/Er nanoplates grafted with PEG-PO_3H_2 further assemble into aligned strings at small interparticle separations. Herein, we investigate the origin of these aligned assemblies using X-ray scattering, electron microscopy, and hybrid particle/self-consistent field theory (hSCFT) simulations. From previous reports, the insertion of a nanoplate in a BCP microdomain is expected to perturb the polymer chains and produce a local domain bulge as the PS/PMMA interface distorts to optimize conformational entropy. While experimental techniques are unable to directly resolve this small distortion, the 2D simulations of the equilibrium BCP nanocomposite structure clearly show bulge formation around the nanoplates. As a function of particle separation, the potential of mean force (PMF) calculation reveals a global minimum corresponding to an equilibrium interparticle spacing of 7.0 nm, which agrees well with a mean experimental value of 6.42 nm. Furthermore, the PMF calculation exhibits a small activation barrier due to the high curvature penalty between two nanoplates at a separation distance of 21.7 nm. Ultimately, nanoplate strings form to fulfill the criteria where the energy benefit of decreasing interfacial area and minimizing chain stretching outweighs the energy penalty associated with reducing the translational entropy affiliated with evenly distributing the nanoplates. The simulations also illustrate a narrow tolerance for orientation angles, supporting the high degree of nanoplate alignment observed experimentally. We anticipate that the ability to align and couple anisotropic nanoparticles in BCPs presents opportunities to create functional PNC with orientation-dependent properties.

Chapter 4. The ability to precisely tune the orientation of anisotropic NPs in thin film PNCs is relevant to designing new materials with properties tailored for a specific application. Although in-plane or parallel orientation of these non-spherical NPs has been readily shown, out-of-plane or

vertical alignment of nanorods and nanoplates in PNCs is less trivial. Methods to create composites with vertical particle structures often rely on multistep processes. However, self-assembling BCPs offer a versatile platform to create hierarchical hybrid materials with minimal operations. To direct out-of-plane alignment of anisotropic NPs, and more specifically the GdF_3:Yb/Er nanoplates synthesized in Chapter 2, the research herein exploits symmetric PS-*b*-PMMA (M_n = 73k-*b*-73k g/mol and M_n = 95k-*b*-95k g/mol) with lamellar microdomains oriented perpendicular to the substrate. We show that functionalizing the nanoplate surfaces with PEG-PO_3H_2 brushes is critical to dispersing the NPs in the PMMA domain without disrupting the equilibrium BCP morphology. Subsequently and most notably, vertically oriented lamellar domains successfully guides out-of-plane alignment of the nanoplates through self-assembly. We expect that the approach disclosed in this Chapter will benefit applications that are based on out-of-plane NP alignment by proposing an easy-to-implement technique to attain these vertically oriented hierarchical PNC films.

There are limited theoretically predicted phase diagrams for PNCs because conventional modeling techniques are largely unable to predict the macroscale phase behavior of PNCs. In Chapter 5, we show that recent field-based methods, including PNC field theory (PNC-FT) and theoretically informed Langevin dynamics (TILD), can be used to calculate phase diagrams for polymer-grafted nanoparticles (gNPs) incorporated into a polymer matrix. We calculate binodal curves for the transition from the miscible, dispersed phase to the macrophase separated state as functions of important experimental parameters, including the ratio of the matrix chain degree of polymerization (P) to the grafted chain degree of polymerization (N), the enthalpic repulsion between the matrix and grafted chains, the grafting density (σ), the size of the NPs, and the NP volume fraction. We demonstrate that thermal and polymer conformational fluctuations enhance the degree of phase separation in gNP-PNCs, a result of depletion interaction effects. We support this conclusion by experimentally investigating the phase separation of PMMA-grafted silica NPs in a PS matrix as a function of P/N. The simulations only agree with experiments when fluctuations

are included because fluctuations are needed to properly capture the depletion interactions between the gNPs. We clarify the role of conformational entropy in driving depletion interactions in PNCs and suggest that inconsistencies in the literature may be due to polymer chain length effects since conformational entropy increases with increasing chain length.

Chapter 6 summarizes the main conclusions from each chapter of this dissertation and also discusses additional projects, proposed for future work. Appendix A, Appendix B, Appendix C, and Appendix D contains the supporting information for Chapter 2, Chapter 3, Chapter 4, and Chapter 5, respectively.

1.6 References

(1) LeBaron, P. C.; Wang, Z.; Pinnavaia, T. J. Polymer-Layered Silicate Nanocomposites: An Overview. *Appl. Clay Sci.* **1999**, 15, 11–29.

(2) Moll, J. F.; Akcora, P.; Rungta, A.; Gong, S.; Colby, R. H.; Benicewicz, B. C.; Kumar, S. K. Mechanical Reinforcement in Polymer Melts Filled with Polymer Grafted Nanoparticles. *Macromolecules* **2011**, 44, 7473-7477.

(3) Moniruzzman, M.; Winey, K. I. Polymer Nanocomposites Containing Carbon Nanotubes. *Macromolecules* **2006**, 39, 5194-5205.

(4) Beecroft, L. L.; Ober, C. K. Nanocomposite Materials for Optical Applications. *Chem. Mater.* **1997**, 9, 1302-1317.

(5) Hore, M. J. A.; Composto, R. J. Nanorod Self-Assembly for Tuning Optical Absorption. *ACS Nano* **2010**, 4, 6941-6949.

(6) Jiang, G.; Hore, M. J. A.; Gam, S.; Composto, R. J. Gold Nanorods Dispersed in Homopolymer Films: Optical Properties Controlled by Self-Assembly and Percolation of Nanorods. *ACS Nano* **2012**, 6, 1578-1588.

(7) Wang, D.; Hore, M. J. A.; Ye, X.; Zheng, C.; Murray, C. B.; Composto, R. J. Gold Nanorod Length Controls Dispersion, Local Ordering, and Optical Absorption in Polymer Nanocomposite Film. *Soft Matter* **2014**, 10, 3404-3413.

(8) Xu, C.; Ohno, K.; Ladmiral, V.; Composto, R. J. Dispersion of Polymer-Grafted Magnetic Nanoparticles in Homopolymers and Block Copolymers. *Polymer* **2008**, 49, 3568-3577.

(9) Lo, C.-T.; Li, M.-H.; Lin, W.-T. The Dispersion State of Magnetic Nanorods in Homopolymer and Block Copolymers. *J. Chem. Phys.* **2015**, 142, 184903.

(10) Winey, K. I.; Vaia, R. I., Polymer Nanocomposites. *MRS Bulletin* **2007**, *32* , 314-322.

(11) Alivisatos, A. P. Semiconductor Clusters, Nanocrystals, and Quantum Dots. *Science*. **1996**, 271, 933-937.

(12) Peng, X.; Manna, L.; Yang, W.; Wickham, J.; Scher, E.; Kadavanich, A.; Alivisatos, A. P. Shape Control of CdSe Nanocrystals. *Nature* **2000**, 404, 59−61.

(13) Robel, I.; Kuno, M.; Kamat, P. V. Size-Dependent Electron Injection from Excited CdSe Quantum Dots into TiO_2 Nanoparticles. *J. Am. Chem. Soc.* **2007**, 129, 4136−4137.

(14) Yun, H. J.; Paik, T.; Diroll, B.; Edley, M. E.; Baxter, J. B.; Murray, C. B. Nanocrystal Size-Dependent Efficiency of Quantum Dot Sensitized Solar Cells in the Strongly Coupled CdSe Nanocrystals/TiO_2 System. *ACS Appl. Mater. Interfaces* **2016**, *23*, 14692-14700.

(15) Kumar, S. K.; Jouault, N. Nanocomposites with Polymer Grafted Nanoparticles. *Macromolecules* **2013**, 46, 3199-3214.

(16) Paik, T.; Ko, D.-K.; Gordon, T. R.; Doan-Nguyen, V.; Murray, C. B. Studies of Liquid Crystalline Self-Assembly of GdF_3 Nanoplates by In-Plane, Out-of-Plane SAXS. *ACS Nano* **2011**, 5, 8322-8330.

(17) Ye, X.; Millan, J. A.; Engel, M.; Chen, J.; Diroll, B. T.; Glotzer, S. C.; Murray, C. B. Shape Alloys of Nanorods and Nanospheres from Self-Assembly. *Nano Lett.* **2013**, 13, 4980-4988.

(18) Paik, T.; Murray, C. B. Shape-Directed Binary Assembly of Anisotropic Nanoplates: A Nanocrystal Puzzle with Shape-Complementary Building Blocks. *Nano Lett.* **2013**, 13, 2952-2956.

(19) Paik, T.; Diroll, B. T.; Kagan, C. R.; Murray, C. B. Binary and Ternary Superlattices Self-Assembled from Colloidal Nanodisks and Nanorods. *J. Am. Chem. Soc.* **2015**, 137, 6662-6669.

(20) Diroll, B. T.; Greybush, N. J.; Kagan, C. R.; Murray, C. B. Smectic Nanorod Superlattices Assembled on Liquid Subphases: Structure, Orientation, Defects, and Optical Polarization. *Chem. Mater.* **2015**, 27, 2998-3008.

(21) Rubinstein, M.; Colby, R., *Polymers Physics*. Oxford: 2003.

(22) Bates, F. S.; Fredrickson, G. H. Block Copolymers—Designer Soft Materials. *Physics Today* **1999**, 52, 32-38.

(23) Matsen, M. W.; Schick, M. Stable and Unstable Phases of a Diblock Copolymer Melt. *Phys. Rev. Lett.* **1994**, 72, 2660-2663.

(24) Matsen, M. W.; Bates, F. S. Unifying Weak- and Strong-Segregation Block Copolymer Theories. *Macromolecules* **1996**, 29, 1091-1098.

(25) Darling, S. B. Directing the Self-Assembly of Block Copolymers. *Prog. Polym. Sci.* **2007**, 32, 1152-1204.

(26) Bates, F. S.; Fredrickson, G. H. Block Copolymer Thermodynamics: Theory and Experiment. *Annu. Rev. Phys. Chem.* **1990**, 41, 525-557.

(27) Kim, B. J.; Bang, J.; Hawker, C. J.; Chiu, J. J.; Pine, D. J.; Jang, S. G.; Yang, S.-M.; Kramer, E. J. Creating Surfactant Nanoparticles for Block Copolymer Composites through Surface Chemistry. *Langmuir* **2007**, 23, 12693-12703.

(28) Pieranski, P. Two-Dimensional Interfacial Colloidal Crystals. *Phys. Rev. Lett.* **1980**, 45, 569-572.

(29) Thompson, R. B.; Ginzburg, V. V.; Matsen, M. W.; Balazs, A. C. Predicting the Mesophases of Copolymer-Nanoparticle Composites. *Science* **2001**, 292, 2469-2472.

(30) Thompson, R. B.; Ginzburg, V. V.; Matsen, M. W.; Balazs, A. C. Block Copolymer-Directed Assembly of Nanoparticles: Forming Mesoscopically Ordered Hybrid Materials. *Macromolecules* **2002**, 35, 1060-1071.

(31) Chiu, J. J.; Kim, B. J.; Kramer, E. J.; Pine, D. J. Control of Nanoparticle Location in Block Copolymers. *J. Am. Chem. Soc.* **2005**, 14, 5036-5037.

(32) Chiu, J. J.; Kim, B. J.; Yi, G.-R.; Bang, J.; Kramer, E. J.; Pine, D. J. Distribution of Nanoparticles in Lamellar Domains of Block Copolymers. *Macromolecules* **2007**, 40, 3361-3365.

(33) Kim, B. J.; Bang, J.; Hawker, C. J.; Kramer, E. J. Effect of Areal Chain Density on the Location of Polymer-Modified Gold Nanoparticles in a Block Copolymer Template. *Macromolecules* **2006**, 39, 4108-4114.

(34) Shan, J.; Tenhu, H. Recent Advances in Polymer Protected Gold Nanoparticles: Synthesis, Properties and Applications. *Chem. Commun.* **2007**, 0, 4580-4598.

(35) Kim, B. J.; Fredrickson, G. H.; Kramer, E. J. Effect of Polymer Ligand Molecular Weight on Polymer-Coated Nanoparticle Location in Block Copolymers. *Macromolecules* **2008**, 41, 436-447.

(36) Kojima, Y.; Usuki, A.; Kawasumi, M.; Okada, A; Fukushima, Y.; Kurauchi, T.; Kamigaito, O. Mechanical Properties of Nylon 6-Clay Hybrid. *J. Mater. Res.* **1993**, 8, 1185-1189.

(37) Tyan, H.-L.; Liu, Y.-C.; Wei, K.-H. Thermally and Mechanically Enhanced Clay/Polyimide Nanocomposite via Reactive Organoclay. *Chem. Mater.* **1999**, 11, 1942-1947.

(38) Wang, P.; Zhang, L.; Xia, Y.; Tong, L.; Xu, X.; Ying, Y. Polymer Nanofibers Embedded with Aligned Gold Nanorods: A New Platform for Plasmonic Studies and Optical Sensing. *Nano Lett.* **2012**, 12, 3145-3150.

(39) Lin, Z.; Liu, Y.; Raghavan, S.; Moon, K. S.; Sitaraman, S. K.; Wong, C. P. Magnetic Alignment of Hexagonal Boron Nitride Platelets in Polymer Matrix: Toward High Performance Anisotropic Polymer Composites for Electronic Encapsulation. *ACS Appl. Mater. Interfaces* **2013**, 5, 7633-7640.

(40) Maity, S.; Wu, W.-C.; Tracy, J. B.; Clarke, L. I.; Bochinski, J. R. Nanoscale Steady-State Temperature Gradients within Polymer Nanocomposites Undergoing Continuous-Wave Photothermal Heating from Gold Nanorods. *Nanoscale* **2017**, 9, 11605-11618.

(41) Li, W.; Zhang, P.; Dai, M.; He, J.; Babu, T.; Xu, Y.-L.; Deng, R.; Liang, R.; Lu, M.-H.; Nie, Z.; Zhu, J. Ordering of Gold Nanorods in Confined Spaces by Direted Assembly. *Macromolecules* **2013**, 46, 2241-2248.

(42) Zhang, Y.; Liu, Q.; Mundoor, H.; Yuan, Y.; Smalyukh, I. I. Metal Nanoparticle Dispersion, Alignment, and Assembly in Nematic Liquid Crystals for Applications in Switchable Plasmonic Color Filters and E-Polarizers. *ACS Nano* **2015**, 9, 3097-3108.

(43) Bockstaller, M. R.; Mickiewicz, R. A.; Thomas, E. L. Block Copolymer Nanocomposites: Perspectives for Tailored Functional Materials. *Adv. Mater.* **2005,** 17, 1331-1349.

(44) Zhang, Q.; Gupta, S.; Emrick, T.; Russell, T. P. Surface-Functionalized CdSe Nanorods for Assembly in Diblock Copolymer Templates. *J. Am. Chem. Soc.* **2005**, 128, 3898-3899.

(45) Son, J. G.; Bae, W. K.; Kang, W.; Nealey, P. F.; Char, K. Placement Control of Nanomaterial Arrays on the Surface-Reconstructed Block Copolymer Thin Films. *ACS Nano* **2009**, 3, 3927-3923.

(46) Ploshnik, E.; Salant, A.; Banin, U.; Shenhar, R. Hierarchical Surface Patterns of Nanorods Obtained by Co-Assembly with Block Copolymers in Ultrathin Films. *Adv. Mater.* **2010**, 22, 2774-2779.

(47) Ploshnik, E.; Salant, A.; Banin, U.; Shenhar, R. Co-Assembly of Block Copolymers and Nanorods in Ultrathin Films: Effects of Copolymer Size and Nanorod Filling Fraction. *Phys. Chem. Chem. Phys.* **2010**, 12, 11885-11893.

(48) Liu, Z.; Huang, H.; He, T. Large-Area 2D Gold Nanorod Arrays Assembled on Block Copolymer Templates. *Small* **2013**, 9, 505-510.

(49) Thorkelsson, K.; Mastroianni, A. J.; Ercius, P.; Xu, T. Direct Nanorod Assembly Using Block Copolymer-Based Supramolecules. *Nano Lett.* **2011**, 12, 498-504.

(50) Thorkelsson, K.; Nelson, J. H.; Alivisatos, A. P.; Xu, T. End-to-End Alignment of Nanorods in Thin Films. *Nano Lett.* **2013**, 13, 4908-4913.

(51) Rasin, B.; Chao, H.; Jiang, G.; Wang, D.; Riggleman, R. A.; Composto, R. J. Dispersion and Alignment of Nanorods in Cylindrical Block Copolymer Thin Films. *Soft Matter* **2016**, 12, 2177-2185.

(52) Deshmukh, R. D.; Liu, Y.; Composto, R. J. Two-Dimensional Confinement of Nanorods in Block Copolymer Domains. *Nano Lett.* **2007**, 7, 3662-3668.

(53) Lo, C.-T.; Lin, W.-T. Effect of Rod Length on the Morpholgoy of Block Copolymer/Magnetic Nanorod Composites. *J. Phys. Chem. B* **2013**, 117, 5261-5270.

(54) Laus, M.; Francescangeli, O.; Sandrolini, F. New Hybrid Nanocomposites Based on an Organophilic Clay and Poly(Strene-*b*-Butadiene) Copolymers. *J. Mater. Res.* **1997**, 12, 3134-3139.

(55) Jain, A.; Gutmann, J. S.; Garcia, C. B. W.; Zhang, Y.; Tate, M. W.; Grunner, S. M.; Wiesner, U. Effect of Filler Dimensionality on the Order-Disorder Transition of a Model Block Copolymer Nanocomposite. *Macromolecules* **2002**, 35, 4862-4865.

(56) Zhao, H.; Shipp, D. A. Preparation of Poly(Styrene-*Block*-Butyl Acrylate) Block Copolymer-Silicate Nanocomposites. *Chem. Mater.* **2003**, 15, 2693-2695.

(57) Carastan, D. J.; Demarquette, N. R.; Vermogen, A.; Masenelli-Varlot, K. Linear Viscoelasticity of Styrenic Block Copolymers-Clay Nanocomposites. *Rheol Acta* **2008**, 47, 521-536.

(58) Rath, T.; Li, Y. Nanocomposites Based on Polystyrene-*b*-Poly(Ethylene-*r*-Butylene)-*b*-Polystyrene and Exfoliated Graphite Nanoplates: Effect of Nanoplatelet Loading on Morphology and Mechanical Properties. *Composites: Part A* **2011**, 42, 1995-2002.

(59) Panaitescu, D. M.; Gabor, R. A.; Nicolae, C. A.; Parau, A. C.; Vitelaru, C.; Raditoiu, V.; Chipara, M. Block Copolymer Elastomer with Graphite Filler: Effect of Processing Conditions and Silane Coupling Agent on the Composite Properties. *Polymers* **2018**, 10, 46.

(60) Lv, Q.-C.; Li, Y.; Zhong, Z.-K.; Wu, H.-J.; He, F.-A., Lam, K.-H. Preparation and Dielectric Properties of Novel Composites Based on Oxidized Styrene-Butadienestyrene Copolymer and Polyaniline Modified Exfoliated Graphite Nanoplates. *Appl. Surf. Sci.* **2018**, 441, 945-954.

(61) Fu, X.; Dong, X.; Liu, Y.; Zhao, X.; Zhang, N.; Qi, S.; Wang, D.; Yang, G. Combined Graphene and Poly(Butylene Terphthalate)-*Block*-Poly(Tetramethylene Glycol) Enhance the Mechanical Performance of Polyamide-6. *Eur. Polym. J.* **2019**, 110, 97-106.

(62) Fisher, H. R.; Gielgens, L. H.; Koster, T. P. M. Nancomposites from Polymers and Layered Minerals. *Acta Polym.* **1999**, 50, 122-126.

(63) Zhao, H.; Farrell, B. P.; Shipp, D. A. Nanopatterns of Poly(Styrene-*Block*-Butyl Acrylate) Block Copolymer Brushes on the Surfaces of Exfoliated and Intercalated Clay Layers. *Polymers* **2004**, 45, 4473-4481.

(64) Mazzucco, M. L. C.; Marchesin, M. S.; Fernandes, E. G.; Da Costo, R. A.; Marini, J.; Bretas, R. E. S.; Bartoli, J. R. Nanocomposites of Acrylonitrile-Butadiene-Styrene/Montmorillonite/ Styrene Block Copolymers: Structural, Rheological, Mechanical and Fammability Studies on the Effect of Oganoclays and Compatibiliers Using Statistically Designed Experiments. *J. Compos. Mater.* **2016**, 50, 771-782.

(65) Khawas, K.; Daripa, S.; Kumari, P.; Kuila, B. K. Electrochemical and Electronic Properties of Transparent Coating from Highly Solution Processable Graphene Using Block Copolymer Supramolecular Assembly: Application Toward Metal Ion Sensing and Resistive Switching Memory. *ACS Omega* **2018**, 3, 7106-7116.

(66) Hasegawa, N.; Usuki, A. Arranged Microdomain Structures Induced by Clay Silicate Layers in Block Copolymer-Clay Nanocomposites *Polym. Bull.* **2003**, 51, 77-83.

(67) Ha, Y.-H.; Kwon, Y.; Breiner, T.; Chan, E. P.; Tzianetopoulou, T.; Cohen, R. E.; Boyce, M. C.; Thomas, E. L. An Orientationally Order Hierarchical Exfoliated Clay-Block Copolymer Nanocomposite. *Macromolecules* **2005**, 38, 5170-5179.

(68) Choi, K.-I.; Kim, T.-H.; Lee, Y.; Kim, H.; Lee, H.; Yuan, G.; Satija, S. K.; Choi, J.-H.; Ahn, H.; Koo, H. Perpendicular Orientation of Diblock Compolymers Induced by Confinement Between Graphene Oxide Sheets. *Langmuir* **2018**, 34, 1681-1690.

CHAPTER 2: Alignment of Nanoplates in Lamellar Diblock Copolymer Domains and the Effect of Particle Volume Fraction on Phase Behavior

Content in this chapter was reprinted (adapted) with permission from Nadia M. Krook, Jamie Ford, Manuel Maréchal, Patrice Rannou, Jeffrey S. Meth, Christopher B. Murray, Russell J. Composto *ACS Macro Lett.* **2018**, 7, 1400-1407.

2.1 Introduction

Polymer nanocomposites (PNCs) are multicomponent systems that integrate fillers, with a characteristic length on the nanoscale, into polymeric matrices. PNCs enable the design and fabrication of heterogeneous materials with enhanced properties that would not be realized with each constituent alone.[1-8] However, the properties of these inorganic-organic hybrid materials depend not only on the individual characteristics of both the nanoparticles (NPs) and the matrix, but also on the dispersion and organization of the NPs.[6] Advances in both theory and experiments describe methods to control the spatial distribution of NPs in polymers by means of tailoring ligand and matrix parameters such as chemistry and chain length.[6,9-13] Both enthalpic and entropic interactions play a critical role in determining the dispersion behavior of NPs. However, control over the organization of nanoscale fillers is limited to variations of either aggregation or dispersion in homopolymer matrices. Instead, nanocomposites that exploit microphase-separating diblock copolymers (BCPs) can facilitate hierarchical arrangements if favorable thermodynamic and geometric factors exist between the particle system and polymer template.[14,15] A large body of work has been dedicated to understanding the polymer physics that drive the placement of isotropic particles (spheres) in BCPs.[16-20] However, if synthetic polymer materials, such as BCPs, could strategically control particle orientation, anisotropic properties of non-spherical NPs (rods, tubes, plates) could be leveraged to influence collective properties of PNCs for advanced coating technologies. For example, PNC films containing aligned CdSe nanorods or nanoplates could

improve solar cell efficiency by enhancing the absorption of solar light.[21-24] Furthermore, self-assembled barrier materials could be formed by orienting anisotropic fillers and creating tortuous paths that decrease permeability of diffusing molecules.[25]

To date, there have been limited studies that incorporate non-spherical particles into BCP matrices. Research on anisotropic NP-BCP composite materials has been limited to the distribution and alignment of one-dimensional NPs, specifically nanorods, in or on the surface of lamellar[26-28] and cylindrical-forming[26,28-31] BCPs. Currently, precise control over the placement and orientation of individually dispersed,[21,24] nanoplates in self-assembling BCPs remains largely unexplored. Instead, strategies to disperse and align nanoplates in PNCs have focused on a variety of processing techniques of two-dimensional materials in homopolymer matrices. These methods have included applying a shear stress,[33-34] magnetic field alignment,[35-37] and top-down approaches.[38,39] However, challenges associated with common two-dimensional materials (e.g. clay and graphite sheets), used in homopolymer composite studies, prevent their integration into BCP domains. These constraints include size and shape polydispersity of the particles, plate dimensions that are incompatible with BCP domain size, and difficulties functionalizing the particle surfaces with polymer brushes for BCP compatibility.

Therein lies the motivation of the presented work: establish a *model nanoplate system* that addresses the challenges, presented above, to study self-assembled thin film PNCs that employ a microphase-separating BCP to both sequester and drive preferential alignment of nanoplates. This research investigates a facile fabrication method to precisely manipulate architectures of nanoplate assemblies, facilitated by polymer brushes, in a lamellar-forming BCP with parallel domains. By understanding the thermodynamic variables that control the position and orientation of nanoplates in BCPs, a wider range of nanocomposite structures designed for specific properties could be made accessible.

2.2 Results

In this work, we synthesize crystalline gadolinium trifluoride rhombic nanoplates doped with ytterbium and erbium [GdF_3:Yb/Er (20/2 mol%)], with oleic acid (OA) on their surfaces, from a large library of rare-earth fluoride based nanocrystals. By varying synthesis parameters such as precursor or rare-earth dopant type and amounts, reaction time and temperature, and ramp rate, a variety of morphologies and sizes have been realized.[40,41] Of this extensive library, GdF_3:Yb/Er NPs have been selected to study nanoplate alignment and organization in BCPs as they are rigid, monodisperse in both size and shape, compatible with BCP dimensions, and surface modifiable.[42] Figure 2.1a features a transmission electron microscopy (TEM) image of these nanoplates assembled in a monolayer. Their longest and shortest diagonals are 35 nm and 22 nm, respectively, and their thicknesses are 3 nm (Figure A.1).

To complement the nanoplate geometry, this study systematically explores a nearly symmetric (M_n= 38k-*b*-36.8k g/mol) lamellar-forming poly(styrene-*b*-methyl methacrylate) (PS-*b*-PMMA) as the host BCP. In this BCP system, PMMA preferentially wets silicon oxide. Consequently, after thermal annealing spin-coated PS-*b*-PMMA films under vacuum at 190ºC for 48 hours, not only do structures with high fidelity form, but the lamellae orient parallel to the substrate. Figure 2.1b shows a representative cross-sectional image of the parallel lamellae. Although the GdF_3:Yb/Er diagonal lengths are commensurate with microdomain period (37 nm[43]), the nanoplate thickness is relatively small. Therefore, with compatible dimensions, the selected PS-*b*-PMMA serves as an ideal template to simultaneously confine and align the nanoplates within its domains.

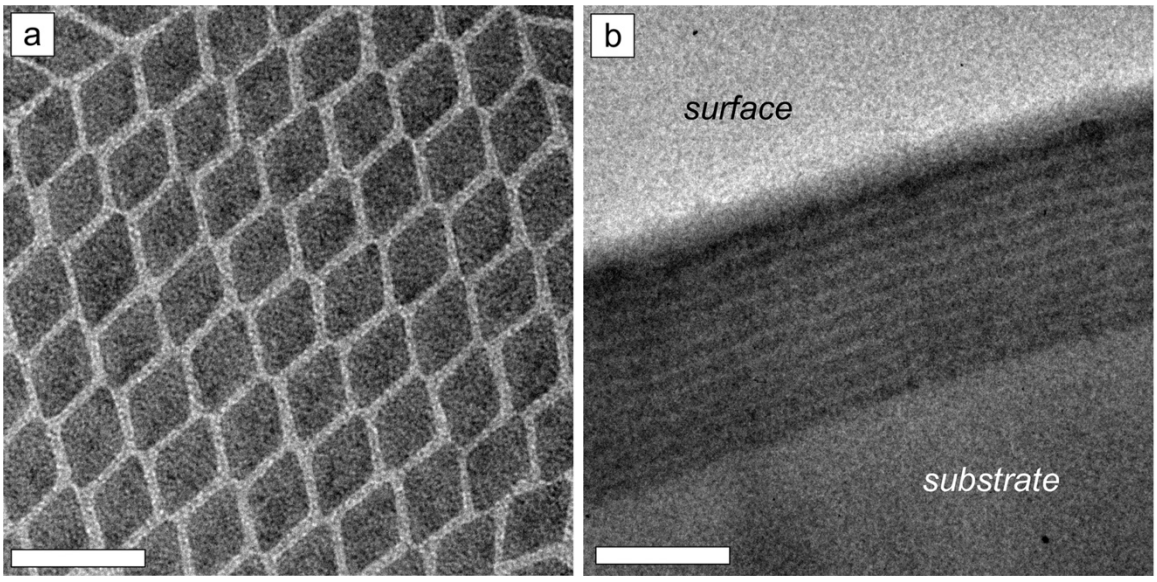

Figure 2.1. A representative (a) top-down TEM (JEM-1400, 120 kV) image of an OA stabilized GdF_3:Yb/Er (20/2 mol%) monolayer and (b) a cross-sectional TEM (JEM-2100, 80 kV) image of a neat lamellar-forming Mn = 38k-*b*-36.8k g/mol PS-b-PMMA film (thickness of ~370 nm) annealed at 190ºC for 48 hours. The light domain is PMMA and the dark domain is PS. The scale bars are (a) 50 nm and (b) 200 nm.

For successful incorporation into the BCP, the nanoplates must be miscible with either block of the PS-*b*-PMMA template. However, decorated with short hydrocarbon chains, the nanoplates are immiscible with both PS and PMMA. Therefore, displacing OA is a requisite to embed the nanoplates into the BCP. More specifically, designing a GdF_3:Yb/Er system with an enthalpic attraction to one of the BCP domains is crucial and relies on chemical modification of the particle surfaces. The following sections will describe the development of the nanoplate/ligand system, its integration into a homopolymer matrix, and the fabrication of thin film BCP PNCs with parallel lamellar domains that direct nanoplate alignment. All experimental details can be found in Appendix A.

A direct solution-phase exchange was established to replace OA with a ligand that interacts favorably with one of the BCP domains. Since the Flory−Huggins interaction parameter (χ) for polyethylene glycol (PEG) and PMMA is slightly negative, mixing of the two polymers is encouraged.[44] Therefore, as depicted in Figure 2.2a, tethering phosphoric acid functionalized M_n = 5 kg/mol PEG (PEG-PO_3H_2) on the nanoplate surfaces introduces chemical specificity to stabilize the NPs in PMMA. Consequently, GdF_3:Yb/Er NPs were functionalized with PEG-PO_3H_2 (Figure A.2) at a grafting density of σ = 0.62 chains/nm^2 (Figure A.3). To confirm polymer compatibility for the PMMA domain of the BCP, the polymer functionalized nanoplates were first dispersed in M_n = 20 kg/mol homopolymer PMMA thin films (~37-52 nm). Figure 2.2 shows the nanocomposite films with increasing nanoplate volume fractions (ϕ = 0.040, ϕ = 0.066, ϕ = 0.10, ϕ = 0.14, and ϕ = 0.20). The top-down TEM characterization qualitatively describes the in-plane dispersion and shows populations of edge-on and planar nanoplates. Not only are the nanoplates well-dispersed in the *xy*-plane, but a tilt series of the PNC from Figure 2.2b (ϕ = 0.040) corroborates that the particles are dispersed with a distribution of orientation angles (Supplementary Digital File 1). Additionally, the PEG-PO_3H_2 modified GdF_3:Yb/Er neither segregate to the air nor substrate surfaces. Not only was establishing good dispersion in PMMA homopolymer important in preparation for nanoplate integration into PS-*b*-PMMA lamellae (shown in the subsequent section), but it also highlights a lack of orientational control that we aim to achieve with a self-assembling BCP template.

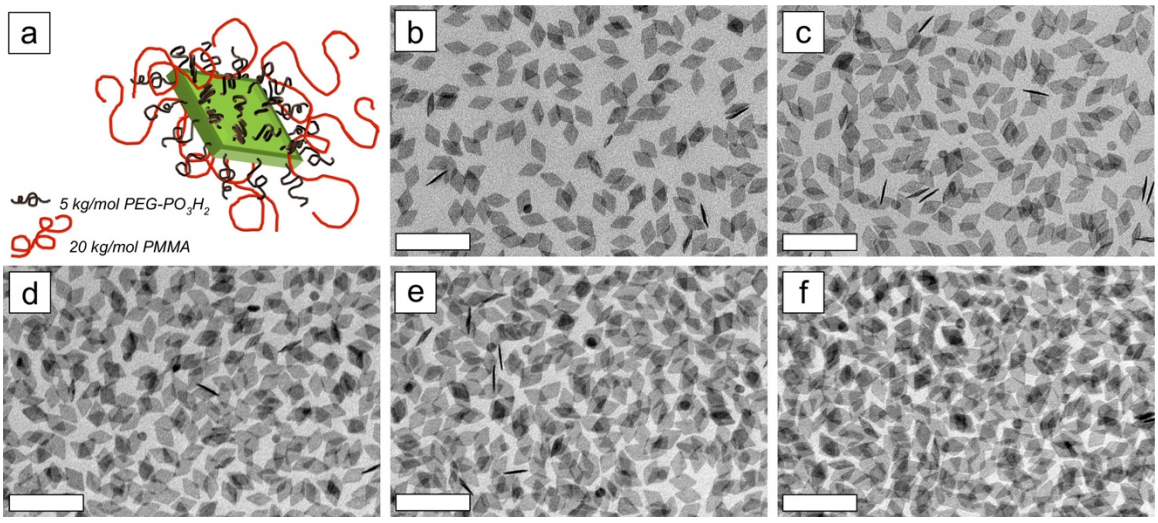

Figure 2.2. Schematic in (a) illustrating 5 kg/mol PEG-PO_3H_2 functionalized GdF_3:Yb/Er (20/2 mol%) in M_n = 20 kg/mol PMMA with representative top-down TEM (JEM-1400, 120 kV) images of the corresponding as-cast composite films (thickness range of ~37-52 nm) with the following volume fractions of nanoplates: (b) ϕ = 0.040, (c) ϕ = 0.066, (d) ϕ = 0.10, (e) ϕ = 0.14, and (f) ϕ = 0.20. All scale bars are 100 nm.

Cross-sectional scanning transmission electron microscopy (STEM) images in Figure 2.3 show the nanoplates dispersed in M_n= 38k-*b*-36.8k g/mol PS-*b*-PMMA at increasing volume fractions (larger versions of the images are included in Figure A.4). The spin-coated films were thermally annealed under vacuum at 190ºC for 48 hours. It is important to note that in the as-cast PNC, before thermal annealing, the nanoplates are well-dispersed and the BCP is disordered (Figure A.5). However, after thermal treatment, we note that in the composites with the lowest NP loadings (ϕ = 0.0083 in Figure 2.3a and ϕ = 0.017 in Figure 2.3b), individual nanoplates not only localize in the light PMMA domain, but parallel lamellae can order in the presence of these nanoplates to direct their alignment. These low loading samples can be classified as ordered BCP systems with aligned nanoplates. Here, the rhombic nanoplates are confined and aligned in the PMMA domain, sandwiched between the BCP chains. At the highest GdF_3:Yb/Er volume fractions

(ϕ = 0.050 in Figure 2.3e and ϕ = 0.064 in Figure 2.3f), lamellar formation is not observed and the nanoplates are isotropically dispersed. These highly loaded samples can be classified as disordered BCP systems with unaligned nanoplates. However, at intermediate volume fractions (ϕ = 0.027 in Figure 2.3c and ϕ = 0.038 in Figure 2.3d) the BCP based PNCs demonstrate a coexisting behavior. These intermediary films show regions devoid of NPs where lamellar formation persists while other regions exhibit a disordered BCP with unaligned nanoplates. The schematic in Figure 2.4 illustrates the transition in phase behavior from ordered BCP with aligned nanoplates to disordered BCP with unaligned nanoplates as a function of NP loading. The nanoplates randomly orient in the absence of lamellar formation (beyond ϕ = 0.038), characteristic of their dispersion behavior in the PMMA homopolymer. Therefore, an ordered BCP is essential to preferentially align nanoplates.

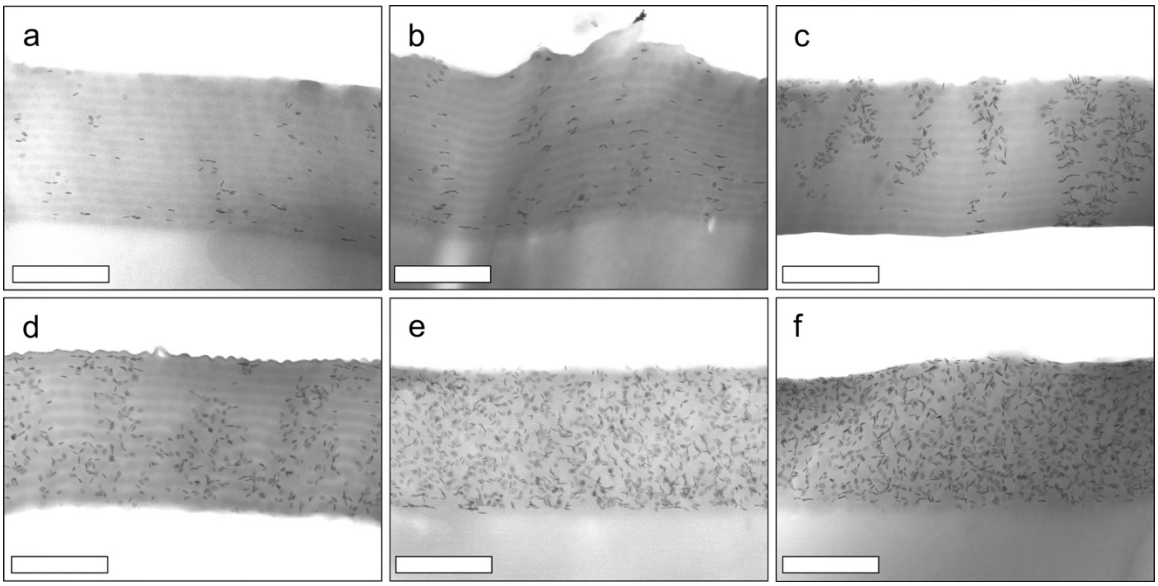

Figure 2.3. Representative cross-sectional STEM (JEOL-7500F HRSEM, 30 kV) images of annealed (190ºC, 48 hours) and ultramicrotomed lamellar-forming M_n = 38k-*b*-36.8k g/mol PS-*b*-PMMA films (thickness range of ~445-550 nm) with the following volume fractions of 5 kg/mol PEG-PO_3H_2 functionalized GdF_3:Yb/Er (20/2 mol%) nanoplates: (a) ϕ = 0.0083, (b) ϕ = 0.017, (c) ϕ = 0.027, (d) ϕ = 0.038, (e) ϕ = 0.050 and (f) ϕ = 0.064. The light domain is PMMA and the dark domain is PS. All scale bars are 300 nm.

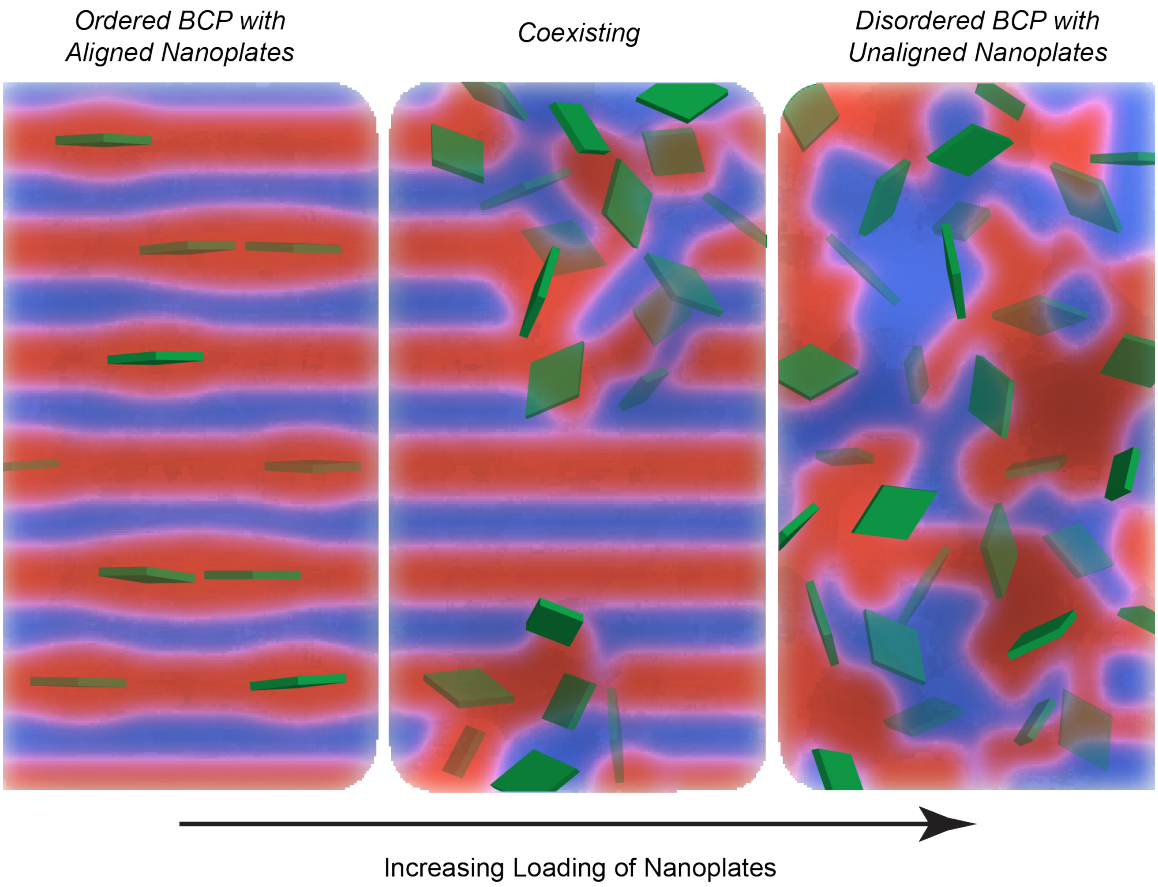

Figure 2.4. Illustration of the transition from an ordered BCP system with aligned nanoplates to a disordered BCP with unaligned nanoplates as loading increases. The red and blue blocks represent the PMMA and PS lamellar domains, respectively.

Tilt series TEM images were captured to highlight the different alignment behaviors between an ordered, low volume fraction and a disordered, high volume fraction BCP system. The tilt series of the BCP nanocomposite from Figure 2.3b with ϕ = 0.017 nanoplates can be seen in Supplementary Digital File 2. Representative tilt angles (0º, -30º, and -60º) of this sequence are shown in the top row of Figure 2.5. At a 0º tilt angle, the nanoplates align in the PMMA domains, appearing edge-on in the cross-sectional TEM image. However, as the sample is tilted to -60º, the lamellar formation persists, but the GdF_3:Yb/Er NPs are no longer edge-on. Instead the faces of the

nanoplates can be seen in plane with the light PMMA domain. In comparison, the tilt series of the BCP nanocomposite from Figure 2.3e with ϕ = 0.050 nanoplates is featured in Supplementary Digital File 3. Representative tilt angles (0º, -30º, and -60º) of this sequence are shown in the middle row of Figure 2.5. In this series, regardless of the tilt angle, the nanoplates assume a range of tilt angles. With a random distribution of orientations appearing in each frame, the ϕ = 0.050 BCP composite can be described as isotropically dispersed, meaning no preferential alignment guided by BCP domains. Therefore, the alignment behavior of the disordered BCP with unaligned nanoplates is analogous to the homopolymer composite films from Figure 2.2. To support this comparison, representative tilt angles (0º, -30º, and -60º) of the homopolymer composite (ϕ = 0.040 in Figure 2.2b) tilt series in Supplementary Digital File 1 are shown in the bottom row of Figure 2.5. In homopolymer PMMA, the NPs are also isotropically dispersed with nanoplate faces and edges appearing simultaneously in each frame.

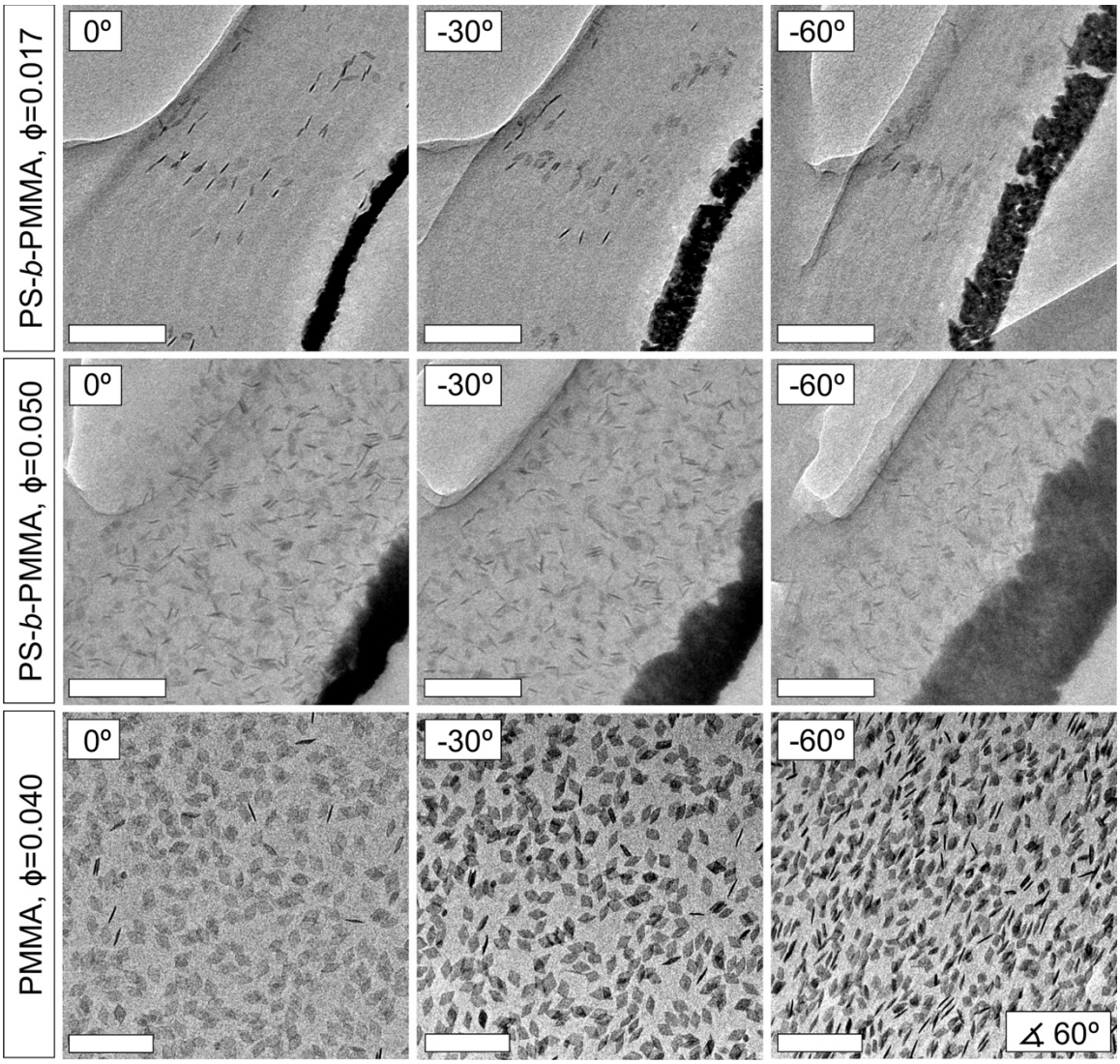

Figure 2.5. Representative cross-sectional TEM (JEM-2100, 80 kV) images of annealed (190ºC, 48 hours) and ultramicrotomed lamellar-forming M_n = 38k-*b*-36.8k g/mol PS-*b*-PMMA films with (top row) ϕ = 0.017 and (middle row) ϕ = 0.050 5 kg/mol PEG-PO_3H_2 functionalized GdF_3:Yb/Er (20/2 mol%) and representative top-down TEM (JEM-1400, 120 kV) images (bottom row) of M_n = 20 kg/mol PMMA with ϕ = 0.040 nanoplates. The series from left to right show images captured at the following goniometer tilt angles where the tilt axis is 60º from the x-axis (indicated in the bottom right corner): 0º, -30º, and -60º. All scale bars are 150 nm. Note, the dark feature lining the cross-sectional films is the Au/Pd tracer layer and indicates the top surface of the films.

2.3 Discussion

In a BCP nanocomposite, containing functionalized NPs, both enthalpic and entropic contributions to free energy will dictate particle placement, and for anisotropic particles, their alignment within a domain. To understand nanoplate alignment in a lamellar-forming BCP, we want to understand the balance between these two constituents and the factors that contribute to the system's free energy. Enthalpically, the surface chemistry of NPs in a BCP determines particle location. By functionalizing their surfaces with PEG-PO_3H_2, we have strategically designed the nanoplates to have a chemical affinity to the PMMA domain and a chemical aversion to the PS domain. Therefore, to maximize favorable enthalpic interactions, the nanoplates locate to the block (PMMA) whose chemistry is favorable with the ligand moiety (PEG).

Once the nanoplates are stabilized in the PMMA domain, the interplay between conformational and translational entropy can help explain why PEG-PO_3H_2 functionalized GdF_3:Yb/Er align in the domain centers as seen in Figure 2.3a and Figure 2.3b. While translational entropy increases, conformational entropy decreases when NPs disperse uniformly in BCP domains. Chains must stretch and compress at the NPs to accommodate the inclusions, thereby decreasing their number of possible conformations. In BCP nanocomposites with relatively large spherical NPs, Thompson *et al.* models a "center-filled lamellar" system, dominated by conformational entropy, where NPs segregate to the middle of the block to avoid the cost of chain stretching.[45,46] By centrally localizing larger NPs, translational entropy is reduced, but not sufficiently to outweigh the gain in conformational entropy. These calculations are also supported by complementary experiments performed by Chiu *et al.*[18]

While Thompson *et al.* also predicts "edge-filled lamella(e)" where relatively small NPs redistribute towards domain edges to instead maximize translational entropy, the "center-filled lamellar" model best supports nanoplate alignment in the center of PMMA domains. As proposed by the aforementioned model for relatively large NPs, at low nanoplate loadings, the particles

appear to align in the middle of the PMMA block as seen in Figure A.4a and Figure A.4b. However, the system would still incur a conformational entropy penalty by confining the nanoplate thickness between the BCP chains. Accommodating a rigid nanoplate mid-block in an unperturbed domain would result in significant entropic costs from BCP chains and PEG ligands compressing at the planar NP interface. As theorized by Bockstaller *et al*., the domain could instead create a bulge around the nanoplate core to retain chain entropy.[14] However, distorting the surrounding region would add unfavorable interfacial area from polymer chains stretching at the nanoplate faces as illustrated in the zoomed inset of Figure 2.4.[14] Therefore, to incorporate nanoplates into BCP lamellae, the system's free energy must balance contributions from the enthalpic interaction between the nanoplate and BCP, translational entropy, conformational entropy from BCP and ligand chains stretching and compressing, as well as excess BCP interfacial area around the rigid NP core. The alignment behavior in Figure 2.3a and Figure 2.3b, suggests that the free energy penalty of two or more aligned adjacent nanoplates is less than isolated plates by way of decreasing the total interfacial area added to the system. We do note that any dilation in the BCP domain could not be resolved using the microscopy techniques employed in these experiments.

The results, however, do indicate a volume fraction limit to aligning PEG-PO_3H_2 functionalized nanoplates in the lamellar-forming PS-*b*-PMMA. Figure 2.3c and Figure 2.3d show films where sections of unaligned nanoplates in disordered BCP coexist with sections of ordered BCP. This suggests that at $\phi = 0.027$ and $\phi = 0.038$ local chain distortions and excess interfacial area around an increasing ϕ of NPs is too great to be accommodated in the BCP domains, leading to phase separation.[20] Therefore, the thermodynamic behavior of these intermediately loaded films is dominated by entropic contributions to the system's free energy. Meanwhile, as NP volume fraction increases to $\phi = 0.050$ and $\phi = 0.064$, the samples are unable to reach the equilibrium, phase separated morphology upon thermal annealing. Instead, the highly loaded films maintain the disordered and unaligned structure of the as-cast BCP composites (Figure A.5e and Figure A.5f).

As the films try to evolve during annealing, the nanoplates jam in a kinetically trapped state. This jamming interferes with BCP ordering and arrests phase separation. The transition from thermodynamic equilibrium is observed at the overlap volume fraction, ϕ^*, when the pervaded volumes of the nanoplates begin to coincide (calculated in Appendix A with Figure A.6 and Figure A.7 to be 0.051). This value agrees with the experimental volume fraction of $\phi = 0.050$ in Figure 2.3e when the nanoplate-BCP system becomes jammed in a disordered BCP and unaligned nanoplate morphology.

2.4 Conclusions

The findings of this work are important to understand how nanoplate loading affects the BCP assembly and consequently the lamellar formation necessary to align nanoplates. We have found that PEG-PO_3H_2 functionalized GdF_3:Yb/Er (20/2 mol%) segregate to and successfully align in the PMMA domains of lamellar-forming PS-*b*-PMMA at low volume fractions ($\phi = 0.0083$ and $\phi = 0.017$). Ultimately, this research aims to elucidate the balance between enthalpic and entropic contributions required to drive alignment. By employing a model nanoplate system, a fundamental understanding of the thermodynamic behavior underlying the alignment of nanoplates in BCPs can be obtained. We have built a platform, to deliberately orient nanoplates, that can be leveraged to explore how various parameters influence nanoplate alignment and PNC phase behavior. Ultimately, a complete portfolio can be translated to develop technologically relevant systems.

2.5 References

(1) LeBaron, P. C.; Wang, Z.; Pinnavaia, T. J. Polymer-Layered Silicate Nanocomposites: An Overview. *Appl. Clay Sci.* **1999**, 15, 11–29.

(2) Moniruzzman, M.; Winey, K. I. Polymer Nanocomposites Containing Carbon Nanotubes. *Macromolecules* **2006**, 39, 5194-5205.

(3) Xu, C.; Ohno, K.; Ladmiral, V.; Composto, R. J. Dispersion of Polymer-Grafted Magnetic Nanoparticles in Homopolymers and Block Copolymers. *Polymer* **2008**, 49, 3568-3577.

(4) Hore, M. J. A.; Composto, R. J. Nanorod Self-Assembly for Tuning Optical Absorption. *ACS Nano* **2010**, 4, 6941-6949.

(5) Hore, M. J. A.; Frischknecht, A. L.; Composto, R. J. Nanorod Assemblies in Polymer Films and Their Dispersion-Dependent Optical Properties. *ACS Macro Lett.* **2012**, 1, 115-121.

(6) Kumar, S. K.; Jouault, N.; Benicewicz, B.; Neely, T. Nanocomposites with Polymer Grafted Nanoparticles. *Macromolecules* **2013**, 46, 3199-3214.

(7) Ferrier, R. C., Jr.; Lee, H.-S.;, Hore, M. J. A.; Caporizzo, M.; Eckman, D. M.; Composto, R. J. Gold Nanorod Linking to Control Plasmonic Properties in Solution and Polymer Nanocomposites. *Langmuir* **2014**, 30, 1906-1914.

(8) Wang, D.; Hore, M. J. A.; Ye, X.; Zheng, C.; Murray, C. B.; Composto, R. J. Gold Nanorod Length Controls Dispersion, Local Ordering, and Optical Absorption in Polymer Nanocomposite Film. *Soft Matter* **2014**, 10, 3404-3413.

(9) Frischknecht, A. L.; Hore, M. J. A.; Ford, J.; Composto, R. J. Dispersion of Polymer-Grafted Nanorods in Homopolymer Films: Theory and Experiment. *Macromolecules* **2013**, 46, 2956-2869.

(10) Martin, T. B.; Mongcopa, K. I. S.; Ashkar, R.; Butler, P.; Krishnamoorti, R.; Jayaraman, A. Wetting-Dewetting and Dispersion-Aggregation Transitions Are Distinct for Polymer Grafter Nanoparticles in Chemically Dissimilar Polymer Matrix. *J. Am. Chem. Soc.* **2015**, 137, 10624-10631.

(11) Ferrier, R. C., Jr.; Koski, J.; Riggleman, R. A.; Composto, R. J. Engineering the Assembly of Gold Nanorods in Polymer Matrices. *Macromolecules* **2016**, 49, 1002-1015.

(12) Zhao, D.; Di Nicola, M.; Khani, M. M.; Jestin, J.; Benicewicz, B. C.; Kumar, S. K. Self-Assembly of Monodisperse versus Bidisperse Polymer-Grafted Nanoparticles. *ACS Macro Lett.* **2016**, 5, 790-795.

(13) Koski, J. P.; Ferrier, R. C., Jr.; Krook, N. M.; Chao, H.; Composto, R. J.; Frischknecht, A. L.; Riggleman, R. A. Comparison of Field-Theoretic Approaches in Predicting Polymer Nanocomposite Phase Behavior. *Macromolecules* **2017**, 50, 8797-8809.

(14) Bockstaller, M. R.; Mickiewicz, R. A.; Thomas, E. L. Block Copolymer Nanocomposites: Perspectives for Tailored Functional Materials. *Adv. Mater.* **2005,** 17, 1331-1349.

(15) Balazs, A. C.; Emrick, T.; Russell, T. P. Nanoparticle Polymer Composites: Where Two Small Worlds Meet. *Science* **2006**, 314, 1107-1110.

(16) Chiu, J. J.; Kim, B. J.; Kramer, E. J.; Pine, D. J. Control of Nanoparticle Location in Block Copolymers. *J. Am. Chem. Soc.* **2005**, 127, 5036-5037.

(17) Kim, B. J.; Bang, J.; Hawker, C. J.; Kramer, E. J. Effect of Areal Chain Density on the Location of Polymer-Modified Gold Nanoparticles in a Block Copolymer Template. *Macromolecules* **2006**, 39, 4108-4114.

(18) Chiu, J. J.; Kim, B. J.; Yi, G.; Band, J.; Kramer E. J.; Pine, D. J. Distribution of Nanoparticles in Lamellar Domains of Block Copolymers. *Macromolecules* **2007**, 40, 3361-3365.

(19) Kim, B. J.; Bang, J.; Hawker, C. J.; Chiu, J. J.; Pine, D. J.; Jang, S. G.; Yang, S.; Kramer, E. J. Creating Surfactant Nanoparticles for Block Copolymer Composites through Surface Chemistry. *Langmuir* **2007**, 23, 12693-12703.

(20) Kim, B. J.; Fredrickson, G. H.; Kramer, E. J. Effect of Polymer Ligand Molecular Weight on Polymer-Coated Nanoparticle Location in Block Copolymers. *Macromolecules* **2008**, 41, 436-447.

(21) Beaudoin, E.; Abecassis, B.; Constantin, D.; Degrouard, J.; Davidson, P. Strain-Controlled Fluorescence Polarization in a CdSe Nanoplatelet-Block Copolymer Composite. *Chem. Commun.* **2015**, 51, 4051-4054.

(22) Diroll, B. T.; Greybush, N. J.; Kagan, C. R.; Murray, C. B. Smectic Nanorods Supperlattices Assembled on Liquid Subphases: Structure, Orientation, Defects, and Optical Polarization. *Chem. Mater.* **2015**, 27, 2998-3008.

(23) Gao, Y.; Weidman, M. C.; Tisdale, W. A. CdSe Nanoplatelet Films with Controlled Orientation of their Transition Dipole Moment. *Nano Lett.* **2017**, 17, 3837-3843.

(24) Beaudoin, E.; Davidson, P.; Abecassis, B.; Bizien, T.; Constantin, D. Reversible Strain Alignment and Reshuffling of Nanoplatelet Stacks Confine in Lamellar Block Copolymer Matrix. *Nanoscale* **2017**, 9, 17371-17377.

(25) Duncan, T. V. Applications of Nanotechnology in Food Packaging and Food Safety: Barrier Materials, Antimicrobials and Sensors. *J. Colloid Interface Sci.* **2011**, 363, 1-24.

(26) Zhang, Q.; Gupta, S.; Emrick, T.; Russell, T. P. Surface-Functionalized CdSe Nanorods for Assembly in Diblock Copolymer Templates. *J. Am. Chem. Soc.* **2005**, 128, 3898-3899.

(27) Deshmukh, R. D.; Liu, Y.; Composto, R. J. Two-Dimensional Confinement of Nanorods in Block Copolymer Domains. *Nano Lett.* **2007**, 7, 3662-3668.

(28) Thorkelsson, K.; Mastroianni, A. J.; Ercius, P.; Xu, T. Direct Nanorod Assembly Using Block Copolymer-Based Supramolecules. *Nano Lett.* **2011**, 12, 498-504.

(29) Ploshnik, E.; Salant, A.; Banin, U.; Shenhar, R. Hierarchical Surface Patterns of Nanorods Obtained by Co-Assembly with Block Copolymers in Ultrathin Films. *Adv. Mater.* **2010**, 22, 2774-2779.

(30) Thorkelsson, K.; Nelson, J. H.; Alivisatos, A. P.; Xu, T. End-to-End Alignment of Nanorods in Thin Films. *Nano Lett.* **2013**, 13, 4908-4913.

(31) Rasin, B.; Chao, H.; Jiang, G.; Wang, D.; Riggleman, R. A.; Composto, R. J. Dispersion and Alignment of Nanorods in Cylindrical Block Copolymer Thin Films. *Soft Matter* **2016**, 12, 2177-2185.

(32) Kojima, Y.; Usuki, A.; Kawasumi, M.; Okada, A; Fukushima, Y.; Kurauchi, T.; Kamigaito, O. Mechanical Properties of Nylon 6-Clay Hybrid. *J. Mater. Res.* **1993**, 8, 1185-1189.

(33) Tyan, H.-L.; Liu, Y.-C.; Wei, K.-H. Thermally and Mechanically Enhanced Clay/Polyimide Nanocomposite via Reactive Organoclay. *Chem. Mater.* **1999**, 11, 1942-1947.

(34) Wang, K.; Liang, S.; Du, R.; Zhang, Q.; Fu, Q. The Interplay of Thermodynamics and Shear on the Dispersion of Polymer Nanocomposite. *Polymer* **2004**, 45, 7953-7960.

(35) Majewski, P. W.; Gopinadhan, M.; Osuji, C. O. Magnetic Field Alignment of Block Copolymeres and Polymer Nanocomposites: Scalable Microstructure Control in Functional Soft Materials. *J. Polym. Sci. B* **2012**, 50, 2-8.

(36) Erb, R. M.; Segmehl, J.; Charilaou, M.; Löffler, J. F.; Studart, A. R. Non-Linear Alignment Dynamics in Suspensions of Platelets Under Rotating Magnetic Fields. *Soft Matter* **2012**, 8, 7604-7609.

(37) Billaud, J.; Bouville, F.; Magrini, T.; Villevieille, C.; Studart, A. R. Magnetically Aligned Graphite Electrodes for High-Rate Performance Li-Ion Batteries. *Nat. Energy* **2016**, 1, 1-6.

(38) Yamamoto, R.; Yoshikawa, T.; Suzuki, M.; Yoshida, Y.; Seki, T.; Yajima, N. Thermal Interface Material including Graphite in Vertical Formation. *Proceedings of JIEP Annual Meeting.* **2009**, 23, 46-47.

(39) Yamamoto, R.; Yoshida, Y.; Yoshikawa, T.; Yajima, M.; Seki, T. Novel Thermally Conductive Sheet Applying Orientation Control of Graphite Particles. *JIEP* **2010**, 13, 462-468.

(40) Ye, X.; Collins, J. E.; Kang, Y.; Chen, J.; Chen, D. T. N.; Yodh, A. G.; Murray, C. B. Morphologically Controlled Synthesis of Colloidal Upconversion Nanophosphors and their Shape-Directed Self-Assembly. *Proc. Natl. Acad. Sci. U.S.A.* **2010**, 107, 22430-22435.

(41) Paik, T.; Chacko, A.; Mikitsh, J. L.; Friedberg, J. S.; Pryma, D. A.; Murray, C. B. Shape-Controlled Synthesis of Isotopic Yttrium-90-Labeled Rare Earth Fluoride Nanocrystals for Multimodal Imaging. *ACS Nano* **2015**, 9, 8718-8728.

(42) Dong, A.; Ye, X.; Chen, J.; Kang, Y.; Gordon, T.; Kikkawa, J. M.; Murray, C. B. A Generalized Ligand-Exchange Strategy Enabling Sequential Surface Functionalization of Colloidal Nanocrystals. *J. Am. Chem. Soc.* **2011**, 133, 998-1006.

(43) Deshmukh, R. D.; Buxton, G. A.; Clarke, N.; Composto, R. J. Nanoscale Block Copolymer Templates Decorated by Nanoparticle Arrays. *Macromolecules* **2007**, 40, 6316-6324.

(44) Mangal, R.; Nath, P.; Tikekar, M.; Archer, L. A. Enthalphy-Driven Stabilization of Dispersions of Polymer-Grafted Nanoparticles in High-Molecular-Weight Polymer Melts. *Langmuir* **2016**, 32, 10621-10631.

(45) Thompson, R. B.; Ginzburg, V. V.; Matsen, M. W.; Balazs, A. C. Predicting the Mesophases of Copolymer-Nanoparticle Composites. *Science* **2001**, 292, 2469-2472.

(46) Thompson, R. B.; Ginzburg, V. V.; Matsen, M. W.; Balazs, A. C. Block Copolymer-Directed Assembly of Nanoparticles: Forming Mesoscopically Ordered Hybrid Materials. *Macromolecules* **2002**, 35, 1060-1071.

CHAPTER 3: Experiments and Simulations Probing Local Domain Bulge and String Assembly of Aligned Nanoplates in a Lamellar Diblock Copolymer

Content in this chapter was reprinted (adapted) with permission from Nadia M. Krook,* Christian Tabedzki,* Katherine C. Elbert, Kevin G. Yager, Christopher B. Murray, Robert A. Riggleman, and Russell J. Composto. This work has been submitted for publication in a peer-reviewed journal. * N.M.K. (experiments) and C.T. (simulations) contributed equally to this work.

3.1 Introduction

Block copolymer-based supramolecules[1-5] and traditional block copolymers (BCPs)[6-8] offer a nanostructured matrix to template the assembly of nanoparticles (NPs). Provided that NP and polymer compatibility (geometric and thermodynamic) has been considered, polymer nanocomposites (PNCs) can be designed with nanoscale building blocks arranged into hierarchical architectures to achieve a desired structure-property relationship. Factors including matrix molecular weight and chemical composition; brush chain length, grafting density, and chemistry; as well as particle size and volume fraction, directly impact how NPs will organize within these hybrid materials. Since the publication of several pioneering studies[9-18] in both theory and experiments, significant progress has been made towards understanding how these factors affect the dispersion of spherical NPs in BCPs.

Meanwhile, fewer studies have explored the effects of particle shape anisotropy (rods[2-4,19-21] and plates[5,22]) in BCP nanocomposites. Directing the orientation of non-spherical NPs is of particular interest for exploiting their shape-dependent properties for a variety of applications[23] including photovoltaics,[24-26] metamaterials,[27,28] biomimetic systems,[29] and thermal interface materials.[30] BCPs deliver a versatile approach to creating large-area, self-assembled nanocomposites that direct anisotropic particle orientation through limited processing steps. However, unresolved questions prevent BCPs from being fully harnessed to engineer hybrid

materials with precisely directed NP orientations. These questions include a fundamental understanding on how locally disrupting the equilibrium BCP microstructure, from polymer chains rearranging to accommodate a non-spherical NP, might lead to interparticle assembly within a domain.

In Chapter 2 we showed that crystalline gadolinium trifluoride rhombic nanoplates doped with ytterbium and erbium [GdF_3:Yb/Er (20/2 mol%)] and functionalized with favorable interactions for one domain will align in ordered BCP lamellae at low NP volume fractions.[22] In this first study, it was observed that the aligned nanoplates further assemble and string together in chains in the confining domain at small interparticle distances. Anisotropic assemblies of polymer grafted NPs have been previously shown in homopolymer[32-35] and BCP[2,4,5,20] matrices. However, without tuning interparticle interactions to intentionally form NP strings, we focus on the thermodynamic origins of nanoplate assemblies from our initial experiments with supporting simulations.

Bockstaller *et al.* predicted that, in the presence of a nanoplate, a bulge would be created in a BCP domain as a result of excessive chain perturbations.[6] However, the present work will discuss the limitations of observing this phenomenon experimentally using electron microscopy and scattering techniques. Instead, polymer field theory allows researchers to effectivity study and model BCP nanocomposite physics.[9,10,36-39] Furthermore, theoretical studies have captured the anticipated domain distortion around spherical NPs.[37-39] By coupling experiments with theory, the present work seeks to elucidate the mechanism by which nanoplates grafted with polyethylene glycol (PEG) confined in poly(styrene-*b*-methyl methacrylate) (PS-*b*-PMMA) lamellae creates a bulge in the microdomain and contributes to the anisotropic assembly of aligned GdF_3:Yb/Er.

The simulation results predict and a deeper experimental exploration corroborates an equilibrium interparticle spacing between GdF_3:Yb/Er NPs assembled in anisotropic strings. Here we propose that nanoplates bridge together to mediate the following energetic penalties: increased

interfacial area between the PS and PMMA domains accompanied by decreased chain entropy from highly stretched and compressed chains around the nanoplates. The simulations also reveal an intermediate nanoplate separation that corresponds to a local free energy maximum. This interparticle spacing relates to a separation where the excess interfacial area of two plates only begin to merge, creating a PS-PMMA interface of highest curvature. We acknowledge that, rather than 1D strings, the nanoplates may be assembling as sheets or 2D arrays in the plane of the PMMA domain in the experimental system. However, since a projection of the film cross-section is captured in the microscopy images, the assemblies have the appearance of strings and will therefore continue to be referred to as such. We also present additional simulations as a function of nanoplate orientation. The findings from these simulations support nanoplate alignment with some tilt allowance in the experimental system by illustrating a narrow tolerance for orientation angles in the specified BCP M_n. Creating aligned NP assemblies within the domain of a BCP may provide a platform to fabricate functional nanomaterials that would benefit from strategically aligning and coupling particles into anisotropic arrays.[40]

3.2 Methods

3.2.1 Materials. All polymers and chemicals were used as received. Phosphoric acid functionalized polyethylene glycol (PEG-PO_3H_2, M_n = 5 kg/mol) was purchased from Nanocs Inc. and lamellar-forming poly(styrene-*b*-methyl methacrylate) (PS-*b*-PMMA, M_n = 38k-*b*-36.8k g/mol, PDI = 1.08) was purchased from Polymer Source Inc. Toluene (99.9%, for HPLC) was purchased from Sigma Aldrich while hydrogen peroxide (H_2O_2, 30%, certified ACS), sodium hydroxide solution (NaOH, 50% w/w, certified), and sulfuric acid (H_2SO_4, certified ACS plus) were purchased from Fisher Scientific. Silicon (Si) wafers with a 300 nm wet thermal oxide layer were purchased from University Wafer. EpoxiCure 2 epoxy hardener and resin were both purchased from Buehler.

The synthesis of oleic acid (OA) stabilized GdF_3:Yb/Er (20/2 mol%) rhombic nanoplates [longest diagonal (d_1) = 35 nm, shortest diagonal (d_2) = 22 nm, and thickness (t) = 3nm] in Figure 3.1a and subsequent surface modification with σ = 0.62 chains/nm^2 of M_n = 5 kg/mol PEG-PO_3H_2 were previously reported.[22] The PEG-PO_3H_2 functionalized nanoplates in Figure 3.1b were dispersed in toluene as a stock solution until further use.

3.2.2 Block Copolymer Nanocomposite Preparation. Si wafers with a 300 nm wet thermal oxide layer were cut to 1 cm^2. The substrates were piranha cleaned (70:30 vol%, H_2SO_4:H_2O_2) at 80ºC for 20 min, rinsed three times with, and stored overnight in DI H_2O before drying with N_2 followed by 10 min of UV ozone treatment. Meanwhile, the polymer functionalized GdF_3:Yb/Er nanoplates were added to 7 wt% solutions of M_n = 38k-*b*-36.8k g/mol PS-*b*-PMMA in toluene and stirred with a magnetic stir bar for at least 2 h at 40ºC. Once the polymer was dissolved, the solutions were spin-coated (2000 rpm, 1 min) onto the cleaned Si substrates. The films were annealed under vacuum at 190ºC for 48 h. The BCP nanocomposite samples that were formed had the following final nanoplate volume fractions: ϕ = 0 (Figure 3.1c), ϕ = 0.0083 (Figure B.1), ϕ = 0.017 (Figure B.2), ϕ = 0.027, ϕ = 0.038, ϕ = 0.050 and ϕ = 0.064. A F3-UV reflectometer (Filmetrics, LS-DT2 light source and SS-5 stage) was used to measure film thicknesses.

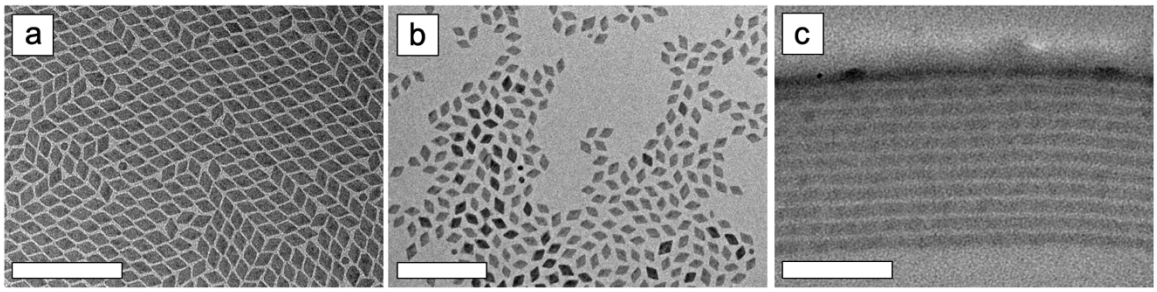

Figure 3.1. Representative TEM (JEM-1400, 120 kV) micrographs of (a) a monolayer of as-synthesized GdF_3:Yb/Er (20/2 mol%) with OA on their surfaces, (b) drop-casted M_n = 5 kg/mol PEG-PO_3H_2 functionalized nanoplates, and (c) an ultramicrotomed cross-section of neat lamellar-forming M_n = 38k-*b*-36.8k g/mol PS-*b*-PMMA film (thickness ~370 nm) annealed at 190ºC for 48

h. The light and dark domains of the BCP are PMMA and PS, respectively. All scale bars are 200 nm.

3.2.3 Grazing-Incidence Small-Angle X-ray Scattering (GISAXS). Experiments were performed at the Soft Matter Interfaces (SMI, 12-ID) and Complex Materials Scattering (CMS, 11-BM) beamlines at the National Synchrotron Light Source II (Brookhaven National Laboratory). Scattering data was collected using pixel-array detectors; conversion from detector to reciprocal-space was calibrated by measuring a standard sample (silver behenate). We define q_z to be the vertical (film normal) direction, and q_x to be the orthogonal horizontal (in-plane) direction, q_y to be the direction along the beam, and $q_r = \sqrt{q_x^2 + q_y^2}$ to be the total magnitude of the in-plane scattering component. To analyze the in-plane repeat-spacing of the structures, we extracted a linecut along the q_r direction (slightly above the Yoneda), fit the first-order peak to a Gaussian, and converted to real-space using $d = 2\pi/q$. To determine the out-of-plane repeat-spacing, one must account for the shift in the scattering peaks arising from refraction distortion effects.[41-43] The nominal peak position (q_0) was determined by taking a linecut along q_z (at the q_r position of the primary peak), and fit the scattering peak to a Gaussian. We note that the refraction correction for a peak arising from the transmission channel (q_T) is different than for the reflection channel (q_R).[41] For the data analysis herein, we confirmed that the scattering peak in question arose from the transmission channel and applied a refraction correction based on the known grazing-incidence angle and a calculated value for the critical angle of the film (0.098º for PMMA at 13.5 keV). Examples of typical peak analyses are shown in Figure B.3.

3.2.4 Transmission Electron Microscopy (TEM). Films were lifted from the substrates by floating them on the surface of a NaOH solution (80:20 vol%, DI H_2O:50% w/w NaOH solution) at 40ºC. Once the films delaminated from the Si, they were rinsed in a DI H_2O bath and lifted onto Teflon®. After water evaporation, the top of the BCP nanocomposite surfaces were sputter-coated

with a thin layer of gold (Au) and palladium (Pd), and transferred from the Teflon® into two-part epoxy. Film cross-sections (~50-70 nm thick) were cut by ultramicrotomy (Leica Ultracut S Ultramicrotome) with a diamond knife. TEM characterization of the BCP nanocomposite cross-sections deposited on carbon coated grids was performed with a JEOL JEM-1400 TEM operated at 120 kV.

3.2.5 Nanoplate Separation Image Analysis. The separation between NP edges within assembled strings of aligned nanoplates was analyzed using ImageJ (v 1.52a). This process is shown in Figure B.4. Briefly, TEM images of the BCP nanocomposite sample containing $\phi = 0.017$ nanoplates (Figure B.4a) were manually thresholded to isolate all of the nanoplate areas and converted into binary images (Figure B.4b). A straight line selection was drawn along the nanoplate strings in the binary images (Figure B.4b). By performing a plot profile analysis to graph the pixel intensities as a function of distance (Figure B.4c), 300 edge-to-edge distances between aligned nanoplates assembled in strings were measured at half the maximum intensity value. All 300 measurements that were taken are listed in Table B.1.

3.2.6 Description of the Simulations. To model the experimental system, hSCFT was implemented based off of previous literature.[21,37,44-49] The model presented herein is adjusted to account for the slightly negative Flory−Huggins interaction parameter (χ) between the PMMA domain of the BCP and the PEG brushes grafted to the nanoplates, as demonstrated by Hore *et al*.[50] To represent shape anisotropy, the following functional form (Γ) for the NP, used by Rasin *et al.* to simulate nanorods,[21] is employed:

$$\Gamma(\boldsymbol{r}) = \frac{\rho_0}{4}\operatorname{erfc}\left(\frac{\left(|\boldsymbol{u}\cdot(\boldsymbol{r}-\boldsymbol{r}_c)|-\frac{L_P}{2}\right)}{\xi}\right)\operatorname{erfc}\left(\frac{\left(|\boldsymbol{u}\times(\boldsymbol{r}-\boldsymbol{r}_c)|-R_p\right)}{\xi}\right) \qquad (3.1)$$

where R_P is the NP radius, L_P is the NP length, ρ_0 is the bulk density of the system, and ξ is the NP interface width which controls how quickly the particle density goes from ρ_0 to 0. Within any given

simulation, the NP positions $\boldsymbol{r}_c$ and orientations $\boldsymbol{u}$ are fixed. The distribution of grafting sites for the model PEG brushes are defined as the normalized magnitude of the NP density gradient.

By applying the Hubbard-Strantovich transformation,[51] the following hybrid partition function is obtained

$$\mathcal{Z} = z_o \int \mathfrak{D}\{w\} \int \mathrm{d}\boldsymbol{r}^{nP} e^{-\mathcal{H}[\{w\}]}, \qquad (3.2)$$

where z_0 accounts for miscellaneous proportionality factors and $\{\omega\}$ represents a collection of different field terms. The effective Hamiltonian ($\mathcal{H}$) provides access to free energy differences under the mean-field approximation; the difference between two effective Hamiltonians is equivalent to the change in free energy. The specific Hamiltonian for this system is derived as

$$\begin{aligned}
&\mathcal{H}\left[w_+, w_{\mathrm{AB}}^{(\pm)}, w_{\mathrm{AC}}^{(\pm)}, w_{\mathrm{BC}}^{(\pm)}\right] \\
&= \frac{\rho_0}{2\kappa}\int \mathrm{d}\boldsymbol{r}\, w_+(\boldsymbol{r})^2 - i\int \mathrm{d}\boldsymbol{r}\, w_+(\rho_0 - \breve{\rho}_{\mathrm{NP}}) + \frac{\rho_0}{\chi_{\mathrm{AB}}}\int \mathrm{d}\boldsymbol{r}(w_{\mathrm{AB}}^{(+)}(\boldsymbol{r})^2 - w_{\mathrm{AB}}^{(-)}(\boldsymbol{r})^2) \\
&+ \frac{\rho_0}{\chi_{\mathrm{AC}}}\int \mathrm{d}\boldsymbol{r}(w_{\mathrm{AC}}^{(+)}(\boldsymbol{r})^2 - w_{\mathrm{AC}}^{(-)}(\boldsymbol{r})^2) + \frac{\rho_0}{-\chi_{\mathrm{BC}}}\int \mathrm{d}\boldsymbol{r}(w_{\mathrm{BC}}^{(+)}(\boldsymbol{r})^2 - w_{\mathrm{BC}}^{(-)}(\boldsymbol{r})^2) - n_{\mathrm{D}}\log Q_{\mathrm{D}} \\
&- n_{\mathrm{PEG}}\int \mathrm{d}\boldsymbol{r}\sigma_{\mathrm{PEG}}(\boldsymbol{r})\ln\left(q_{\mathrm{PEG}}(\boldsymbol{r})\right), \qquad (3.3)
\end{aligned}$$

where w_+ is the field enforcing the Helfand compressibility potential that discourages deviations from ρ_0 while κ is proportional to the incompressibility of the system; $\kappa = \infty$ corresponds to the incompressible limit. $\breve{\rho}_{\mathrm{NP}}$ is the microscopic density of the NPs convolved with the density of the particles, $\breve{\rho} = \sum_i^{N_{\mathrm{P}}}(\delta * \Gamma)(\boldsymbol{r})$ where $*$ represents a convolution of the two functions. The $w_{\alpha\beta}^{\pm}$ terms together represent the field conjugate to the Flory−Huggins interaction between species α and β.[44] The number of BCP chains is denoted by n_{D}, and their partition function is represented as Q_{D}. Likewise, the partition function of the grafted chain is q_{PEG} and the number of grafted PEG brushes is n_{PEG}. The specific forms of Q_{D} and q_{PEG} and the various density operators can be found in the monograph by Fredrickson[51] as Model E and Model K and in other previous works.[21,37,44-49] The negative value of χ_{BC} accounts for the slightly negative χ between PMMA and PEG; χ_{AB}

represents the repulsive interactions between PS and PMMA and χ_{AC} between PS and PEG. The inclusion of a negative χ requires a slightly different gradient scheme from Koski *et al.*,[44] and complete details can be found in Appendix B.

3.2.7 Numerical Parameters. We approximate the experimental system, which has M_n = 38k-*b*-36.8k g/mol, as a discrete Gaussian chain A-B diblock copolymer with f_A = 0.5 and a simulated molecular weight of M_n = 38k-*b*-36.625k g/mol. The data presented by Eitouni and Balsara[52] was then used to determine the statistical equivalent number of monomers and statistical segment size, which was then used to calculate R_g^2. To obtain the necessary values for the calculations, the weighted average between the physical properties (monomer volume and statistical segment length) of the PS block and PMMA block were taken since $\phi_{PS} = \phi_{PMMA} = 0.50$. Each block of the BCP constituted of 30 beads with each 1*b* unit representing 1.2332 nm; the statistical segment size for both blocks of the BCP are assumed to be the same. Therefore, one bead corresponds to roughly 12 monomeric units of the BCP. By maintaining the same statistical segment size for the grafted chain, each grafted simulation bead represents about 14 monomeric units of PEG.

Our simulations are performed in 2D, and as a result the rhombic nanoplates were modeled as 2D rods; the third dimension is assumed to be uniform, so this model corresponds to plates of infinite width. The thicknesses of the simulated plates (correspondingly, the diameter of the 2D rod) were 1.2918*b* units to match the 3 nm experimental size. The "diameter" of the simulated NPs (length of the 2D rod) is the average of the two unique experimental diagonals (d_1 and d_2) and is 6.1318*b*. The interface width of the NP ξ was chosen to be 0.2*b* units. The dimensionality of the 0.62 chains/nm^2 grafting density was reduced following the procedure established by Ferrier *et al.*[47] and then converted it to *b* units to obtain a grafting density of 1.43 chains/*b*. The χ values were also mapped from the experiments using the data collected by Balsara[52] and are as follows: $\chi_{PS/PMMA}$ =

0.501609, $\chi_{PS/PEG}$ = 1.13437, and $\chi_{PS/PMMA}$ = −0.018209 using a reference volume of 0.1 nm^3. As defined by Balsara, the N used for the χN calculations, were 60 (BCP degree of polymerization, N_D) for χ_{AB} and 9 (grafted brush degree of polymerization, N_G) for χ_{BC} and χ_{AC}. A κ of 50 was used to since the system equilibrates more easily than a truly incompressible system ($\kappa = \infty$) while having negligible effects on the final results.

For the potential of mean force (PMF) simulations, the box size was 52.0b by 90.0b units with 525 by 875 collocation points, respectively, to contain four lamellar periods, and the SCFT equations were implemented and solved using pseudo-spectral techniques.[52] The angle rotation data was generated in a box with 65.0b by 70.0b units with 625 by 675 grid points, respectively, and contained five lamellar periods to minimize the amount of disturbance felt by the farthest BCP interface in the simulation. Unless noted, the NP dimensions, grafting density, χ, composition, and κ were all held constant. For discussion, the experimental equivalent of the simulation units will be used to for ease of the reader and authors.

3.2.8 Potential Mean Force Curves. The PMF curves were generated with the aforementioned model and numerical parameters. The interparticle distance was varied between two explicit NPs at fractional distance of the box height, from 0.14 to 0.45. The farthest distance between simulated plates was used as the reference point to ensure that there are no interactions between the NPs. A separate set of simulations rotated a single explicit NP to generate the angle dependent PMF curves from 0° to 10° in increments of 1° and higher angles of 20°, 30°, 45° and 90°. No angle higher than 90° was probed due to symmetry. The 0° calculation was the reference state since this configuration minimizes the distortion to the BCP interface. Certain effects cannot be properly captured (such as NP tilt out-of-plane in the z-direction) since the simulations are 2D and not 3D.

3.3 Results

The formation of ordered BCP nanocomposite films, containing aligned nanoplates and NP string assemblies, requires the surface modification of the as-synthesized, OA stabilized GdF_3:Yb/Er nanoplates in Figure 3.1a. Consequently, OA was displaced by PEG-PO_3H_2 through a solution-phase ligand exchanged. By establishing favorable interactions, the PEG-PO_3H_2 functionalized nanoplates in Figure 3.1b were incorporated and aligned in the PMMA domain of the parallel PS-b-PMMA lamellae in Figure 3.1c. We previously showed in Chapter 2 that these aligned and ordered films were attainable at low NP loadings (redisplayed in Figure B.1 and Figure B.2 for $\phi = 0.0083$ and $\phi = 0.017$, respectively). The nanoplate alignment and lamellae ordering behavior, however, breaks down at higher volume fractions and was the subject of our first study.[22] Here, we will instead focus on the emergence of interparticle assemblies and the anticipated domain distortion as a result of significant polymer chain stretching around rigid GdF_3:Yb/Er nanoplates.

While nanoplate alignment is clearly shown at $\phi = 0.0083$ and $\phi = 0.017$, the domain bulge cannot be resolved in the TEM images. Since PMMA sustains degradation by electron beam irradiation, the PMMA domains appear lighter than the PS domains in TEM due to increased Z-contrast.[53-55] This beam damage, in combination with the natural undulations in the BCP lamellae, also prevent the expected distortion around the nanoplates from being detected. To try and circumvent the limitations, posed by TEM, in experimentally visualizing the domain bulge, we performed GISAXS experiments on the BCP nanocomposites with $\phi = 0$, $\phi = 0.0083$, $\phi = 0.017$, $\phi = 0.027$, $\phi = 0.038$, $\phi = 0.050$ and $\phi = 0.064$ PEG-PO_3H_2 functionalized GdF_3:Yb/Er and obtained an average lamellar period (λ). For high loadings of $\phi = 0.038$, $\phi = 0.050$ and $\phi = 0.064$, the lamellar scattering peak was not observed, as seen in the top image of Figure B.3, indicating a disordered (or predominantly disordered for $\phi = 0.038$) lamellar matrix. These results agree with our previous electron microscopy observations, which were described in Chapter 2.[22] However, as long as lamellar formation persisted after processing the films, λ could be determined from the scattering

data as shown in the bottom image of Figure B.3. We present λ for the evaluated ordered BCP nanocomposite samples as a function of NP volume fraction in Figure 3.2. For the neat (ϕ = 0) BCP, λ = 36.7 ± 0.2 nm. For the PS-*b*-PMMA lamellae with ϕ = 0.0083, ϕ = 0.017, and ϕ = 0.027 PEG-PO_3H_2 functionalized nanoplates, λ = 36.5 ± 0.5 nm, 36.2 ± 0.2 nm, and 35.9 ± 0.5 nm, respectively. Figure 3.2 and its inset show that there is no statistically significant difference in λ when nanoplates are incorporated into the PMMA domains, which could have confirmed the predicted domain dilation had λ increased upon nanoplate insertion. We note that GISAXS provides an average measure of structural order, and thus a given structural signal must be present in sufficient concentration to measurably shift a scattering peak. Given that the distortion introduced by the nanoplate is local, and the concentration of the NPs is modest, it is not surprising that these local domain distortions do not measurably shift the GISAXS peak position.

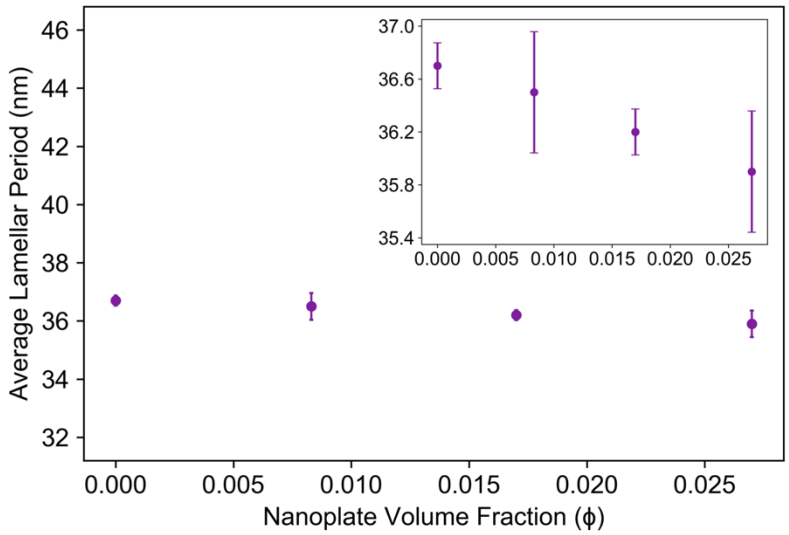

Figure 3.2. Average lamellar period (λ), experimentally determined from GISAXS, of ordered BCP nanocomposite films with ϕ = 0, ϕ = 0.0083 and ϕ = 0.017 PEG-PO_3H_2 functionalized GdF_3:Yb/Er (20/2 mol%) and of a partially ordered sample with ϕ = 0.027 nanoplates. The inset portrays the data with a narrower *y*-axis range. Error bars correspond to one standard deviation for three measurements collected in different locations on each sample.

While TEM and GISAXS are unable to experimentally corroborate the creation of a bulge around the GdF_3:Yb/Er nanoplates in the PMMA domains, as forecasted by Bockstaller *et al*.,[6] there is evidence in the TEM results that suggests that the nanocomposite system finds a means to decrease the entropic cost attributed to expanding the PS/PMMA interface. By way of stringing nanoplates together in anisotropic arrays, the additional interfacial area from local domain distortions would decrease. This process of consolidating PS/PMMA interface is represented by the illustration shown in Figure B.5. Merging at least two plates in a string would decrease the total amount of PS/PMMA interface added to the system. Examples of these prevalent string assemblies for the ordered BCP film with $\phi = 0.017$ aligned GdF_3:Yb/Er are featured in Figure 3.3. The regions seen in Figure 3.3 showcase nanoplates coupled in strings of two, three, and up to six NPs in a row.

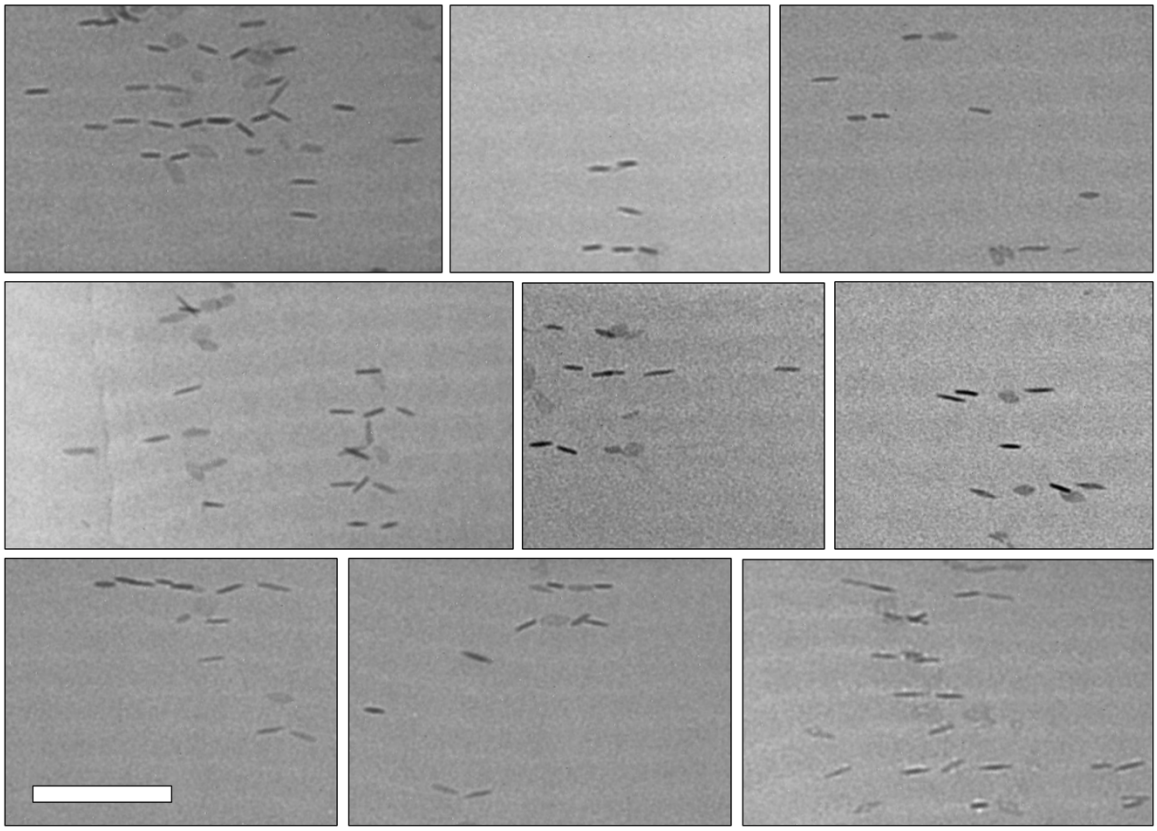

Figure 3.3. Representative TEM (JEM-1400, 120 kV) images of regions in annealed (190ºC, 48 h) and ultramicrotomed lamellar-forming M_n = 38k-*b*-36.8k g/mol PS-b-PMMA film cross-sections

with ϕ = 0.017 M_n = 5 kg/mol PEG-PO_3H_2 functionalized GdF_3:Yb/Er (20/2 mol%) highlighting nanoplates bridging together in strings. The light and dark domains of the BCP are PMMA and PS, respectively. Here, the imaging conditions are optimized to clearly visualize the nanoplate assemblies, sacrificing optimum contrast between PMMA and PS domains. The scale bar is 100 nm.

To understand the origin of the anisotropic NP assemblies, the PMF curve shown in Figure 3.4 was calculated to represent the free energy of two PEG grafted nanoplates at fixed edge-to-edge separations (0.8 nm to 67.6 nm) while constrained to the center of the PMMA domain in a M_n = 38k-*b*-36.5k g/mol PS-*b*-PMMA lamellar diblock copolymer. A few notable features emerge in the PMF curve including a global free energy maximum at a NP separation of 0.8 nm, a global minimum at 7.0 nm, a local maximum or activated state at 21.7 nm, and a plateau around 67.6 nm. The significance of these points can be explained by examining the BCP morphologies at these specific interparticle spacings. The 2D simulations in Figure 3.4 portray the morphological evolution of the system at the four points of interest for nanoplate separation. Importantly, at any of the depicted NP edge-to-edge distances, a bulge is observed around the nanoplates resulting in an increase of unfavorable PS/PMMA interface. The bulge propagates to nearest neighbor domains, analogous to dislocations where the energy penalty adversely affects a few adjacent planes. While, the global maximum at 0.8 nm can best be characterized as hard NP overlap, the plateau occurring at the furthest most point corresponds to a region where particle-particle interactions start to become insignificant as the nanoplates are semi-infinitely spaced. The global minimum at 7.0 nm is associated with an equilibrium nanoplate separation originating from depletion-attraction interactions. As shown in Figure 3.4 (top), the domain distortions around two approaching nanoplates combine into one bulge, thereby decreasing the total PS/PMMA area and minimizing the stretching and compressing of the BCP and PEG chains. The free energy well centered around

the minimum at an interparticle spacing of 7.0 nm is presented in the inset of Figure 3.4. The energy barrier identified at an intermediate NP separation of 21.7 nm seems to occur when the greatest degree of curvature in the interface is observed in Figure 3.4 (top). The source of this activated state will be explored further in our discussion.

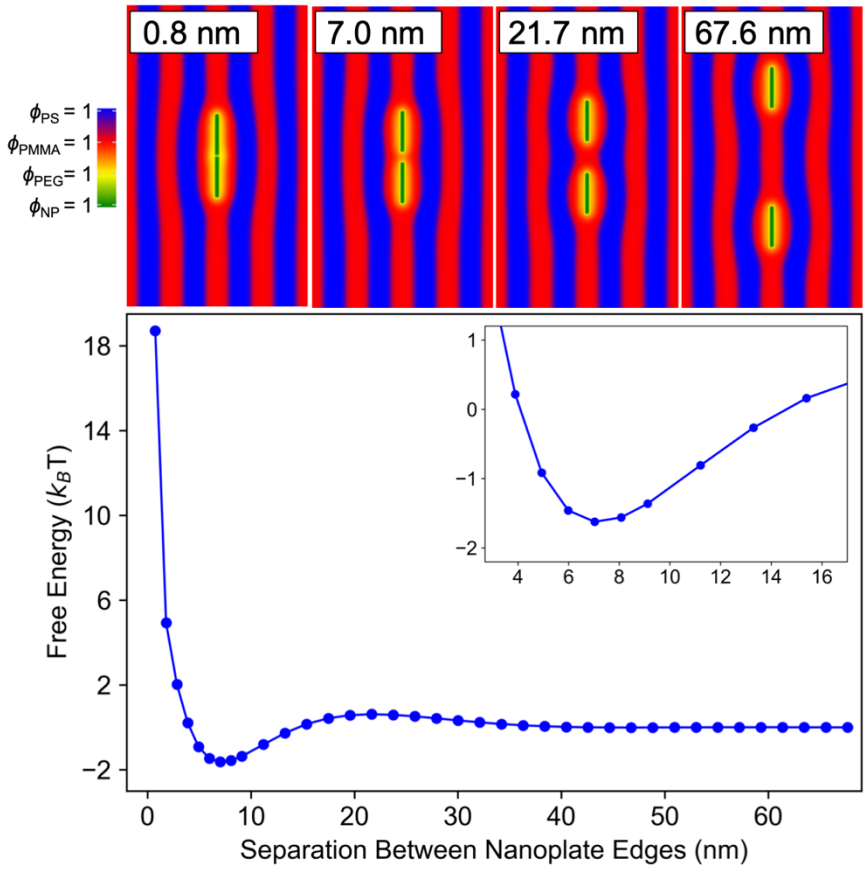

Figure 3.4. Potential of mean force curve to describe free energy as a function of edge-to-edge separation for two PEG grafted nanoplates in the PMMA domain of PS-b-PMMA lamellae. The inset expands the region near the free energy minimum. (top) 2D simulations show system representations at nanoplate separations of 0.8 nm, 7.0 nm, 21.7 nm, and 67.6 nm. PS, PMMA, PEG, and NP rich regions are displayed as blue, red, yellow, and green, respectively.

To correlate the simulations to experiments and determine an experimental equilibrium interparticle spacing, 300 distances between nanoplate edges were measured from TEM images.

All 300 measurements are shown in Table B.1 and recast as a histogram exhibited in the top image of Figure 3.5 with a bin size of 0.5 nm. The mean nanoplate spacing is 6.42 nm with a standard deviation of 1.44 nm. To convert the data represented in the histogram to an experimental free energy, probability values were first calculated by normalizing the histogram results over the total number of measurements (300). The probability (P) of finding two plates with a given separation can be related to the exponential of the free energy (F) by assuming equilibrium statistics hold

$$\frac{F}{k_{\mathrm{B}}T} = -\ln P - \frac{F_0}{k_{\mathrm{B}}T} \qquad (3.4)$$

where k_{B} is the Boltzmann constant, T is temperature, and F_0 is an irrelevant constant shift in the free energy. The resulting experimental free energy as a function of the nanoplate edge-to-edge distance is reproduced in the bottom plot of Figure 3.5 and can be compared to the simulations data in Figure 3.4. The equilibrium interparticle spacings corresponding to the global minima established by the PMF calculations and experimental data are 7.0 nm and 6.42 nm, respectively. Not only are these strikingly similar separation values, but there is excellent agreement between the asymmetric shape of the curves where the slope is steeper to the left and shallower to the right of the minimum. Therefore, simulations and experiments together suggest that nanoplate string formation occurs at interparticle spacings prescribed by the lowest energy states in the well. The anisotropic assemblies emerge to avoid penalties posed by the energy barriers associated with (1) closely approaching the nanoplates to where the PEG chains would be severely compressed and NP overlap would occur and (2) isolating the GdF_3:Yb/Er particles at intermediate distances (~21.7 nm) where highest curvature in the PS/PMMA interface is formed from adjoining domain bulges.

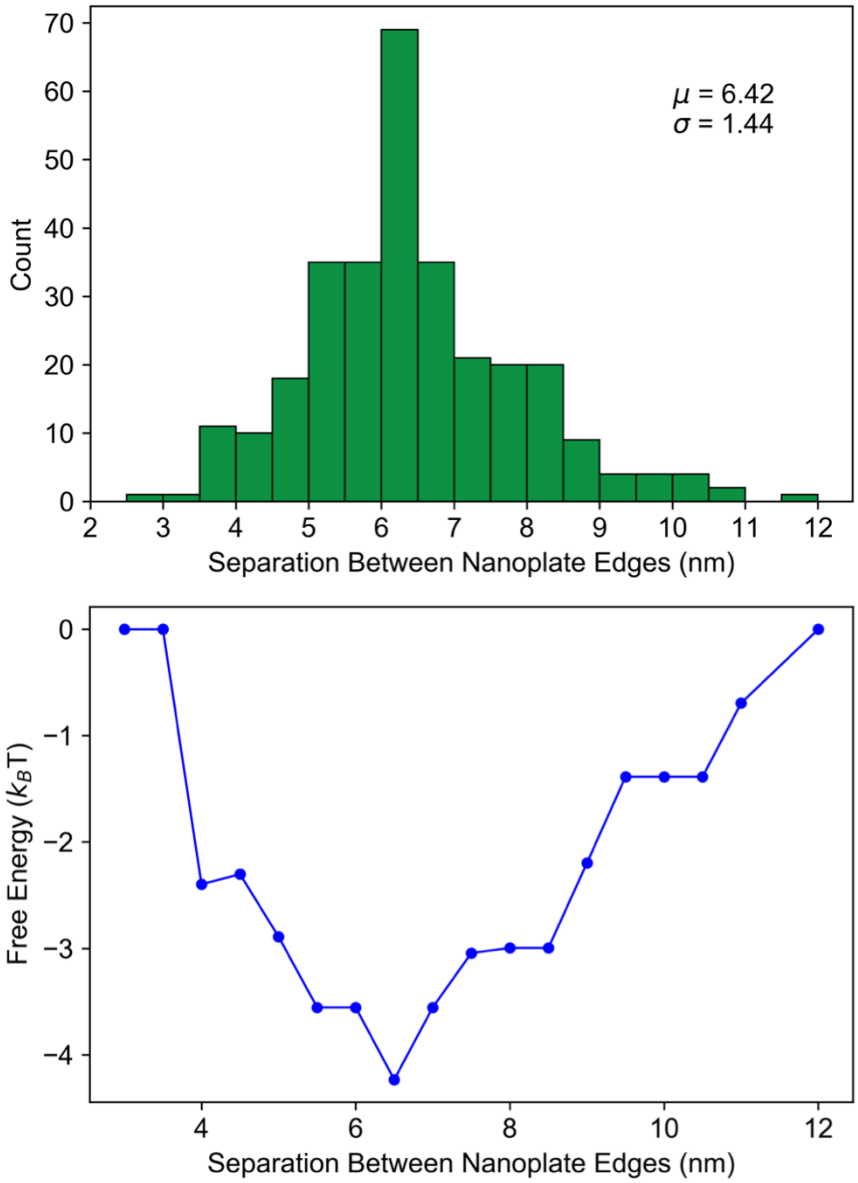

Figure 3.5. (top) Histogram of experimentally measured separations between edges of PEG-PO_3H_2 functionalized nanoplates that are aligned in the PMMA domain of lamellar-forming PS-*b*-PMMA films. Nanoplates are bridging together in strings at a mean interparticle spacing (μ) of 6.42 nm with a standard deviation (σ) of 1.44 nm. (bottom) Experimental free energy as a function of nanoplate edge-to-edge separation calculated by normalizing results in (top) over the total number of data points (300) to relate probability to energy using a Boltzmann distribution. The bin size is 0.5 nm.

Another noticeable characteristic of the GdF_3:Yb/Er nanoplate alignment behavior is shown in Figure 3.3. Both the nanoplates assembled in strings and the nanoplates at far enough separation distances to remain isolated appear either well aligned or only slightly tilted in the PMMA domains. To understand the tolerance for nanoplate orientation in confined lamellar PS-*b*-PMMA domains, the PMF curve in Figure 3.6 was calculated to represent the free energy of one PEG grafted nanoplate at fixed orientations (0º to 90º) while constrained to the center of the PMMA domain in a M_n = 38k-*b*-36.5k g/mol PS-*b*-PMMA lamellar diblock copolymer. Here, confinement indicates that the domain spacing of the nearly symmetric BCP is smaller than the longest and shortest diagonal of rhombic nanoplate, but larger than the nanoplate thickness. At low nanoplate tilts (0º to 10º), shown by the inset in Figure 3.6, the change in free energy is relatively small compared to high orientation angles. By considering the BCP morphologies in the 2D simulations of Figure 3.6, the domain distortion and thus the PS/PMMA interface are shown to increase substantially as the nanoplate is tilted from 0º to 10º to 30º and to 90º. Bordering domains are also more significantly perturbed at higher nanoplate orientation angles. Interestingly, when the PMF data is fit with a quadratic regression performed over 0º to 5º (shown in Figure 3.6), the fit curve quickly overestimates the energy cost of high angles. This deviation will be further investigated in our discussion. The simulations, however, verify that GdF_3:Yb/Er nanoplates are able to assume a range of low tilt angles in the PMMA domain of the nanocomposite films because the energy penalties are relatively small, $<1\ k_BT$.

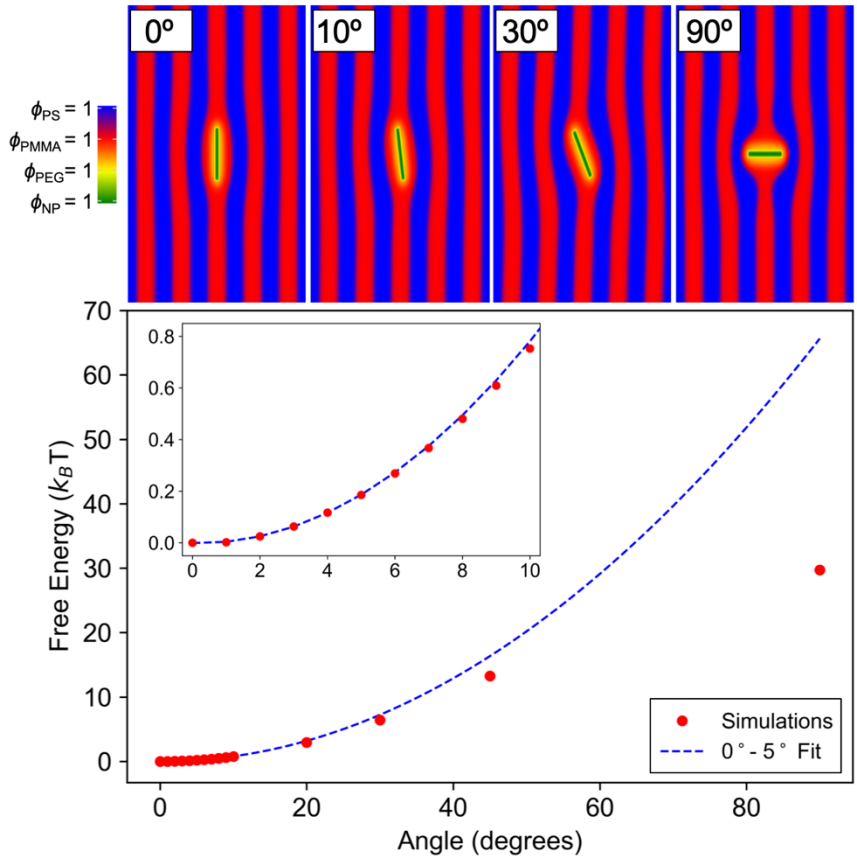

Figure 3.6. Potential of mean force curve to describe free energy (red) as a function of orientation for one PEG grafted in the PMMA domain of PS-*b*-PMMA lamellae. A quadratic regression (blue) was performed from 0º to 5º. The inset focuses in on the simulations data and the quadratic fit at small orientation angles (0º to 10º). (top) 2D simulations show system representations at nanoplate orientations of 0º, 10º, 30º, and 90º. PS, PMMA, PEG, and NP rich regions are displayed as blue, red, yellow, and green, respectively.

3.4 Discussion

We will first consider the origin of the free energy reduction, demonstrated in the PMF curve of Figure 3.4, as two nanoplates are moved from a separation distance of 21.7 nm to 7.0 nm, which corresponds to the locations of the energy barrier and the equilibrium interparticle spacing, respectively. Listak and Bocktaller previously showed that PS functionalized spherical NPs

dispersed in nearly symmetric bulk lamellar-forming poly(styrene-*b*-ethylene propylene) (PS-*b*-PEP) localize at high energy defects like high tilt (omega-type) and T-junction grain boundaries.[56] By redistributing NPs to these unfavorable lamellar structures, the authors elucidate a mechanism where NPs accumulate to stabilize the grain boundaries. More specifically, energetic costs related to perturbing the equilibrium BCP morphology are diminished by swelling these junctions with NPs. NP segregation alleviates the conformational energy penalties of highly stretched BCP chains imposed by forming the omega-type and T-junction defects. The T-junctions, in particular, not only contain exceptionally curved PS/PEP interfaces, but also produce more interfacial area than the equilibrium microstructure. As a result, Listak and Bockstaller observed "3D 'stringlike' particle aggregates" along these structures. Experiments by Rasin *et al.* also show that poly(2-vinylpyridine) (P2VP) grafted gold nanorods dispersed in cylindrical-forming PS-*b*-P2VP collect at the base of vertical P2VP cylinders.[21] The nanorods relieve local chain stretching caused by the minority P2VP domain wetting the substrate in a T-junction-like defect. Subsequent simulations from Koski *et al*. show that as the tilt angle of omega-type like defects in a BCP decrease (therefore curvature of A/B interface increases), NP accumulation becomes more prominent as a result of a greater extent of chain stretching.[57]

In the present system, intermediate separations of aligned PEG-PO_3H_2 grafted GdF_3:Yb/Er nanoplates promote the greatest distortion in the equilibrium BCP morphology. At these edge-to-edge nanoplate distances, the added PS/PMMA interfacial area formed from the domain bulges converge to create a region of PS/PMMA interface with the greatest possible curvature. This high energy state accounts for the energy barrier seen by the local maximum in the simulation results in Figure 3.4. Therefore, at a predicted separation of 21.7 nm between nanoplate edges, the conformational entropy penalty associated with chains from the PMMA block stretching to fill the space created by the defect is presumed to be the greatest. Therefore, bridging PEG-PO_3H_2 functionalized nanoplates into string assemblies not only decreases the degree of chain stretching,

but also decreases the interfacial area between the PS and PMMA microdomains. The nanoplates are, in essence, attracted to each other to create anisotropic assemblies with interparticle spacings prescribed by the energy well shown in simulations (Figure 3.4) and corroborated by experiments (Figure 3.5). Ultimately, the gain in free energy associated with decreasing interfacial area and minimizing chain stretching must be outweighed by the energy penalty associated with reducing the translational entropy associated with evenly distributing GdF_3:Yb/Er nanoplates. Both the simulations and the emergence of anisotropic PEG-PO_3H_2 functionalized GdF_3:Yb/Er nanoplate assemblies aligned in the PMMA domain of M_n = 38k-*b*-36.5k g/mol PS-*b*-PMMA shown experimentally in Figure 3.3 indicate that this energetic criteria is fulfilled.

In the experimental BCP nanocomposites films containing ϕ = 0.0083 and ϕ = 0.017 PEG grafted GdF_3:Yb/Er nanoplates, the NPs are highly oriented in the ordered parallel lamellae. The free energy calculations in Figure 3.6 support the alignment of nanoplates confined in the PMMA domain at low orientation angles. However, the inset in Figure 3.6 shows that, beyond ~7º, the free energy begins to deviates from quadratic behavior. Pryamitsyn and Ganesan present analogies that have been made between polymer brushes grafted onto flat substrates and the A and B polymers of an A-B lamellar-forming BCP.[58] Based on prior results, the authors express the pressure field [$P(z)$ in k_BT] on a polymer brush as

$$P(z) = \frac{3\pi^2 h^2}{8N^2 b^5}\left(1 - \frac{z^2}{h^2}\right) \qquad (3.5)$$

in terms of brush height (h), degree of polymerization (N), statistical segmental length (b), and distance from the surface (z).[58] The elastic energy cost, $\Delta E_{br}(z)$, of a NP placed within the brush is then casted as

$$\Delta E_{br}(z) \cong P(z)\frac{4\pi R^3}{3} \qquad (3.6)$$

where R is the NP dimension.[58]

Importantly, Pryamitsyn and Ganesan note that $\Delta E_{br}(z)$ applies when the distortions, attributed to inserting a NP mid-block, are relatively small.[58] This hypothesis is consistent with the simulation results shown in Figure 3.6. At higher nanoplate tilt angles the quadratic approximation breaks down due to large perturbations of the surrounding BCP chains and, importantly, the dynamic behavior of the A/B BCP interface distorting around the NP, helping to restore chains from highly compressed states. Therefore, we credit the strong alignment of nanoplates in lamellar-forming M_n = 38k-*b*-36.8k g/mol PS-b-PMMA film to the entropic cost attributed to large chain deformations. This conclusion is also supported by previous results from Deshmukh *et al.* where a narrow tolerance of orientation angles ($-5 \leq \theta \leq 5$) was observed in 71% of PEG-thiol functionalized gold nanorods aligned in PS-b-PMMA lamellae.[19]

3.5 Conclusions

The formation of anisotropic string assemblies of and the anticipated domain bulge around M_n = 5 kg/mol PEG-PO_3H_2 functionalized GdF_3:Yb/Er (20/2 mol%) nanoplates aligned in parallel lamellar-forming M_n = 38k-*b*-36.8k g/mol PS-b-PMMA films were investigated. Although electron microscopy and scattering techniques were unable to experimentally probe the local domain distortion, nanoplate strings with a mean interparticle spacing of 6.42 nm were observed. Complementary hSCFT simulations mapped the pairwise interactions between two PEG grafted nanoplates aligned in the PMMA domain. The 2D simulations not only show the morphological effects of nanoplate insertion, clearly depicting the local domain distortion, but also predicts an equilibrium interparticle spacing of 7.0 nm that is in good agreement with experiments. The free energy well, centered around the free energy minima, of the calculated PMF curves is corroborated by the experiments where the edge-to-edge distances in nanoplate strings range from ~2.5 nm to ~12 nm. The emergence of anisotropic nanoplate assemblies within this span of interparticle spacings is consistent with minimizing the effects of (1) excessive PEG chain compression at small

separations and (2) forming regions of high curvature in the PS/PMMA interface accompanied by large conformational entropy costs at intermediate separations. Additional simulations show non-quadratic behavior at high tilt orientations of nanoplates, which supports the high degree of alignment observed experimentally. Harnessing the shape-dependent properties of nanoplates and not only directing their orientation, but also controlling their interparticle spacing in a polymer matrix is particularly attractive for a variety of applications, including plasmonic coupling. To further tune the edge-to-edge separation of nanoplates in a BCP film, the effect of higher BCP molecular weights on the shape of the PMF curves, the location of important features, and consequently the formation of string assemblies will be the subject of a future publication.

3.6 References

(1) Zhao, Y.; Thorkelsson, K.; Mastroianni, A. J.; Schilling, T.; Luther, J. M.; Rancatore, B. J.; Matsunaga, K.; Jinnai, H.; Wu, Y.; Poulsen, D.; Fréchet, J. M. J.; Alivisatos, A. P.; Xu, T. Small-Molecule-Directed Nanoparticle Assembly Towards Stimuli-Responsive Nanocomposites. *Nat. Mat.* **2009**, 8, 979-985.

(2) Thorkelsson, K.; Mastroianni, A. J.; Ercius, P.; Xu, T. Direct Nanorod Assembly Using Block Copolymer-Based Supramolecules. *Nano Lett.* **2011**, 12, 498-504.

(3) Li, W.; Zhang, P.; Dai, M.; He, J.; Babu, T.; Xu, Y.-L.; Deng, R.; Liang, R.; Lu, M.-H.; Nie, Z.; Zhu, J. Ordering of Gold Nanorods in Confined Spaces by Directed Assembly. *Macromolecules* **2013**, 46, 2241-2248.

(4) Thorkelsson, K.; Nelson, J. H.; Alivisatos, A. P.; Xu, T. End-to-End Alignment of Nanorods in Thin Films. *Nano Lett*. **2013**, 13, 4908-4913.

(5) Hsu, S.-W.; Xu, T. Tailoring Co-assembly of Nanodiscs and Block Copolymer-Based Supramolecules by Manipulating Interparticle Interactions. *Macromolecules*. **2019**, 52, 2833-2842.

(6) Bockstaller, M. R.; Mickiewicz, R. A.; Thomas, E. L. Block Copolymer Nanocomposites: Perspectives for Tailored Functional Materials. *Adv. Mater.* **2005,** 17, 1331-1349.

(7) Hoheisel, T. N.; Hur, K.; Wiesner, U. B. Block Copolymer-Nanoparticle Hybrid Self-Assembly. *Prog. Polym. Sci.* **2015**, 40, 3-32.

(8) Sarkar, B.; Alexandridis, P. Block Copolymer-Nanoparticle Composites: Structure, Functional Properties, and Processing. *Prog. Polym. Sci.* **2015**, 40, 33-62.

(9) Thompson, R. B.; Ginzburg, V. V.; Matsen, M. W.; Balazs, A. C. Predicting the Mesophases of Copolymer-Nanoparticle Composites. *Science* **2001**, 292, 2469-2472.

(10) Thompson, R. B.; Ginzburg, V. V.; Matsen, M. W.; Balazs, A. C. Block Copolymer-Directed Assembly of Nanoparticles: Forming Mesoscopically Ordered Hybrid Materials. *Macromolecules* **2002**, 35, 1060-1071.

(11) Bockstaller, M. R.; Lapetnikov, Y.; Marge, S.; Thomas, E. L. Size-Selective Organization of Enthalpic Compatibilized Nanocrystals in Ternary Block Copolymer/Particle Mixtures. *J. Am. Chem. Soc.* **2003**, 125, 5276-5277.

(12) Lin, Y.; Böker, A.; He, J.; Sill, K.; Xiang, H.; Abetz, C.; Li, X.; Wang, J.; Emrick, T.; Long, S.; Wang, Q.; Balazs, A.; Russell, T. P. Self-Directed Self-Assembly of Nanoparticle/Copolymer Mixtures. *Nature* **2005**, 434, 55-59.

(13) Chiu, J. J.; Kim, B. J.; Kramer, E. J.; Pine, D. J. Control of Nanoparticle Location in Block Copolymers. *J. Am. Chem. Soc.* **2005**, 127, 5036-5037.

(14) Balazs, A. C.; Emrick, T.; Russell, T. P. Nanoparticle Polymer Composites: Where Two Small Worlds Meet. *Science* **2006**, 314, 1107-1110.

(15) Kim, B. J.; Bang, J.; Hawker, C. J.; Kramer, E. J. Effect of Areal Chain Density on the Location of Polymer-Modified Gold Nanoparticles in a Block Copolymer Template. *Macromolecules* **2006**, 39, 4108-4114.

(16) Chiu, J. J.; Kim, B. J.; Yi, G.; Band, J.; Kramer E. J.; Pine, D. J. Distribution of Nanoparticles in Lamellar Domains of Block Copolymers. *Macromolecules* **2007**, 40, 3361-3365.

(17) Kim, B. J.; Bang, J.; Hawker, C. J.; Chiu, J. J.; Pine, D. J.; Jang, S. G.; Yang, S.; Kramer, E. J. Creating Surfactant Nanoparticles for Block Copolymer Composites through Surface Chemistry. *Langmuir* **2007**, 23, 12693-12703.

(18) Kim, B. J.; Fredrickson, G. H.; Kramer, E. J. Effect of Polymer Ligand Molecular Weight on Polymer-Coated Nanoparticle Location in Block Copolymers. *Macromolecules* **2008**, 41, 436-447.

(19) Deshmukh, R. D.; Liu, Y.; Composto, R. J. Two-Dimensional Confinement of Nanorods in Block Copolymer Domains. *Nano Lett.* **2007**, 7, 3662-3668.

(20) Ploshnik, E.; Salant, A.; Banin, U.; Shenhar, R. Hierarchical Surface Patterns of Nanorods Obtained by Co-Assembly with Block Copolymers in Ultrathin Films. *Adv. Mater.* **2010**, 22, 2774-2779.

(21) Rasin, B.; Chao, H.; Jiang, G.; Wang, D.; Riggleman, R. A.; Composto, R. J. Dispersion and Alignment of Nanorods in Cylindrical Block Copolymer Thin Films. *Soft Matter* **2016**, 12, 2177-2185.

(22) Krook N. M.; Ford, J.; Maréchal, M.; Rannou, P.; Meth, J. S.; Murray, C. B.; Composto R. J. Alignment of Nanoplates in Lamellar Diblock Copolymer Domains and the Effect of Particle Volume Fraction on Phase Behavior. *ACS Macro Lett.* **2018**, 7, 1400–1407.

(23) Zhang, S.; Pelligra, C. I.; Osuji, C. O. Directed Assembly of Hybrid Nanomaterials. *Adv. Mater.* **2018**, 30, 1705794.

(24) Zhang, S.; Pelligra, C. I.; Keskar, G.; Jiang, J.; Majewski, P. W.; Taylor, A. D.; Ismail-Beigi, S.; Pfefferle, L. D.; Osuji, C. O. Directed Self-Assembly of Hybrid Oxide/Polymer Core/Shell Nanowires with Transport Optimized Morphology for Photovoltaics. *Adv. Mater.* **2012**, 24, 82-87.

(25) Pelligra, C. I.; Majewski, P. W.; Osuji, C. O. Large Area Vertical Alignment of ZnO Nanowires in Semiconducting Polymer Thin Films Directed by Magnetic Fields. *Nanoscale* **2013**, 5, 10511-10517.

(26) Diroll, B. R.; Greybush, N. J.; Kagan, C. R.; Murray, C. B. Smetic Nanorod Superlattices Assembled on Liquid Subphases: Structure, Orientation, Defects, and Optical Polarization. *Chem. Mater.* **2015**, 27, 2998-3008.

(27) Stebe, K. J.; Lewandowski, E.; Ghosh, M. Oriented Assembly of Metamaterials. *Science* **2009**, 325, 159-160.

(28) Liu, Q.; Ackerman, P. J.; Lubensky, T. C.; Smalyukh, I. I. Biaxial Ferromagnetic Liquid Crystal Colloids. *Proc. Natl. Acad. Sci. U. S. A.* **2016**, 113, 10479-10484.

(29) Liu, Z.; Xu, Z.; Hu, X.; Gao, C. Lyotropic Liquid Crystal of Polyacrylonitrile-Grafted Graphene Oxide and its Assembled Continuous Strong Nacre-Mimetic Fibers. *Macromolecules* **2013**, 46, 6931-6941.

(30) Chen, J.; Huang, X.; Sun, B.; Wang, Y.; Zhu, Y.; Jiang, P. Vertically Aligned and Interconnected Boron Nitride Nanosheets for Advanced Flexible Nanocomposite Thermal Interface Materials. *ACS Appl. Mater. Interfaces* **2017**, 9, 30909-30917.

(32) Akcora, P.; Liu, H.; Kumar, S. K.; Moll, J.; Li, Y.; Benicewicz, B. C.; Schadler, L. S.; Acehan, D.; Panagiotopoulos, A. Z.; Pryamitsyn, V.; Ganesan, V.; Ilavsky, J.; Thiyagarajan, P.; Colby, R. H.; Douglas, J.F. Anisotropic Self-Assembly of Spherical Polymer-Grafted Nanoparticles. *Nat. Mater.* **2009**, 8, 354-359.

(33) Gao, B.; Arya, G.; Tao, A. R. Self-Orienting Nanocubes for the Assembly of Plasmonic Nanojunctions. *Nat. Nanotechnol.* **2012**, 7, 433-437.

(34) Ferrier, R. C., Jr.; Lee, H.-S.; Hore, M. J. A.; Caporizzo, M.; Eckmann, D. M.; Composto, R. J. Gold Nanorod Linking to Control Plasmonic Properties in Solution and Polymer Nanocomposites. *Langmuir* **2014**, 30, 1906-1914.

(35) Gurunatha, K. L.; Marvi, S.; Arya, G.; Tao, A. R. Computationally Guided Assembly of Oriented Nanocubes by Modulating Grafted Polymer-Surface Interactions. *Nano Lett.* **2015**, 15, 7377-7382.

(36) Lee, J. Y.; Shou, Z.; Balazs, A. C. Predicting the Morphologies of Confined Copolymer/Nanoparticle Mixtures. *Macromolecules* **2003**, 36, 7730-7739.

(37) Sides, S. W.; Kim, B. J.; Kramer, E. J.; Fredrickson, G. H. Hybrid Particle-Field Simulations of Polymer Nanocomposites. *Phys. Rev. Lett.* **2006**, 96, 250601.

(38) Matsen, M. W.; Thompson, R. B. Particle Distributions in a Block Copolymer Nanocomposite. *Macromolecules* **2008**, 41, 1853-1860.

(39) Hur, K.; Henning, R. G.; Escobedo, F. A.; Wiesner, U. Mesoscopic Structure Prediction of Nanoparticle Assembly and Coassembly: Theoretical Foundation. *J. Chem. Phys.* **2010**, 133, 194108.

(40) Ting, C. L.; Composto, R. J.; Frischknecht, A. L. Orientational Control of Polymer Grafted Nanorods. *Macromolecules* **2016**, 49, 1111-1119.

(41) Lee, B.; Park, I.; Yoon, J.; Park, S.; Kim, J.; Kim, K.-W.; Chang, T.; Ree, M. Structural Analysis of Block Copolymer Thin Films with Grazing Incidence Small-Angle X-ray Scattering. *Macromolecules* **2005**, 38, 4311-4323.

(42) Lu, X.; Yager, K. G.; Johnston, D.; Black, C. T.; Ocko, B. M. Grazing-Incidence Transmission X-ray Scattering: Surface Scattering in the Born Approximation. *J. Appl. Cryst.* **2013**, 46, 165-172.

(43) Liu, J.; Yager, K. G. Unwarping GISAXS Data. *IUCrJ* **2018**, 5, 737-752.

(44) Koski, J.; Chao, H.; Riggleman, R. A. Field Theoretic Simulations of Polymer Nanocomposites. *J. Chem. Phys.* **2013**, 139, 244911.

(45) Hickey, R. J.; Koski, J.; Meng, X.; Riggleman, R. A.; Zhang, P.; Park, S.-J. Size-Controlled Self-Assembly of Superparamagnetic Polymersomes. *ACS Nano* **2014**, 8, 495-502.

(46) Koski, J.; Chao, H.; Riggleman, R. A. Predicting the Structure and Interfacial Activity of Diblock Brush, Mixed Brush, and Janus-Grafted Nanoparticles. *Chem. Commun.* **2015**, 51, 5440-5443.

(47) Ferrier, R. C., Jr.; Koski, J.; Riggleman, R. A.; Composto, R. J. Engineering the Assembly of Gold Nanorods in Polymer Matrices. *Macromolecules* **2016**, 49, 1002-1015.

(48) Koski, J. P.; Riggleman, R. A. Field-Theoretic Simulations of Block Copolymer Nanocomposites in a Constant Interfacial Tension Ensemble. *J. Chem. Phys.* **2017**, 146, 164903.

(49) Chao, H.; Lindsay, B. J.; Riggleman, R. A. Field-Theoretic Simulations of the Distribution of Nanorods in Diblock Copolymer Thin Films. *J. Phys. Chem. B.* **2017**, 121, 11198-11209.

(50) Hore, M. J. A.; Composto, R. J. Using Miscible Polymer Blends to Control Depletion-Attraction Forces Between Au Nanorods in Nanocomposite Films. *Macromolecules* **2012**, 45, 6078-6086.

(51) Fredrickson, G. H. *The Equilibrium Theory of Inhomogeneous Polymers*; Oxford University Press: 2006.

(52) Eitouni, H. B.; Balsara, N. P. Thermodynamics of Polymer Blends. Chapter 19 in *Physical Properties of Polymers Handbook*, 2nd ed.; Mark, J. E.; Springer: New York, 2007; p 339-356.

(53) Choi, J. O.; Moore, J. A.; Corelli, J. C.; Silverman, J. P.; Bakhru, H. Degradation of Poly(Methylmethacylate) by Deep Ultraviolet, X-ray, Electron Beam, and Proton Beam Irradiation. *J. Vac. Sci. Technol. B* **1988**, 6, 2286-2289.

(54) Tang, C.; Lennon, E. M.; Fredrickson, G. H.; Kramer, E. J.; Hawker, C. J. Evolution of Block Copolymer Lithography to Highly Ordered Square Arrays. *Science* **2008**, 322, 429-432.

(55) Egerton, R. F. Mechanisms of Radiation Damage in Beam-Sensitive Specimens, for TEM Accelerating Voltages Between 10 and 300 kV. *Microsc. Res. Tech.* **2012**, 75, 1550-1556.

(56) Listak, J.; Bockstaller, M. R. Stabilization of Grain Boundary Morphologies in Lamellar Block Copolymer/Nanoparticle Blends. *Macromolecules* **2006**, 39, 5820-5825.

(57) Koski, J.; Hagberg, B.; Riggleman, R. A. Attraction of Nanoparticles in Tilt Grain Boundaries in Block Copolymers. *Macromol. Chem. Phys.* **2016**, 217, 509-518.

(58) Pryamitsyn, V.; Ganesan, V. Strong Segregation Theory of Block Copolymer-Nanoparticle Composites. *Macromolecules* **2006**, 39, 8499-8510.

CHAPTER 4: Vertical Alignment of Nanoplates Guided by Perpendicular Lamellar Domains in Self-Assembled Diblock Copolymer Nanocomposites

Content in this chapter was reprinted (adapted) with permission from Nadia M. Krook, Boris Rasin, Jeffrey S. Meth, Christopher B. Murray, Robert A. Riggleman, and Russell J. Composto. This work is in preparation to be submitted for publication in a peer-reviewed journal.

4.1 Introduction

Nature has been successful at producing sophisticated hierarchical architectures with precise control over both the dispersion and orientation of anisotropic reinforcements for enhanced properties.[1,2] Among such materials, like wood and bones, nacre (the inner shell of a mollusk also known as mother-of-pearl) has especially impressive properties from the combination of organic and inorganic components. Nacre interlays aligned brittle inorganic platelets (made of calcium carbonate, calcium phosphate, and amorphous silica) at nearly 95 wt% with soft biopolymers (keratin, collagen, and chitin).[3] The impressive strength of nacre would not be realized by these two constituents alone or without the highly oriented internal structure. Hierarchical biomaterials like these continue to serve as models for what has yet to be achieved in *self-assembling* polymer nanocomposites (PNCs) in terms of fully tuning the placement and alignment of reinforcing particles.

To create synthetic nacre mimetic materials, Wei *et al.*[4] formed multi-layer films that relied on the sedimentation of copper sulfide nanoplates in poly(vinylidene fluoride) while Grossman *et al.*[5] implemented a vacuum-assisted magnetic alignment process to create aligned α-alumina microplate scaffolds that are then infiltrated with epoxy. During these techniques as well as through other common processing methods of PNCs, including spin-coating,[6] doctor blading,[7] and microfluidic assembly,[8] anisotropic particles (rods, tubes, and plates) tend to align in the direction of material flow. Therefore, external forces align non-spherical nanoparticles (NPs) parallel to

substrate and free surface. Consequently, with NP building blocks preferentially oriented in the plane of the film, in-plane versus out-of-plane properties will differ.

However, out-of-plane alignment of anisotropic NPs is more advantageous than in-plane alignment for a variety of applications.[9] Properties through the thickness of PNCs have the potential to be enhanced when the long-axis of nanoplates and nanorods are oriented perpendicular to the plane of the films. For example, liquid crystal electrode films containing vertically aligned 2D titanium dioxide exhibit fast out-of-plane ion diffusion for improved energy storage capabilities.[10] Hybrid materials, well suited for ordered bulk heterojunction solar cells, have also been formed by vertically orienting either titanium dioxide nanorods[11] or zinc oxide nanowires.[12] Vertically aligned plates such as graphite[13,14] or boron nitride[15,16] are also of particular interest to create high performance thermal interface materials for managing heat dissipation in microelectronic packaging. To produce such structures with anisotropic NPs oriented out-of-plane, various strategies in practice include liquid-air interface or solvent-mediated assembly,[17-20] directed templating with DNA brushes,[21] applying a magnetic[12,15] or electric field,[22,23] and exploiting flow-induced alignment as a preliminary processing step.[13,14] However, with several of these methods, the particles are either not contained in a polymer matrix, which would better lend itself to be used as a coating or freestanding film, or the fabrication process requires multiple steps. For instance, Hitachi Chemical Company developed flexible, heat-dissipating sheets by vertically orienting graphite in a thermosetting resin through a multistep process.[13,14] Despite the thermal conductivity through the thickness of the composite sheets being enhanced tenfold compared to if the graphite particles were orientated horizontally, the process to achieve this structure was very much a top-down approach. The heat-dissipating composite was made by kneading graphite with the thermoset resin, compressing the mixture into sheets (particles aligned horizontally from external forces at this point), laminating sheets together, and cutting perpendicular slices of the laminate. The final laminate slices then contained the vertically aligned graphite particles.

Therefore, the purpose of the present research is to demonstrate a tractable, limited-step process to create large area, thin film PNCs with vertically oriented anisotropic NPs. To do so, the work herein exploits a symmetric self-assembled block copolymer (BCP) and the lamellar morphology, resulting from microphase separation, to orient anisotropic NPs, and more specifically rhombic nanoplates [gadolinium trifluoride doped with ytterbium and erbium GdF_3:Yb/Er (20/2 mol%)], perpendicular to the substrate. Previously, Xu and coworkers directed the assembly of nanorods and nanoplates in BCP-based supramolecules.[24-26] Although the anisotropic NPs were aligned along the cylindrical or lamellar domains, there was no preferential orientation (parallel or vertical) of the microdomains. Consequently, the NPs were randomly oriented within the overall PNCs. Meanwhile, Composto and coworkers established parallel alignment of both nanorods and nanoplates (parallel nanoplates shown in Chapter 2 and Chapter 3) in traditional lamellar-forming BCPs by orienting the lamellae parallel to the substrate in thin films PNCs.[27,28] While horizontally oriented BCP domains has been shown to align anisotropic NPs parallel to the substrate, using vertically oriented microdomains to orient non-spherical NPs perpendicular to the substrate is less explored. Therefore, as illustrated in Figure 4.1a, generating thin films with lamellar domains oriented vertically is at the crux of the present research to be able to self-assemble PNCs that guide out-of-plane GdF_3:Yb/Er nanoplates alignment. This work serves as a foundation to be adapted to other NP systems that would benefit from perpendicular alignment for functional polymeric coatings.

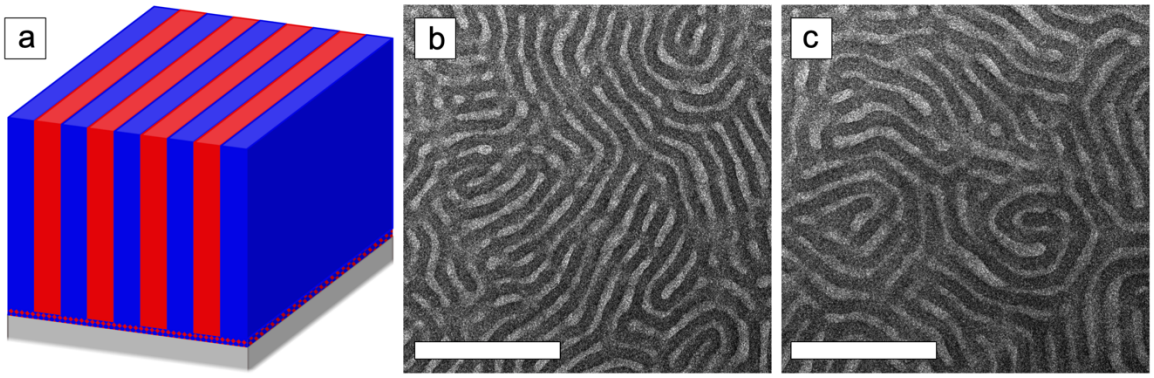

Figure 4.1. (a) An idealized schematic (red and blue blocks depict the PMMA and PS lamellar domains, respectively) portraying the representative top-down TEM (JEM-1400, 120 kV) images of (b) M_n = 73k-*b*-73k g/mol and (c) M_n = 95k-*b*-95k g/mol PS-*b*-PMMA films [thicknesses of (a) ~160 nm and (b) ~180 nm] after solvent annealing (20 min in THF) and thermal annealing (220ºC, 24 h) with lamellae oriented perpendicular to the substrate. The light and dark microdomains are PMMA and PS, respectively, and the scale bars are 300 nm.

4.2 Results and Discussion

Substrate and surface interactions govern the wetting behavior and thus the self-assembly direction of BCP domains in thin films. In a lamellar-forming poly(styrene-*b*-methyl methacrylate) (PS-*b*-PMMA) BCP, PMMA preferentially wets silicon (Si) substrates. After processing, the lamellae will ultimately orient parallel to the substrate. To combat preferential wetting of one BCP block and induce vertical microdomain alignment, a variety of techniques have been developed to either modify the chemical nature of the substrate or mediate the surface tension at the free interface. Strategies such as chemical surface patterning, solvent annealing, and applying an electric field have been previously established.[29-31] Pioneering work from Mansky *et al*. grafted statistically random copolymers to Si for specific interfacial energies.[32] A comparable procedure, briefly described in the Appendix C, was adapted from Ji *et al*. to graft hydroxy terminated PS and PMMA

to Si oxide substrates to create a neutral brush mat for the M_n = 73k-*b*-73k g/mol and M_n = 95k-*b*-95k g/mol PS-*b*-PMMA used in this study.[33]

Thin films of M_n = 73k-*b*-73k g/mol and M_n = 95k-*b*-95k g/mol of lamellar-forming PS-*b*-PMMA were spin-coated onto the neutral layers. Even though effectively equal surface tensions are created for PS and PMMA between thermal annealing temperatures of 170ºC and 230ºC,[34] at 190ºC and at relatively large BCP molecular weights, the quality of M_n = 73k-*b*-73k g/mol and M_n = 95k-*b*-95k g/mol lamellar formation decreases, as shown in Figure C.2. Studies implementing mixed annealing techniques (solvent and thermal) have shown improved structure quality.[35,36] Figure C.3 and Figure C.4 first demonstrate the effect of only solvent annealing samples with tetrahydrofuran (THF) for 20 min and 40 min, respectively. Solvent vapors of THF, a nearly neutral solvent for PS and PMMA, swell the BCP films and increase chain mobility by effectively lowering its glass transition temperature.[37] As seen in Figure C.3, solvent annealing for 20 min shows the highest fidelity structure whereas over processing the film and annealing for 40 min can cause adverse effects. The resulting disordered lamellae is featured in Figure C.4. After solvent annealing alone with THF, the PS-*b*-PMMA morphologies are kinetically trapped in a metastable state.[37] Ultimately, by coupling 20 min of solvent annealing with 24 h of thermal annealing under vacuum at 220ºC, a thermal equilibrium structure is reached. Through this combination of annealing methods, continuous and optimized vertical M_n = 73k-*b*-73k g/mol (Figure 4.1b) and M_n = 95k-*b*-95k g/mol (Figure 4.1c) PS-*b*-PMMA lamellae were formed to serve as templates for guiding the vertical alignment of GdF_3:Yb/Er nanoplates. Complete experimental details can be found in Appendix C.

The synthesis of the rhombic GdF_3:Yb/Er (20/2 mol%) nanoplates is fully described elsewhere and in Appendix A.[28] After rapid thermal decomposition of the relevant rare earth precursors, the GdF_3:Yb/Er nanoplates measure 35 nm along the longest diagonal, 22 nm along the shortest diagonal, and only 3 nm thick. After purifying the reaction and as schematized in Figure

4.2a, the NPs are stabilized with a short hydrocarbon oleic acid (OA) ligand. With these plate dimensions, the NPs are commensurate with the microdomain spacing of both the M_n = 73k-*b*-73k g/mol and M_n = 95k-*b*-95k g/mol PS-*b*-PMMA lamellae. However, after mixing the as-synthesized nanoplates with the BCP solutions and processing the films with the prescribed annealing schedule, the NPs are neither integrated in the domains nor individually dispersed. Instead, the nanoplates with OA form stacks of varying lengths as shown in Figure 4.2b and Figure 4.2c. Not only do the nanoplates group together face-to-face, but the NPs also appear to disrupt the lamellar formation. Compared to the persistent fingerprint pattern characteristic of well-formed vertical lamellae in Figure 4.1b and Figure 4.1c, several structural defects emerge in Figure 4.2b and Figure 4.2c. Relative to the M_n = 73k-*b*-73k g/mol BCP nanocomposite (Figure 4.2b), more defects materialize in the M_n = 95k-*b*-95k g/mol composite (Figure 4.2c), resembling the disordered lamellae in Figure C.4.

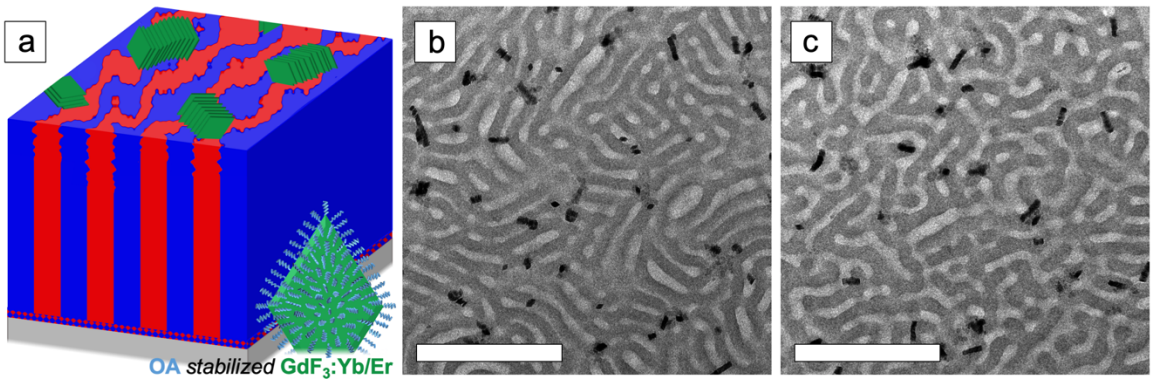

Figure 4.2. (a) An idealized schematic (red and blue blocks depict the PMMA and PS lamellar domains, respectively) portraying the representative top-down TEM (JEM-1400, 120 kV) images of (b) M_n = 73k-*b*-73k g/mol and (c) M_n = 95k-*b*-95k g/mol PS-*b*-PMMA films [thicknesses of (a) ~180 nm and (b) ~185 nm] containing ϕ = 0.0083 OA stabilized GdF_3:Yb/Er (20/2 mol%) nanoplates after solvent annealing (20 min in THF) and thermal annealing (220ºC, 24 h) with lamellae oriented perpendicular to the substrate. The light and dark microdomains are PMMA and PS, respectively, and the scale bars are 300 nm.

Oleic acid is immiscible with both PS and PMMA. Therefore, we surmise that the OA stabilized GdF_3:Yb/Er nanoplates segregate to the free surface of the film to minimize unfavorable interactions with the PS and PMMA domains and, as illustrated in Figure 4.2a, distort the underlying equilibrium BCP morphology. To confirm this theory, we perform AFM characterization on the composites from Figure 4.2b and Figure 4.2c. The respective topography images are shown in Figure 4.3a and Figure 4.3b. The topographical information confirms that the GdF_3:Yb/Er nanoplates, decorated with OA, assemble in stacks at the composite/air interface and appear as bright stripes in Figure 4.3a and Figure 4.3b. Interestingly, both the TEM and AFM images show that the stacks do not co-assemble in the direction of either the PS or PMMA microdomains. In contrast to the cooperative assembly of PS grafted nanorods with the PS block in ultrathin PS- *b*-PMMA films observed by Ploshnik *et al.*,[38,39] the GdF_3:Yb/Er seem to have no simultaneous ordering with the underlying morphology. Furthermore, the TEM and topographical AFM results give the impression that nanoplate stacks span multiple lamellar periods. The AFM phase image of the M_n = 73k-*b*-73k g/mol PS-*b*-PMMA composite in Figure 4.4 more effectively demonstrates the negative morphological effect that the BCP incurs when as-synthesized nanoplates stack at the film surfaces. Figure 4.4 clearly shows regions of disruption in the lamellar formation across several periods. Within these clusters, the distinct shape of the rhombic nanoplates is seen breaking through the film surface. Therefore, as a result of enthalpic incompatibility, the GdF_3:Yb/Er NPs neither disperse well in the composite system nor colocalize within or on top of either of the PS or the PMMA microdomains.

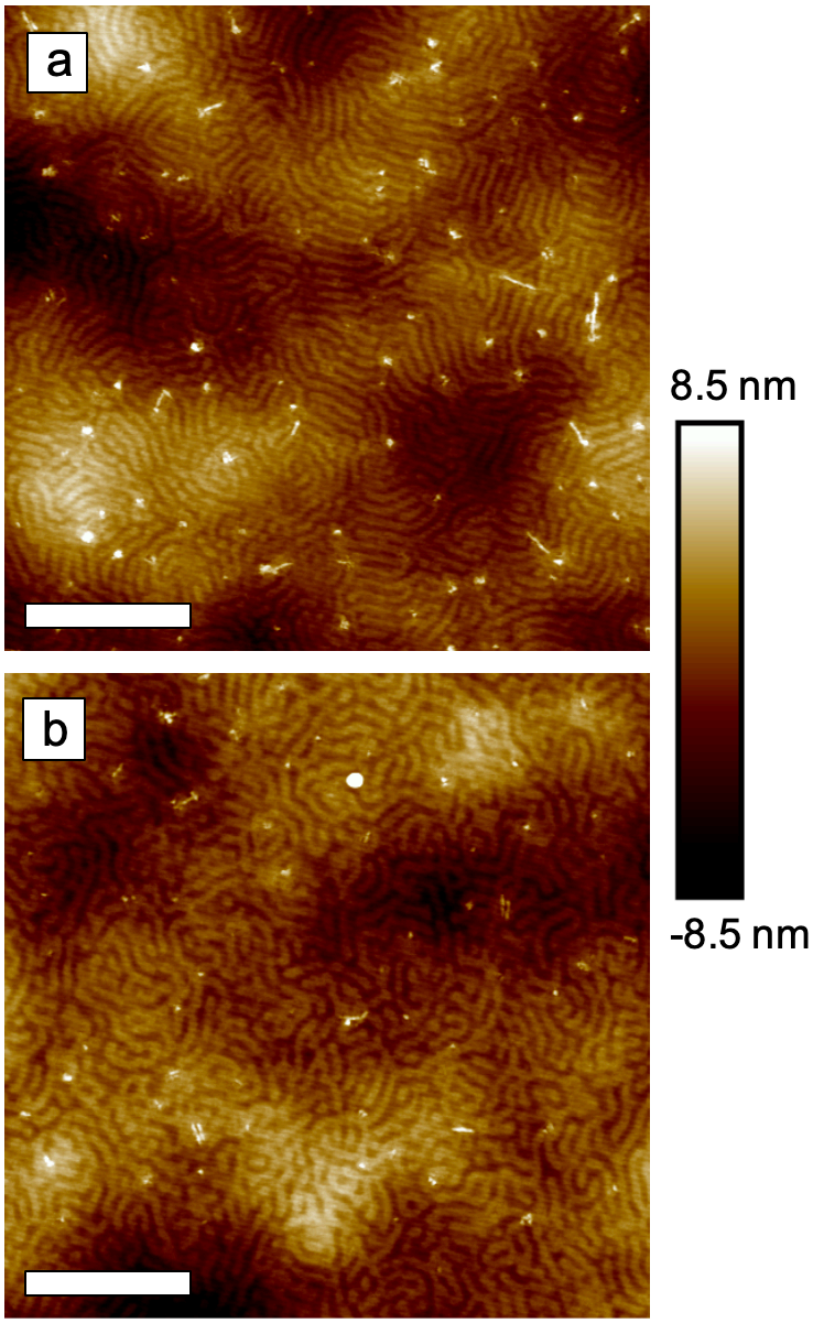

Figure 4.3. Representative AFM topography images of (a) M_n = 73k-*b*-73k g/mol and (b) M_n = 95k-*b*-95k g/mol PS-*b*-PMMA films [thicknesses of (a) ~180 nm and (b) ~185 nm] containing ϕ = 0.0083 OA stabilized GdF_3:Yb/Er (20/2 mol%) nanoplates after solvent annealing (20 min in THF) and thermal annealing (220ºC, 24 h) with lamellae oriented perpendicular to the substrate. The scale bars are 1 μm.

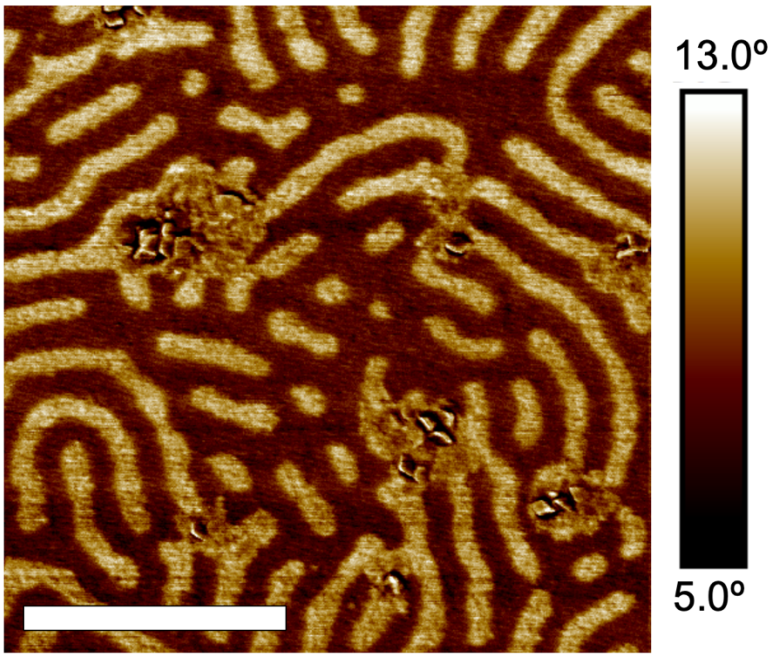

Figure 4.4. Representative AFM phase image of M_n = 73k-*b*-73k g/mol (thickness ~180 nm) containing ϕ = 0.0083 OA stabilized GdF_3:Yb/Er (20/2 mol%) nanoplates after solvent annealing (20 min in THF) and thermal annealing (220ºC, 24 h) with lamellae oriented perpendicular to the substrate. The scale bar is 400 nm.

To create a NP system with favorable interactions to one of the BCP blocks, a solution-phase ligand exchange procedure was previously developed to displace OA with M_n = 5 kg/mol phosphoric acid functionalized polyethylene glycol (PEG-PO_3H_2).[28] With PEG grafted to the nanoplate surfaces, the particles now have proper chemical compatibilization for the PMMA domain and chemical dislike to the PS domain. We predict that (1) the PEG functionalized GdF_3:Yb/Er NPs will disperse in the PMMA block and (2) that the vertically oriented lamellar domains will direct out-of-plane alignment of the nanoplates as depicted by Figure 4.5a. After mixing and spin-coating the PEG modified nanoplates, combined in solution with both M_n = 73k-*b*-73k g/mol and M_n = 95k-*b*-95k g/mol PS-*b*-PMMA, the composite films were annealed with the stipulated solvent and thermal treatment. Figure 4.5b and Figure 4.5c show PEG-PO_3H_2

functionalized GdF_3:Yb/Er well distributed in the lighter, PMMA domain. Regardless of BCP molecular weight, the nanoplates appear edge-on in the top-down TEM micrographs, indicative of vertical alignment. Importantly, the insertion of polymer modified NPs does not disrupt the equilibrium lamellar morphology, which consequently promotes the vertical orientation of the nanoplates.

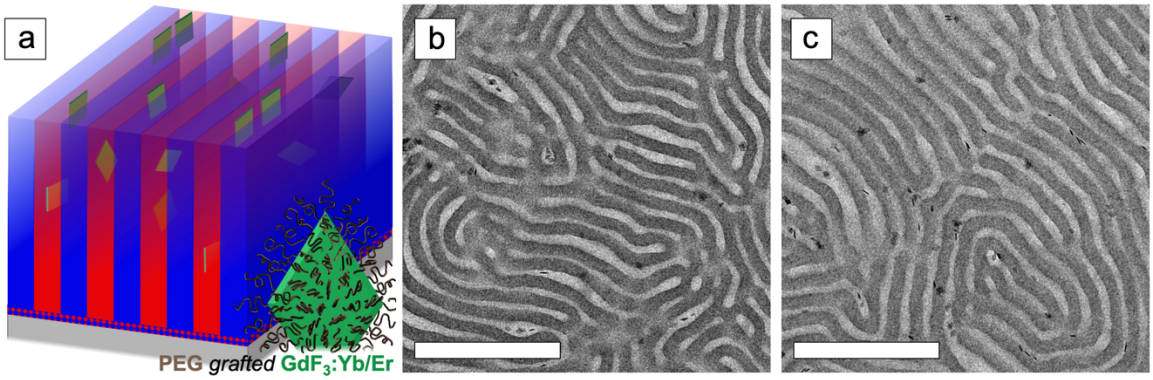

Figure 4.5. (a) An idealized schematic (red and blue blocks depict the PMMA and PS lamellar domains, respectively) portraying the representative top-down TEM (JEM-1400, 120 kV) images of (b) M_n = 73k-*b*-73k g/mol and (c) M_n = 95k-*b*-95k g/mol PS-*b*-PMMA films [thicknesses of (a) ~180 nm and (b) ~190 nm] containing ϕ = 0.0083 M_n = 5 kg/mol PEG-PO_3H_2 functionalized GdF_3:Yb/Er (20/2 mol%) nanoplates after solvent annealing (20 min in THF) and thermal annealing (220ºC, 24 h) with lamellae oriented perpendicular to the substrate. The light and dark microdomains are PMMA and PS, respectively, and the scale bars are 300 nm.

4.3 Conclusions

In this work, we demonstrate out-of-plane alignment of PEG-PO_3H_2 functionalized GdF_3:Yb/Er nanoplates through a facile self-assembly process that could be applied to a large area. By orienting the microdomains of M_n = 73k-*b*-73k g/mol and M_n = 95k-*b*-95k g/mol lamellar-forming PS-*b*-PMMA perpendicular to the substrate, the nanoplates assembled vertically in the thin films. We show that properly functionalizing the NP surfaces is imperative. With the native OA

surface molecule, the nanoplates segregate to the composite surfaces and perturb the lamellar structure. However, grafting PEG-PO_3H_2 to the nanoplates creates complimentary interactions between the particles and PMMA block, which facilitates dispersion. In combination with vertical BCP domains, out-of-plane orientation of the nanoplates is achieved without disturbing the equilibrium morphology. The approach presented in this investigation promises to offer an alternative fabrication method to more intensive processes for vertically aligning anisotropic NPs. This flexible method can then be adapted to other composite combinations and applied to systems of technological importance including coatings for solar cell applications and thermal management materials. The focus of future work would be to increase the density of the vertically aligned NPs by enhancing the enthalpic attraction between the GdF_3:Yb/Er nanoplates and the BCP domains.

4.4 References

(1) Bonderer, L. J.; Studart, A. R.; Gauckler, L. J. Bioinspired Design and Assembly of Platelet Reinforced Polymer Films. *Science* **2008**, 319, 1069-1073.

(2) Munch, E.; Launey, M. E.; Alsem, D. H.; Saiz, E.; Tomsia, A. P.; Ritchie, R. O. Tough, Bio-Inspired Hybrid Materials. *Science* **2008**, 322, 1516-1520.

(3) Yao, H.-B.; Fang, H.-Y.; Wang, X.-H.; Yu, S.-H. Hierarchical Assembly of Micro-/Nano-Building Blocks: Bio-Inspired Rigid Strutural Functional Materials. *Chem. Soc. Rev.* **2011**, 40, 3764-3785.

(4) Wei, Y.-Z.; Wang, G.-S.; Wu, Y.; Yue, Y.-H.; Wu, J.-T.; Lu, C.; Guo, L. Bioinspired Design and Assembly of Platelet Reinforced Polymer Films with Enhanced Absorption Properties. *J. Mater. Chem. A* **2014**, 2, 5516-5524.

(5) Grossman, M.; Bouville, F.; Masania, K.; Studart, A. R. Quantifying the Role of Mineral Bridges on the Fracture Resistance of Nacre-Like Composites. *PNAS* **2018**, 115, 12698-12703.

(6) Ferrier, R. C., Jr.; Koski, J.; Riggleman, R. A.; Composto, R. J. Engineering the Assembly of Gold Nanorods in Polymer Matrices. *Macromolecules* **2016**, 49, 1002-1015.

(7) Tyan, H.; Liu, Y.; Wei, K. Thermally and Mechanically Enhanced Clay/Polyimide Nanocomposite via Reactive Organoclay. *Chem. Mater.* **1999**, 11, 1942-1947.

(8) Xin, G.; Zhu, W.; Deng, Y.; Cheng, J.; Zhang, L. T.; Chung, A. J.; De, S.; Lian, J. Microfluidics-Enabled Orientation and Microstructure Control of Macroscopic Graphene Fibres. *Nat. Nanotechnol.* **2019**, 14, 168-175.

(9) Zhang, S.; Pelligra, C. I.; Feng, X.; Osuji, C. O. Directed Assembly of Hybrid Nanomaterials and Nanocomposites. *Adv. Mater.* **2018**, 20, 1705794.

(10) Xia, Y.; Mathis, T. S.; Zhao, M.-Q.; Anasori, B.; Dang, A.; Zhou, Z.; Cho, H.; Gogotsi, Y.; Yang, S. Thickness-Independent Capacitance of Vertically Aligned Liquid-Crystalline MXenes. *Nature* **2018**, 557, 409-412.

(11) Kuo, C. Y.; Tang, W. C.; Gau, C.; Guo, T. F.; Jeng, D. Z. Ordered Bulk Heterojunction Solar Cells with Vertically Aligned TiO_2 Nanorods Embedded in a Conjugated Polymer. *Appl. Phys. Lett.* **2008**, 93, 033307.

(12) Pelligra, C. I.; Majewski, P. W.; Osuiji, C. O. Large Area Vertical Alignment of ZnO Nanowires in Semiconducting Polymer Thin Films Directed by Magnetic Fields. *Nanoscale* **2013**, 5, 10511.

(13) Yamamoto, R.; Yoshida, Y.; Yoshikawa, T.; Yajima, M.; Seki, T. Novel Thermally Conductive Sheet Applying Orientation Control of Graphite Particles. *JIEP* **2010**, 13, 462-468.

(14) Yamamoto, R.; Yoshikawa, T.; Suzuki, M.; Yoshida, Y.; Seki, T.; Yajima, N. Thermal Interface Material including Graphite in Vertical Formation. *Proceedings of JIEP Annual Meeting.* **2009**, 23, 46-47.

(15) Lin, Z.; Liu, Y.; Raghavan, S.; Moon, K. S.; Sitaraman, S. K.; Wong, C. P. Magnetic Alignment of Hexagonal Boron Nitride Platelets in Polymer Matrix: Toward High Performance Anisotropic Polymer Composites for Electronic Encapsulation. *ACS Appl. Mater. Interfaces* **2013**, 5, 7633-7640.

(16) Chen, J.; Huang, X.; Sun, B.; Wang, Y.; Zhu, Y.; Jiang, P. Vertically Aligned and Interconnected Boron Nitride Nanosheets for Advanced Flexible Nanocomposite Thermal Interface Materials. *ACS Appl. Mater. Interfaces* **2017**, 9, 30909-30917.

(17) Xiao, J.; Li, Z.; Ye, X.; Ma, Y.; Qi, L. Self-Assembly of Gold Nanorods into Vertically Aligned, Rectangular Microplates with a Supercrystalline Structure. *Nanoscale* **2014**, 6, 996-1004.

(18) Diroll, B. T.; Greybush, N. J.; Kagan, C. R.; Murray, C. B. Smectic Nanorod Supperlattices Assembled on Liquid Subphases: Structure Orientation, Defects, and Optical Properties. *Chem. Mater.* **2015**, 27, 2998-3008.

(19) Gao, Y.; Weidman, M. C.; Tisdale, W. A. CdSe Nanoplatelet Films with Controlled Orientation of their Transition Dipole Moment. **2017**, 17, 3837-3843.

(20) Erdem, O.; Gungor, K.; Guzelturk, B.; Tanriover, I.; Sak, M.; Olutus, M. Dede, D.; Kelestemur, Y.; Demir, H. V. Orientation-Controlled Nonradiative Energy Transfer to Colloidal Nanoplatelets: Engineering Dipole Orientation Factor. *Nano Lett.* **2019.**

(21) Nakamura, S.; Mitomo, H.; Aizawa, M.; Tani, T.; Matsuo, Y.; Niikura, K.; Pike, A.; Naya, M.; Shishido, A.; Ijiro, K. DNA Brush-Directed Vertical Alignment of Extensive Gold Nanorod Arrays with Controlled Density. *ACS Omega* **2017**, 2, 2208-2213.

(22) Ryan, K. M.; Mastroianni, A.; Stancil, K. A.; Liu, h.; Alivisatos, A. P. Electric-Field-Assisted Assembly of Perpendicularly Oriented Nanorod Superlattices. *Nano Lett.* **2006**, 6, 1479-1482.

(23) Gupta, S.; Zhang, Q.; Emrick, T.; Russell, T. P. "Self-Corralling" Nanorods Under an Applied Electric Field. *Nano Lett.* **2006**, 6, 2066-2069.

(24) Thorkelsson, K.; Mastroianni, A. J.; Ercius, P.; Xu, T. Direct Nanorod Assembly Using Block Copolymer-Based Supramolecules. *Nano Lett.* **2012**, 12, 498-504.

(25) Thorkelsson, K.; Nelson, J. H.; Alivisatos, A. P.; Xu, T. End-to-End Alignment of Nanorods in Thin Films. *Nano Lett.* **2013**, 12, 4908-4913.

(26) Hsu, S.-W., Xu, T. Tailoring Co-Assembly of Nanodiscs and Block Copolymer-Based Supramolecules by Manipulating Interparticle Interactions. *Macromolecules* **2019**, 52, 2833-2842.

(27) Deshmukh, R. D. Liu, Y.; Composto, R. J. Two-Dimensional Confinement of Nanorods in Block Copolymer Domains. **2007**, 7, 3662-3668.

(28) Krook N. M.; Ford, J.; Maréchal, M.; Rannou, P.; Meth, J. S.; Murray, C. B.; Composto, R. J. Alignment of Nanoplates in Lamellar Diblock Copolymer Domains and the Effect of Particle Volume Fraction on Phase Behavior. *ACS Macro Lett.* **2018**, 7, 1400-1407.

(29) Stoykovich, M. P.; Kang, H.; Daoulas, K. C.; Liu, G.; Liu, C.; de Pablo, J. J.; Müller, M.; Nealey, P. F. Directed Self-Assembly of Block Copolymers for Nanolithography: Fabrication of Isolated Features and Essential Integrated Circuit Geometries. *ACS Nano* **2007**, 1, 168-175.

(30) Gu, X.; Gunkel, I.; Hexemer, A.; Gu, W.; Russell, T. P. An In Situ Grazing Incidence X-Ray Scattering Study of Block Copolymer Thin Films During Solvent Vapor Annealing. *Adv. Mater.* **2014**, 26, 273-281.

(31) Xu, T.; Zhu, Y.; Gido, S. P.; Russell, T. P. Electric Field Alignment of Symmetric Diblock Copolymer Thin Films. *Macromolecules* **2004**, 37, 2625-2629.

(32) Mansky, P.; Liu, Y.; Huang, E.; Russell, T. P.; Hawker, C. Controlling Polymer-Surface Interactions with Random Copolymer Brushes. *Science* **1997**, 275, 1458-1460.

(33) Ji, S.; Liu, G.; Zheng, F.; Craig, G. S. W.; Himpsel, F. J.; Nealey, P. F. Preparation of Neutral Wetting Brushes for Block Copolymer Films from Homopolymer Blends. *Adv. Mater.* **2008**, 20, 3054-3060.

(34) Albert, J. N. L; Epps III, T. H., Self-Assembly of Block Copolymer Thin Films. *Mater. Today* **2010**, 13, 24-33.

(35) Kim, E.; Ahn, H.; Park, S.; Lee, H.; Lee, M.; Lee, S.; Kim, T.; Kwak, E.-A.; Lee, J. H.; Lei, X.; Huh, J.; Bang, J.; Lee, B.; Ryu, D. Y. Directed Assembly of High Molecular Weight Block Copolymers: Highly Ordered Line Patterns of Perpendicularly Oriented Lamellae with Large Periods. *ACS Nano* **2013**, 3, 1952-1960.

(36) Kim, K.; Park, S.; Kim, Y.; Bang, J.; Park, C.; Ryu, D. Y. Optimized Solvent Vapor Annealing for Long-Range Perpendicular Lamellae in PS-*b*-PMMA Films. *Macromolecules* **2016**, 49, 1722-1730.

(37) Peng, J; Kim, D. H.; Knoll, W.; Xuan, Y.; Li, B.; Han, Y. Morphologies in Solvent-Annealed Thin Films of Symmetric Diblock Copolymer. *J. Chem. Phys.* **2006**, 125, 064702.

(38) Ploshnik, E.; Salant, A.; Banin, U.; Shenhar, R. Hierarchical Surface Patterns of Nanorods Obtained by Co-Assembly with Block Copolymers in Ultrathin Films. *Adv. Mater.* **2010**, 22, 2774-2779.

(39) Ploshnik, E.; Salant, A.; Banin, U.; Shenhar, R. Co-Assembly of Block Copolymers and Nanorods in Ultrathin Films: Effects of Copolymer Size and Nanorod Filling Fraction. *Phys. Chem. Chem. Phys.* **2010**, 12, 11885-11893.

CHAPTER 5: Phase Behavior of Grafted Polymer Nanocomposites from Field-Based Simulations

* J.P.K. (simulations) and N.M.K. (experiments) contributed equally to this work.

5.1 Introduction

Historically, the ability to calculate predictive phase diagrams has significantly enhanced efforts to design materials for various applications. For example, developing field theory methods to calculate block copolymer (BCP) phase diagrams has advanced the field of these self-assembling polymers.[1,2] A comparable predictive capability has, until recently, been lacking for polymer nanocomposites (PNCs).[3] PNCs offer a platform to improve the mechanical, optical, electrical, or fire retardant properties of polymer melts by adding nanoparticles (NPs) to polymer matrices.[4] The grand challenge in PNCs is controlling the spatial distribution of the NPs, which dictates the resulting material properties. A common strategy to control the NP spatial distribution is to graft polymer chains onto the NP surfaces, forming grafted NPs (gNPs). While experimental phase diagrams exist for some gNP-PNCs,[5-7] the ability to calculate predictive PNC phase diagrams would not only enhance understanding but would also accelerate and inform the design of PNCs for specific applications.

Calculating gNP-PNC phase diagrams using particle simulations, such as molecular dynamics simulations or Monte Carlo methods, is challenging due to the wide range of length scales involved, which span the monomer size, NP radius, and the polymer chain size. Additionally, it is computationally intensive to calculate free energies from particle simulations,[8] and so often PNC

phase behavior is inferred from two-body NP interactions,[9] three-body interactions,[10] visual observations,[11,12] or the upturn in the structure factor at low wavevectors.[13] Calculating polymeric phase diagrams with polymer field theory has been successful because field theory, unlike particle simulations, can efficiently treat long chains and large systems, and directly calculate the free energy and hence the phase boundaries. Furthermore, polymer field theories can evaluate the same molecular model at different levels of approximation, and are formulated in terms of experimentally accessible parameters, particularly the Flory−Huggins interaction parameter (χ), which better facilitates direct comparisons with experiment than in particle simulations. Field-theoretic simulations have been instrumental in developing phase diagrams for numerous polymer architectures including BCPs[14-17] and polyelectrolytes.[18-20] However, to date in the field of gNP-PNCs, field theory has primarily been used to calculate potentials of mean force between gNPs,[21,22] as have other theoretical techniques[23] such as self-consistent PRISM theory[24-26] and classical density functional theory.[27,28] Though some phase maps have been generated from a hybrid polymer field theory/density functional theory,[29,30] in general, phase diagrams calculated from ensembles of gNPs in polymer matrices have been lacking. The Riggleman group previously developed a PNC field theory (PNC-FT) in which the NPs are incorporated directly into the field theory and treated in a similar manner as the polymer chains.[31-35] For this reason, PNC-FT can be used for calculations with ensembles of gNPs.

However, a significant challenge in the field theory framework is the inclusion of thermal fluctuations at experimentally relevant matrix molecular weights. Numerical field theory calculations are most tractable when a mean-field approximation is used,[36] which omits thermal fluctuations. The mean-field approximation is most accurate for dense polymer melts in which large molecular weight polymers interact with many other polymers and concentration fluctuations are sufficiently averaged out. Conversely, the complex Langevin (CL) method[36-39] samples the fully fluctuating field theory, thus including thermal fluctuations, and can therefore be used for lower,

more experimentally accessible molecular weights. Often thermal fluctuations play a prominent role in determining the phase behavior, as in polyelectrolytes,[18] low molecular weight polymer melts,[16,40] and BCPs near the order−disorder transition.[41,42] Despite significant advances in the CL method, a dimensionless chain density value of $C = \frac{n_M R_g^3}{V} \approx 3$ is the smallest the framework can handle before numerical inefficiencies limit its use, where n_M is the number of matrix chains, R_g is the polymer's radius of gyration, and V is the volume of the system. For context, a dimensionless chain density of $C = 3$ corresponds to a polystyrene (PS) melt with a molecular weight of approximately 62.5 kg/mol. However, experiments are frequently performed with lower molecular weights (with $C < 3$) to facilitate equilibration, particularly in PNCs with slow kinetics.

Therefore, to include thermal fluctuations for systems with lower molecular weight polymers, the Riggleman group recently implemented a hybrid particle-field method called theoretically informed Langevin dynamics (TILD).[35,43,44] The TILD method uses Langevin dynamics to sample the dynamic partition function of the system. The coordinates of each polymer and NP are explicitly tracked using a particle representation, while the nonbonded interactions are calculated using density fields generated from a particle-to-mesh scheme. The TILD framework is similar to other methods that implement a particle-to-mesh scheme to interpolate from a particle-based model to a field-based model, such as self-consistent Brownian dynamics,[45] single-chain-in-mean-field[46] and theoretically informed coarse-grained simulations.[47] Previous work from the Riggleman group has shown that TILD quantitatively agrees with CL simulations,[43] but unlike the CL method, TILD performs well at low values of C. TILD can be used to efficiently isolate the role of thermal fluctuations by comparing its results with those of the mean-field PNC-FT. Furthermore, since the TILD method is a hybrid particle-field-based method, it benefits from having access to the particle coordinates while being computationally less expensive than pure particle-based methods. Chao *et al.*[43] demonstrated that TILD scales linearly with C while an analogous

dissipative particle dynamics simulation scales quadratically with C and is approximately 10 times slower at $C = 1$. The Riggleman group previously used TILD to investigate macrophase separation in gNP-PNCs using two-dimensional simulations[35] and more recently to understand pattern formation in mixed-brush NPs.[48]

Herein, we focus on calculating gNP-PNC phase diagrams for both athermal systems (chemically identical grafted and matrix chains) and enthalpic systems (chemically distinct grafted and matrix chains). In athermal systems, gNPs with low grafting densities tend to aggregate into anisotropic aggregates, presumably because the gNPs have bare, attractive regions on their surfaces[5,49] or as it was recently shown, an increased steric repulsion at the junction of two aggregated gNPs.[10] At higher grafting densities, the grafted polymers can screen the interactions between the particle cores. A key parameter is the ratio $\alpha \equiv P/N$, where P is the degree of polymerization of the matrix chains and N is the degree of polymerization of the grafted chains. Experiments[5-7] and simulations[22,50-52] show that PNCs phase separate for large α because of the large entropic penalty for the matrix chains to penetrate into the grafted brush layer. This entropic cost causes the matrix chains to dewet the grafted polymer, which leads to depletion attractions between the gNPs and consequently gNP aggregation. The ratio of the NP radius (R_P) to the R_g of the grafted chains, the grafting density (σ), and the NP volume fraction are also critical variables that determine PNC phase behavior. In gNP-PNCs with chemically distinct chains, the interactions between the grafted and matrix chains can either be attractive ($\chi < 0$) or more commonly, repulsive ($\chi > 0$). These interactions can promote or reduce miscibility in gNP- PNCs, respectively. Because of the considerable parameter space to consider in predicting gNP-PNC miscibility, methods to efficiently predict macroscale phase behavior are necessary to guide experiments.

Using our field-based simulation methods, we investigate the macrophase separation of gNPs in PNCs as a function of α, χ, σ, R_P, and volume fraction. We focus on densely grafted

systems, for which the grafted polymers completely cover the NPs and the grafted polymers form a polymer brush on the NP surface. Phase diagrams are computed by extracting the equilibrium volume fraction of each phase from large simulation cells with an explicit interface between gNP-rich and gNP-poor phases. By comparing the results between mean-field PNC-FT calculations and fluctuating TILD simulations, we show that thermal fluctuations enhance phase separation. We present experimental data for the macrophase separation of poly(methyl methacrylate) grafted silica nanoparticles (PMMA-*g*-SiO_2 NPs) in PS matrices for three values of α. The TILD simulations are more consistent with the experiments and better predict phase separation, while the mean-field PNC-FT calculations inaccurately predict mixing in the three experimental systems. Additionally, the mean-field PNC-FT fails to predict any phase separation in athermal systems, which are known to phase separate experimentally. We conclude that thermal fluctuations play a critical role in accurately describing depletion interactions, which are well-understood to drive the aggregation of gNPs in PNCs. Finally, we compare the TILD results with the available data on gNP-PNC phase behavior in the literature and demonstrate that simulations can help to interpret different experimental findings.

5.2 Methods

5.2.1 Fixation of ATRP-Initiator on SiO_2 NPs. (ATRP)-Initiator on SiO_2 NPs. {[(2-Bromo-2-methylpropionyl)oxy]propyl}triethoxysilane (BPE), a silane coupling agent containing an atom transfer radical polymerization (ATRP) initiating site, was synthesized following a previously reported procedure and used to immobilize ATRP-initiator sites on SiO_2 NPs.[53,54] A mixture of ethanol (400 mL) and BPE (7.5 g) was added dropwise to a mixture of SiO_2 NPs (5 g) in ethylene glycol (10 mL) over 2 h with vigorous stirring, and to which, a mixture of ethanol (250 mL) and ammonium hydroxide solution (16.5 g) was added dropwise over 2 h with vigorous stirring to prevent particle aggregation. The reaction mixture was continuously stirred at room

temperature for 10 days. The ATRP-initiator-fixed SiO_2 NPs were collected by centrifugation (20 000 rpm, 2 h), subsequently washed by three consecutive centrifugations (20 000 rpm, 2 h), and finally redispersed in ethanol. *N,N*-Dimethylformamide (DMF) (10 g) was added to the dispersion and the mixture was rotary evaporated to obtain a stock ATRP-initiator-fixed SiO_2 NPs suspension in DMF.

5.2.2 Surface-Initiated-ATRP on the Initiator-Fixed SiO_2 NPs. A mixture of ATRP-initiator-fixed SiO_2 NPs (0.5 g), DMF (7.2 g), methyl methacrylate (MMA, 3 g), ethyl 2-bromoisobutyrate (EBiB, 30 mg), and 4,4′-dinonyl-2,2′-dipyridyl (306 mg) was quickly added to a glass tube charged with copper (I) chloride (30 mg) and copper (II) dichloride (10 mg). Oxygen in the solution was removed by three freeze-pump-thaw cycles, and the tube was sealed under vacuum. The polymerization was performed at room temperature for 8 h. An aliquot of the polymerization solution was used to determine monomer conversion through ^1H NMR spectroscopy as well as molecular weight and the distribution of the EBiB-initiated polymer using gel permeation chromatography. The remainder of the reaction mixture was diluted with chloroform, washed once with 2 wt% aqueous ethylenediaminetetraacetic acid disodium salt dihydrate (EDTA-Na_2) to remove the copper catalyst, and subsequently washed three times with water. The chloroform solution was diluted with 1:1 tetrahydrofuran (THF)/pentane, and then centrifuged (20 000 rpm, 2 h) to collect the PMMA-*g*-SiO_2 NPs. The particles were redispersed in 1:1 THF/pentane and the suspension was centrifuged (20 000 rpm, 2 h); this procedure was repeated three times. The collected PMMA-*g*-SiO_2 NPs were dried in a vacuum. The amount of grafted polymer was determined through thermal gravimetric analysis (TGA). The grafted polymer was cleaved from the SiO_2 NPs by hydrofluoric acid etching following a previously reported procedure.[53,54] The polymerization yielded PMMA grafts with M_n = 7.9 kg/mol and M_w/M_n = 1.10, where M_n and M_w/M_n are the number-average molecular weights and the polydispersity index,

respectively. The grafting density was calculated to be σ = 0.26 chains/nm^2 from the amount of grafted polymer measured using TGA and its M_n.

5.2.3 Preparation of Nanocomposite Samples. To form the bulk gNP-PNC films, dried PMMA-*g*-SiO_2 NPs were added to 30 wt% PS (M_n = 0.95, 2.7, and 10 kg/mol) solutions in THF. The weight addition of the PMMA-*g*-SiO_2 NPs produced samples with a final SiO_2 NP core volume fraction of ϕ_{NP} = 0.01. The PNC solutions were mixed with a rotating magnetic stir bar, overnight, until all of the constituents were dissolved. 20 μL of the PNC solutions were spin-coated (1000 rpm, 1 min) onto Kapton films that were adhered to silicon wafers (1 cm^2) with double-coated carbon conductive tape and consequently cleaned with methanol and toluene. Unless indicated (as-cast films as the exception), the samples were thermally annealed under vacuum at 150°C for 3 and 5 days.

5.2.4 Characterization of Nanocomposite Samples. After thermal annealing, the PNC films were lifted from the silicon substrates (with the Kapton films beneath), topped with Kapton tape to form a blister pack with the sample sandwiched between Kapton, and embedded in two-part epoxy. Cross-sectional surfaces of PMMA-*g*-SiO_2 and PS nanocomposites were prepared by cryomicrotomy at approximately -110°C using a diamond knife (Leica Ultracut S Ultramicrotome). Scanning electron microscopy (SEM) characterization of the cryomicrotomed surfaces was performed with a FEI Quanta 600 ESEM and operated at 15 kV.

5.2.5 Model Details. The model and method derivations closely follow our previous work for both the PNC-FT[31,33,35,48] and TILD[35,43,48,55] methods. All calculations are in three dimensions with periodic boundary conditions. The NPs are grafted with G type polymer chains in an M type polymer matrix. The NPs are enthalpically neutral with respect to both the grafted and matrix chains. The density of a single NP is given by

$$\hat{\rho}_{NP}(\mathbf{r}) = \frac{\rho_0}{2}\,\mathrm{erfc}\left(\frac{|\mathbf{r}|-R_P}{\xi}\right) \qquad (5.1)$$

where ρ_0 is the total system density, R_P is the radius of the particle, and ξ is the length scale on which the particle density goes from ρ_0 inside the particle core to 0 outside the core. In the PNC-FT calculations, grafted chains are attached to the NP surface with a uniform distribution given by

$$\Gamma_{\sigma,\mathrm{uni}}(\mathbf{r}) = \frac{1}{\sigma_0}\exp\left[-\left(\frac{3(|\mathbf{r}|-R_P-\xi)}{2b^2}\right)^2\right] \qquad (5.2)$$

In the TILD simulations, grafted chains are attached with a random distribution given by

$$\Gamma_{\sigma,\mathrm{rand}}(\mathbf{r}) = \frac{1}{\sigma_0}\sum_i^{n_G}\exp\left[-\left(\frac{3(|\mathbf{r}|-[(R_P+\xi)\cdot\mathbf{u}_i])}{2b^2}\right)^2\right] \qquad (5.3)$$

where σ_0 is defined as $\int \mathrm{d}\mathbf{r}\Gamma_\sigma(\mathbf{r}) = 1$, n is the number of polymer chains, and the G subscript denotes the chains are grafted rather than M for the matrix chains. $\mathbf{u}_i$ is a randomly determined orientation vector of magnitude 1.

The polymers are modeled as discrete Gaussian chains with N (grafted) or P (matrix) monomers. Each chain is connected via a Gaussian bonding potential

$$\beta U_0 = \sum_i^{n_K}\sum_j^{N_K-1}\frac{3|\mathbf{r}_{i,j}-\mathbf{r}_{i,j+1}|^2}{2b^2} \qquad (5.4)$$

Where b is the statistical segment length of the polymer and K denotes either N or P. Here, we assume that the statistical segment lengths are equal, $b_G = b_M = b$. A Helfand compressibility potential is used to enforce excluded volume interactions in the system via an energetic penalty for deviations away from the average system density, ρ_0, given by

$$\beta U_1 = \frac{\kappa}{2\rho_0}\int \mathrm{d}\mathbf{r}[\hat{\rho}_+(\mathbf{r}) - \rho_0]^2 \qquad (5.5)$$

where $\hat{\rho}_+ = \hat{\rho}_G + \hat{\rho}_M + \hat{\rho}_{NP}$ is the spatially varying total microscopic density, $\hat{\rho}_I$ is the microscopic density of component I, and κ controls the strength of the density fluctuations. Finally, a repulsive Flory−Huggins like potential is used to include enthalpic repulsions between chemically dissimilar components

$$\beta U_2 = \frac{\chi_{GM}}{\rho_0}\int \mathrm{d}\mathbf{r}\hat{\rho}_G(\mathbf{r})\hat{\rho}_M(\mathbf{r}) \qquad (5.6)$$

where χ_{GM} is the Flory−Huggins interaction parameter governing the strength of the interaction between the grafted and matrix polymers. Details of the PNC-FT and TILD methods can be found in Appendix D.

5.2.6 Numerical Parameters and Theory-Experiment Mapping. For the reader's convenience, Table 5.1 provides a summary of the parameter notation used in this paper. To help generalize the theoretical results, we also use reduced parameters throughout the paper. A summary of the reduced parameters is shown in Table 5.2.

Table 5.1. Symbol and description of parameters used in this chapter.

Symbol	Description
P	*matrix polymer degree of polymerization*
N	*grafted polymer degree of polymerization*
$M_{n,G}$	*number-average molecular weight of grafted chains*
$M_{n,M}$	*number-average molecular weight of matrix chains*
R_P	*nanoparticle radius*
σ	*grafting density*
ϕ	*volume fraction*
χ	*Flory−Huggins interaction parameter*
κ	*compressibility parameter*
R_g	*polymer radius of gyration*
ρ_0	*total system density*
b	*statistical segment size of the polymer*
a	*length scale determining monomer interfacial width*
ξ	*length scale determining nanoparticle interfacial width*

Table 5.2. Symbol, definition, and description of reduced parameters used in this chapter.

Symbol	Definition	Description
α	P/N	*ratio of matrix chain length to grafted chain length*
σ^*	σb^2	*dimensionless grafting density*
R_P^*	$R_P/R_{g,N}$	*dimensionless nanoparticle radius*
C	$n_M R_g^3/V = R_{g,M}^3 \rho_0/P$	*dimensionless chain density*

The dimensionless chain density $C = R_g^3\rho_0/P$ is used to map to the experiments. In using this mapping, the statistical segment size of the polymer, b, and the total system density, ρ_0, determine how the experimental molecular weights of the polymers map to the number of discrete Gaussian chain beads. Here, we map P to PS and use the same mapping for N (PMMA) since PS and PMMA have similar statistical segment lengths (0.5 nm for PS and 0.54 nm for PMMA[56]). For a given PS molecular weight, the value of C is calculated. For example, for 1 kg/mol PS with a degree of polymerization $P = 9.6$, the experimental value is $C = 0.033$ (being careful to calculate all quantities at the same reference volume). This same value of C is used in the simulations (for each molecular weight). Since

$$C = \frac{R_{g,M}^3\rho_0}{P} = \frac{\rho_0 b^3\sqrt{P}}{6\sqrt{6}} \qquad (5.7)$$

choices need to be made for the model values of b, ρ_0, and P. In all systems, we choose the dimensionless statistical segment length $b = 1$. The value of ρ_0 is then chosen so that the number of discrete Gaussian beads in the chains is a reasonable (and integer) value. For example, to represent a 1 kg/mol PS chain by $P = 2$ discrete Gaussian chain beads require $\rho_0 = 3.943$, and to represent a 1 kg/mol PS chain by $P = 6$ discrete Gaussian chain beads require $\rho_0 = 2.276$. After choosing P and calculating ρ_0 from the experimental value of C, the unperturbed radius of gyration R_g in the model can be used to determine the value of b in nm. Thus, for a 1 kg/mol PS chain with $P = 6$, $b = 0.846$ nm. This value of b is used to determine the model values of σ and R_P that match experiments. Finally, the model value for χ is determined by setting the experimental χP equal to the simulation χP. For PS-PMMA blends, the experimental bare $\chi = 0.0175$ at $T = 150°C$ for a reference volume of 0.1 nm^3.[56]

We use simulation boxes that are $25b \times 25b \times 250b$ in size. The grid size for the particle-to-mesh scheme is $\approx 0.72b$. In all calculations and simulations, $\kappa = 25$, $a = 0.5b$, $\xi = 0.5b$, and the

total matrix chain volume fraction $\phi_{\mathrm{M}}^{0} \approx 0.8$. Here, a is the length scale determining the monomer interfacial width via the functional form

$$\hat{\rho}_{\mathrm{poly}}(\mathbf{r}) = \left(\frac{1}{2\pi a^2}\right)^{3/2} \exp\left(-\frac{\mathbf{r}^2}{2a^2}\right) \qquad (5.8)$$

Test simulations demonstrated that $\kappa = 25$ was high enough to prevent substantial overlap of the nanoparticles and polymer monomers while not being so high as to hinder equilibration. The values of a and ξ were chosen as approximately half a monomer's statistical segment length.

In Figure 5.2, we use $P = 6$ discrete Gaussian chain beads to represent 1 kg/mol PS chains since this figure includes calculations for very short chains. In the rest of the paper (Figure 5.5 and Figure 5.6), we use $P = 2$ discrete Gaussian chain beads to represent 1 kg/mol PS chains because we only simulate longer chains and the more coarse discretization of the chains accelerates equilibration. The smallest polymer we use in the later part of the paper has $M_{\mathrm{n,M}} = 7.5$ kg/mol ($P = 15$). Figure D.3 shows that the difference in the phase behavior between using 45 coarse-grained monomers and 15 coarse-grained monomers to represent the same polymer chain is minimal. The difference in the discretization choice becomes even smaller for longer polymer chains.

5.3 Results

We begin investigating the importance of thermal fluctuations in predicting the macroscopic phase behavior of gNP-PNCs by studying enthalpically repulsive systems, in which the grafted polymers are chemically distinct from the polymer matrix. First, we study the gNP-PNC phase behavior experimentally using 15 nm diameter silica (SiO_2) NPs grafted with poly(methyl methacrylate) (PMMA). The PMMA-*g*-SiO_2 NPs were grafted with $M_{\mathrm{n,G}} = 7.9$ kg/mol molecular weight chains at a grafting density of $\sigma = 0.26$ chains/nm^2. Here, M_{n} is the number-average molecular weight. Bulk gNP-PNC films were formed by spin-coating solutions of PS and the gNPs. We used three PS matrix molecular weights, $M_{\mathrm{n,M}} = 0.95$, 2.7, and 10 kg/mol, for which $\alpha = 0.12$, 0.34, and 1.27, respectively. For each experimental condition, the PNC films with $\phi_{\mathrm{gNP}} = 0.01$ were

annealed at 150°C for either 0 days ("as-cast"), 3 days, or 5 days, and then imaged with a scanning electron microscope (SEM) to track the evolution of the phase behavior (Figure 5.1). At the annealing temperature of 150°C, $\chi_{PS\text{-}PMMA} = 0.0175$ for a reference volume of 0.1 nm^3.[56] Complete experimental details can be found in the Methods section.

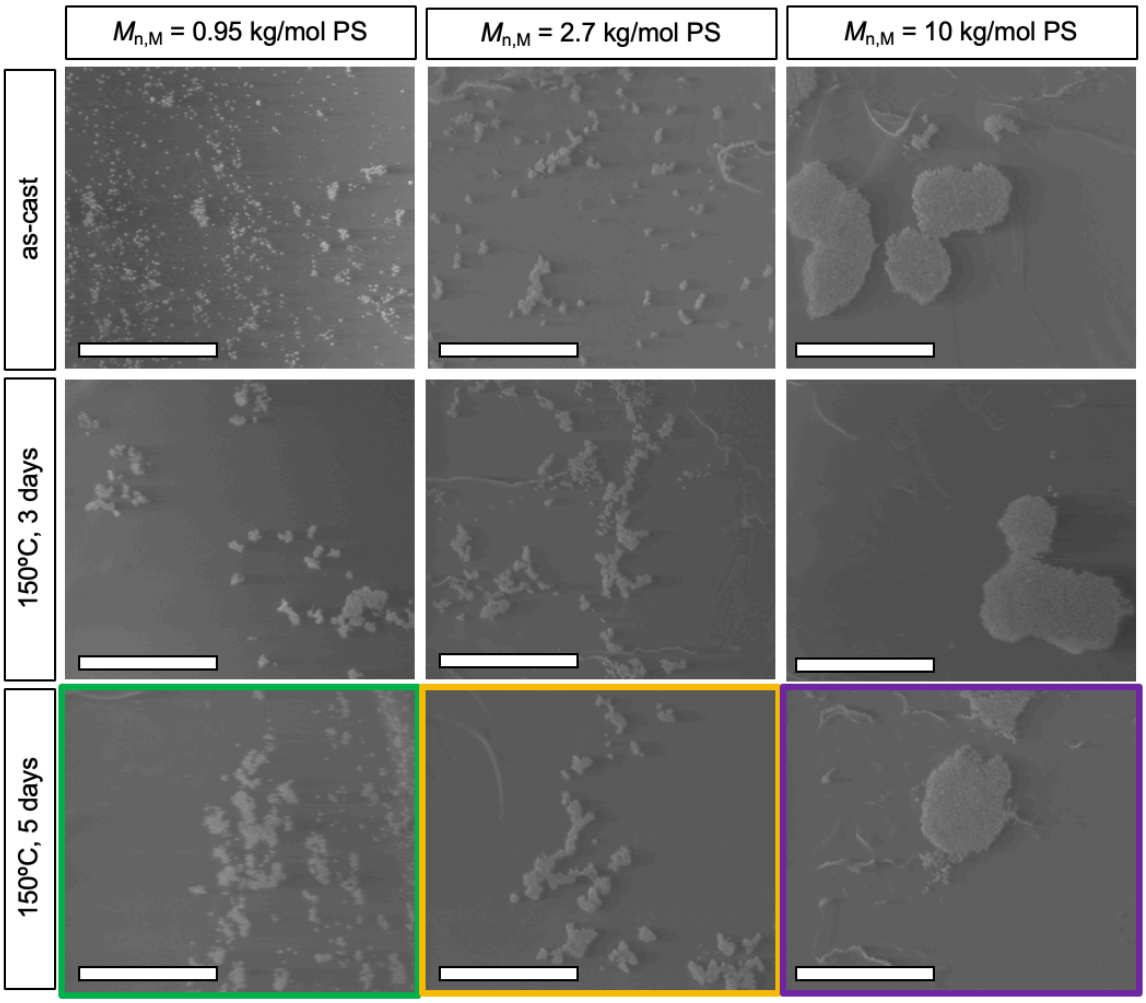

Figure 5.1. Representative SEM images of cryomicrotomed (approximately −100°C) cross-sectional surfaces of $\phi_{gNP} = 0.01$ PMMA-*g*-SiO_2 NPs in PS matrices with (left column) $M_{n,M} = 0.95$ kg/mol, (middle column) $M_{n,M} = 2.7$ kg/mol, and (right column) $M_{n,M} = 10$ kg/mol. Each gNP-PNC was characterized (top row) as-cast, or after annealing under vacuum at 150°C for (middle row) 3

days and (bottom row) 5 days. The colored boxes in the last row correspond to the simulation data presented in Figure 5.2 and Figure 5.3. All scale bars are 1 μm.

The top row of Figure 5.1 features the as-cast samples where the left-hand image shows that individually dispersed NPs coexist with small NP aggregates in $M_{n,M}$ = 0.95 kg/mol (α = 0.12) PS. As the number-average molecular weight of the PS matrix increases to $M_{n,M}$ = 2.7 kg/mol (α = 0.34), shown in the center image of the top row, there are many small NP aggregates in the absence of discrete NPs. However, the gNPs are already strongly phase separated for as-cast $M_{n,M}$ = 10 kg/mol (α = 1.27) in the right-hand image of the top row. After annealing for three days at 150°C, the two lower $M_{n,M}$ systems (left-hand and center images of the middle row) show coarsening into larger NP aggregates. This coarsening trend continues upon further annealing for five days for $M_{n,M}$ = 0.95 and 2.7 kg/mol (left-hand and center images of the bottom row, respectively). Meanwhile, the $M_{n,M}$ = 10 kg/mol gNP-PNCs are comparably phase separated regardless of thermal treatment (i.e., are strongly segregated after casting and remain unnoticeably changed after annealing). Ultimately, all three gNP-PNCs exhibit the macrophase separation of the gNPs. This is a surprising result because the α values are relatively low in these systems, as are the polymer graft and matrix molecular weights. Based on previous experiments in athermal systems we would expect the gNPs to disperse[5-7] for at least α = 0.12 and 0.34, and likely for α = 1.27 as well. This is because, for spherical gNPs with low values of α, the polymer brush on the NP is wet by the matrix chains, which leads to good dispersion of the gNPs. Instead, for PMMA-*g*-SiO_2 NPs in PS, the enthalpic repulsion between the matrix and grafted chains appears to dominate the phase behavior and promotes macrophase separation, even at values as low as α = 0.12 (i.e., a wet brush condition).

We use both mean-field PNC-FT calculations and TILD simulations to calculate the expected phase behavior for the experimental system. In all of the simulations, we model the polymers as discrete Gaussian chains. Each NP is represented as a cavity function that prevents

polymer chains from entering the NP core. NPs are enthalpically neutral with respect to both the grafted and matrix polymers. We perform calculations with 15 nm diameter NPs, $M_{n,G}$ = 8 kg/mol grafted chains, and varying matrix molecular weights. For these systems, the ratio of the particle radius to the grafted chains' radius of gyration is R_P/R_g = 3.15. We include 1, 3, and 10 kg/mol matrix chains to closely match the experiments (see the Methods section for details of our conversion from simulation to experimental units). The grafted and matrix chain interaction is described by a Flory−Huggins repulsion of strength χ that is mapped to PS/PMMA based on our chosen reference volume. The choice of the number of discrete monomers used to model the polymers is important and can influence the phase behavior of the system, most notably when the polymers are short. This point is discussed in greater detail in Appendix D. For the calculations shown in Figure 5.2 and Figure 5.3, six discrete Gaussian chain monomers correspond to a PS molecular weight of 1 kg/mol.

To calculate phase diagrams, we simulate two explicit interfaces for each state point. The central region of the simulation box is initialized with a particle-rich phase, surrounded on both sides with a matrix polymer-rich phase, as shown schematically in Figure 5.2a. The gNPs are allowed to diffuse outward to equilibrate. We consider the system equilibrated if the density distribution of the components is no longer changing significantly with respect to the simulation time (see Appendix D for details). Note that the PNC-FT calculations result in a single deterministic solution, whereas TILD is a stochastic simulation method that will lead to different results depending on the initial configuration of all of the particles (NPs and polymer monomers) and on the random noise used in the Langevin dynamics. Comparing two independent trajectories allows an estimation of our uncertainties, which are typically on the order of the size of the symbol in the figure (see Figure 5.5). As a result, we ran a single TILD trajectory for all remaining state points.

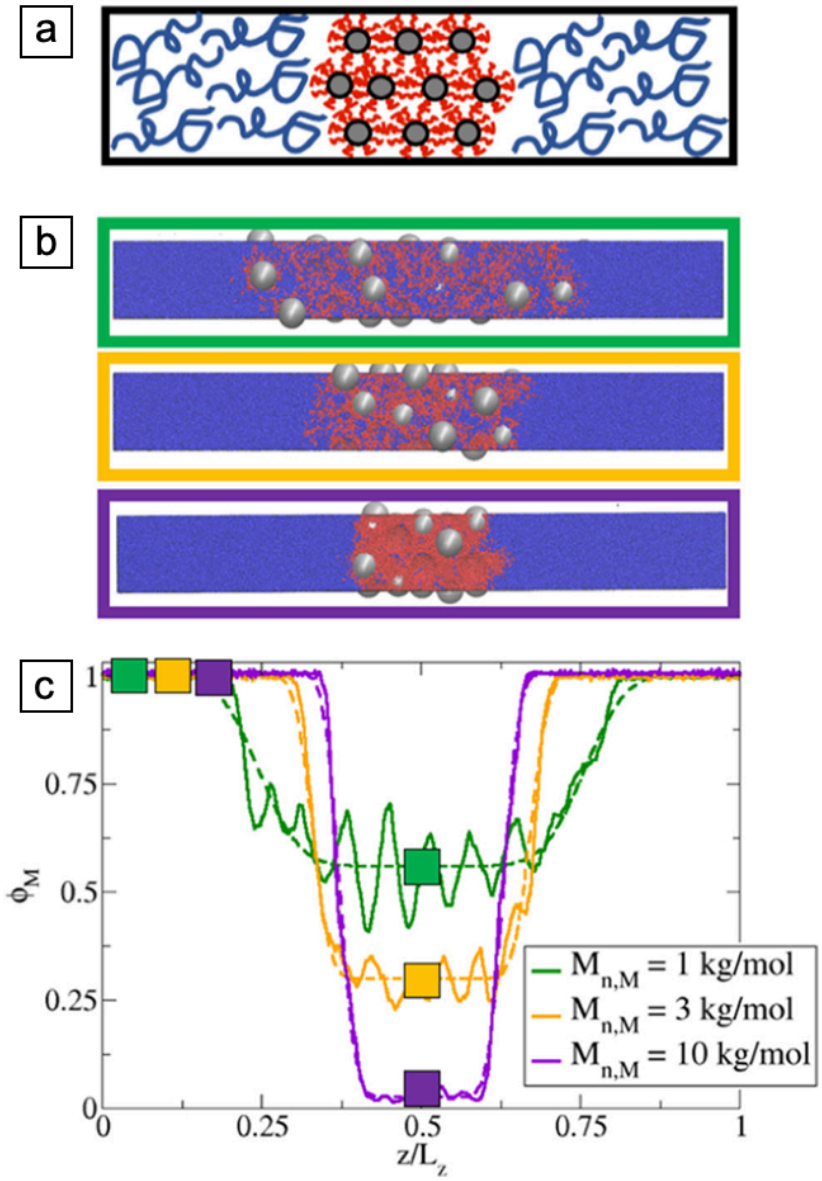

Figure 5.2. (a) Schematic showing the system and simulation setup with neutral NPs (gray) grafted with A chains (red) in a B matrix (blue). The gNPs are initially placed in the center of the box and allowed to diffuse outward until equilibrated. (b) Visualizations of equilibrated TILD simulations for matrix chain lengths of $M_{n,M}$ = 1 kg/mol (green), 3 kg/mol (orange), and 10 kg/mol (purple). The colors of the outlined boxes correspond to the analogous experimental conditions in Figure 5.1. (c) Matrix volume fraction versus the normalized z-direction. The solid lines show the raw data while the dashed lines represent a fit based on 2 error functions described by Equation 5.9.

Figure 5.2b shows visualizations of TILD simulations with matrix molecular weights of 1, 3, and 10 kg/mol, going from top to bottom. Figure 5.2c shows the volume fraction of the matrix chains (ϕ_M) averaged over the *xy*-plane along the *z*-direction from the TILD simulations. Each colored square in this plot marks the matrix volume fraction in either the matrix-dense phase or the gNP-dense phase. Note that the gNPs spread into the matrix for $M_{n,M}$ = 1 kg/mol but form a dense, nearly matrix-free phase for $M_{n,M}$ = 10 kg/mol. The dashed lines are from fits to error functions given by

$$\phi(z) = \phi_M + \frac{\phi_{gNP} - \phi_M}{2}\left(\mathrm{erf}\left[\frac{z - \frac{L_z}{2} + z_0}{\Delta\sqrt{2}}\right] - \mathrm{erf}\left[\frac{z - \frac{L_z}{2} - z_0}{\Delta\sqrt{2}}\right]\right) \qquad (5.9)$$

where ϕ_x is the volume fraction of component *x* (*x* = *M* or gNP and corresponds to the matrix and gNP components, respectively), L_z is the length in the *z*-direction, $\frac{L_z}{2} \pm z_0$ is the location of the interfaces, and Δ is a measure of the interfacial width. A dispersed system would have no interface, unlike the three systems shown in Figure 5.2b. We use these fits to determine the composition of each phase. The phase diagrams calculated from both the mean-field PNC-FT and the fluctuating TILD simulations are shown in Figure 5.3 as a function of $M_{n,M}$ and ϕ_M. At sufficiently low $M_{n,M}$ the gNPs are dispersed and the system is in one phase (white region). At higher $M_{n,M}$ the gNPs aggregate and the system macrophase separates into coexisting particle-rich and particle-poor phases (shaded regions). The black curve is the PNC-FT binodal while the red curve is the TILD binodal. A striking result from this data is that the inclusion of fluctuations shifts the binodal (phase boundary) to lower $M_{n,M}$, which indicates that thermal fluctuations enhance phase separation. Figure 5.3 shows the three experimental state points (filled circles) using the measured average volume fraction of the matrix for ϕ_M. The mean-field PNC-FT predicts that the gNPs should disperse at $M_{n,M}$ = 0.95 kg/mol (green filled circle) and $M_{n,M}$ = 2.7 kg/mol (yellow filled circle), whereas the TILD simulations correctly predict that the gNPs should phase separate at all three experimental state points. This result suggests that thermal fluctuations contribute to the phase

behavior of gNP-PNCs. Furthermore, the mean-field approximation overestimates the miscibility of gNPs in the polymer, particularly at low molecular weights. For example, at $M_{n,M}$ = 5.5 kg/mol, ϕ_M for the gNP-rich coexisting phase decreases from 0.44 for the PNC-FT to 0.125 for the TILD predictions.

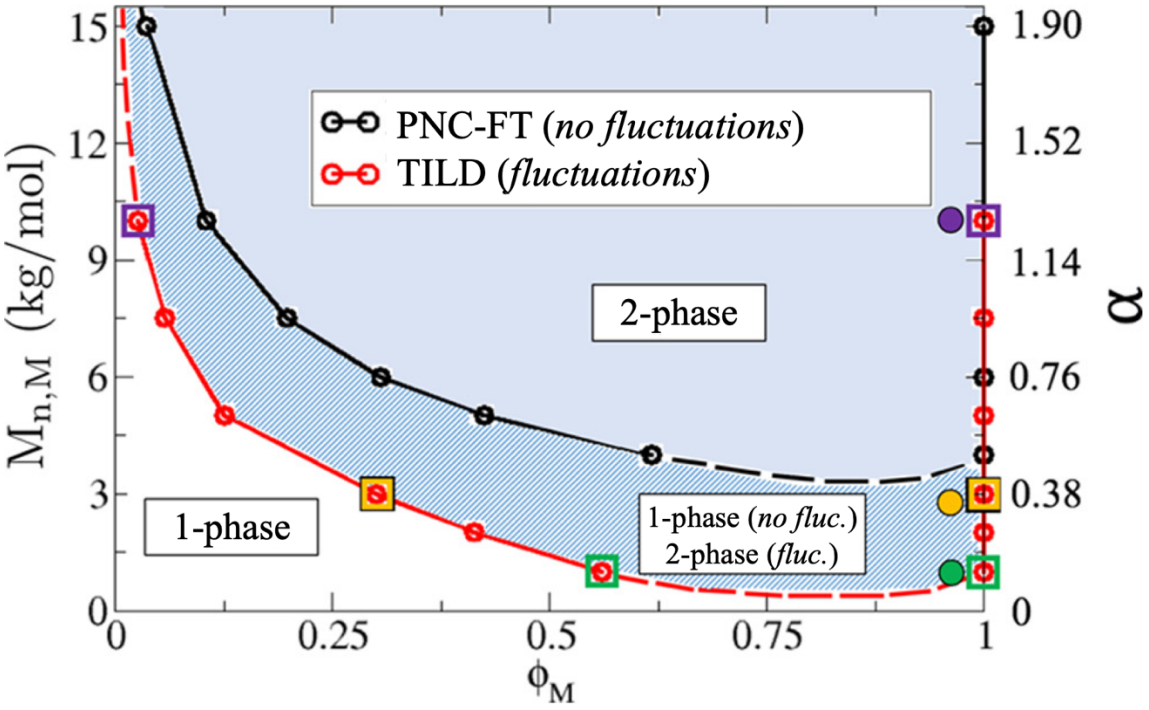

Figure 5.3. Phase diagrams from (black circles) the PNC-FT calculations and (red circles) the TILD simulations showing the dispersed and macrophase separated phases as a function of matrix molecular weight $M_{n,M}$ (left y-axis) or α (right y-axis) versus matrix volume fraction ϕ_M. The solid lines connect each point while the dashed lines are drawn to estimate the regions of the phase diagram that were not explicitly calculated. The boxes show the coexisting compositions extracted from Figure 5.2c and the filled circles represent the state points of the experiments shown in Figure 5.1.

Clearly, the mean-field PNC-FT is missing important physics. In homogeneous phases (with no internal microstructure), such as both the dispersed and macrophase separated phases

considered in this study, it can be shown that the mean-field PNC-FT free energy F reduces to a Flory−Huggins-like free energy

$$\frac{\beta F}{\rho_0 V} = \frac{1-\phi_{\mathrm{M}}}{V_{\mathrm{gNP}}}\log(1-\phi_{\mathrm{M}}) + \frac{\phi_{\mathrm{M}}}{P}\log\phi_{\mathrm{M}} \qquad (5.10)$$

(see the Appendix D for the derivation). Here, $\beta = 1/k_{\mathrm{B}}T$, V is the total system volume, V_{gNP} is the volume of the gNPs (core plus grafts), and ρ_0 is the molar density. The first two terms on the right-hand side of Equation 5.10 represent the translational entropies of the gNPs and matrix polymers, while the third term represents the enthalpic interactions between the matrix and grafted chains. The phase diagram calculated from Equation 5.10 agrees quantitatively with the mean-field PNC-FT calculations (see Figure D.1). Note that the conformational entropy of the chains does not play a role in the mean-field free energy for homogeneous phases. This in turn means that the mean-field theory does not correctly capture the effects of depletion interactions, which include conformational entropy effects.

To further explain this point, the schematic in Figure 5.4 illustrates the differences between mean-field PNC-FT and the TILD method. The fully fluctuating system described by TILD is sketched in the left column and the mean-field PNC-FT system in the right column. In mean-field theory, only one average chain conformation is included, while the TILD method includes many different chain conformations since all of the chains are modeled explicitly. During the TILD simulations, the individual chains can change conformations due to thermal fluctuations. A major contributor to the aggregation of gNPs in homopolymer matrices is the depletion attraction, which is an effective attractive interaction between the particles that occurs because the matrix chains lose translational and conformational entropy when confined between two NPs. The system can gain entropy by excluding the matrix chains from between particles, leading to NP aggregation. The matrix chains lose additional conformational entropy when they penetrate and wet the polymer brush on the gNPs, an effect that is stronger for longer matrix chains. In the gNP-PNCs studied

here (Figure 5.1, Figure 5.3, and Figure 5.3), the combination of depletion interactions and the enthalpic repulsions drive phase separation, sketched as the transition from the top to the bottom row in Figure 5.4. The mean-field theory only includes translational entropy while the fluctuating TILD theory also accounts for the conformational entropy and thus TILD includes a much larger entropy gain upon phase separation. The lack of conformational depletion interactions explains why mean-field theory cannot predict phase separation at all in athermal PNCs (note that Equation 5.10 always predicts mixing when $\chi = 0$), while experiments show that athermal PNCs macrophase separate at large values of α.

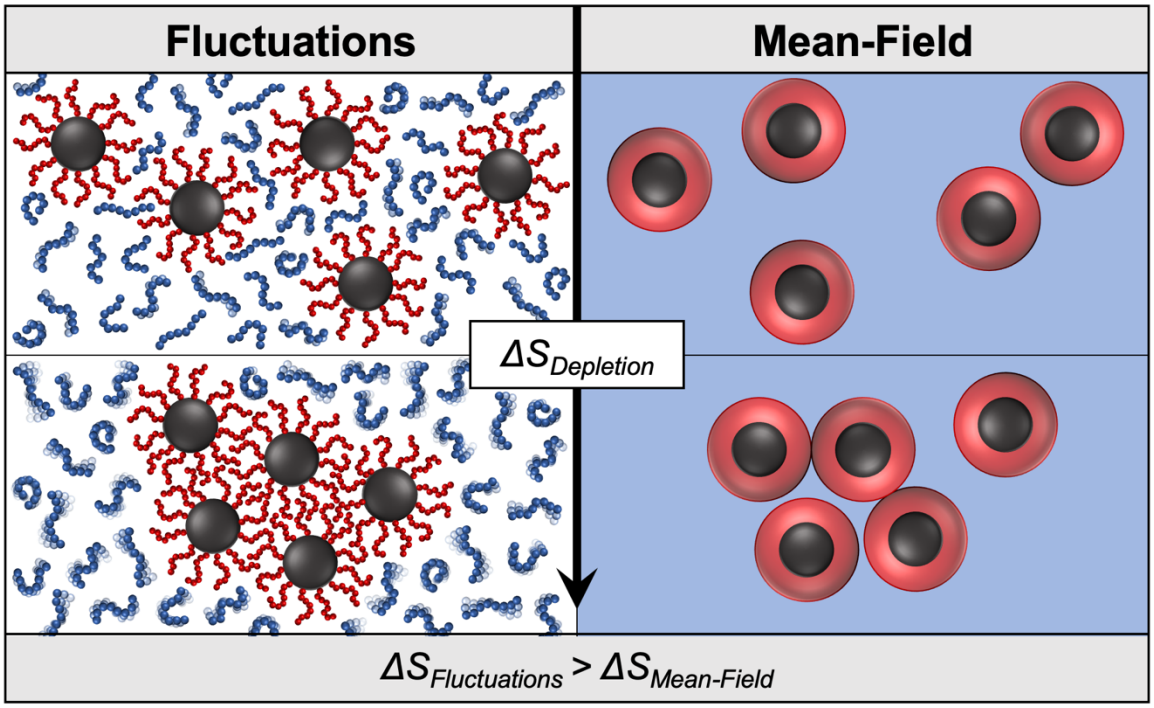

Figure 5.4. Schematic showing gNPs in a polymer matrix. Each column represents the same state point, with the fluctuating system shown on the left and the mean-field system shown on the right. The top row represents an initially dispersed system while the bottom row shows phase separated gNPs. During phase separation, the matrix chains that are expelled from both the brush layer and the regions between the gNPs have a greater increase in entropy for the fluctuating case than in the mean-field case because both the translational and conformational entropies increase. The increase

in the conformational entropy of the matrix chains from the fluctuations enhances the degree of phase separation.

Now that the importance of conformational entropy and thermal fluctuations has been established, we next use TILD to explore PNC phase behavior as a function of χP, α, R_{P}^{*}, and σ^{*}, where R_{P}^{*} and σ^{*} are the dimensionless NP radius and grafting density given by $R_{\mathrm{P}}^{*} = R_{\mathrm{P}}/R_{\mathrm{g,N}}$ and $\sigma^{*} = \sigma b^{2}$, respectively ($R_{\mathrm{g,N}}$ is the grafted chains' unperturbed radius of gyration and b is the statistical segment length of a polymer). Unless otherwise mentioned, simulations are for $R_{\mathrm{P}}^{*} = 1.53$ grafted with $N = 30$ chains at a grafting density of $\sigma^{*} = 0.86$. Since we do not change N in any of the simulations, we note that $\sigma b^{2} = \sigma R_{\mathrm{g}}^{2}$ to within a constant of order unity. For all of the simulations, the grafting density is sufficiently high that the grafted chains form a dense polymer brush around the particles, and there are many chains grafted to each particle. In particular, for $\sigma^{*} = 0.86$ on NPs with $R_{\mathrm{P}}^{*} = 1.53$, there are 125 chains grafted to each NP. Note that as χ is varied, the chemical identity of the polymer changes (i.e., the calculations no longer correspond to one specific gNP-PNC system).

Figure 5.5 shows three different slices through our high-dimensional phase space. Figure 5.5a shows the binodal curves for P as a function of ϕ_{M} as χ increases from 0 (athermal) to 1/20, Figure 5.5b shows χP as a function of ϕ_{M} as α increases from 0.5 to 16, and Figure 5.5c shows α as a function of ϕ_{M} as χP increases from 0 (athermal) to 2. In all three figures, the bold lines are from TILD simulations while the dashed curves represent the mean-field calculations. The differences between the bold and dashed curves are a qualitative measure of the contribution of depletion interactions originating from conformational entropy to the overall phase behavior. For all cases, $\phi_{\mathrm{M}} \approx 1$ in the matrix rich phase. Here, we will focus on the gNP-rich phase. In Figure 5.5a, each curve represents a PNC with the same chemistry (fixed χ) and varying matrix chain length. Figure 5.5a exemplifies most experimental studies of gNP-PNCs, including ours in Figure 5.1, Figure 5.2,

and Figure 5.3, in which the same set of gNPs are incorporated into polymer matrices of varied molecular weights ($M_{n,M}$) and measured at a single temperature. For each χ value, the phase boundary occurs at higher P with larger volume fractions of gNPs (lower matrix volume fractions ϕ_M). The binodal curves shift toward lower P as χ increases. Similar to Figure 5.3, the inclusion of fluctuations enhances macrophase separation as per the discussion following Figure 5.3. There is no black dashed curve in Figure 5.5a and Figure 5.5c because the mean-field model always predicts dispersion when $\chi = 0$.

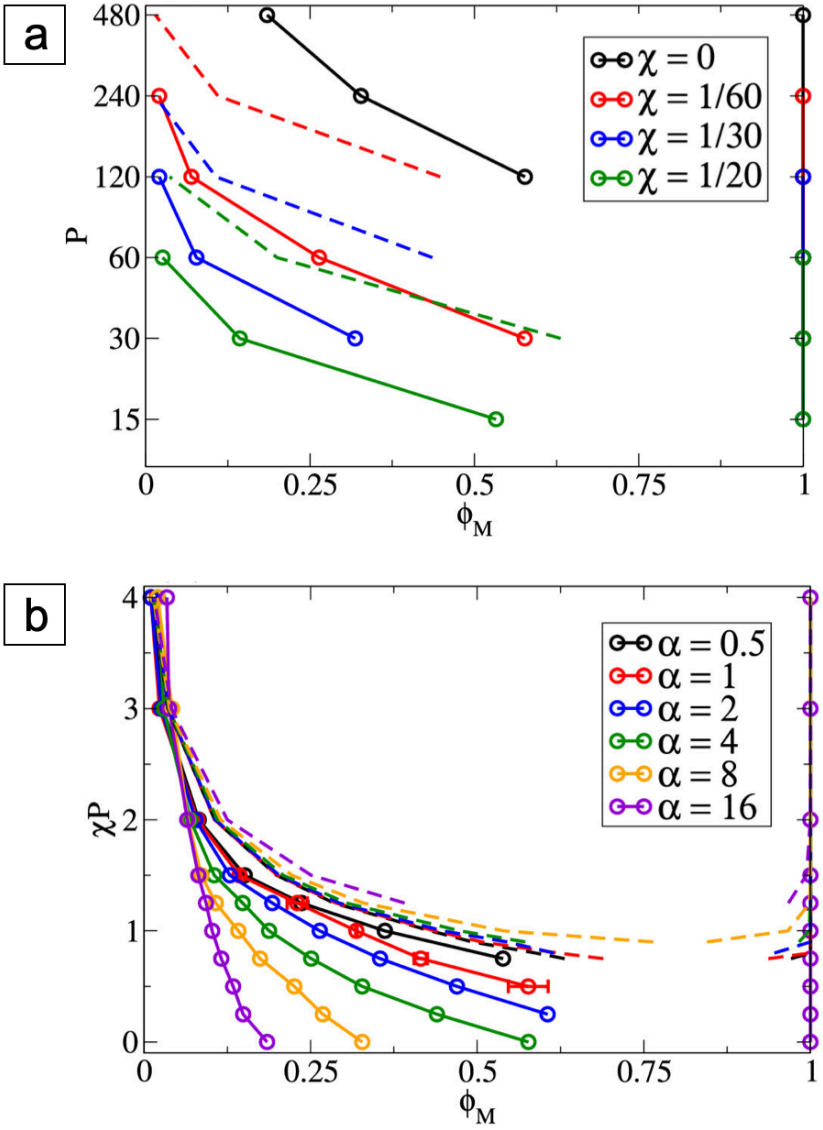

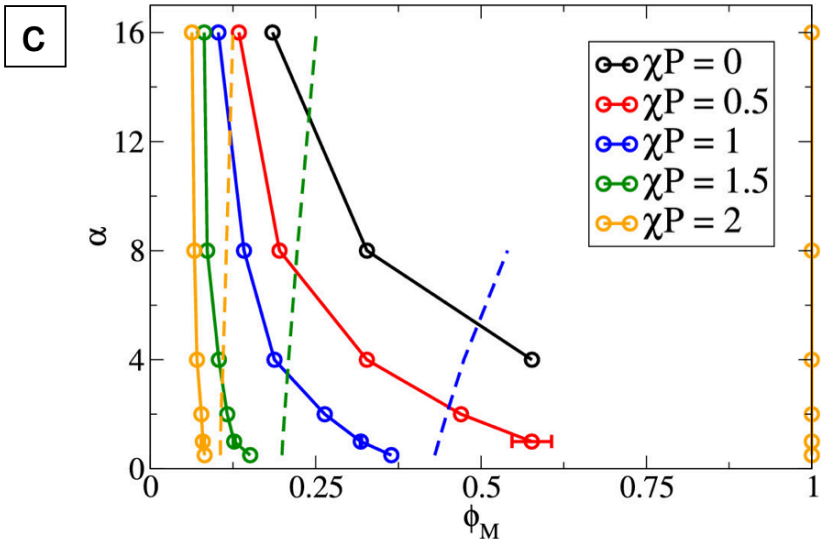

Figure 5.5. Binodal curves plotted as (a) matrix degree of polymerization, P (b) enthalpic repulsion, χP, and (c) α, all as a function of ϕ_M for PNC-FT calculations (dashed curves), and TILD simulations (solid curves with points). In all cases, $N = 30$, $\sigma^* = 0.86$, and $R_P^* = 1.53$. In (a), each χ value is based on the chosen reference volume described in the Methods section. In (b), χP is changed by varying χ for each α. In (c), we simultaneously increase P and decrease χ to keep χP constant. In (b), error bars for $\alpha = 1$ represent the standard deviation between two different TILD trajectories.

The trends presented in Figure 5.5a are the result of simultaneous changes in two different contributions to the phase behavior. As P is increased at constant χ, there are increases in both the magnitude of the enthalpic repulsion, largely characterized by χP, and in the magnitude of the depletion interactions, largely characterized by α. Note that in all calculations, N is kept fixed, so we characterize the strength of the enthalpic interactions by χP rather than by χN. One advantage of simulations, compared with experiment, is the ability to decouple thermodynamic contributions to the phase behavior. Therefore, to isolate the characteristics driving phase separation, Figure 5.5b describes the strength of the enthalpic repulsion between the matrix chains and gNPs by plotting χP as a function of ϕ_M, while Figure 5.5c describes the strength of the depletion interactions due to

conformational entropy by plotting α as a function of ϕ_M. For each curve in Figure 5.5b at fixed $\alpha = P/N$, P is kept constant and only χ is changed on the y-axis. The same data is shown plotted as χ vs ϕ_M in Figure D.4. In the case of a temperature-dependent χ, Figure 5.5b is representative of experiments in which chain lengths are kept constant and the temperature is changed. For each curve in Figure 5.5c at fixed χP, χP is kept constant and P is increased (which increases α) while χ is decreased simultaneously. As a result, as χP increases across each phase boundary in Figure 5.5b, macrophase separation is driven solely by an increase in enthalpic repulsion, with no contribution from the matrix chain entropy. Conversely, increasing α across each phase boundary in Figure 5.5c corresponds to macrophase separation driven by increasing the length of the matrix chains, which reflects the penalty due to conformational entropy loss. In Figure 5.5b and Figure 5.5c, increasing α increases the entropic force driving the phase separation while increasing χP increases the enthalpic force driving the phase separation. These phenomena are reflected in the upturns of the curves at low ϕ_M, which become sharper with increasing α and χP, respectively. Notably, Figure 5.5b shows that in the athermal case of $\chi = 0$, the gNPs are dispersed for $\alpha = 0.5$, 1, and 2. However, the gNP phase separate from the matrix at low ϕ_{gNP} (high ϕ_M) for $\alpha \geq 4$.

The clear differences between the fluctuating models and the mean-field results presented in Figure 5.5 further highlight the importance of fluctuations. In Figure 5.5b, the mean-field curves (dashed lines) show the phase boundary shifting upward with increasing α, while the TILD predicts the phase boundary shifts downward with increasing α. This mean-field trend may seem counterintuitive because larger matrix chains lead to a decrease in the translational entropy, which should result in an enhanced phase separation (lower phase boundary). Plotting the binodals in Figure 5.5b in terms of χ as a function of ϕ_M (instead of χP as a function of ϕ_M) shows that the binodals move downward with increasing α in both the TILD and mean-field simulations. The mean-field binodals shift downward less than the TILD binodals, and thus when the mean-field

binodals are plotted as a function of χP, the large increase in P leads to a reversal in the order of the curves in Figure 5.5b (see the Appendix D for more details on this point).

To explore the effects of σ^* and R_{P}^*, Figure 5.6 shows phase diagrams as a function of χP versus the matrix volume fraction while varying σ^* (Figure 5.6a) from 0.43 to 1.29 and while varying R_{P}^* (Figure 5.6b) from 0.67 to 1.53. Figure 5.6a shows that at fixed R_{P}^* but increasing σ^*, the phase separation is enhanced. In the PNC-FT, this is due to somewhat decreased translational entropy due to the larger overall volume of the gNPs with higher σ^* and to increased enthalpic repulsion between the larger number of grafted chains and the matrix (see Equation 5.10). There is a greater difference between the PNC-FT and TILD curves with increasing σ^*, indicating increased depletion interactions as well in the TILD simulations. With increased grafting density, it is more difficult for the matrix chains to penetrate the brush of the gNP and there is an increased driving force for the matrix chains to be expelled from the grafted layer. The matrix chains lose more conformational entropy, an effect included only in the TILD simulations, which is why there is the increasing difference between TILD and PNC-FT with increasing σ^*. Changing R_{P}^* at fixed σ^* is less straightforward than changing σ^* at fixed R_{P}^* because this also results in a change in the number of grafted chains on each particle. For the TILD simulations shown in Figure 5.6b, there is a slightly enhanced phase separation with larger particles, whereas the mean-field curves are nearly identical for different R_{P}^*. The similarities in the PNC-FT curves are the result of minor translational entropy and enthalpic contributions to the free energy for this small range of particle sizes. The difference between the PNC-FT and TILD curves increases with increasing R_{P}^*. This is because the depletion interactions increase with the larger numbers of grafted chains since σ^* is constant.

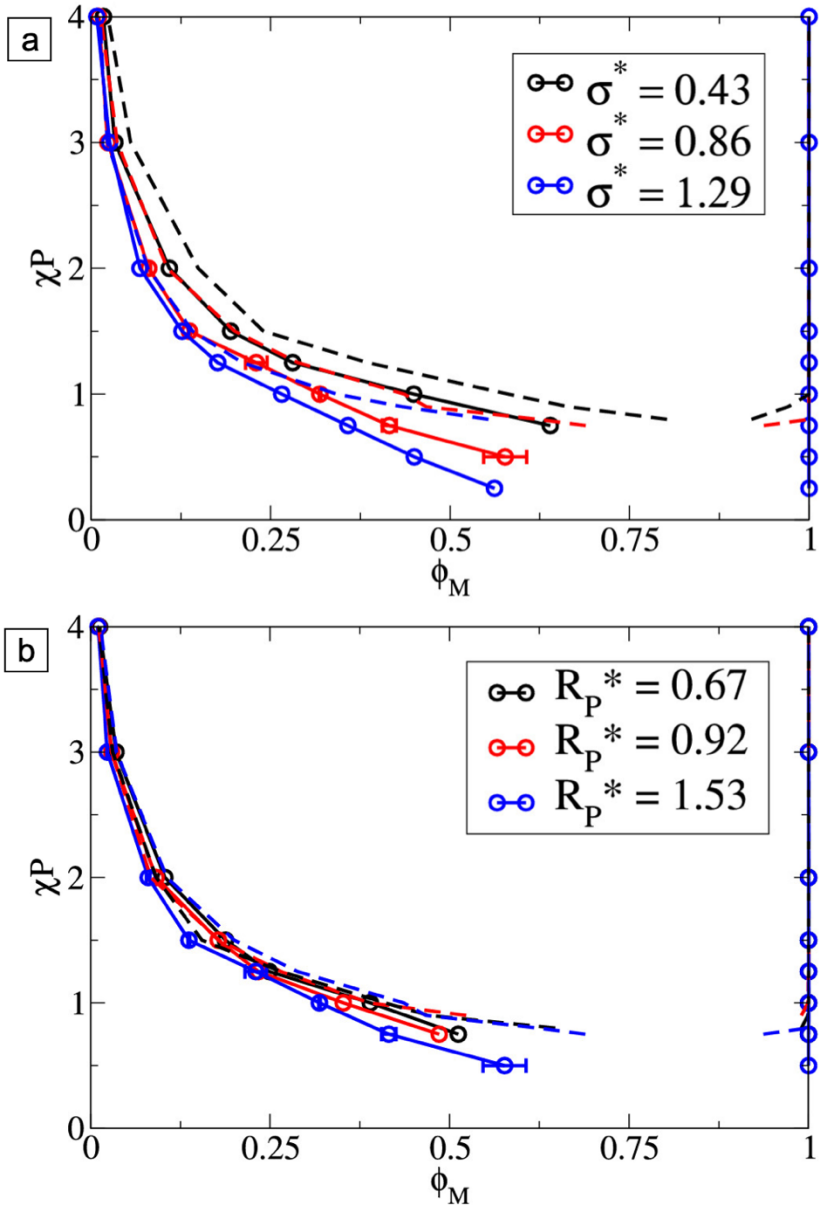

Figure 5.6. Binodals plotted as enthalpic repulsion (i.e., χP) versus matrix volume fraction (ϕ_M) at α = 1, for different values of (a) σ^* and (b) R_P^*. The solid lines show PNC-FT calculations (no fluctuations) while the dashed lines represent TILD simulations (fluctuations). In (a), the different colors represent different σ^* values with (black) σ^* = 0.43, (red) σ^* = 0.86, and (blue) σ^* = 1.29. In (b), the different colors represent different R_P^* values with (black) R_P^* = 0.67, (red) R_P^* = 0.92,

and (blue) $R_P^* = 1.53$. The red curves in (a) are the same as the blue curves in (b). To change χP, we varied the value of χ while holding P constant. $P = N = 30$ in all cases.

5.4 Discussion

The transition from dispersed to macrophase separated PNCs is determined by the balance among translational entropy, enthalpic repulsion, and depletion interactions (or conformational entropy). In the phase diagrams, the binodals are extremely asymmetric because of the extreme volume difference between the matrix chains and the gNPs. Experimental studies typically investigate low particle volume fractions (low ϕ_{gNP}, high ϕ_M), where the binodal occurs at fairly low values of χP. At high ϕ_{gNP} values, a dispersed state is expected since there are not enough matrix chains to phase separate from the gNPs. Experimentally, increasing α leads to enhanced phase separation (discussed further below), which is consistent with our TILD simulations. Here, we make some more detailed comparisons with results in the literature.

5.4.1 Enthalpic Systems ($\chi \neq 0$). There are only a few studies on the effect of χ on gNP-PNCs. Martin *et al.*[13] examine deuterated PS-*g*-SiO_2 NPs in poly(vinyl methyl ether) (PVME). PS/PVME blends have a lower critical solution temperature, so they are miscible with $\chi > 0$ at room temperature but phase separate at higher temperatures. Here, the authors find that increasing temperature results in a transition from dispersed to aggregated gNPs, with a spinodal temperature around 143°C. The experimental system is at $\alpha \approx 12$, with grafting densities of 0.7 chains/nm^2 and $R_P^* \approx 1.2$. Therefore, for positive χ the results are in agreement with the TILD simulations, which predict phase separation at positive χ for the experimental matrix volume fraction of $\phi_M = 0.82$. Martin *et al*. also performed extensive Brownian dynamics simulations of a coarse-grained model and their simulated phase diagram is also in good qualitative agreement with our TILD simulations. They observe phase separation for $\chi > 0$ and for $0.8 < \phi_M < 0.95$ at $\alpha = 5$, for similar particle sizes and grafting densities as shown in Figure 5.5 ($R_P^* = 1.9$, $\sigma^* = 0.76$). Mangal *et al.*[57] study a negative

χ system and analyze the competition between entropy and enthalpy in the dispersion of PEG-*g*-SiO_2 NPs in a PMMA matrix; their results are not directly comparable to ours since we only consider $\chi \geq 0$. They do find that as P (or α) increases at low σ and N for $\chi < 0$, the gNP-PNC undergoes phase separation.

5.4.2 Athermal Systems (χ = 0). We can also compare our results with previous experimental studies of athermal systems, for which the bulk of the work on gNP-PNCs has been done. We restrict the discussion to systems in which the gNP-PNCs are in the regime of steric stabilization where the NP cores are completely shielded by the grafted polymer brush. One recent study investigated the miscibility of small volume fractions of PS homopolymer in PS-grafted SiO_2 NPs.[58] Interestingly, it was found that for a system with $\alpha = 7$ and $\sigma = 0.6$ chains/nm^2, the matrix polymer was miscible with the gNPs up to at least $\phi_M = 0.26$, but showed clear macrophase separation for $\phi_M = 0.35$. This result appears to be consistent with the TILD results in Figure 5.5b, where systems with $\alpha = 8$ are miscible up to about $\phi_M = 0.31$ at $\chi = 0$. One significant difference is that the NPs in the experiments were much larger than those studied here, with $R_P^* = 18$.

Next, we consider gNP-PNCs with small overall gNP volume fractions ($\leq$ 5%) with densely grafted brushes. To make comparisons between systems, it is helpful to compare the values of $\sigma^*\sqrt{N}$. The combination $\sigma^*\sqrt{N}$ comes from scaling theories for brushes on flat surfaces, and roughly describes the extent of crowding of the brush; dense brushes typically form for $\sigma^*\sqrt{N} \gtrsim 2$.[5] The three grafting densities studied here correspond to $\sigma^*\sqrt{N}$ = 2.35, 4.7, and 7.1. For these systems, phase separation typically occurs near α = 4−5, but depends somewhat on σ and R*. Srivastava *et al.*[7] conducted a series of experiments on $M_{n,G}$ = 5 kg/mol poly(ethylene glycol) (PEG) grafted onto R_P = 5 nm SiO_2 NPs in a PEG matrix. For R_P^* = 1.9, they found that phase separation occurs for $5 < \alpha < 6$, relatively independent of grafting density (they used σ = 0.8, 1.25, and 2.0 chains/nm^2, corresponding to $\sigma^*\sqrt{N}$ = 4.4, 6.9, and 11, respectively). For shorter grafted chains

with R_P^* = 6, phase separation occurred for α a bit less than 5. Sunday *et al*.[6] conducted a series of experiments with $M_{n,G}$ = 60-68 kg/mol PS-grafted onto R_P = 9 nm SiO_2 NPs in a PS matrix. For R_P^* = 1.3, they found a stronger dependence on grafting density, with phase separation occurring above α = 1.6 at σ = 0.7 chains/nm^2 ($\sigma^*\sqrt{N}$ = 4.2) and above α = 7.8 for σ = 0.27 chains/nm^2 ($\sigma^*\sqrt{N}$= 1.6). Clearly, there are discrepancies between the two studies, particularly regarding the effect of σ on phase separation. It is also worth noting that the size of the NPs and grafted chains are also significantly different, which could factor into the different behavior observed in the two studies.

For athermal systems, the TILD simulations predict phase separation for $\alpha \geq 4$ at R_P^* = 1.53 and $\sigma^*\sqrt{N}$ = 4.7. This is in good qualitative agreement with Sunday *et al*.[6] who found phase separation above α = 2.4 for somewhat larger grafting densities, $\sigma^*\sqrt{N}$ = 5.9, and similar particle sizes of R_P^* = 1.3. From Figure 5.6, we expect that the TILD simulations would predict phase separation at lower α for larger σ, in agreement with the trends found by Sunday *et al*., but not observed in the study by Srivastava *et al*. One possible explanation is that since the total volume (including the grafted chains) of the gNPs used by Srivastava *et al*. are approximately a factor of 8 smaller than the gNPs used by Sunday *et al*., the difference in translational entropy leads to the gNPs phase separating at higher α values. Unfortunately, it is difficult to explain the trends by Srivastava *et al*., particularly when compared to Sunday *et al*., without additional simulations.

In this work, we did not investigate the effects of varying the absolute chain lengths at fixed α and R_P^*. Since depletion interactions in gNP-PNCs are a conformational entropy effect, an increase in P and N increases the relative importance of conformational entropy to the systems' thermodynamics. It would be interesting to see if a greater degree of macrophase separation is observed when fluctuations are included at higher values of P and N for fixed α. Such an effect would be due to matrix chains having a larger driving force to increase the overall entropy of the system by expelling themselves from between two separated NPs. This is a plausible explanation

for why Srivastava *et al*., who used $M_{n,G}$ = 5 kg/mol PEG chains, saw a less pronounced phase separation at the same α than for Sunday *et al*., who used $M_{n,G}$ = 60-68 kg/mol PS chains.

Finally, we note that at low grafting densities, anisotropic NP aggregates are observed because there are patches on the NP surfaces that are not covered by the grafted chains and therefore attract each other. For this reason, we do not discuss in detail the anisotropic structures that are observed in Ackora *et al*.[49] or Moll *et al*.[59] In the TILD framework, it is straightforward to include vdW attractions between the NPs, which can be important at lower grafting densities. Further studies at low σ could provide insight into the formation of the observed experimental structures, whether isotropic or anisotropic (e.g., strings, connected sheets, etc.). Here, we have demonstrated that the TILD method is able to predict macroscale gNP-PNC phase behavior and further investigations of these unresolved questions are possible. Further exploration of the effects of all of the relevant parameters on gNP-PNC phase behavior will be the focus of future work. Additional future work will include implementing more efficient methods, such as the Gibbs ensemble,[60,61] to calculate phase diagrams for gNP-PNCs.

5.5 Conclusions

We have developed theoretically predictive phase diagrams for gNP-PNCs using field-based methods. By implementing both the mean-field PNC-FT method and the fluctuating TILD method, we are able to isolate the effects of thermal fluctuations. Direct comparisons between new experiments on PMMA-grafted NPs in PS matrices and simulations using both methods show that only the TILD simulations agree with the experiments. Thus, the thermal fluctuations that are included in TILD are critical for correctly capturing the chains' conformational entropy and hence depletion interactions, which play a significant role in the phase behavior of gNP- PNCs. We then calculated a series of phase diagrams, varying the relevant experimental parameters α, χP, σ, R_P, and ϕ_M to explore how each contributes to macrophase separation. We showed that phase separation

is driven by both enthalpic repulsion when $\chi > 0$ and by depletion interactions due to translational and conformational entropy changes as α increases. The trends in phase behavior broadly agree with the available experimental data in the literature. Additionally, some of the remaining inconsistencies in previous experimental results may be explained by future investigation of the effects of varying the absolute chain lengths P and N, since longer chains can result in larger conformational entropy effects. With the TILD method, we now have a framework to both accurately and efficiently predict macroscale phase behavior of gNP-PNCs. The effects of vdW interactions and of the absolute chain lengths at constant α and R_{p}^{*} will be the focus of future work.

5.6 References

(1) Leibler, L. Theory of Microphase Separation in Block Copolymers. *Macromolecules* **1980**, 13, 1602−1617.

(2) Bates, F. S.; Hillmyer, M. A.; Lodge, T. P.; Bates, C. M.; Delaney, K. T.; Fredrickson, G. H. Multiblock Polymers: Panacea or Pandora's Box? *Science* **2012**, 336, 434−440.

(3) Kumar, S. K.; Ganesan, V.; Riggleman, R. A. Perspective: Outstanding Theoretical Questions in Polymer-Nanoparticle Hybrids. *J. Chem. Phys.* **2017**, 147, 020901.

(4) Moniruzzaman, M.; Winey, K. I. Polymer Nanocomposites Containing Carbon Nanotubes. *Macromolecules* **2006**, 39, 5194−5205.

(5) Kumar, S. K.; Jouault, N.; Benicewicz, B.; Neely, T. Nanocomposites with Polymer Grafted Nanoparticles. *Macromolecules* **2013**, 46, 3199−3214.

(6) Sunday, D.; Ilavsky, J.; Green, D. L. A Phase Diagram for Polymer-Grafted Nanoparticles in Homopolymer Matrices. *Macromolecules* **2012**, 45, 4007−4011.

(7) Srivastava, S.; Agarwal, P.; Archer, L. A. Tethered Nanoparticle-Polymer Composites: Phase Stability and Curvature. Langmuir **2012**, *28*, 6276−6281.

(8) Meng, D.; Kumar, S. K.; Lane, J. M. D.; Grest, G. S. Effective Interactions Between Frafted Nanoparticles in a Polymer Matrix. *Soft Matter* **2012**, 8, 5002−5010.

(9) Smith, G. D.; Bedrov, D. Dispersing Nanoparticles in a Polymer Matrix: Are Long, Dense Polymer Tethers Really Necessary? *Langmuir* **2009**, 25, 11239−11243.

(10) Tang, T.-Y.; Arya, G. Anisotropic Three-Particle Interactions Between Spherical Polymer-Grafted Nanoparticles in a Polymer Matrix. *Macromolecules* **2017**, 50, 1167−1183.

(11) Khani, S.; Jamali, S.; Boromand, A.; Hore, M. J. A.; Maia, J. Polymer-Mediated Nanorod Self-Assembly Predicted by Dissipative Particle Dynamics Simulations. *Soft Matter* **2015**, 11, 6881−6892.

(12) Chen, Y.; Xu, Q.; Jin, Y.; Qian, X.; Liu, L.; Liu, J.; Ganesan, V. Design of End-to-End Assembly of Side-Grafted Nanorods in a Homopolymer Matrix. *Macromolecules* **2018**, 51, 4143−4157.

(13) Martin, T. B.; Mongcopa, K. I. S.; Ashkar, R.; Butler, P.; Krishnamoorti, R.; Jayaraman, A. Wetting-Dewetting and Dispersion Aggregation Transitions Are Distinct for Polymer Grafted Nano- particles in Chemically Dissimilar Polymer Matrix. *J. Am. Chem. Soc.* **2015**, 137, 10624−10631.

(14) Bates, F. S.; Fredrickson, G. H. Block copolymer Thermodynamics: Theory and Experiment. *Annu. Rev. Phys. Chem.* **1990**, 41, 525−557.

(15) Matsen, M. W. Phase Behavior of Block Copolymer/Homopolymer Blends. *Macromolecules* **1995**, 28, 5765−5773.

(16) Delaney, K. T.; Fredrickson, G. H. Recent Developments in Fully Fluctuating Field-Theoretic Simulations of Polymer Melts and Solutions. *J. Phys. Chem. B* **2016**, 120, 7615−7634.

(17) Matsen, M. W.; Thompson, R. Equilibrium Behavior of Symmetric ABA Triblock Copolymer Melts. *J. Chem. Phys.* **1999**, 111, 7139−7146.

(18) Lee, J.; Popov, Y. O.; Fredrickson, G. H. Complex Coacervation: A Field Theoretic Simulation Study of Polyelectrolyte Complexation. *J. Chem. Phys.* **2008**, 128, 224908.

(19) Delaney, K. T.; Fredrickson, G. H. Theory of Polyelectrolyte Complexation-Complex Coacervates are Self-Coacervates. *J. Chem. Phys.* **2017**, 146, 224902.

(20) Audus, D. J.; Gopez, J. D.; Krogstad, D. V.; Lynd, N. A.; Kramer, E. J.; Hawker, C. J.; Fredrickson, G. H. Phase Behavior of Electrostatically Complexed Polyelectrolyte Gels Using an Embedded Fluctuation Model. *Soft Matter* **2015**, 11, 1214−1225.

(21) Xu, J.; Qiu, F.; Zhang, H.; Yang, Y. Morphology and Interactions of Polymer Brush-Coated Spheres in a Polymer Matrix. J. *Polym. Sci., Part B: Polym. Phys.* **2006**, 44, 2811−2820.

(22) Trombly, D. M.; Ganesan, V. Curvature Effects Upon Interactions of Polymer-Grafted Nanoparticles in Chemically Identical Polymer Matrices. *J. Chem. Phys.* **2010**, 133, 154904.

(23) Ganesan, V.; Jayaraman, A. Theory and Simulation Studies of Effective Interactions, Phase Behavior and Morphology in Polymer Nanocomposites. *Soft Matter* **2014**, 10, 13−38.

(24) Nair, N.; Jayaraman, A. Self-Consistent PRISM Theory-Monte Carlo Simulation Studies of Copolymer Grafted Nanoparticles in a Homopolymer Matrix. *Macromolecules* **2010**, 43, 8251−8263.

(25) Martin, T. B.; Dodd, P. M.; Jayaraman, A. Polydispersity for Tuning the Potential of Mean Force between Polymer Grafted Nanoparticles in a Polymer Matrix. *Phys. Rev. Lett.* **2013**, 110, 018301.

(26) Martin, T. B.; Jayaraman, A. Polydisperse Homopolymer Grafts Stabilize Dispersions of Nanoparticles in a Chemically Identical Homopolymer Matrix: an Integrated Theory and Simulation Study. *Soft Matter* **2013**, 9, 6876−6889.

(27) Frischknecht, A. L. Forces Between Nanorods with End-Adsorbed Chains in a Homopolymer Melt. *J. Chem. Phys.* **2008**, 128, 224902.

(28) Frischknecht, A. L.; Hore, M. J. A.; Ford, J.; Composto, R. J. Dispersion of Polymer-Grafted Nanorods in Homopolymer Films: Theory and Experiment. *Macromolecules* **2013**, 46, 2856−2869.

(29) Ginzburg, V. V. Polymer-Grafted Nanoparticles in Polymer Melts: Modeling Using the Combined SCFT−DFT Approach. *Macromolecules* **2013**, 46, 9798−9805.

(30) Ginzburg, V. V. Modeling the Morphology and Phase Behavior of One-Component Polymer-Grafted Nanoparticle Systems. *Macromolecules* **2017**, 50, 9445−9455.

(31) Koski, J.; Chao, H.; Riggleman, R. A. Field Theoretic Simulations of Polymer Nanocomposites. *J. Chem. Phys.* **2013**, 139, 244911.

(32) Chao, H.; Hagberg, B. A.; Riggleman, R. A. The Distribution of Homogeneously Grafted Nanoparticles in Polymer Thin Films and Blends. *Soft Matter* **2014**, 10, 8083−8094.

(33) Koski, J.; Chao, H.; Riggleman, R. A. Predicting the Structure and Interfacial Activity of Diblock Brush, Mixed Brush, and Janus-Grafted Nanoparticles. *Chem. Commun*. **2015**, 51, 5440−5443.

(34) Koski, J. P.; Riggleman, R. A. Field-Theoretic Simulations of Block Copolymer Nanocomposites in a Constant Interfacial Tension Ensemble. *J. Chem. Phys.* **2017**, 146, 164903.

(35) Koski, J. P.; Ferrier, R. C., Jr.; Krook, N. M.; Chao, H.; Composto, R. J.; Frischknecht, A. L.; Riggleman, R. A. Comparison of Field-Theoretic Approaches in Predicting Polymer Nanocomposite Phase Behavior. *Macromolecules* **2017**, 50, 8797−8809.

(36) Fredrickson, G. H. The Equilibrium Theory of Inhomogeneous Polymers; Oxford University Press: New York, **2006**.

(37) Klauder, J. R. Coherent-state Langevin Equations for Canonical Quantum Systems with Applications to the Quantized Hall Effect. *Phys. Rev. A* **1984**, 29, 2036.

(38) Parisi, G. On Complex Probabilities. *Phys. Lett. B* **1983**, 131, 393.

(39) Fredrickson, G. H.; Ganesan, V.; Drolet, F. Field-Theoretic Computer Simulation Methods for Polymers and Complex Fluids. *Macromolecules* **2002**, 35, 16−39.

(40) Vorselaars, B.; Stasiak, P.; Matsen, M. W. Field-Theoretic Simulation of Block Copolymers at Experimentally Relevant Molecular Weights. *Macromolecules* **2015**, 48, 9071−9080.

(41) Fredrickson, G. H.; Helfand, E. Fluctuation Effects in the Theory of Microphase Separation in Block Copolymers. *J. Chem. Phys.* **1987**, 87, 697−705.

(42) Qin, J.; Morse, D. C. Fluctuations in Symmetric Diblock Copolymers: Testing Theories Old and New. *Phys. Rev. Lett.* **2012**, 108, 238301.

(43) Chao, H.; Koski, J.; Riggleman, R. A. Solvent Vapor Annealing in Block Copolymer Nanocomposite Films: a Dynamic Mean Field Approach. *Soft Matter* **2017**, 13, 239−249.

(44) In previous publications, our method was previously referred to as dynamic mean-field theory (DMFT) and we include a discussion of the name change in Appendix D for the interested reader.

(45) Ganesan, V.; Pryamitsyn, V. Dynamical Mean-Field theory for Inhomogeneous Polymeric Systems. *J. Chem. Phys.* **2003**, 118, 4345− 4348.

(46) Daoulas, K. C.; Müller, M. Single Chain in Mean Field Simulations: Quasi-Instantaneous Field Approximation and Quantitative Comparison with Monte Carlo Simulations. *J. Chem. Phys.* **2006**, 125, 184904.

(47) Pike, D. Q.; Detcheverry, F. A.; Müller, M.; de Pablo, J. J. Theoretically Informed Coarse Grain Simulations of Polymeric Systems. *J. Chem. Phys.* **2009**, 131, 084903.

(48) Koski, J. P.; Frischknecht, A. L. Fluctuation Effects on the Brush Structure of Mixed Brush Nanoparticles in Solution. *ACS Nano* **2018**, 12, 1664−1672.

(49) Akcora, P.; Liu, H.; Kumar, S. K.; Moll, J.; Li, Y.; Benicewicz, B. C.; Schadler, L. S.; Acehan, D.; Panagiotopoulos, A. Z.; Pryamitsyn, V.; Ganesan, V.; Ilavsky, J.; Thiyagarajan, P.; Colby, R. H.; Douglas, J. F. Anisotropic Self-Assembly of Spherical Polymer-Grafted Nanoparticles. *Nat. Mater.* **2009**, 8, 354.

(50) Hore, M. J.; Composto, R. J. Functional Polymer Nanocomposites Enhanced by Nanorods. *Macromolecules* **2014**, 47, 875− 887.

(51) Frischknecht, A. L.; Hore, M. J.; Ford, J.; Composto, R. J. Dispersion of Polymer-Grafted Nanorods in Homopolymer Films: Theory and Experiment. *Macromolecules* **2013**, 46, 2856−2869.

(52) Jayaraman, A.; Schweizer, K. S. Effective Interactions and Self-assembly of Hybrid Polymer Grafted Nanoparticles in a Homopolymer Matrix. *Macromolecules* **2009**, 42, 8423−8434.

(53) Ohno, K.; Morinaga, T.; Koh, K.; Tsujii, Y.; Fukuda, T. Synthesis of Monodisperse Silica Particles Coated with Well-Defined, High-Density Polymer Brushes by Surface-Initiated Atom Transfer Radical Polymerization. *Macromolecules* **2005**, 38, 2137−2142.

(54) Ohno, K.; Akashi, T.; Huang, Y.; Tsujii, Y. Surface-Initiated Living Radical Polymerization from Narrowly Size-Distributed Silica Nanoparticles of Diameters Less than 100 nm. *Macromolecules* **2010**, 43, 8805−8812.

(55) Lin, C.-C.; Griffin, P. J.; Chao, H.; Hore, M. J. A.; Ohno, K.; Clarke, N.; Riggleman, R. A.; Winey, K. I.; Composto, R. J. Grafted Polymer Chains Suppress Nanoparticle Diffusion in Athermal Polymer Melts. *J. Chem. Phys.* **2017**, 146, 203332.

(56) Mark, J. E. Physical Properties of Polymers Handbook; Springer, **2007**; Vol. 1076.

(57) Mangal, R.; Nath, P.; Tikekar, M.; Archer, L. A. Enthalpy-Driven Stabilization of Dispersions of Polymer-Grafted Nanoparticles in High-Molecular-Weight Polymer Melts. *Langmuir* **2016**, 32, 10621−10631.

(58) Schmitt, M.; Hui, C. M.; Urbach, Z.; Yan, J.; Matyjaszewski, K.; Bockstaller, M. R. Tailoring Structure Formation and Mechanical Properties of Particle Brush Solids via Homopolymer Addition. *Faraday Discuss*. **2016**, 186, 17−30.

(59) Moll, J. F.; Akcora, P.; Rungta, A.; Gong, S.; Colby, R. H.; Benicewicz, B. C.; Kumar, S. K. Mechanical Reinforcement in Polymer Melts Filled with Polymer Grafted Nanoparticles. *Macromolecules* **2011**, 44, 7473−7477.

(60) Panagiotopoulos, A. Z. Direct Determination of Phase Coexistence Properties of Fluids by Monte Carlo Simulation in a New Ensemble. *Mol. Phys.* **1987**, 61, 813−826.

(61) Riggleman, R. A.; Fredrickson, G. H. Field-Theoretic Simulations in the Gibbs Ensemble. *J. Chem. Phys.* **2010**, 132, 024104.

CHAPTER 6: Conclusions and Future Work

6.1 Conclusions

Since their nascence in the late 1900s, polymer nanocomposites (PNCs) have been and continue to be extensively studied.[1] As materials scientists, we seek to create new materials and improve current materials by building upon our evolving understanding of the structure-property relationship within various material systems. By designing and developing PNCs, researchers take advantage of the processability of polymers in which to embed unlimited combinations of nanoparticles (NPs). How NPs are organized within the matrices will dictate the internal structure and thus directly affect the behavior of the composites. Polymer chains are often grafted to NP surfaces to mediate the interactions between the particles and the matrix polymer to ultimately control the spatial distribution of NPs. As expected, the parameter space of PNCs is exhaustive and includes variables related to the polymer matrix (molecular weight and chemistry), polymer brushes (chain length, composition, and grafting density), and NPs (size, composition, and shape). With regards to particle shape anisotropy, NP orientation or lack thereof will also impact the resulting PNC properties. To take advantage of potential shape and orientation-dependent properties of non-spherical NPs, precise orientational control is required. The studies presented in this dissertation demonstrate that block copolymers (BCPs) can facilitate NP alignment through self-assembly. Limited research explorations have pursued nanoplates in combinations with BCPs since common plate materials like clay or graphite are polydisperse, incompatible with BCP dimensions, and difficult to functionalize with polymer chains. This dissertation develops a model nanoplate system that addresses these obstacles and then adapts the current polymer physics understanding for isotropic NPs in BCPs to nanoplate alignment within these self-assembling matrices.

In Chapter 2, monodisperse rhombic gadolinium trifluoride nanoplates doped with ytterbium and erbium [GdF_3:Yb/Er (20/2 mol%)] were synthesized through rapid thermal

decomposition with oleic acid (OA) on their surfaces. Measuring 35 nm along the longest diagonal, 22 nm along the shortest diagonal, and 3 nm in thickness, the nanoplate dimensions are commensurate with the domain spacing (~18 nm) of a M_n = 38k-*b*-36.8k g/mol lamellar-forming poly(styrene-*b*-methyl methacrylate) (PS-*b*-PMMA) BCP. When grafted with M_n = 5 kg/mol phosphoric acid functionalized polyethylene glycol (PEG-PO_3H_2) brushes and after thermal annealing, the BCP composite assembles into an ordered lamellar morphology and the nanoplates segregate to the PMMA block at low volume fractions (ϕ = 0.0083 and ϕ = 0.017). With lamellae oriented parallel to the silicon (Si) substrates, the nanoplates confined in the PMMA microdomains are also aligned parallel to the substrate. As ϕ increases to ϕ = 0.027 and ϕ = 0.038, the morphology evolves and the PNC undergoes phase separation into regions of disordered lamellae with unaligned nanoplates coinciding with regions of ordered lamellae. The phase separation indicates that the local chain distortions and excess PS/PMMA interface around the nanoplates accumulates as ϕ is increased to these intermediate volume fractions. Therefore, the entropic penalties become too great to integrate the nanoplates into the BCP domains. As ϕ is further increased to ϕ = 0.050 and ϕ = 0.064, the nanoplates are isotropically dispersed and the lamellae are completely disordered. This transition agrees with the calculated overlap concentration (ϕ^* = 0.051) where the NPs jam in a kinetically trapped state and arrest phase separation. The work detailed in Chapter 2 has been published in *ACS Macro Letters* (2018, DOI: 10.1021/acsmacrolett.8b00665).[2]

Chapter 3 investigates the thermodynamic basis for the aligned nanoplate string assemblies observed at an average interparticle spacing of 6.42 nm in the ϕ = 0.0083 and ϕ = 0.017 ordered BCP composites from Chapter 2. Although theoretical predictions forecast a local bulge around nanoplates inserted into BCP lamellae, the domain thicknesses appear to remain unchanged via X-ray scattering and electron microscopy characterization. We rationalize this inconsistency by describing the experimental limitations of both methods. Instead, simulations using the hybrid particle/self-consistent field theory (hSCFT) help visualize the distortion in PS/PMMA interface

with supporting potential of mean forces (PMF) calculations as a function of nanoplate edge-to-edge distance. The calculated free energy minimum occurs at an equilibrium interparticle spacing of 7.0 nm (in accordance with experimental observations). Through our evaluation of the critical features in the PMF curves, we conclude that the nanoplate string assemblies, featured in the micrographs, form to decrease added PS/PMMA interfacial area and to reduce the conformational entropy cost associated with significant chain stretching. Ultimately, the culmination of results from Chapter 2 and Chapter 3 provides the groundwork for future explorations of parallel nanoplate alignment and interparticle assemblies using BCP matrices. The work detailed in Chapter 3 has been submitted for publication in a peer-reviewed journal.

While parallel nanoplate orientation was the focus of Chapter 2 and Chapter 3, Chapter 4 pursues vertical alignment of nanoplates through BCP self-assembly. By grafting hydroxy terminated PS and PMMA homopolymers to Si, the neutral wetting layer orients M_n = 73k-*b*-73k g/mol and M_n = 95k-*b*-95k g/mol PS-*b*-PMMA lamellae perpendicular to the substrate. Without modifying the GdF_3:Yb/Er NP surfaces with PEG-PO_3H_2 brushes, OA stabilized nanoplates are expelled to the free surface of the thin films and disrupt the equilibrium lamellar morphology underneath. However, if ϕ = 0.0083 PEG-PO_3H_2 functionalized nanoplates are incorporated into the two molecular weight PS-*b*-PMMA films, the vertical domains successfully direct the nanoplates perpendicular to the substrate without interfering with the lamellar formation. To our knowledge, this is the first time vertical and parallel nanoplate alignment has been accomplished with self-assembling, lamellar-forming BCPs. This achievement provides an opportunity to devise easy-to-manufacture nanocomposite coatings that profit from either mode of alignment. The work detailed in Chapter 4 is in preparation to be submitted for publication in a peer-reviewed journal.

Although Chapter 5 does not pertain to nanoplate alignment in lamellar-forming PS-*b*-PMMA films, it begins to address the continued need to develop theoretical models that predict the phase behavior of experimental PNCs. We compare the accuracy of both the mean-field PNC field

theory (PNC-FT) and the fluctuating theoretically informed Langevin dynamics (TILD) methods in forecasting the phase separation of an enthalpically repulsive PNC. Isotropic silica NPs, grafted with M_n = 7.9 kg/mol PMMA, were dispersed in M_n = 0.95 kg/mol, M_n = 2.7 kg/mol, and M_n = 10 kg/mol PS matrices. By calculating the binodal curves for both methods, delineating the transition from dispersed to phase separated as a function of various experimental parameters, we identify that the TILD phase diagrams more accurately depict the phase separation observed in each experimental state point. By including thermal fluctuations and fluctuations in the polymer conformation, a higher degree of depletion interactions between the polymer grafted NPs is appropriately captured. Using the TILD method, we develop a phase diagram with enhanced predictive capability for the behavior of experimental PNC systems. The progress demonstrated in this chapter signifies our efforts in engineering solutions that marry simulations with experimental studies to limit the experimental parameter space when designing new materials with a specific phase behavior. The work detailed in Chapter 5 has been published in *Macromolecules* (2019, DOI: 10.1021/acs.macromol.9b00720).[3]

6.2 Future Work

Self-assembling BCPs are convenient for creating PNCs with well-ordered hierarchical structures through limited processing steps. However, research that exploits BCPs to align anisotropic NPs is still in its infancy. From the studies presented in this dissertation, we acknowledge that nanoplate alignment is demonstrated for only moderate NP loadings. To create functional hybrid materials, a higher volume fraction of aligned particles is essential. There are still several open questions pertaining to how other factors in the large PNC parameter space affect nanoplate order and orientation in BCPs as well as how the fundamental understanding gained through these works can be translated to creating functional materials. For example, how would BCP molecular weight and chemistry influence nanoplate assembly? Can we achieve higher

loadings of nanoplate aligned either in the plane or out of the plane of polymer films by tuning any of the variables? The GdF_3:Yb/Er nanoplate system is an ideal candidate with which to explore these parameters. Once the criteria for increased volume fraction are examined, what other NP systems can we investigate and align to impart interesting functionalities to PNC films? The goal of the suggested fundamental studies is to reach a deeper polymer physics understanding for nanoplates dispersed in BCP matrices – all with the intent of creating new composite materials with accessible properties. We then recommend a few NP systems as viable options for measurable properties, but maintain the outlook of creating PNC films that exploit self-assembling BCPs capable of covering large areas through limited manufacturing operations.

6.2.1 Effect of Molecular Weight on Nanoplate String Assembly. Chapter 3 showed that $\phi = 0.0083$ and $\phi = 0.017$ M_n = 5 kg/mol PEG-PO_3H_2 grafted GdF_3:Yb/Er nanoplates not only align in the parallel PMMA domains of ordered M_n = 38k-*b*-36.8k g/mol PS-*b*-PMMA lamellae, but that the NPs also assemble closely together in strings at small interparticle distances. It could be advantageous for applications that rely on NPs coupling at specific separations if the edge-to-edge spacing within the anisotropic nanoplate arrays were tunable through self-assembly.[4] Conversely, individually dispersed nanoplates could also be more beneficial than stringed nanoplates for some applications. The microdomain period (λ) of a lamellar-forming BCP period scales as $\sim 1.03 a N^{2/3} \chi_{AB}^{1/6}$ where a is a monomer size scale, N is the total degree of polymerization, and χ_{AB} is the Flory−Huggins interaction parameter between the A block and B block.[5,6] Therefore, as BCP molecular weight increases, the lamellar dimensions increase. Will nanoplate strings still form when the domains are wider? With longer BCP chains extending into the PMMA domain, it is possible that the conformational entropy penalty sustained by the chains surrounding the NPs is relatively lower when PEG-PO_3H_2 functionalized GdF_3:Yb/Er particles are incorporated at higher BCP molecular weights. If so, the local bulge around the nanoplates could be less extreme. With more mild domain bulging, the curvature in the PS/PMMA interface would also be less severe and

the nanoplates would no longer need to redistribute into strings to stabilize the energy costs related to highly stretched BCP chains. Preliminary experimental results of $\phi = 0.017$ $M_n = 5$ kg/mol PEG-PO_3H_2 grafted nanoplates aligned in the PMMA domain of ordered M_n = 95k-*b*-95k g/mol and M_n = 133k-*b*-130k g/mol PS-*b*-PMMA lamellae shown in Figure 6.1a and Figure 6.1b, respectively, show little to no nanoplate string assemblies and are thus consistent with this hypothesis. However, additional hybrid particle/self-consistent field theory (hSCFT) simulations would need to be completed and potential of mean forces (PMF) curves as a function of nanoplate separation would need to be generated for BCP molecular weights higher than M_n = 38k-*b*-36.8k g/mol to fully understand the thermodynamics underlying these initial observations, namely fewer nanoplate strings. Additionally, the molecular weight of the polymer brush grafted to the nanoplate surfaces could be modified in hSCFT simulations to monitor its effect on nanoplate edge-to-edge spacing. We surmise that increasing or lowering the brush molecular weight would either enlarge or shrink the gap between nanoplates assembled in strings. This set of experiments would help to inform how BCP and polymer brush molecular weight could reduce or expand the separation between nanoplates or even completely dissolve the nanoplate string assemblies altogether to create BCP nanocomposites with tuned particle separations.

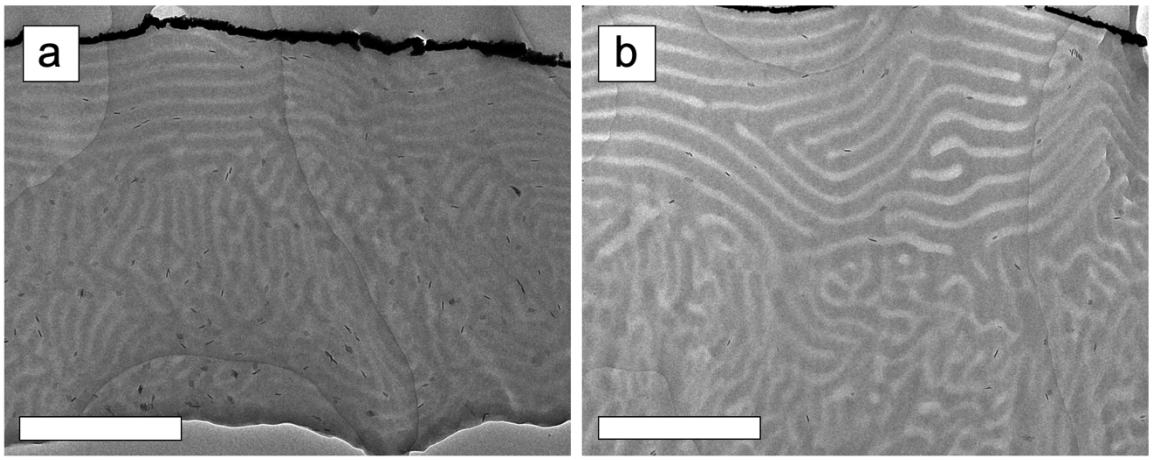

Figure 6.1. Representative TEM (JEM-1400, 120 kV) images of ultramicrotomed cross-sections of lamellar-forming (a) M_n = 95k-*b*-95k g/mol and (b) M_n = 133k-*b*-130k g/mol PS-*b*-PMMA films with ϕ = 0.017 M_n = 5 kg/mol PEG-PO_3H_2 functionalized GdF_3:Yb/Er (20/2 mol%) slowing evaporated from toluene over 48 h and then thermally annealed (190ºC, 48 h). The light and dark domains of the BCP are PMMA and PS, respectively. The scale bars are 300 nm.

6.2.2 Solvent Annealing Mediated Assembly. In Chapter 2, PEG-PO_3H_2 grafted nanoplates are isotropically dispersed in disordered lamellae at volume fractions exceeding ϕ = 0.050. We would have expected the phase behavior of these highly loaded films to match that of the ϕ = 0.027 and ϕ = 0.038 nanocomposites and therefore phase separate into areas of ordered lamellae and areas of disordered lamellae with unaligned nanoplates. Instead of observing proportionally larger regions of disorder and unalignment, the entire film is disordered. We concluded that, rather than attaining thermodynamic equilibrium, the NPs jam into a kinetically trapped state. These films were formed through thermal annealing alone. To verify the existence of and overcome this metastable state, we propose experiments where the BCP nanoplate composites are processed through solvent annealing. Solvent mediated assembly, with a favorable solvent, effectively swells polymer films. By adding free volume to the system, we hypothesize that nanoplate mobility would no longer be impeded by the calculated critical overlap volume fraction

(ϕ^*) of ~0.051 for a dry film. Instead, we anticipate that ϕ^* would shift higher for a solvated film and that the BCP composites would phase separate at $\phi^* > 0.051$ until a new critical overlap volume fraction is obtained. The implications of such findings would provide means to overcome potential kinetic barriers when pursuing higher particle loadings in aligned nanoplate BCP composites.

6.2.3 Block Copolymer and Polymer Brush Systems for Enhanced Interactions. Although mixing is encouraged between PEG and PMMA, the Flory−Huggins interaction parameter for the two polymers is only slightly negative.[7] Future work should explore alternative ligand systems to functionalize to the nanoplate surfaces. Could the conformational entropic penalties that lead to phase separation be overcome by enhanced enthalpic interactions between the nanoplates and either of the BCP domains? If so, a greater density of aligned nanoplates could be ascertained in the BCP nanocomposites. Research produced from the Watkins group has accomplished ultrahigh loading of NPs in BCP matrices by facilitating hydrogen bonding between small molecule ligands and the host domain.[8] This sort of interaction could be one possible direction to entertain. Another important question is how changing $\chi_{AB}N$ would influence nanoplate integration, alignment, and the overall phase behavior. Possible BCPs to explore are more strongly segregating systems including lamellar-forming poly(styrene-*b*-ethylene oxide) and poly(isoprene-*b*-ethylene oxide) synthesized by the Hickey group.[9] In these systems, it would also be worth exploring if OA or another short ligand could remain on the nanoplate surfaces thus creating a less bulky nanoplate system for diminished entropic penalties.

6.2.4 Loading Induced Morphological Transition from Cylinders to Lamellae. Morphological transitions have previously been demonstrated in BCPs upon the addition of a homopolymer at increasing concentrations.[10-12] By blending a homopolymer of identical chemistry to one of the BCP domains, the volume fraction of that block is essentially increased and thus provides access to a different morphology without changing the original BCP molecular weight. For example, ordered cylinders can undergo a transition to ordered lamellae by adding

homopolymer to the minority phase. It would therefore be worthwhile adding the PEG-PO_3H_2 grafted nanoplates to cylindrical-forming PS-*b*-PMMA with a minority PMMA block (PMMA cylinders). It would be interesting if this addition would induce a similar morphological transition, from cylinders to lamellae, to what has been formerly observed in homopolymer and BCP blends. If successful, a higher concentration of aligned nanoplates may be possible via this route.

6.2.5 Incorporation of Functional Nanoplates. With both parallel and vertical alignment of nanoplates established through self-assembly, future studies should explore nanoplate systems with quantifiable properties of technological relevance. GdF_3:Yb/Er nanoplates have served as a superior model system to begin the early stages of discovery for nanoplate alignment in lamellar-forming BCP nanocomposites because they are monodisperse in size and shape, have dimensions on the order of BCP dimensions, and are capable of surface modification. If would be interesting to first progress towards incorporating NP systems like boron nitride or cadmium selenide nanoplates to measure the thermal and optical properties, respectively, as a function of particle orientation. Once this area of research matures and further fundamental advances are made, the integration of more complex platelet systems like graphite or clay sheets that are polydisperse, large, and difficult to functionalize should be considered.

6.2.6 Tuning Plasmonic Nanoparticle and Upconverting Nanophosphor Separation. Upconversion nanophosphors (UCNPs) convert long-wavelength, near-infrared radiation to visible emission. A nonlinear optical process gives rise to upconversion luminescence. Here, consecutive absorption of two or more photons by long-lived, metastable excited energy states is followed by the emission of the short-wavelength, higher energy radiation in the visible range.[13] This class of materials has garnered significant interest for applications including anti-counterfeiting,[14,15] biomedical imaging,[16-20] display technologies,[21] and solar cells.[22-25] High efficiency, room temperature upconversion occurs in lanthanide doped lattices where the host material dictates the environment of the dopants and thus directly influences the upconversion process.[13,26] Although

GdF_3:Yb/Er (20/2 mol%) is considered a UCNPs, GdF_3 is a poor host for upconversion. Currently, the most efficient UCNP is hexagonal phase sodium yttrium fluoride doped with ytterbium and erbium [β-$NaYF_4$:Yb/Er (20/2 mol%)].[27-29] Ye *et al.* reported a generalized approach to synthesize monodisperse β-$NaYF_4$:Yb/Er UCNPs with a wide range of sizes and morphologies.[30] Ye *et al.* noted that emission intensity increased as the β-$NaYF_4$:Yb/Er particle size increased.[30] However, the absolute quantum yield for upconversion luminescence continues to be limited and has thus propelled research in the direction of developing techniques to improve efficiency.[31]

One strategy to enhance upconversion luminescence is to combine UCNPs with plasmonic materials. Surface plasmon resonances in metal NPs are induced when the frequency of the incident photons matches that of the particles' resonant frequency. At this concurrent wavelength, electric field hotspots develop from the oscillations of the conduction electrons, greater than the incident electromagnetic field. The plasmonic particles (amplifiers) can thus enhance the luminescence of UCNPs (emitters) that are nearby if their emission wavelength also coincides. Single particle studies as well as studies on large ensemble arrays for this metal-induced plasmonic enhancement effect of UCNPs have been completed.[32,33] By assembling particles over large areas and controlling the separation between multilayers of amplifying NP species and monolayers of emitting NPs using a dielectric aluminum oxide spacer, Saboktakin *et al.* interrogated the effect of particle separation on plasmon enhanced upconversion efficiency.[33] Saboktakin *et al.* investigated 5 nm diameter gold (Au) and silver (Ag) NPs with plasmonic wavelengths of ~550 nm and ~420 nm, respectively. Hexagonal phase $NaYF_4$ NPs were codoped with either Yb^{3+}/Er^{3+}:20/2 mol% (emission at ~540 nm and ~640 nm and diameter of ~25 nm) or Yb^{3+}/Tm^{3+}:20/2 mol% (emission at ~450 nm and ~475 nm and diameter of ~20 nm). The authors concluded that regardless of the codopant, upconversion luminescence was most significantly enhanced by Au NPs and Ag NPs separated from the UCNP monolayers by 5 nm and 10 nm, respectively, in comparison to pure UCNP layers.

If the emitters and amplifiers are placed too closely together, however, quenching dominants and metal-coupled luminescence enhancement does not occur.[34]

Though diverging from nanoplate alignment in BCP lamellae, this suggested study aims to enhance upconversion luminescence and continues with the theme of developing flexible, solution-processable coatings that could be applied over a large area for the specific purpose of advancing the efficiency of photovoltaic cells. Specifically, this research promises to control separation of emitting and amplifying NP species with nanometer precision using the self-assembling lamellar-forming PS-*b*-PMMA BCPs with microdomains oriented parallel to the substrate. Emitting particles would be segregated to the PMMA domain by synthesizing small spherical β-$NaYF_4$:Yb/Er NPs and functionalizing the surfaces with PEG-PO_3H_2, following the ligand exchange procedure described in Appendix A. To partition amplifying NPs to the PS domain, either spherical Au or Ag NPs can be synthesized and functionalized with thiol terminated PS (PS-SH). The schematic in Figure 6.2 illustrates the intended design for this system. To precisely tune the separation of the NPs in adjacent domains, small amounts of either PS or PMMA homopolymer can be added to the composite solution to incrementally swell the domains.[35] Such self-contained coatings, intended for applications with solar cell technologies, could maximize the absorption of broadband light by more efficiently trapping and converting regions of the solar spectrum that would have been lost than if UCNPs alone were applied.

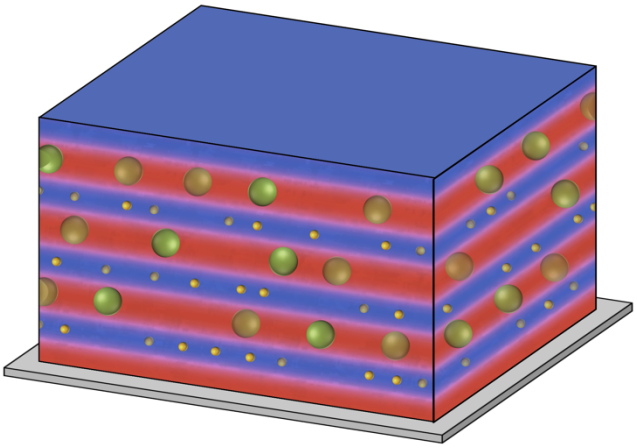

Figure 6.2. An idealized schematic (red and blue blocks depict the PMMA and PS lamellar domains, respectively) portraying emitting β-$NaYF_4$:Yb/Er NPs (green) segregated to the PMMA domains and amplifying NPs (gold) partitioned to the PS domains to create self-assembled coatings with enhanced upconversion luminescence.

6.3 References

(1) Winey, K. I.; Vaia, R. I., Polymer Nanocomposites. *MRS Bulletin* **2007**, *32* , 314-322.

(2) Krook N. M.; Ford, J.; Maréchal, M.; Rannou, P.; Meth, J. S.; Murray, C. B.; Composto R. J. Alignment of Nanoplates in Lamellar Diblock Copolymer Domains and the Effect of Particle Volume Fraction on Phase Behavior. *ACS Macro Lett.* **2018**, 7, 1400–1407.

(3) Koski, J. P.; Krook, N. M.; Ford, J.; Yahata, Y.; Ohno, K.; Murray, C. B.; Frischknecht, A. L.; Composto, R. J.; Riggleman, R. A. *Macromolecules* **2019**.

(4) Ting, C. L.; Composto, R. J.; Frischknecht, A. L. Orientational Control of Polymer Grafted Nanorods. *Macromolecules* **2016**, 49, 1111-1119.

(5) Bates, F. S.; Fredrickson, G. H. Block Copolymer Thermodynamics: Theory and Experiment. *Annu. Rev. Phys. Chem.* **1990**, 41, 525-557.

(6) Bates, F. S.; Fredrickson, G. H. Block Copolymers—Designer Soft Materials. *Physics Today* **1999**, 52, 32-38.

(7) Eitouni, H. B.; Balsara, N. P. Thermodynamics of Polymer Blends. Chapter 19 in *Physical Properties of Polymers Handbook*, 2nd ed.; Mark, J. E.; Springer: New York, 2007; p 339-356.

(8) Yao, L.; Lin, Y.; Watkins, J. J. Ultrahigh Loading of Nanoparticles into Ordered Block Copolymer Composites. *Macromolecules* **2018**, 47, 1844-1849.

(9) Lang, C.; Shan, Y.-X.; LaNasa, J. A.; Ye, D.; Song, W.; Zimudzi, T. J.; Hickner, M. A.; Gomez, E. D.; Gomez, E. W.; Kumar, M.; Hickey, R. J. Creating Cross-Linked Lamellar Block Copolymer Supporting Layers for Biomimetic Membranes. *Faraday Discuss.* **2018**, 209, 179-191.

(10) Winey, K. I.; Thomas, E. L.; Fetters, L. J. Ordered Morphologies in Binary Blends of Diblock Copolymer and Homopolymer and Characterization of Their Intermaterial Dividing Surfaces. *J. Chem. Phys.* **1991**, 95, 9367-9375.

(11) Winey, K. I.; Thomas, E. L.; Fetters, L. J. The Ordered Bicontinuous Double-Diamond Morphology in Diblock Copolymer/Homopolymer Blends. *Macromolecules* **1992**, 25, 422-428.

(12) Winey, K. I.; Thomas, E. L.; Fetters, L. J. Isothermal Morphology Diagrams for Binary Blends of Diblock Copolymer and Homopolymer. *Macromolecules* **1992**, 25, 2645-2650.

(13) Haase, M.; Schäfer, H. Upconverting Nanoparticles. *Angew. Chem. Int. Ed. Engl.* **2011**, 50, 5808-5829.

(14) Liu, Y.; Ai, K.; Lu, L. Designing Lanthanide-Doped Nanocrystals with Both Up- and Down-Conversion Luminescence for Anti-Counterfeiting. *Nanoscale* **2011**, 3, 4804-4810.

(15) Park, K.; Jung, K.; Kwon, S. J.; Jang, H. S.; Byun, D.; Han, I. K.; Ko, H. Plasmonic Nanowire-Enhanced Upconversion Luminescence for Anticounterfeit Devices. *Adv. Funct. Mater.* **2016**, 26, 7836-7846.

(16) Paik, T.; Gordon, T. R.; Prantner, A. M.; Yun, H.; Murray, C. B. Designing Tripodal and Triangular Gadolinium Oxide Nanoplates and Self-Assembled Nanofibrils as Potential Multimodal Bioimaging Probes. *ACS Nano* **2013**, 7, 2850-2859.

(17) Paik, T.; Chacko, A.; Mikitsh, J. L.; Friedberg, J. S.; Pryma, D. A.; Murray, C. B. Shape-Controlled Synthesis of Isotopic Yttrium-90-Labeled Rare Earth Fluoride Nanocrystals for Multimodal Imaging. *ACS Nano* **2015**, 9, 8718-8728.

(18) Chen, Z.; Chen, H.; Hu, H.; Yu, M.; Li, F.; Zhang, Q.; Zhou, Z.; Yi, T.; Huang, C. Versatile Synthesis Strategy for Carboxylic Acid-Functionalized Upconverting Nanophosphors as Biological Labels. *J. Am. Chem. Soc.* **2008**, 130, 3023-3029.

(19) Chatterjee, D. K.; Rufaihah, A. J.; Zhang, Y. Upconversion Fluorescence Imaging of Cells and Small Animals Using Lanthanide Doped Nanocrystals. *Biomaterials* **2008**, 29, 937-943.

(20) Wang, M.; Mi, C.; Wang, W.; Liu, C.; Wu, Y.; Xu, Z.; Mao, C.; Xu, S. Immunolabeling and NIR-Excited Fluorescent Imaging of HeLa Cells by Using NaYF4: Yb, Er Upconversion Nanoparticles. *ACS Nano* **2009**, 3, 1580-1586.

(21) Rapaport, A.; Milliez, J.; Bass, M.; Cassanho, A.; Jenssen, H. Review of the Properties of Up-Conversion Phosphors for New Emissive Displays. *J. Display Technol.* **2006**, 2, 68-78.

(22) Trupke, T.; Green, M. A.; Würfel, P. Improving Solar Cell Efficiencies by Up-Conversion of Sub-Band-Gap Light. *J. Appl. Phys.* **2002**, 92, 4117-4122.

(23) Shalav, A.; Richards, B. S.; Trupke, T.; Krämer, K. W.; Güdel, H. U. Application of $NaYF_4:Er^{3+}$ Up-Converting Phosphors for Enhanced Near-Infrared Silicon Solar Cell Response. *Appl. Phys. Lett.* **2005**, 86.

(24) Van Der Ende, B. M.; Aarts, L.; Meijerink, A. Lanthanide Ions as Spectral Converters for Solar Cells. *Phys. Chem. Chem. Phys.* **2009**, 11, 11081-11095.

(25) Wang, H.; Batentschuk, M.; Osvet, A.; Pinna, L.; Brabec, C. J. Rare-Earth Ion Doped Up-Conversion Materials for Photovoltaic Applications. *Adv. Mater.* **2011**, 23, 2675-2680.

(26) Wang, F.; Liu, X. Recent Advances in the Chemistry of Lanthanide-Doped Upconversion Nanocrystals. *Chem. Soc. Rev.* **2009**, 38, 976-989.

(27) Menyuk, N.; Dwight, K.; Pierce, J. W. NaYF4: Yb, Er—an Efficient Upconversion Phosphor. *Appl. Phys. Lett.* **1972**, 21, 159-161.

(28) Krämer, K. W.; Biner, D.; Frei, G.; Güdel, H. U.; Hehlen, M. P.; Lüthi, S. R. Hexagonal Sodium Yttrium Fluoride Based Green and Blue Emitting Upconversion Phosphors. *Chem. Mater.* **2004**, 16, 1244-1251.

(29) Suyver, J. F.; Grimm, J.; van Veen, M. K.; Biner, D.; Krämer, K. W.; Güdel, H. U. Upconversion Spectroscopy and Properties of $NaYF_4$ Doped with Er^{3+}, Tm^{3+} and/or Yb^{3+}. *J. Lumin.* **2006**, 117, 1-12.

(30) Ye, X.; Collins, J. E.; Kang, Y.; Chen, J.; Chen, D. T. N.; Yodh, A. G.; Murray, C. B. Morphologically Controlled Synthesis of Colloidal Upconversion Nanophosphors and their Shape-Directed Self-Assembly. *PNAS* **2010**, 107, 22430-22435.

(31) Boyer, J.; van Veggel, F. C. J. M. Absolute quantum yield measurements of colloidal $NaYF_4$: Er^{3+}, Yb^{3+} upconverting nanoparticles. *Nanoscale* **2010**, 2, 1417-1419.

(32) Greybush, N. J.; Saboktakin, M.; Ye, X.; Della Giovampaola, C.; Oh, S. J.; Berry, N. E.; Engheta, N.; Murray, C. B.; Kagan, C. R. Plasmon-Enhanced Upconversion Luminescence in Single Heterodimers Formed through Nanophosphor-Nanorod Template-Assisted Self-Assembly. *ACS Nano*, **2014**, 8, 9482-9491.

(33) Saboktakin, M.; Ye, X.; Oh, S. J.; Hong, S.; Fafarman, A. T.; Chettiar, U. K.; Engheta, N.; Murray, C. B.; Kagan, C. R. Metal-Enhanced Upconversion Luminescence Tunable through Metal Nanoparticle-Nanophosphor Separation. *ACS Nano*, **2012**, 6, 8758-8766.

(34) Anger, P.; Bharadwaj, P.; Novotny, L. Enhancement and Quenching of Single-Molecule Fluorescence. *Phys. Rev. Lett.* **2006**, 96, 113002.

(35) Winey, K. I.; Thomas, E. L.; Fetters, L. J. Swelling a Lamellar Diblock Copolymer and Homopolymer: Influences of Homopolymer Concentration and Molecular Weight. *Macromolecules* **1992**, 24, 6182-6188.

APPENDIX A: Supporting Information for Chapter 2

A.1 Materials

All chemicals were used as received without further purification. Erbium oxide (Er_2O_3, 99.9%), gadolinium oxide (Gd_2O_3, 99.9%), and ytterbium oxide (Yb_2O_3, 99.9%) were purchased from GFS Chemicals. EMD Millipore Amicon Ultra-15 centrifugal filter units (*MWCO* = 30000d), ethanol (95%, USP, Decon Labs), hydrochloric acid solution (HCl, 0.1N, certified, Fisher Chemical), hydrogen peroxide (H_2O_2, 30%, certified ACS, Fisher Chemical), lithium fluoride (LiF, 99.98%, extra pure, Acros Organics), methanol (≥99.9%, for HPLC), 1-octadecene (ODE, 90%, technical grade, Acros Organics), sodium hydroxide solution (NaOH, 1N, certified, Fisher Chemical), NaOH solution (50% w/w, certified, Fisher Chemical), sulfuric acid (H_2SO_4, certified ACS plus, Fisher Chemical), and trifluoroacetic acid ($C_2HF_3O_2$, 99.5%, for biochemistry, Acros Organics) were purchased from Fisher Scientific. Chloroform (≥99.9%, for HPLC), hexane (≥98.5%, mixture of isomers, for HPLC), oleic acid (OA, 90%, technical grade, Aldrich), and toluene (99.9%, for HPLC) were purchased from Sigma Aldrich. Chitosan ChitoClear® Cg-10 (M_w = 60 kDa, degree of deacetylation = 87%, Primex ehf.) was donated by Colgate-Palmolive Company. Nalgene syringe filters (13 mm) with 0.2 μm polyethersulfone (PES) membranes and polypropylene housing were purchased from Thermo Fisher Scientific. Phosphoric acid functionalized polyethylene glycol (PEG-PO_3H_2, M_n = 5 kg/mol) was purchased from Nanocs Inc. Poly(methyl methacrylate) (PMMA, M_n = 20 kg/mol, PDI = 1.14) and lamellar-forming poly(styrene-*b*-methyl methacrylate) (PS-*b*-PMMA, M_n = 38k-*b*-36.8k g/mol, PDI = 1.08) were purchased from Polymer Source Inc. EpoxiCure 2 epoxy hardener and epoxy resin were both

purchased from Buehler. N-type, <100> oriented silicon wafers (dopant Ph, 10-20 Ω·cm resistivity, 475-575 μm thickness, single side polished) were purchased from Silicon Quest International. P-type, <100> oriented silicon wafers (dopant B, 0.001-0.005 Ω·cm resistivity, 500 μm thickness, single side polished) with a 300 nm wet thermal oxide layer were purchased from University Wafer.

A.2 Methods

A.2.1 Synthesis of GdF_3:Yb/Er (20/2 mol%) Nanoplates. The procedure for preparing the gadolinium trifluoroacetate [$Gd(CF_3COO)_3$], ytterbium trifluoroacetate [$Yb(CF_3COO)_3$], and erbium trifluoroacetate [$Er(CF_3COO)_3$] precursors can be found elsewhere.[1] Gadolinium trifluoride rhombic nanoplates doped with ytterbium and erbium [GdF_3:Yb/Er (20/2 mol%)] were synthesized through rapid thermal decomposition using standard Schlenk line procedures. Briefly, 30 mL of OA and 30 mL of ODE were added to 1.62 mmol of $Gd(CF_3COO)_3$, 8.33 mmol LiF, 0.042 mmol $Yb(CF_3COO)_3$, and 0.0042 mmol $Er(CF_3COO)_3$ in a three-necked flask. Note, this work assumes that the rare-earth precursors are in hexahydrate form. The solvent and precursor mixture was magnetically stirred, heated to 125ºC under vacuum, and degassed for 3 h. The solution was then purged under high N_2 flow for 5 min before ramping to the reaction temperature (maintained at 290ºC) at a rate of ~20ºC/min. The reaction was carried out for 4 h under high N_2 flow and magnetic stirring. Upon reaction completion, the solution was cooled to room temperature. The crystalline GdF_3:Yb/Er nanoplates were purified three times by adding mixtures of hexanes and ethanol and performing centrifugation. No size selective precipitation was performed. GdF_3:Yb/Er nanoplates, stabilized with OA, were dispersed in hexanes and stored in colloidal solutions with a concentration of 20.0 mg/mL.

A.2.2 Ligand Exchange on GdF_3:Yb/Er Nanoplates. A solution phase ligand exchange was performed to displace OA from the GdF_3:Yb/Er particle surfaces and functionalize them with M_n = 5 kg/mol PEG-PO_3H_2. First, 50 mg of the GdF_3:Yb/Er nanoplates were transferred to

chloroform using an antisolvent method. Ethanol was added to 2.5 mL of the OA stabilized GdF_3:Yb/Er nanoparticles in hexanes (20 mg/mL) and centrifuged (1157×g, 2 min). The supernatant was removed and the resulting product was dried. Meanwhile, a polymeric ligand solution was made by dissolving 206 mg of M_n = 5 kg/mol PEG-PO_3H_2 in 1 mL of chloroform at 40ºC with vigorous magnetic stirring. Once dried, the GdF_3:Yb/Er precipitate was redispersed in 5 mL of chloroform (10 mg/mL) by sonication and then added to the ligand solution. The exchange solution was maintained at 40ºC overnight with vigorous magnetic stirring. The following day, the PEG-PO_3H_2 modified nanoplates were recovered from the exchange solution by precipitation with hexanes and centrifugation (4629×g, 5 min). The supernatant was discarded and the precipitate was dried. After completing drying off the organic solvent, the functionalized nanoplates and free molecules were redispersed in 45 mL of deionized water (DI H_2O). The aqueous nanoplate solution was divided into three centrifugal filter units and centrifuged (4942×g, 20 min) to remove the excess ligands. The particles were collected and dried under vacuum. The solid was redispersed in 1.25 mL of toluene at 40ºC (40 mg/mL). Figure A.2 features a representative transmission electron micrograph of the purified PEG-PO_3H_2 functionalized GdF_3:Yb/Er nanoplates drop-casted from toluene. The inset of Figure A.2 shows the chemical structure of the PEG-PO_3H_2.

A.2.3 Thermogravimetric Analysis. Thermogravimetric analysis (TGA) of OA, 5 kg/mol PEG-PO_3H_2, OA stabilized GdF_3:Yb/Er nanoplates, and M_n = 5 kg/mol PEG-PO_3H_2 functionalized GdF_3:Yb/Er nanoplates was performed on a TA Instruments Q600 SDT tool. The temperature range of the experiments was 25ºC to 550ºC at a heating rate of 10ºC/min under an argon flow. The results of these three TGA runs are shown in Figure A.3. The grafting density (σ_{TGA}) of M_n = 5 kg/mol PEG-PO_3H_2 functionalized GdF_3:Yb/Er particles was determined to be 0.62 chains/nm^2 using

$$\sigma_{\mathrm{TGA}} = \frac{\frac{wt\%_{\mathrm{shell}}}{wt\%_{\mathrm{core}}}\rho_{\mathrm{core}} V_{\mathrm{core}} N_{\mathrm{A}}}{MW\ SA_{\mathrm{core}}} \qquad \text{(A.1)}$$

where $wt\%_{shell}$ is the weight loss associated with the ligands (37%, assuming only PEG-PO_3H_2 and no OA), $wt\%_{core}$ is the remaining weight associated with the nanoplates (58%), ρ_{core} is the density of GdF_3:Yb/Er ($7.1x10^{-21}$ g/nm^3), V_{core} is the volume of a single GdF_3:Yb/Er nanoplate (1155 nm^3), N_A is Avagadro's number, MW is the molecular weight of the ligand (5000 g/mol), and SA_{core} is the surface area of a single GdF_3:Yb/Er nanoparticle (1018 nm^2).

A.2.4 Homopolymer Based Sample Preparation. To facilitate lifting of the PMMA based composite films for transmission electron microscopy (TEM) characterization, a sacrificial chitosan layer was first spin-coated onto the silicon substrates. A 0.1 wt% aqueous chitosan solution was made by dissolving the chitosan in 2 mL of 0.1N HCl by sonication. The acidic solution was diluted with 18 mL of DI H_2O. Its pH was adjusted between 4-5 using 0.1N HCl and 1N NaOH before being filtered through 0.2 μm PES syringe filters. Silicon wafers (1 cm^2) were cleaned with methanol and toluene and treated with UV ozone for 30 min. The aqueous chitosan solution was then spin-coated (3000 rpm, 90 s) onto the substrates. To form the composite films, concentrated PEG-PO_3H_2 functionalized GdF_3:Yb/Er nanoplates were added to 1 wt% M_n = 20 kg/mol PMMA solutions in toluene at 40ºC. The volumetric addition of the concentrated nanoplate stock solution was adjusted to form films with final particle volume fractions of either $\phi = 0.040$, $\phi = 0.066$, $\phi = 0.10$, $\phi = 0.14$, or $\phi = 0.20$. The polymer nanocomposite (PNC) solutions were mixed with a rotating magnetic stir bar at 40ºC until the polymer was dissolved (at least a couple of hours). The PNC solution was spin-coated (4000 rpm, 1 min) onto the chitosan layer and after solvent evaporation, film thicknesses were measured using a F3-UV reflectometer (Filmetrics, LS-DT2 light source and SS-5 stage). The PNC films were scored into sections, lifted from the substrates with DI H_2O, and subsequently transferred to carbon coated TEM grids. Characterization of these films was completed with a JEM-1400 TEM with details described further in the Electron Microscopy Characterization section below.

A.2.5 Block Copolymer Based Sample Preparation. Silicon wafers with a 300 nm wet thermal oxide layer were cleaned in piranha (70:30 vol%, H_2SO_4:H_2O_2) at 80ºC for 20 min, rinsed three times with DI H_2O, and dried under N_2 flow. The substrates were subsequently treated with UV ozone for 10 min. To form the block copolymer (BCP) based nanocomposite films, concentrated PEG-PO_3H_2 functionalized GdF_3:Yb/Er nanoplates were added to 7 wt% lamellar-forming M_n = 38k-*b*-36.8k g/mol PS-*b*-PMMA solutions in toluene at 40ºC. The volumetric addition of the concentrated nanoplate stock solution was adjusted to form films with final particle volume fractions of $\phi = 0.0083$, $\phi = 0.017$, $\phi = 0.027$, $\phi = 0.038$, $\phi = 0.050$ and $\phi = 0.064$. The PNC solutions were mixed with a rotating magnetic stir bar at 40ºC until the polymer was dissolved (at least a couple of hours). The PNC solution was spin-coated (2000 rpm, 1 min) onto the 300 nm wet thermal oxide layer. Unless specified (as-cast samples as the exception), after solvent evaporation, the samples were thermally annealed under vacuum at 190ºC for 48 h. Since PMMA preferentially wets silicon substrates in the PS-*b*-PMMA system, lamellae oriented parallel to the substrate were formed. Film thicknesses were measured using a F3-UV reflectometer (Filmetrics, LS-DT2 light source and SS-5 stage). To lift the films from the silicon substrates, the samples were scored and floated on the liquid-air interface of a NaOH solution (80:20 vol%, DI H_2O:50% w/w NaOH solution) heated to 40ºC. By etching the 300 nm wet thermal oxide layer, the films floated on the liquid surface, were transferred to DI H_2O and then onto Teflon®, sputter-coated with a gold (Au) and palladium (Pd) layer, lifted from the Teflon®, and embeded in two-part epoxy. Cross-sections of ~50-70 nm were prepared by ultramicrotomy (Leica Ultracut S Ultramicrotome) with a diamond knife and subsequently transferred to carbon coated TEM grids. The sections of the unannealed (as-cast) samples were imaged with a JEM-1400 TEM with details described in the Electron Microscopy Characterization section below. The sections of the annealed samples were imaged with a JEOL-7500F high resolution scanning electron microscope (JEOL-7500F HRSEM) with details described in the Electron Microscopy Characterization section below.

A.2.6 Electron Microscopy Characterization. TEM characterization was performed with either a JEOL JEM-1400 TEM operated at 120 kV or a JEOL-2100 TEM operated at 80 kV. Scanning transmission electron microscopy (STEM) characterization was performed with a JEOL-7500F HRSEM equipped with a scanning-transmission electron detector and operated at 30 kV in transmission mode.

Tomography, JEM-1400 TEM. The electron tomograph of the homopolymer based PNC film containing nanoplates at a volume fraction of ϕ = 0.040 (Figure 2.2b) was collected using a Model 2040 Dual-Axis Tomography Holder (Fischione Instruments). The -60º to 60º tilt series was captured using SerialEM. The image stacks were processed using Etomo within the IMOD package. This tilt series movie can be found in Supplementary Digital File 1. The tilt axis of the video is the y-axis. To create Figure 2.5, the frames of interest were rotated so that the tilt axis is 60º from the x-axis.

Tomography, JEOL-2100 TEM. The electron tomographs of the BCP based PNC film cross-sections containing nanoplates at volume fractions of ϕ = 0.027 (Figure 2.3b) and ϕ = 0.050 (Figure 2.3b) were collected using a JEOL High Tilt Retainer (EM-21311). The -60º to 60º tilt series was captured using SerialEM. The image stacks were processed using Etomo within the IMOD package. The tilt series movies of the BCP based PNC film cross-sections with nanoplate volume fractions of ϕ = 0.027 and ϕ = 0.050 can be found in Supplementary Digital File 2 and Supplementary Digital File 3, respectively. The tilt axes of the videos are 60º from the x-axis.

A.2.7 Overlap Volume Fraction Calculation. The critical concentration at which the pervaded volume (v_p) of GdF_3:Yb/Er nanoplates start to come into contact was calculated as the overlap volume fraction (ϕ^*). The volume of a single rhombic nanoplate, v_{NC}, can be calculated using

$$v_{NC} = \frac{1}{2} d_1 d_2 t \qquad \text{(A.2)}$$

where d_1 and d_2 are the two diagonals across the plate face and t is the particle thickness. These dimensions were measured from TEM images to be 35 nm, 22 nm, and 3 nm, respectively. The v_p is given by the volume of a sphere

$$v_p = \frac{4}{3}\pi\left(\frac{d_1}{2}\right)^3 \qquad \text{(A.3)}$$

which assumes that a fully rotating nanoplates sweeps out the space of a sphere. The ϕ^*, the ratio of v_{NC} to v_p, is expressed by

$$\phi^* = \frac{v_{NC}}{v_p} = \frac{3d_1t}{\pi d_2^2} \qquad \text{(A.4)}$$

and calculated to be 0.051. A schematic illustrating the two diagonals (d_1 and d_2) and the v_p of a single nanoplate can be visualized in the Figure A.6 and a schematic demonstrating pervaded volumes of multiple nanoplates beginning to overlap at ϕ^* is show in Figure A.7.

A.3 Additional Results

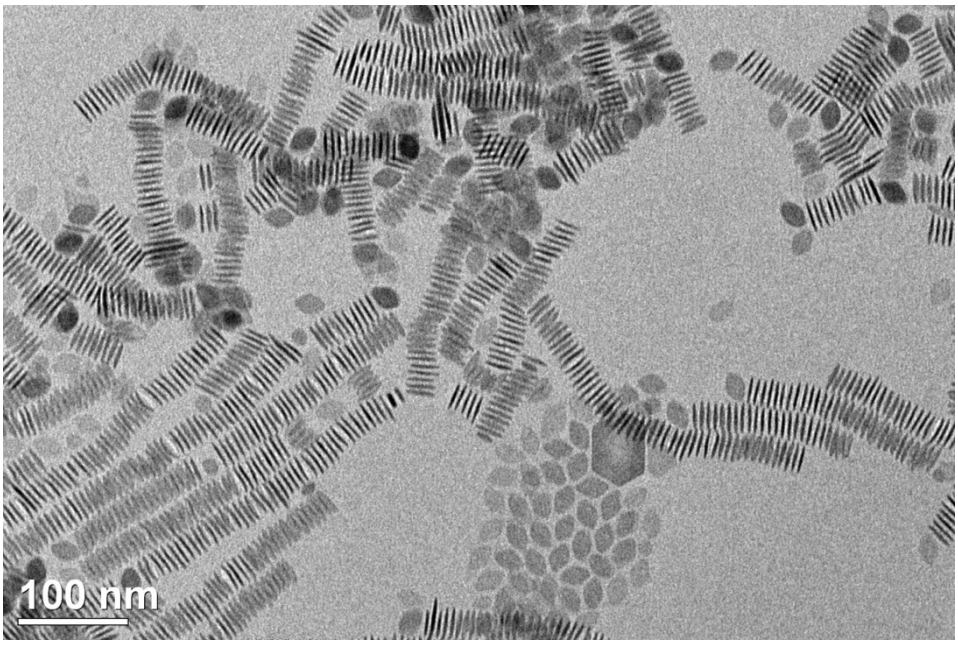

Figure A.1. Representative TEM (JEM-1400, 120 kV) micrograph of OA stabilized GdF_3:Yb/Er (20/2 mol%) nanoplates drop-casted onto a carbon coated TEM grid from hexanes demonstrate nanoplate thickness (3 nm) from particles stacking in rows, edge-on.

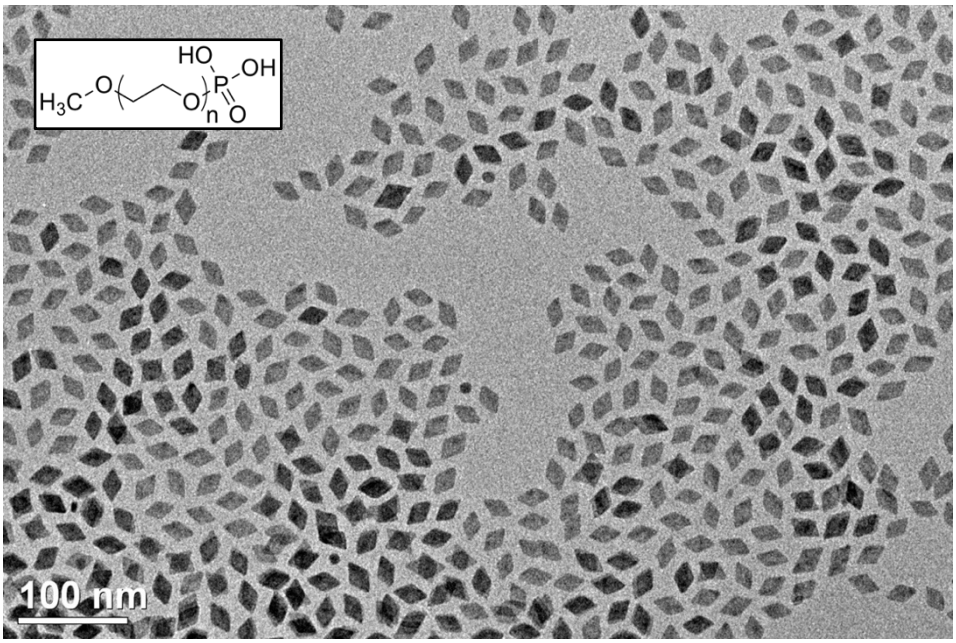

Figure A.2. Representative TEM (JEM-1400, 120 kV) micrograph of purified 5 kg/mol PEG-PO_3H_2 functionalized GdF_3:Yb/Er (20/2 mol%) nanoplates drop-casted onto a carbon coated TEM grid from toluene shows a well-defined nanoplate/ligand system without aggregation. The inset exhibits the chemical structure of the PEG-PO_3H_2 ligand purchased from Nanocs Inc.

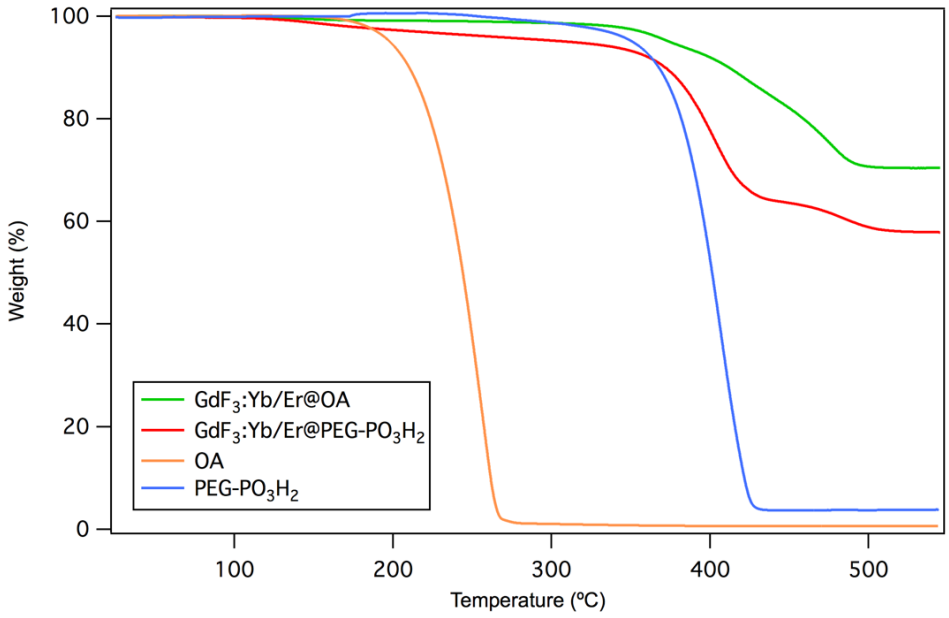

Figure A.3. TGA of OA stabilized GdF_3:Yb/Er (20/2 mol%), 5 kg/mol PEG-PO_3H_2 functionalized GdF_3:Yb/Er (20/2 mol%), OA, and 5 kg/mol PEG-PO_3H_2. The grafting density of 5 kg/mol PEG-PO_3H_2 functionalized GdF_3:Yb/Er (20/2 mol%) was determined to be 0.62 chains/nm^2.

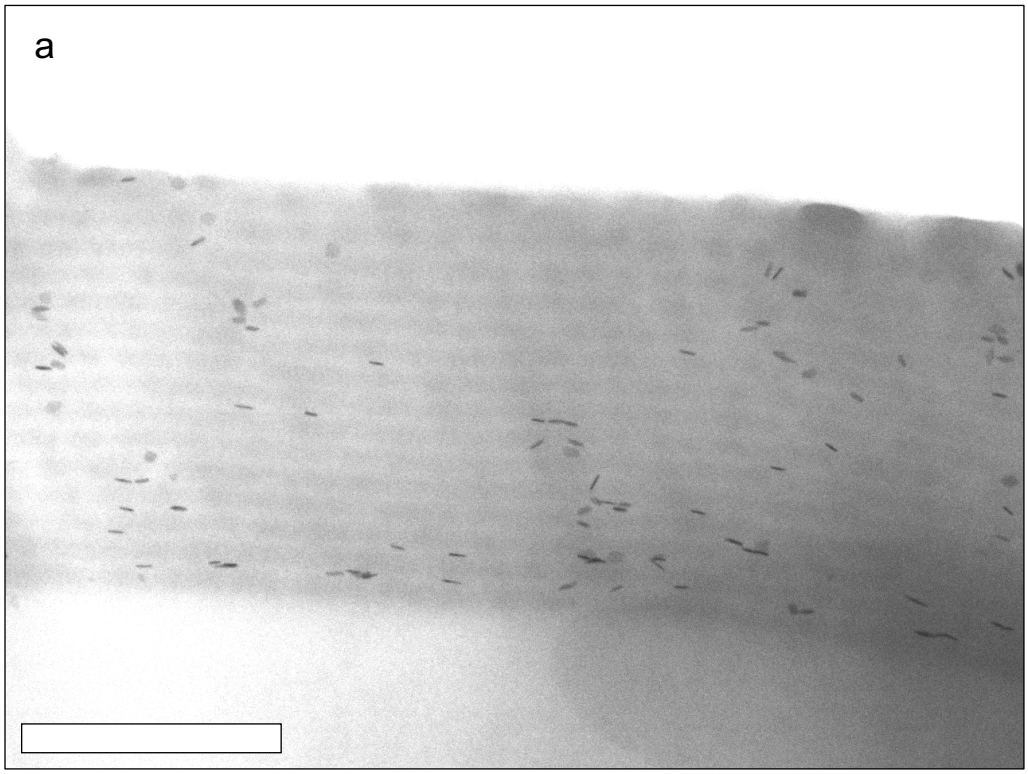

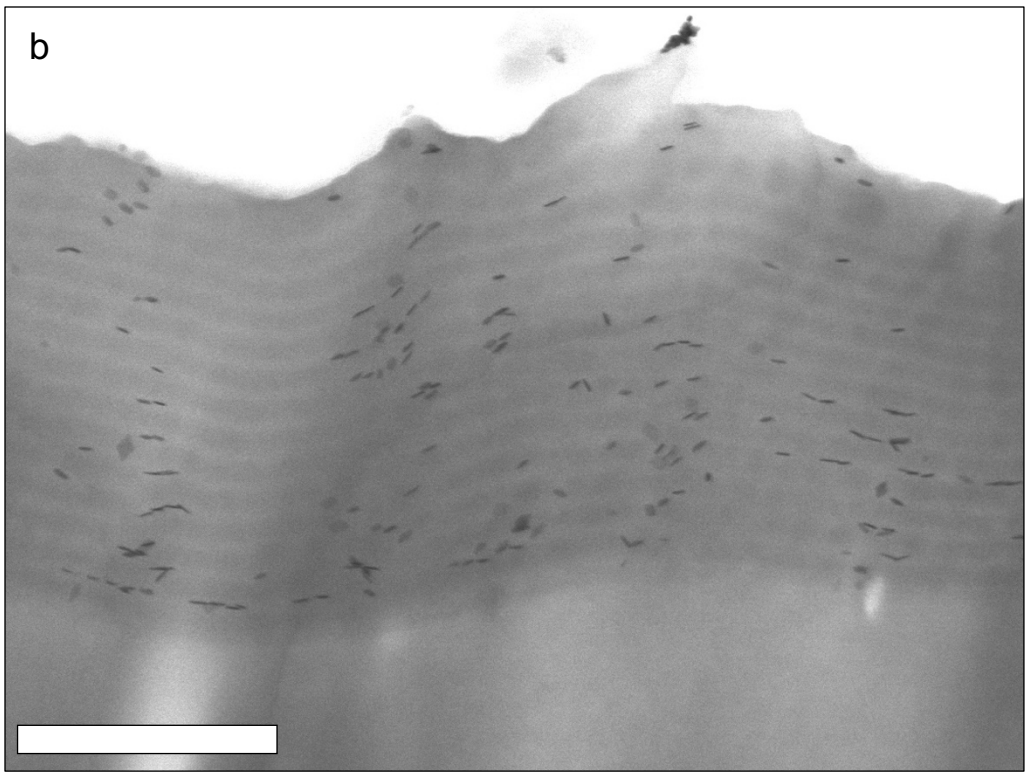
b

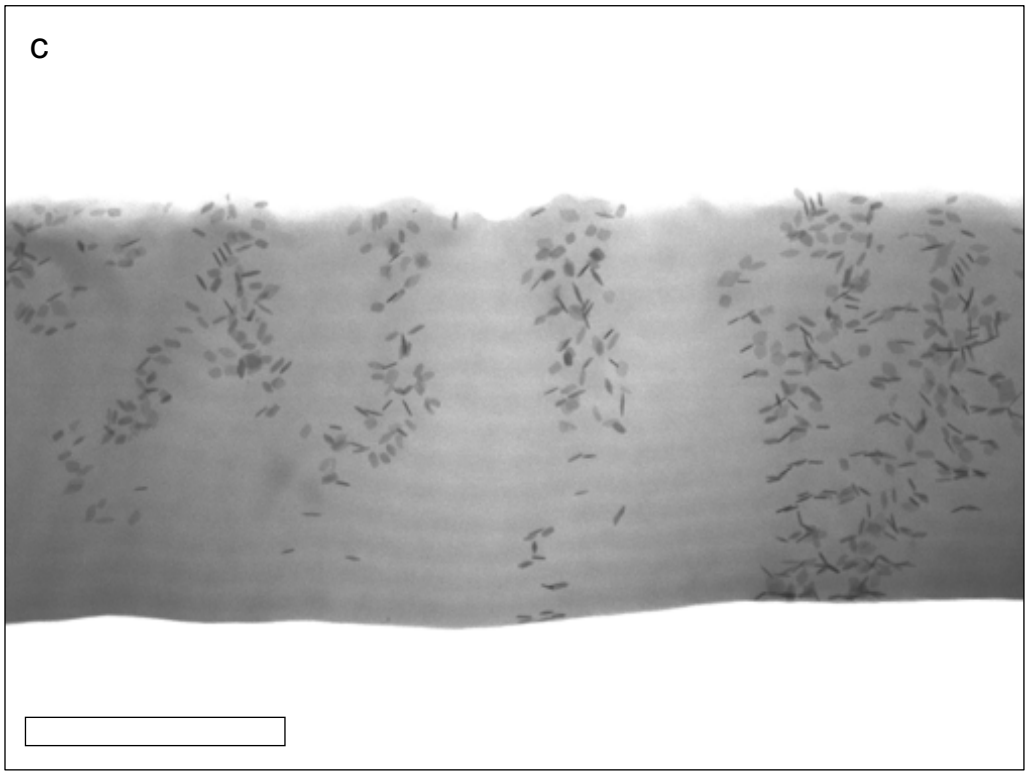
c

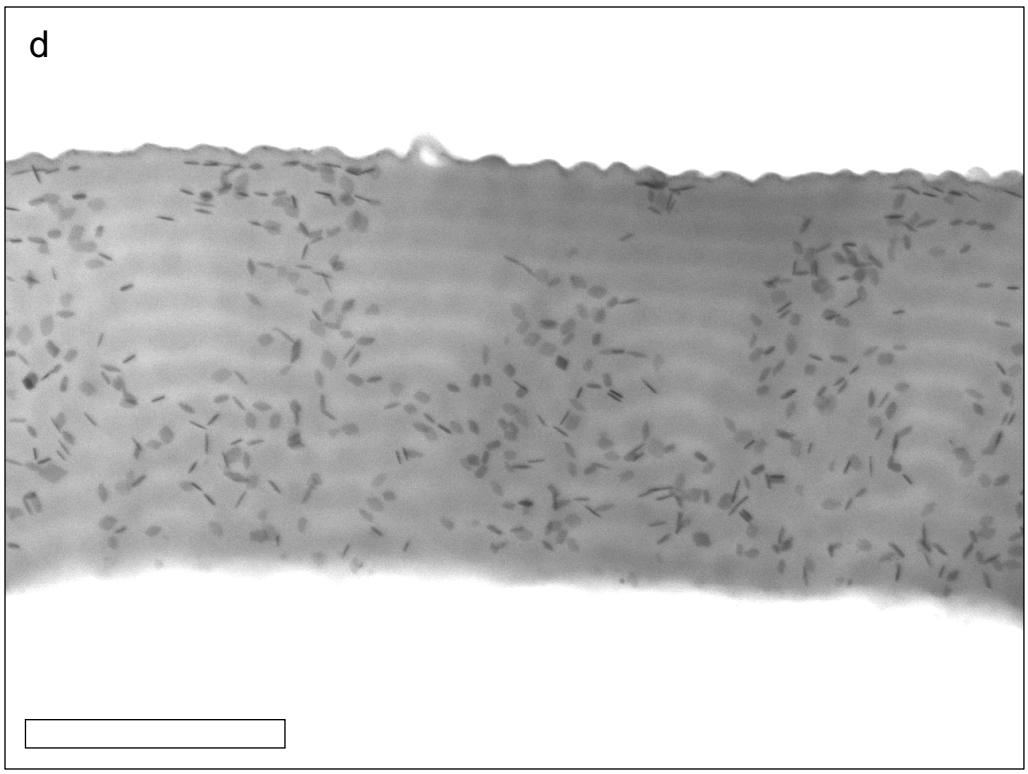
d

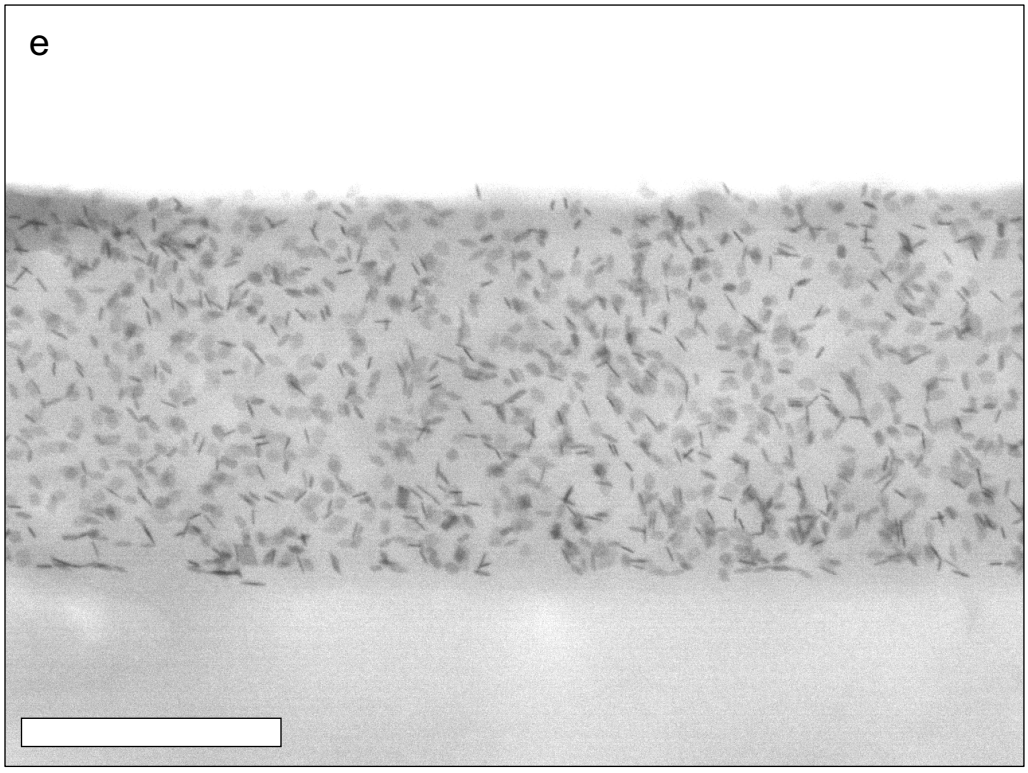
e

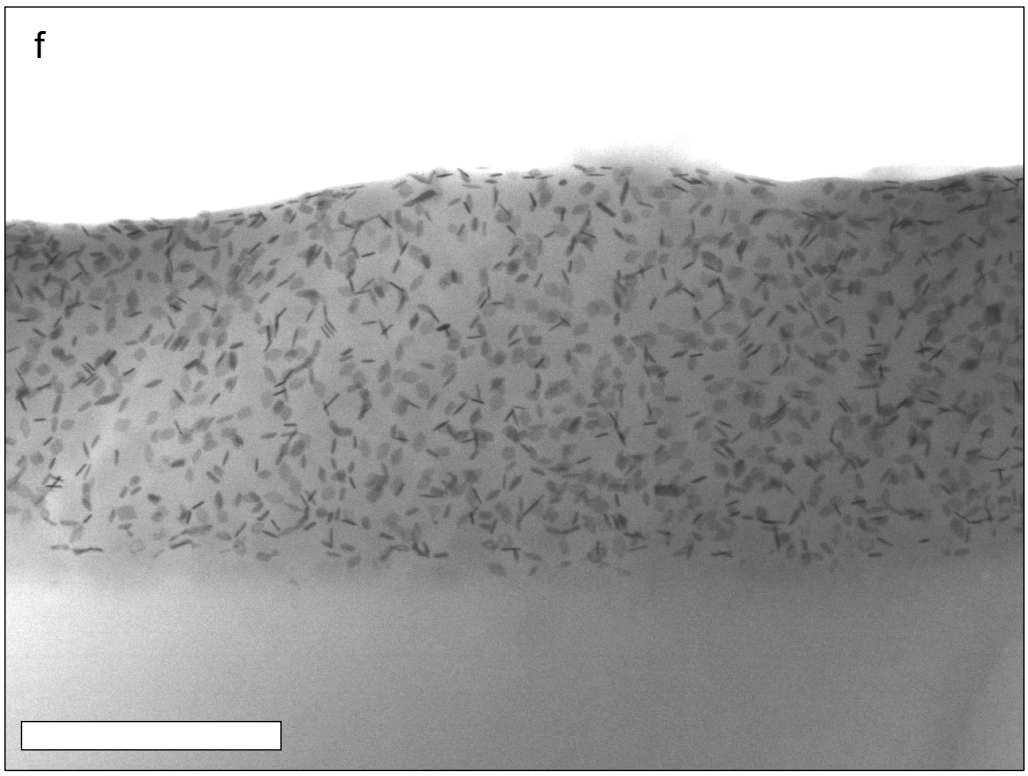

Figure A.4. Larger versions of the representative cross-sectional STEM (JEOL-7500F HRSEM, 30 kV) images from Figure 2.3 of annealed (190ºC, 48 h) and ultramicrotomed lamellar-forming M_n = 38k-*b*-36.8k g/mol PS-*b*-PMMA films (thickness range of ~445-550 nm) with the following volume fractions of 5 kg/mol PEG-PO_3H_2 functionalized GdF_3:Yb/Er (20/2 mol%) nanoplates: (a) ϕ = 0.0083, (b) ϕ = 0.017, (c) ϕ = 0.027, (d) ϕ = 0.038, (e) ϕ = 0.050 and (f) ϕ = 0.064. The light domain is PMMA and the dark domain is PS. All scale bars are 300 nm.

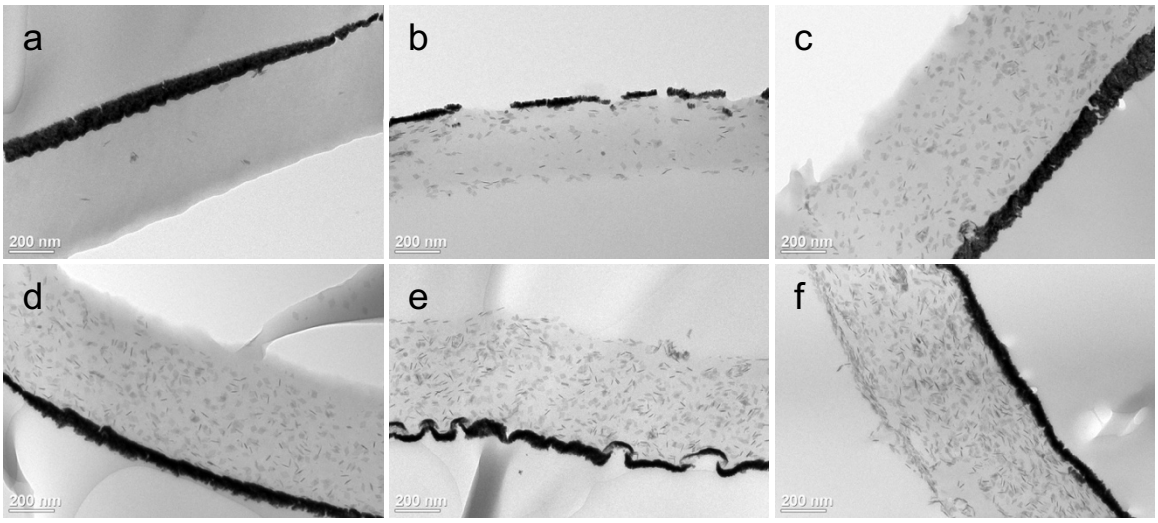

Figure A.5. Representative TEM (JEM-1400, 120 kV) images of as-cast lamellar-forming M_n = 38k-*b*-36.8k g/mol PS-*b*-PMMA films with the following volume fractions of 5 kg/mol PEG-PO_3H_2 functionalized GdF_3:Yb/Er (20/2 mol%) nanoplates: (a) ϕ = 0.0083, (b) ϕ = 0.017, (c) ϕ = 0.027, (d) ϕ = 0.038, (e) ϕ = 0.050 and (f) ϕ = 0.064. Note, the dark feature lining the films is the Au/Pd tracer layer and indicates the top surface of the films. All scale bars are 300 nm.

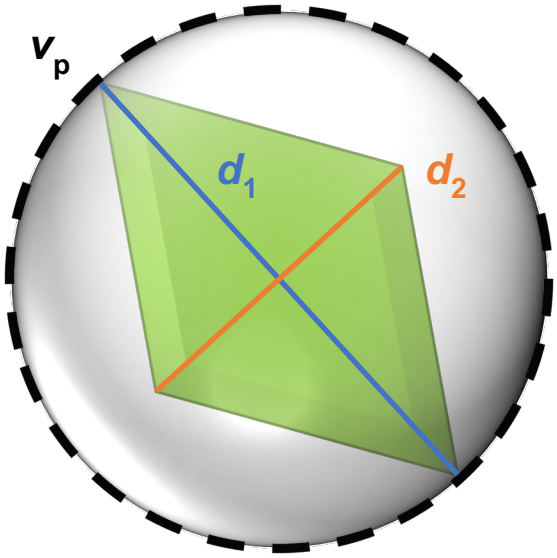

Figure A.6. Schematic of the pervaded volume (v_p) that a single GdF_3:Yb/Er (20/2 mol%) nanoplate occupies. The two diagonals of the nanoplate face are indicated by d_1 and d_2.

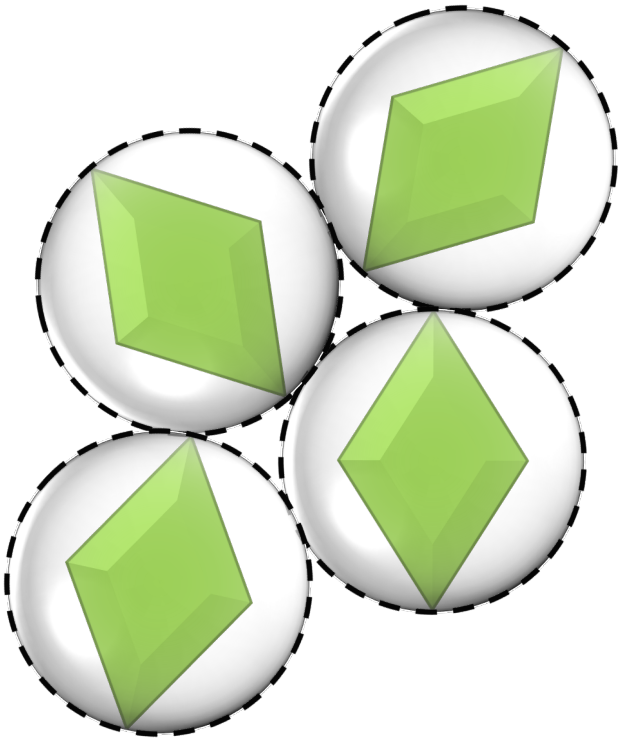

Figure A.7. Schematic of the pervaded volume (v_p) of multiple nanoplates beginning to overlap at ϕ^*.

A.4 References

(1) Najmr, S.; Jishkariani, D.; Elbert, K. C.; Donnio, B.; Murray, C. B. A Semi-Combinatorial Approach for Investigating Polycatenar Ligand-Controlled Synthesis of Rare-Earth Fluoride Nanocrystals. *Nanoscale* **2017**, 9, 8107-8112.

APPENDIX B: Supporting Information for Chapter 3

Content in this appendix was reprinted (adapted) with permission from Nadia M. Krook,* Christian Tabedzki,* Katherine C. Elbert, Kevin G. Yager, Christopher B. Murray, Robert A. Riggleman, and Russell J. Composto. This work has been submitted for publication in a peer-reviewed journal. * N.M.K. (experiments) and C.T. (simulations) contributed equally to this work.

B.1 1S Update Scheme Details.

For the convergence, a 1S update scheme was used. The updates are performed in Fourier space in order to perform convolutions; transformed variables are represented with a caret (ˆ). The update scheme of the compressibility field is

$$\widehat{w}_+^{t+1} = \frac{\widehat{w}_+^t - \lambda_{\text{real}}\left(F - L\widehat{\omega}_+^t\right)}{1+\lambda_{\text{real}}M} \qquad \text{(B.1)}$$

where λ_{real} represents the step size for the real fields and M, L, and F are defined as

$$M = \frac{\rho_0}{\kappa} + \hat{h}^2\phi_{\text{D}}\rho_0 N_{\text{D}}(\hat{g}_{\text{AA}} + 2\hat{g}_{\text{AB}} + \hat{g}_{\text{BB}}) + \phi_{\text{g}}N_{\text{G}}\hat{g}_{\text{G}}\rho_0\hat{h}^2 \qquad \text{(B.2)}$$

$$L = \hat{h}^2\phi_{\text{D}}\rho_0 N_{\text{D}}(\hat{g}_{\text{AA}} + 2\hat{g}_{\text{AB}} + \hat{g}_{\text{BB}}) + \phi_{\text{g}}N_{\text{G}}\hat{g}_{\text{G}}\rho_0\hat{h}^2 \qquad \text{(B.3)}$$

$$F = -i\rho_0\delta(\mathbf{k}) + i\left(\hat{\rho}_{\text{A,c}}\hat{h} + \hat{\rho}_{\text{B,c}}\hat{h} + \hat{\rho}_{\text{G,c}}\hat{h}\right) \qquad \text{(B.4)}$$

where $\hat{h}$ is the Fourier transform of

$$h = \left(\frac{1}{2\pi a^2}\right)^{\frac{d}{2}} \exp\left(-\frac{|\boldsymbol{r}|^2}{2a^2}\right) \qquad \text{(B.5)}$$

and is used to "smear" the microscopic densities of the nanoparticles (NPs) from point densities; d represents the system dimensionality. In the update scheme, $\hat{g}$ is the Fourier transform of the Debye function,[1] N_{D} is the degree of polymerization of the block copolymer (BCP), N_{G} is the degree of polymerization of the grafted polymer brush, $\rho_\alpha = \sum_i^{n_\alpha}\sum_j^{N_\alpha}\delta\left(r - r_{i,j}\right)$, and n_α is the number of chains that contain bead type α. ϕ_{D} equals the volume fraction of the BCP chain and ϕ_{G} equals the

volume fraction of the grafted brush. As these updates are in Fourier space, $\delta(\mathbf{k})$ represents the Dirac delta function in Fourier space.

Depending on the sign of $\chi_{\alpha\beta}$, there are two slightly different gradient schemes for $\widehat{w}_{\alpha\beta}^{(\pm)}$ due to the two different forms of the Hubbard-Stratonovich equation. For a positive χ system, the real field is $w_{\alpha\beta}^{(+)}$ while $w_{\alpha\beta}^{(-)}$ ends up being imaginary. However, when χ is negative, the real field is $w_{\alpha\beta}^{(-)}$ and $w_{\alpha\beta}^{(+)}$ is the imaginary field. If the untransformed field is real, then the scheme is relatively simple

$$\widehat{w}_{\alpha\beta}^{(\pm)}\Big|_{t+1} = \frac{\widehat{w}_{\alpha\beta}^{(\pm)}\Big|_t + \lambda_{\mathrm{real}}\left(\widehat{\rho}_{\alpha,c}\widehat{h} \pm \widehat{\rho}_{\beta,c}\widehat{h}\right)}{1+\lambda_{\mathrm{real}}\frac{2\rho_0}{\chi_{\alpha\beta}}} \qquad \text{(B.6)}$$

If the field is imaginary, the update becomes mildly more complicated

$$\widehat{w}_{\alpha\beta}^{(\pm)}\Big|_{t+1} = \frac{\widehat{w}_{\alpha\beta}^{(\pm)}\Big|_t - \lambda_{\mathrm{imag}}\left(F - L\,\widehat{w}_{\alpha\beta}^{(\pm)}\Big|_t\right)}{1+\lambda_{\mathrm{imag}}M} \qquad \text{(B.7)}$$

where λ_{imag} is the step size for the imaginary field, and where

$$F = +i\left(\widehat{\rho}_{\alpha,c}\widehat{h} \pm \widehat{\rho}_{\beta,c}\widehat{h}\right) \qquad \text{(B.8)}$$

$$M = \frac{2\rho_0}{\chi_{\alpha\beta}} + L \qquad \text{(B.9)}$$

The form of L depends on whether α and β are the same chain or not. If they are on the same chain the form is

$$L = \hat{h}^2\phi_{\mathrm{D}}\rho_0 N_{\mathrm{D}}\left(\hat{g}_{\mathrm{AA}} + \hat{g}_{\mathrm{AB}} \pm \left(\hat{g}_{\mathrm{AB}} + \hat{g}_{\mathrm{AB}}\right)\right) \qquad \text{(B.10)}$$

If α and β reside on separate chains, then the form is

$$L = \hat{h}^2\phi_{\mathrm{D}}N_{\mathrm{D}}(\hat{g}_{\alpha\alpha}) \pm \hat{h}^2\phi_{\mathrm{G}}\rho_0 N_{\mathrm{G}}\hat{g}_{\mathrm{G}} \qquad \text{(B.11)}$$

where g_{G} is the Debye function applied for the grafted homopolymer, g_{AB} is the Debye function applied for the whole BCP, g_{AA} is the Debye function applied for the *A* component of the BCP, and g_{BB} is the Debye function applied for the *B* component of the BCP.

B.2 Additional Results

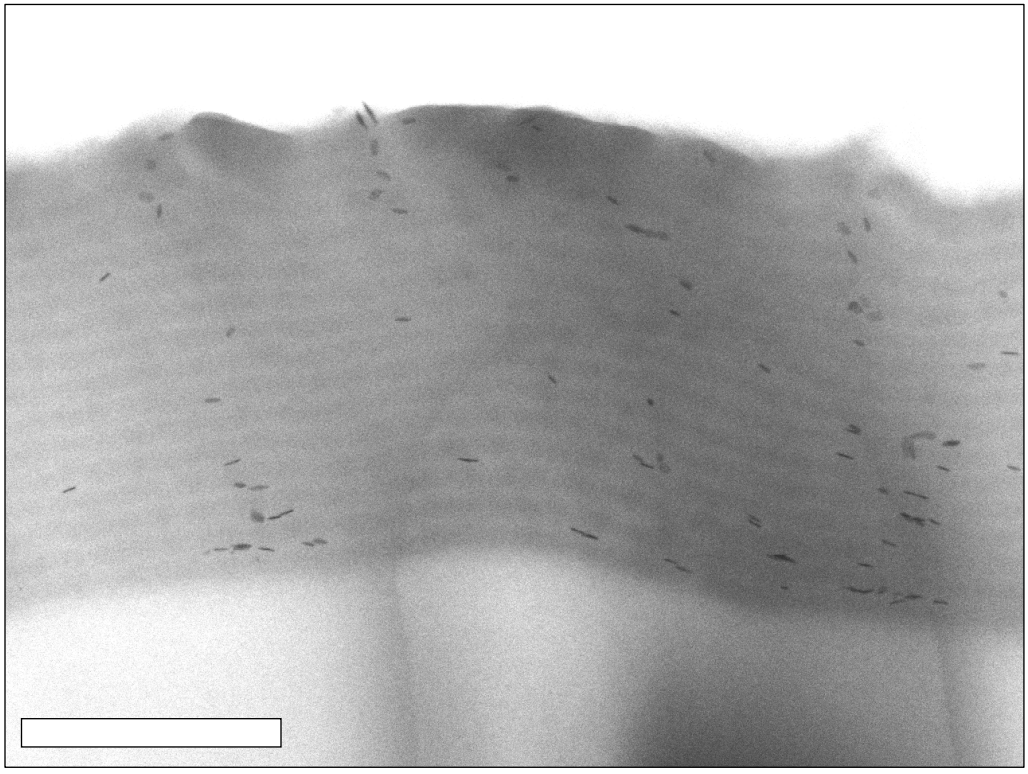

Figure B.1. Representative cross-sectional scanning transmission electron microscopy (STEM, JEOL-7500F HRSEM, 30 kV) image of annealed (190ºC, 48 h) and ultramicrotome lamellar-forming Mn = 38k-b-36.8k g/mol PS-b-PMMA films (thickness ~550 nm) with ϕ = 0.0083 Mn = 5 kg/mol PEG-PO3H2 functionalized GdF3:Yb/Er (20/2 mol%) nanoplates. The light domain is PMMA and the dark domain is PS. The scale bar is 300 nm.

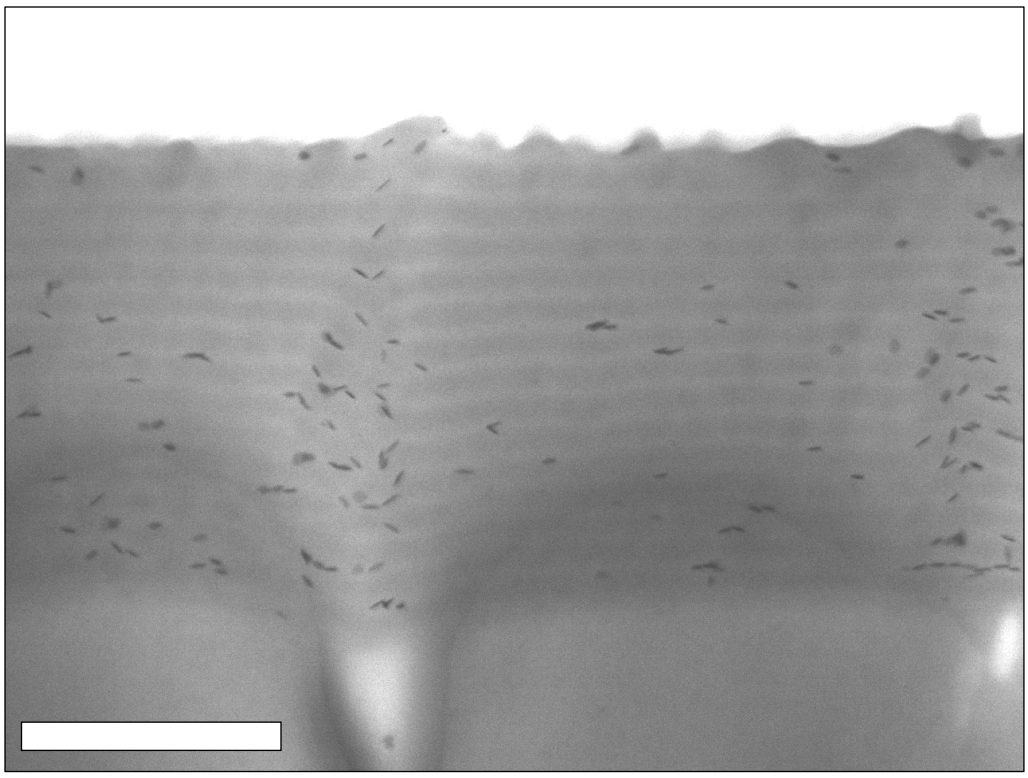

Figure B.2. Representative cross-sectional STEM (JEOL-7500F HRSEM, 30 kV) image of annealed (190ºC, 48 h) and ultramicrotome lamellar-forming M_n = 38k-*b*-36.8k g/mol PS-*b*-PMMA films (thickness ~540 nm) with ϕ = 0.017 M_n = 5 kg/mol PEG-PO_3H_2 functionalized GdF_3:Yb/Er (20/2 mol%) nanoplates. The light domain is PMMA and the dark domain is PS. The scale bar is 300 nm.

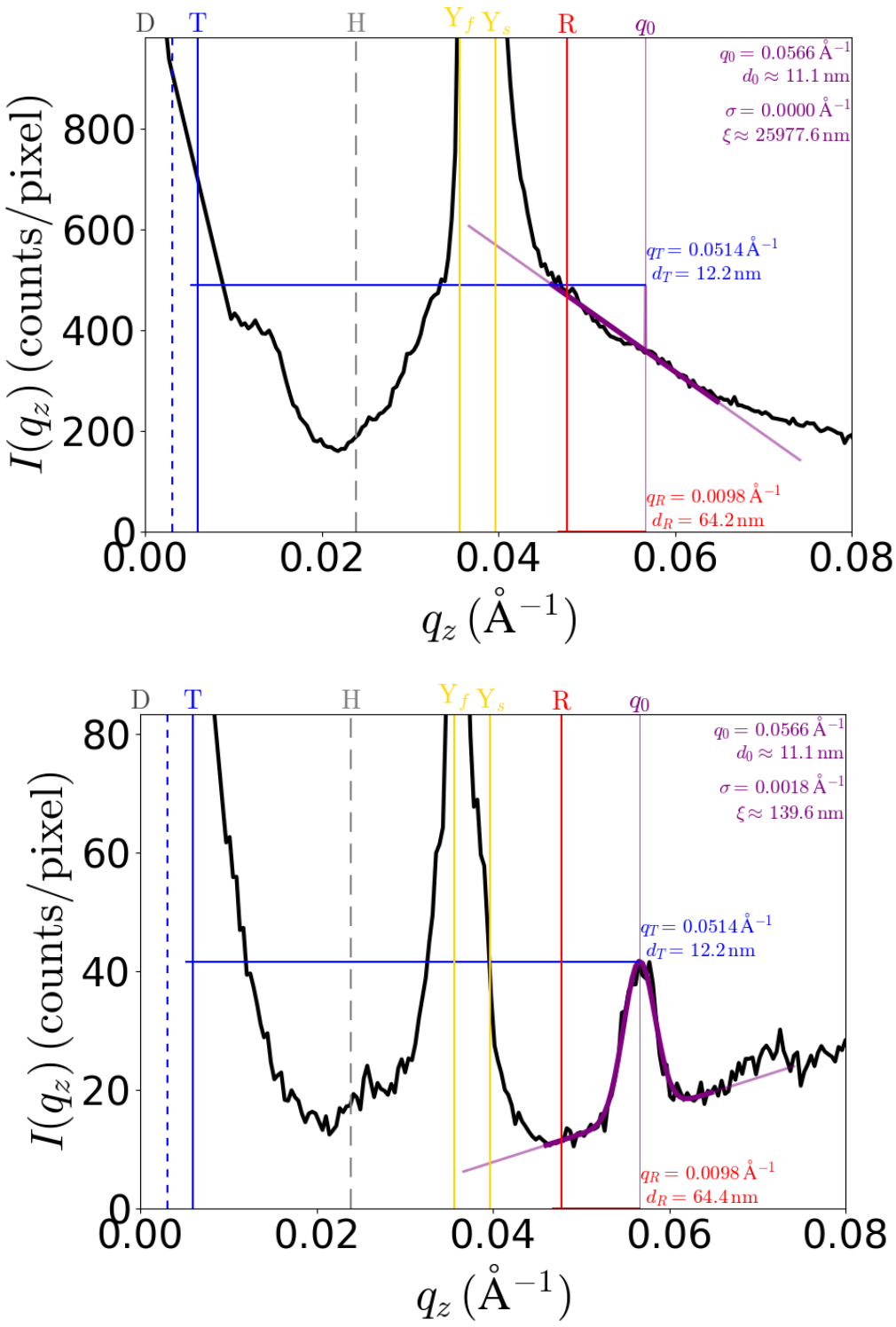

Figure B.3. Examples of typical peak analysis to determine the out-of-plane (q_z direction) repeat-spacing. The extracted scattering intensity (black line) is fit to a Gaussian peak (purple), from which

we extract a nominal peak position (q_0). Based on the known grazing-incident angle and material critical angle, we compute refraction corrections. Various features along q_z are noted: the position of the direct beam (D), the transmitted/refracted beam (T), the sample horizon (H), the Yoneda of the film (Y_f) and substrate (Y_s), and the reflected beam (R). From the nominal peak position, a corrected peak position can be computed by applying a refraction correction; the correction assuming the peak comes from the transmitted (q_T) or reflected beam (q_R) is different. In the present analysis we confirmed that the peaks of interest arose from the direct beam, and thus convert this corrected peak position (q_T) into real-space distance ($d_T = 2\pi/q_T$). The top analysis is representative scattering data for a sample with disordered lamellae (ϕ = 0.050 GdF_3:Yb/Er nanoplates) where the lamellar scattering peak was not observed and the bottom analysis shows a representative peak fit for a sample with ordered lamellae (ϕ = 0 GdF_3:Yb/Er nanoplates).

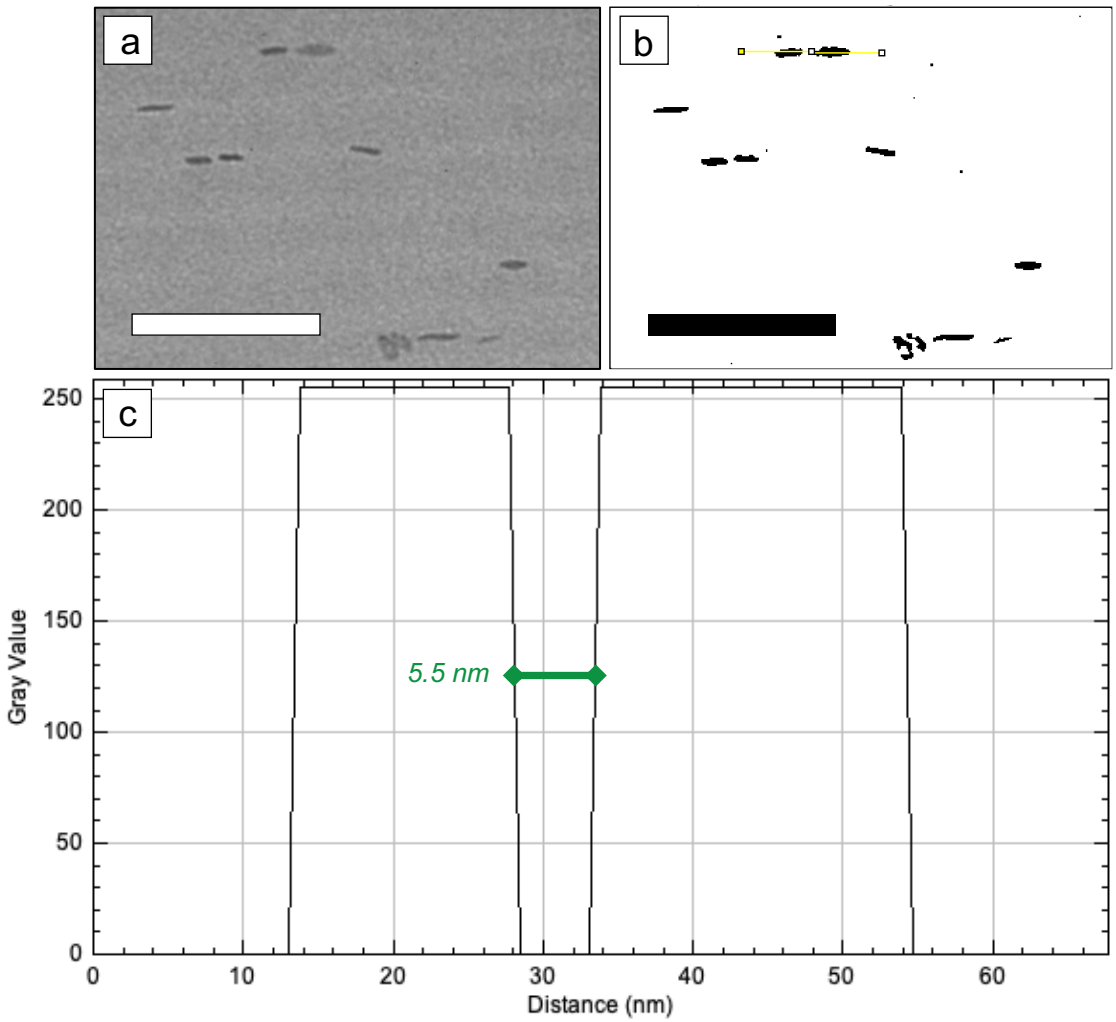

Figure B.4. Characteristic ImageJ (v 1.52a) analysis to determine edge-to-edge separation of aligned nanoplates within assembled strings in PMMA domains of M_n = 38k-*b*-36.8k g/mol PS-*b*-PMMA lamellae. (a) TEM image featuring a region of the BCP nanocomposite film with ϕ = 0.017 NPs that demonstrates nanoplates bridging together. (b) The greyscale TEM image from (a) adjusted to a binary image (NP = 255 and background = 0) by manual thresholding which also includes a straight line selection drawn along one of the nanoplate strings. (c) The line scan from (b) converted to an intensity as a function of distance profile to measure nanoplate edge separation at half the maximum intensity value. The scale bars are 100 nm.

Table B.1. 300 measurements in nm of the edge-to-edge distance between NPs bridging together in strings in a film of $\phi = 0.017$ $M_n = 5$ kg/mol PEG-PO_3H_2 functionalized GdF_3:Yb/Er (20/2 mol%) nanoplates aligned in ordered M_n = 38k-*b*-36.8k g/mol PS-*b*-PMMA lamellae, determined via the process illustrated in Figure B.4.

5.25	*7.80*	*4.53*	*9.61*	*5.14*	*6.02*	*5.09*	*5.25*	*6.02*	*5.81*
5.42	*4.72*	*5.51*	*7.61*	*6.86*	*6.12*	*6.36*	*7.57*	*6.31*	*5.33*
4.65	*8.96*	*7.16*	*7.58*	*4.70*	*6.26*	*5.76*	*5.82*	*6.11*	*5.93*
6.00	*7.64*	*8.35*	*8.49*	*6.78*	*4.09*	*5.95*	*6.12*	*6.33*	*5.71*
6.34	*7.10*	*7.09*	*10.08*	*10.45*	*6.26*	*6.14*	*5.81*	*6.45*	*5.78*
6.79	*5.38*	*7.19*	*5.40*	*10.92*	*4.44*	*5.13*	*8.50*	*6.17*	*5.97*
7.67	*6.11*	*6.68*	*8.63*	*6.52*	*7.04*	*4.91*	*5.54*	*6.13*	*7.60*
6.67	*7.03*	*3.97*	*6.78*	*5.83*	*6.07*	*6.95*	*6.27*	*6.22*	*6.46*
5.40	*8.92*	*4.50*	*6.27*	*8.94*	*6.75*	*4.26*	*5.21*	*6.86*	*6.29*
7.22	*10.10*	*7.89*	*6.19*	*6.46*	*6.36*	*6.17*	*5.98*	*6.23*	*4.63*
7.29	*10.38*	*3.89*	*6.71*	*8.31*	*5.43*	*6.54*	*5.45*	*6.15*	*6.41*
8.06	*8.12*	*3.37*	*6.45*	*8.63*	*7.24*	*6.13*	*5.71*	*8.45*	*5.79*
5.53	*3.89*	*8.36*	*6.58*	*6.04*	*8.32*	*4.58*	*6.07*	*8.24*	*5.18*
7.10	*4.56*	*9.15*	*7.57*	*5.82*	*7.52*	*6.13*	*7.66*	*7.06*	*6.33*
7.77	*4.88*	*7.60*	*4.93*	*4.53*	*6.49*	*6.02*	*5.46*	*5.46*	*6.55*
7.64	*3.86*	*5.22*	*9.50*	*5.26*	*6.03*	*6.35*	*5.80*	*6.44*	*5.15*
8.94	*9.68*	*4.50*	*6.57*	*6.27*	*6.94*	*8.54*	*6.91*	*5.53*	*6.38*
6.45	*6.48*	*11.60*	*7.63*	*7.48*	*9.11*	*5.58*	*5.92*	*6.30*	*4.98*
9.04	*5.11*	*6.43*	*6.24*	*8.93*	*6.55*	*5.62*	*6.05*	*4.23*	*4.17*
4.50	*6.99*	*5.18*	*5.18*	*6.50*	*6.70*	*5.28*	*7.67*	*6.08*	*7.34*
3.89	*10.79*	*5.83*	*5.37*	*5.91*	*7.49*	*5.23*	*6.32*	*6.75*	*4.23*
6.97	*6.55*	*6.10*	*5.41*	*7.05*	*6.04*	*4.71*	*9.07*	*7.16*	*5.55*
3.93	*6.05*	*8.16*	*8.13*	*6.10*	*6.08*	*3.93*	*4.70*	*7.72*	*6.74*
5.57	*6.55*	*7.09*	*6.57*	*6.39*	*6.26*	*6.60*	*5.77*	*8.16*	*7.45*
5.69	*3.85*	*8.27*	*8.20*	*6.84*	*8.12*	*5.18*	*6.04*	*6.08*	*5.02*
9.79	*2.75*	*3.85*	*7.48*	*6.39*	*5.04*	*4.99*	*4.02*	*5.98*	*5.50*
8.49	*5.03*	*7.26*	*5.24*	*6.48*	*8.00*	*6.59*	*6.61*	*6.31*	*6.01*
8.04	*5.23*	*3.98*	*5.78*	*7.94*	*6.51*	*8.58*	*6.03*	*6.45*	*6.38*
4.53	*6.47*	*7.85*	*7.82*	*7.13*	*6.00*	*5.76*	*6.01*	*5.67*	*6.75*
5.30	*3.65*	*8.39*	*4.01*	*6.62*	*5.42*	*4.55*	*5.42*	*6.90*	*6.18*

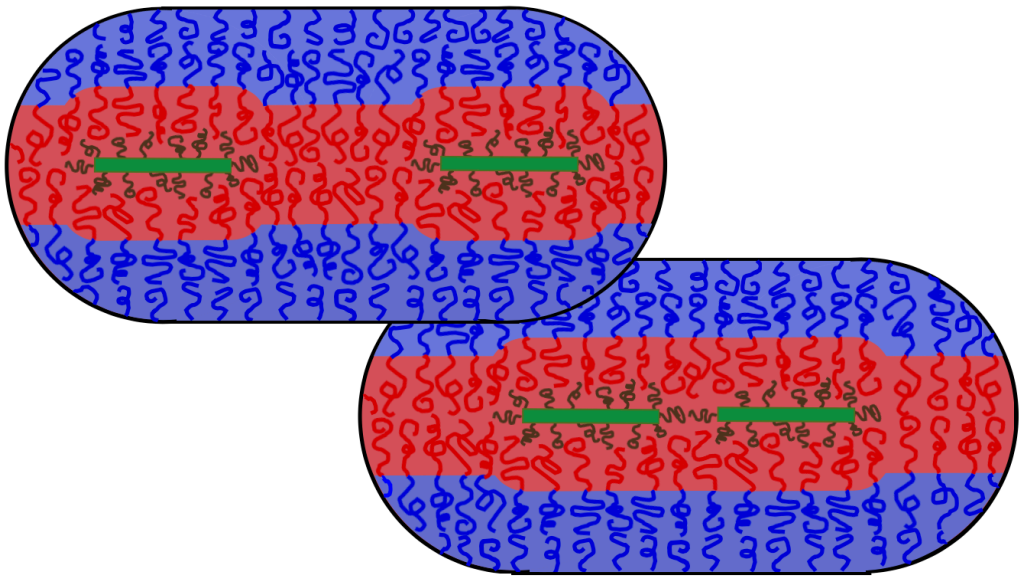

Figure B.5. Illustration of two nanoplates stringing together to reduce the total interfacial area between the PMMA (red) and PS (blue) domains by merging the local bulges created around the NPs.

B.3 References

(1) Fredrickson, G. H. *The Equilibrium Theory of Inhomogeneous Polymers*; Oxford University Press: 2006.

APPENDIX C: Supporting Information for Chapter 4

Content in this appendix was reprinted (adapted) with permission from Nadia M. Krook, Boris Rasin, Jeffrey S. Meth, Christopher B. Murray, Robert A. Riggleman, and Russell J. Composto. This work is in preparation to be submitted for publication in a peer-reviewed journal.

C.1 Materials

The polymers and chemicals purchased for this study were used without further purification. P-type, <100> oriented silicon (Si) wafers with a 300 nm wet thermal oxide layer were received from University Wafer. Sulfuric acid (H_2SO_4, certified ACS plus), hydrogen peroxide (H_2O_2, 30%, certified ACS), and sodium hydroxide solution (NaOH, 50% w/w, certified) were obtained from Fisher Scientific. Tetrahydrofuran (THF, ≥99.0%, contains 250 ppm BHT as inhibitor, ACS reagent) and toluene (99.9%, for HPLC) were purchased from Sigma Aldrich. Hydroxy terminated poly(methyl methacrylate) (PMMA-OH, M_n = 6.5 kg/mol, PDI = 1.18), hydroxy terminated polystyrene (PS-OH, M_n = 6 kg/mol, PDI = 1.05), and the following poly(styrene-*b*-methyl methacrylate) (PS-*b*-PMMA) block copolymers (BCPs) were purchased from Polymer Source Inc.: M_n = 5k-*b*-5k g/mol (PDI = 1.18), M_n = 73k-*b*-73k g/mol (PDI = 1.2), and M_n = 95k-*b*-95k g/mol (PDI = 1.18). Phosphoric acid functionalized polyethylene glycol (PEG-PO_3H_2, M_n = 5 kg/mol) was received from Nanocs Inc.

C.2 Methods

C.2.1 Neutral Layer Preparation for Vertical Block Copolymer Nanocomposite. To prepare films with vertically oriented PS-*b*-PMMA lamellae, a polymer brush layer, neutral to the PS and PMMA microdomains, was grafted to the surface of Si substrates. The process to create the neutralization layer was adapted from the procedure established by Ji *et al*. using a ternary polymer solution composition the authors denoted as "556."[1] Briefly, the number designation corresponds

to a 1 wt% polymer blend composed of 40 wt% hydroxy terminated polymers (M_n = 6.5 kg/mol PMMA-OH and M_n = 6 kg/mol PS-OH PS-OH) at a 5:5 weight ratio and 60 wt% M_n = 5k-*b*-5k g/mol PS-*b*-PMMA dissolved in toluene while magnetically stirred. Concurrently, Si wafers with a 300 nm thermal oxide layer were cut to 1 cm^2 and piranha cleaned (70:30 vol%, H_2SO_4:H_2O_2) at 80ºC for 20 min. After piranha treatment, the substrates were rinsed three times with DI H_2O, stored overnight in DI H_2O, and dried under N_2 flow. The ternary blend solution was spin-coated onto the cleaned substrates (4000 rpm, 1 min) and, after solvent evaporation, annealed under vacuum at 160ºC for 48 h. After thermal annealing, the M_n = 5k-*b*-5k g/mol PS-*b*-PMMA (an emulsifying agent for PMMA-OH and PS-OH) and any unbound hydroxy terminated homopolymer was removed by submerging the samples into 60ºC toluene and sonicating for 15 min.

C.2.2 Vertical Block Copolymer Nanocomposite Preparation. To create the thin film BCP nanocomposites with vertically oriented lamellar microdomains, gadolinium trifluoride rhombic nanoplates doped with ytterbium and erbium [GdF_3:Yb/Er (20/2 mol%)] and either stabilized with oleic acid (OA) or functionalized with M_n = 5 kg/mol PEG-PO_3H_2 were added to 4 wt% solutions of M_n = 73k-*b*-73k g/mol and M_n = 95k-*b*-95k g/mol PS-*b*-PMMA in toluene. The synthesis of GdF_3:Yb/Er nanoplates stabilized with OA and the PEG-PO_3H_2 surface functionalization were previously established and described elsewhere[2] and in Appendix A. Concentrated nanoplate stock solutions were added volumetrically to the BCP solutions to form nanocomposites with ϕ = 0.0083 nanoparticles (NPs). Neat BCP films (ϕ = 0) were also produced. The solutions were stirred at 40ºC with a rotating magnetic stir bar for at least a couple of hours. Once all of the constituents were dispersed, the solutions were spin-coated (4000 rpm, 1 min) onto the Si wafers grafted with the neutralization layer. A glass jar solvent annealing chamber (schematic with dimensions shown in Figure C.1) was prepared and filled with 35 mL THF. To form the BCP lamellae, the samples were placed on a platform (also shown in the schematic with dimensions in Figure C.1), sealed in the chamber, and solvent annealed for either 20 min or 40 min. After drying

and unless specified (as-solvent annealed films in Figure C.2 as the exception), the samples were thermally annealed under vacuum at 190ºC or 220ºC for 24 h. The BCP nanocomposite thin films were then prepared for characterization with details described in the subsequent section (Microscopy Characterization). Film thicknesses were determined using a F3-UV reflectometer (Filmetrics, LS-DT2 light source and SS-5 stage).

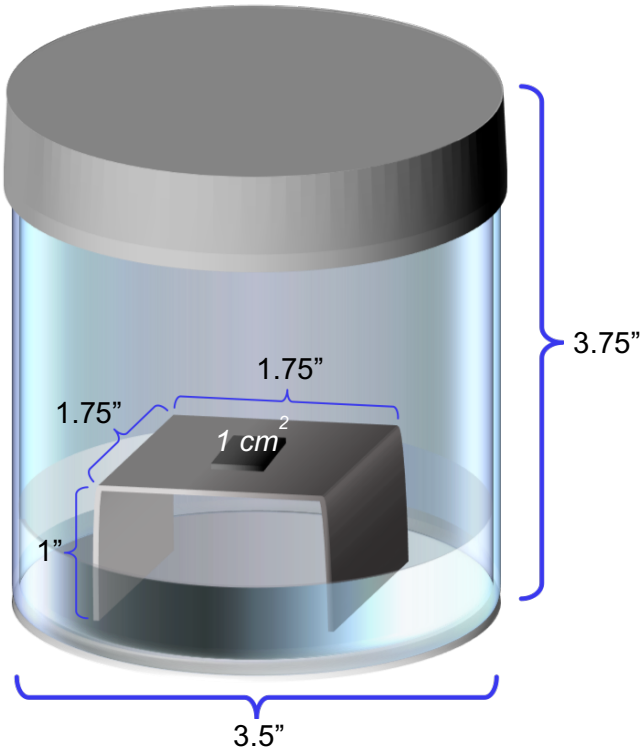

Figure C.1. Illustration of the sealable glass jar (diameter = 3.5 in and height = 3.75 nm) used as a solvent annealing chamber in which 1 cm^2 samples were positioned on a stage (length = 1.75 in, width = 1.75 in, height = 1 in) submerged in 35 mL of THF for 20 min.

C.2.3 Microscopy Characterization. The details for microscopy characterization and the relevant sample preparation steps taken are as follows:

Transmission Electron Microscopy (TEM). Approximately 2 mm^2 sections were cut from the 1 cm^2 samples and floated on top of NaOH solutions (80:20 vol%, DI H_2O:50% w/w NaOH solution) heated to 40ºC. Once the films delaminated from the Si wafers, the films were first rinsed

at the surface of a DI H_2O bath before placing them onto carbon coated grids. Top-down TEM images were captured with either a JEOL JEM-1400 TEM operated at 120 kV or a JEOL JEM-2100 TEM operated at 80 kV.

Atomic Force Microscopy (AFM). AFM characterization was performed on the as-prepared samples, without further preparation, with a Bruker Dimension Icon instrument in tapping mode.

C.3 Additional Results

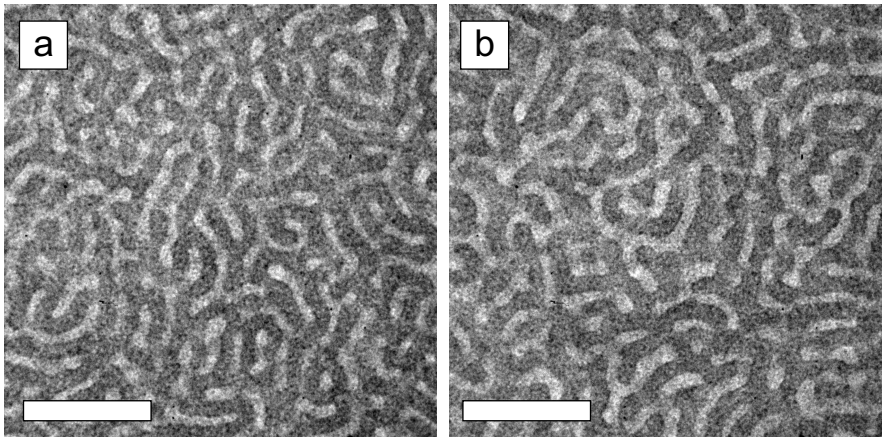

Figure C.2. Representative top-down TEM (JEM-2100, 80 kV) images of (a) M_n = 73k-*b*-73k g/mol and (b) M_n = 95k-*b*-95k g/mol PS-*b*-PMMA films [thicknesses of (a) ~160 nm and (b) ~180 nm] after only thermal annealing (190ºC, 24 h). The light and dark microdomains are PMMA and PS, respectively. The scale bars are 300 nm.

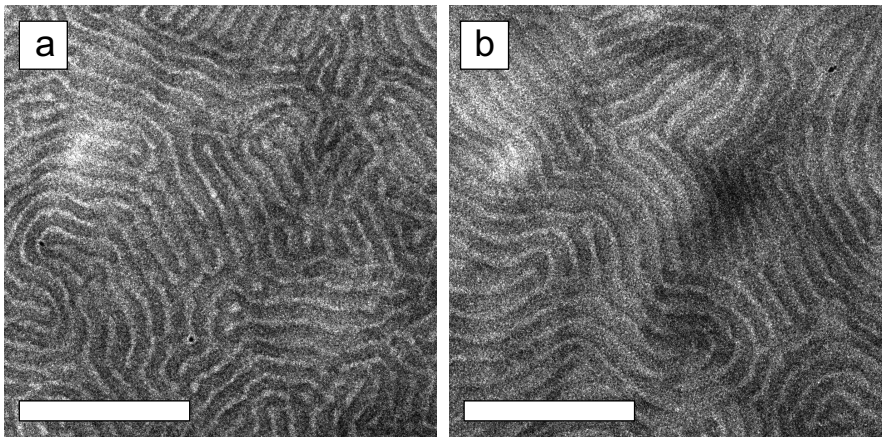

Figure C.3. Representative top-down TEM (JEM-1400, 120 kV) images of (a) M_n = 73k-*b*-73k g/mol and (b) M_n = 95k-*b*-95k g/mol PS-*b*-PMMA films [thicknesses of (a) ~160 nm and (b) ~180 nm] after solvent annealing (20 min in THF) with lamellae oriented perpendicular to the substrate. The light and dark microdomains are PMMA and PS, respectively. The scale bars are 300 nm.

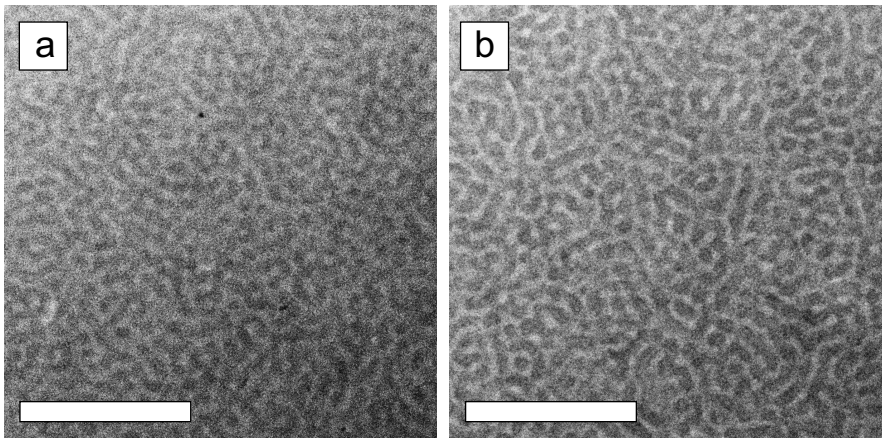

Figure C.4. Representative top-down TEM (JEM-1400, 120 kV) images of (a) M_n = 73k-*b*-73k g/mol and (b) M_n = 95k-*b*-95k g/mol PS-*b*-PMMA films [thicknesses of (a) ~160 nm and (b) ~180 nm] after solvent annealing (40 min in THF). The light and dark microdomains are PMMA and PS, respectively. The scale bars are 300 nm.

C.4 References

(1) Ji, S.; Liu, G.; Zheng, F.; Craig, G. S. W.; Himpsel, F. J.; Nealey, P. F. Preparation of Neutral Wetting Brushes for Block Copolymer Films from Homopolymer Blends. *Adv. Mater.* **2008**, *20*, 3054-3060.

(2) Krook N. M.; Ford, J.; Maréchal, M.; Rannou, P.; Meth, J. S.; Murray, C. B.; Composto R. J. Alignment of Nanoplates in Lamellar Diblock Copolymer Domains and the Effect of Particle Volume Fraction on Phase Behavior. *ACS Macro Lett.* **2018**, 7, 1400–1407.

APPENDIX D: Supporting Information for Chapter 5

* J.P.K. (simulations) and N.M.K. (experiments) contributed equally to this work.

D.1 Polymer Nanocomposite Field Theory

In the PNC-FT calculations, the grafted chains are evenly distributed on the surface of the NP following the uniform distribution in Equation 5.6 in the main text. Hubbard-Stratonovich transformations are used to decouple the intermolecular interactions and transform the relevant degrees of freedom from particle coordinates to chemical potential fields.[1,2] The result of the particle-to-field transformation is the field-theoretic partition function,

$$\mathcal{Z} = z_1 \int \mathfrak{D}w_+ + \int \mathfrak{D}w_{\mathrm{GM}}^{(\pm)} e^{-\mathcal{H}[\{w\}]} \qquad \text{(D.1)}$$

where z_1 contains the numerical prefactors such as the thermal de Broglie wavelengths and the normalization constants from the Gaussian functional integrals used to de-couple the particle interactions, $\mathcal{H}[\{w\}]$ is the effective Hamiltonian of the system, and $\{w\} = \left\{w_+, w_{\mathrm{GM}}^{(+)}, w_{\mathrm{GM}}^{(-)}\right\}$is the set of chemical potential fields for our system. The effective Hamiltonian is given by

$$\begin{aligned}\mathcal{H}[\{w\}] = \frac{\rho_0}{2\kappa}\int \mathrm{d}\mathbf{r}\, w_+(\mathbf{r})^2 - i\rho_0 \int \mathrm{d}\mathbf{r}\, w_+(\mathbf{r}) \\ + \frac{\rho_0}{\chi_{\mathrm{GM}}}\int \mathrm{d}\mathbf{r}\, w_{\mathrm{GM}}^{(+)}(\mathbf{r})^2 + \frac{\rho_0}{\chi_{\mathrm{GM}}}\int \mathrm{d}\mathbf{r}\, w_{\mathrm{GM}}^{(-)}(\mathbf{r})^2 \\ - n_{\mathrm{P}}\ln Q_{\mathrm{P}}[\mu_{\mathrm{P}}] - n_{\mathrm{M}}\ln Q_{\mathrm{M}}[\mu_{\mathrm{M}}], \qquad \text{(D.2)}\end{aligned}$$

where Q_{P} and Q_{M} are the partition functions of a single grafted nanoparticle and matrix polymer chain, respectively.

To speed up equilibration and for easier analysis, we initialize the $w_{\mathrm{GM}}^{(-)}$ field by a hyperbolic tangent function of the form $w_{\mathrm{GM}}^{(-)} = \frac{1}{2}\tanh\left(\cos(2\pi \mathbf{z}/L_z)\right)$ where L_z is the length of the box in the z-direction. The mean-field (self-consistent field theory) solution for the fields appearing in the partition function and corresponding Hamiltonian (*e.g.* Equation D.1 and Equation D.2) is found by a continuous steepest descent scheme,

$$\left(\frac{\partial w(\mathbf{r})}{\partial t}\right) = -\lambda\left(\frac{\partial \mathcal{H}}{\partial w(\mathbf{r})}\right) \qquad \text{(D.3)}$$

where t is a fictious time and λ is the step size of the field evolution. A discretized form of Equation D.3 is then used to evolve the fields according to a first-order semi-implicit operator splitting technique.[3]

D.2 Theoretically-Informed Langevin Dynamics

The fluctuating model is developed by writing an overdamped Langevin equation of motion for the monomers, neglecting hydrodynamic interactions:

$$\frac{d\mathbf{r}_{k,s}}{dt} = D\beta\left(\mathbf{f}_{k,s}^{\mathrm{b}}(t) + \mathbf{f}_{k,s}^{\mathrm{nb}}(t)\right) + \Theta_{k,s}(t). \qquad \text{(D.4)}$$

Here, $\mathbf{r}_{k,s}$ is the position of monomer s on the k^{th} chain, D is the monomeric diffusion coefficient, $\mathbf{f}_{k,s}^{\mathrm{b}}$ is the bonded force, $\mathbf{f}_{k,s}^{\mathrm{nb}}$ is the nonbonded force, and $\Theta_{k,s}(t)$ is Gaussian white noise that satisfies

$$\langle\Theta_{k,s}(t)\rangle = 0 \qquad \text{(D.5)}$$

$$\langle\Theta_{k,s}(t)\Theta_{k',s'}(t')\rangle = 2D\beta\delta_{k,k'}\delta_{s,s'}\delta_{t,t'}. \qquad \text{(D.6)}$$

We use discrete Gaussian chains with $\mathbf{f}_{k,s}^{\mathrm{b}} = (-3/b^2)\left[\left(\mathbf{r}_{k,s} - \mathbf{r}_{k,s-1}\right) + \left(\mathbf{r}_{k,s} - \mathbf{r}_{k,s+1}\right)\right]$, where the first term is neglected for the first segment, the second term is neglected for the last segment, and the t dependence on $\mathbf{r}$ is suppressed for clarity. We place a phantom grafting site at $R_{\mathrm{P}} + \xi$ and the first segment interacts with the grafting site using a Gaussian bonding potential. The grafting site spatial distribution is given by Equation 5.7 in Chapter 5.

The nonbonded force has the general form $\mathbf{f}_{k,s}^{\mathrm{nb}} = -\int d\mathbf{r}'\nabla u\big(\mathbf{r}_{k,s}(t) - \mathbf{r}'\big)\rho(\mathbf{r}', t)$ where $\rho(\mathbf{r}, t)$ is a continuous density field that is interpolated onto a grid from the particle positions using a fourth-order particle-to-mesh technique.[4-6] In the implementation of the theory, the trajectories of all the monomers and solvents are followed explicitly, with the bonded forces calculated directly from the molecular configurations. The non-bonded forces $\mathbf{f}^{(\mathrm{nb})}(\mathbf{r}, t)$ are given as the convolution between the gradient of the non-bonded potential $-\nabla u(\mathbf{r})$ and the density field $\rho(\mathbf{r}, t)$ with the form

$$\mathbf{f}^{(\mathrm{nb})}(\mathbf{r}, t) = -\int d\mathbf{r}'\nabla u(\mathbf{r} - \mathbf{r}')\rho(\mathbf{r}', t). \qquad \text{(D.7)}$$

Previous works[7-9] show that u is a convolution between the density functions that describe each component (h for the polymers and Γ for the nanoparticles). For example,[9] the TILD non-bonded potential arising from the Helfand compressibility potential defined in Equation 5.5 between a polymer and nanoparticle is given by $u(\mathbf{r} - \mathbf{r}') = \frac{\kappa}{2\rho_0}\int d\mathbf{r}''h(\mathbf{r}'' - \mathbf{r})\Gamma(\mathbf{r}'' - \mathbf{r})$. Finally, the $\mathbf{f}^{(\mathrm{nb})}(\mathbf{r}, t)$ are mapped from the values on the mesh-grid to the chain segment (k,s) by using the particle-mesh technique again, which gives the non-bonded forces $\mathbf{f}_{k,s}^{\mathrm{nb}}(t)$ on that segment.

To evolve Equation D.3 we use the numerical GJF discretization.[10] Previous work[11] has shown this scheme leads to stable trajectories and accurate thermodynamic properties with much larger timesteps than an Euler-Maruyama discretization. For a given polymer segments (k,s), its position is updated as

$$\mathbf{r}_{k,s}(t_{\mathrm{n}}) = 2b_t\mathbf{r}_{k,s}(t_{\mathrm{n}-1}) - a_{\mathrm{t}}\mathbf{r}_{k,s}(t_{\mathrm{n}-2}) + b_{\mathrm{t}}\delta t^2\left[\mathbf{f}_{k,s}^{(\mathrm{b})}(t_{\mathrm{n}-1}) + \mathbf{f}_{k,s}^{(\mathrm{nb})}(t_{\mathrm{n}-1})\right]$$
$$+\frac{b_{\mathrm{t}}\delta t}{2}\left[\theta_{k,s}(t_{\mathrm{n}}) + \theta_{k,s}(t_{\mathrm{n}-1})\right], \qquad \text{(D.8)}$$

where δt is the time step, and the superscripts (b) and (nb) refer to the bonded and non-bonded forces, respectively. Here a_{t} and b_{t} are two integration parameters defined by

$$a_{\mathrm{t}} = \frac{1 - \frac{\delta t}{2D\beta m_{k,s}}}{1 + \frac{\delta t}{2D\beta m_{k,s}}}, \qquad \text{(D.9)}$$

$$b_{\mathrm{t}} = \frac{1}{m_{k,s} + \frac{\delta t}{2D\beta}}, \qquad \text{(D.10)}$$

where $m_{k,s}$ is the mass of segment (k,s). The mass and diffusion coefficients of both the polymers and solvent are set to 1. The Gaussian random variable $\theta_{k,s}(t_{\mathrm{n}})$ used in the above equations has the statistics

$$\langle \theta_{k,s}(t_n) \rangle = 0, \qquad \text{(D.11)}$$

$$\langle \theta_{k,s}(t_n) \theta_{k',s'}(t_{n'}) \rangle = \frac{2\delta t}{D\beta} \delta_{n,n'} \delta_{k,k'} \delta_{s,s'}. \qquad \text{(D.12)}$$

D.3 Mean-Field Flory−Huggins Derivation

Here we derive the free energy for a grafted-nanoparticle/homopolymer blend from the polymer nanocomposite field theory (PNC-FT) under the homogeneous mean-field (HMF) approximation. We begin from the partition function in Equation D.1:

$$\mathcal{Z} = z_1 \int \mathfrak{D} w_+ + \int \mathfrak{D} w_{\mathrm{GM}}^{(\pm)} e^{-\mathcal{H}[\{w\}]}, \qquad \text{(D.13)}$$

$$\begin{aligned} \mathcal{H}[\{w\}] = {} & \frac{\rho_0}{2\kappa} \int \mathrm{d}\mathbf{r}\, w_+(\mathbf{r})^2 - i\rho_0 \int \mathrm{d}\mathbf{r}\, w_+(\mathbf{r}) \\ & + \frac{\rho_0}{\chi_{\mathrm{GM}}} \int \mathrm{d}\mathbf{r}\, w_{\mathrm{GM}}^{(+)}(\mathbf{r})^2 + \frac{\rho_0}{\chi_{\mathrm{GM}}} \int \mathrm{d}\mathbf{r}\, w_{\mathrm{GM}}^{(-)}(\mathbf{r})^2 \\ & - n_{\mathrm{P}} \ln Q_{\mathrm{P}}[\mu_{\mathrm{P}}] - n_{\mathrm{M}} \ln Q_{\mathrm{M}}[\mu_{\mathrm{M}}], \end{aligned} \qquad \text{(D.14)}$$

$$\mu_{\mathrm{P}} = [\Gamma_{\mathrm{P}} * i w_+](r) - \frac{n_{\mathrm{G}}}{n_{\mathrm{P}}} \left[\Gamma_{\mathrm{P}} * \log q_{\mathrm{g}}[\mu_{\mathrm{G}}] \right](r) \qquad \text{(D.15)}$$

$$\mu_{\mathrm{G}} = \left[\Gamma_{\mathrm{G}} * \left(i w_+ + i w_{\mathrm{GM}}^{(+)} + w_{\mathrm{GM}}^{(-)} \right) \right](r) \qquad \text{(D.16)}$$

$$\mu_{\mathrm{M}} = \left[\Gamma_{\mathrm{M}} * \left(i w_+ + i w_{\mathrm{GM}}^{(+)} + w_{\mathrm{GM}}^{(-)} \right) \right](r). \qquad \text{(D.17)}$$

The mean-field equations are

$$\frac{\delta\mathcal{H}}{\delta w_+(r)} = \frac{\rho_0}{\kappa} w_+(r) - i\rho_0 + i\left[\Gamma_{\mathrm{P}} * \rho_{\mathrm{pc}}\right](r) + i[\Gamma_{\mathrm{G}} * \rho_{\mathrm{G}}](r) + i[\Gamma_{\mathrm{M}} * \rho_{\mathrm{M}}](r) = 0 \qquad \text{(D.18)}$$

$$\frac{\delta\mathcal{H}}{\delta w_{\mathrm{GM}}^{(+)}(r)} = \frac{2\rho_0}{\chi_{GM}} w_{GM}^{(+)}(r) + i[\Gamma_{\mathrm{G}} * \rho_{\mathrm{G}}](r) + i[\Gamma_{\mathrm{M}} * \rho_{\mathrm{M}}](r) = 0 \qquad \text{(D.19)}$$

$$\frac{\delta\mathcal{H}}{\delta w_{\mathrm{GM}}^{(-)}(r)} = \frac{2\rho_0}{\chi_{GM}} w_{GM}^{(-)}(r) + [\Gamma_{\mathrm{G}} * \rho_{\mathrm{G}}](r) + [\Gamma_{\mathrm{M}} * \rho_{\mathrm{M}}](r) = 0 \qquad \text{(D.20)}$$

Under the HMF approximation, the spatial dependence is dropped in each equation. Taking into consideration that $\int dr\Gamma_{\mathrm{P}}(r) = v_{\mathrm{P}}$ and $\Gamma_{\mathrm{M}}(r) = \Gamma_{\mathrm{G}}(r)$ with $\int dr\Gamma_{\mathrm{M}}(r) = v_{\mathrm{M}} = 1$, we have for the two + fields

$$w_+ = \frac{i\kappa}{\rho_0}\left[\rho_0 - \frac{v_{\mathrm{P}}n_{\mathrm{P}} + N_{\mathrm{G}}n_{\mathrm{G}} + N_{\mathrm{M}}n_{\mathrm{M}}}{V}\right] \qquad \text{(D.21)}$$

If we assume the total density is constant everywhere, then we can set $w_+ = 0$ and ignore it from here forward. This enables us to focus on the exchange fields, given as

$$w_{GM}^{(+)} = -\frac{i\chi}{2\rho_0}\left[\frac{N_{\mathrm{G}}n_{\mathrm{G}} + N_{\mathrm{M}}n_{\mathrm{M}}}{V}\right] = -\frac{i\chi}{2}(\phi_{\mathrm{M}} + \phi_{\mathrm{G}}) \qquad \text{(D.22)}$$

$$w_{GM}^{(-)} = \frac{\chi}{2\rho_0}\left[\frac{n_{\mathrm{M}}N_{\mathrm{M}} - n_{\mathrm{G}}N_{\mathrm{G}}}{V}\right] = \frac{\chi}{2}(\phi_{\mathrm{M}} - \phi_{\mathrm{G}}), \qquad \text{(D.23)}$$

where we have defined the volume fractions of the grafted polymers and the matrix chains as $\phi_{\mathrm{M}} = n_{\mathrm{M}}N_{\mathrm{M}}/\rho_0 V$ and $\phi_{\mathrm{G}} = n_{\mathrm{G}}N_{\mathrm{G}}/\rho_0 V$, respectively. Substituting these variables into the above equations, the fields for the grafts and the matrix reduce to

$$\mu_{\mathrm{G}} = \chi\phi_{\mathrm{M}} \qquad \text{(D.24)}$$

$$\mu_{\mathrm{M}} = \chi\phi_{\mathrm{G}} \qquad \text{(D.25)}$$

The matrix polymer partition function is given by

$$Q_{\mathrm{m}} = \frac{1}{V}\int dr^{N_{\mathrm{M}}}\, e^{-\mu_{\mathrm{M}}(r_0)}\Phi_{0,1}e^{-\mu_{\mathrm{M}}(r_1)}\Phi_{1,0} \ldots \Phi_{N-1,N}e^{-\mu_{\mathrm{M}}(r_N)}, \qquad \text{(D.26)}$$

where $\Phi_{i,i+1}$ is the normalized bond transition probability for the bonds connecting particles i and $i + 1$. Using the above expression for μ_{M} and substituting into Q_{M}, we obtain the expression for the matrix polymer partition function

$$Q_{\mathrm{M}} = e^{-\chi N_{\mathrm{M}} \phi_{\mathrm{G}}}, \qquad \text{(D.27)}$$

which intuitively penalizes states where the matrix polymers mix with grafted-polymer rich domains if $\chi > 0$.

To construct the analytic results under the HMF approximation for the gNPs, we work from the grafted chains in towards the particle core. The partition function of a grafted chain that has monomer 0 bonded to the grafting site at r_{g} is given by

$$q_{\mathrm{G}}(r_{\mathrm{g}}) = \int dr^{N_{\mathrm{G}}}\, \Phi_{\mathrm{g},0} e^{-\mu_{\mathrm{G}}(r_0)} \Phi_{0,1} \ldots \Phi_{N_{\mathrm{G}}-1,N_{\mathrm{G}}} e^{-\mu_{\mathrm{G}}\left(r_{N_{\mathrm{G}}}\right)}, \qquad \text{(D.28)}$$

Here $\Phi_{\mathrm{g},0} = \Phi(r_{\mathrm{g}} - r_0)$ is the normalized Gaussian bond distribution function between the graft site at r_{G} and the first monomer at r_0. Again using the HMF results presented above, we find

$$q_{\mathrm{G}} = e^{-\chi N_{\mathrm{G}} \phi_{\mathrm{M}}}, \qquad \text{(D.29)}$$

and we note the difference in sign in the argument of the exponential compared to Q_{M} above.

Substituting into μ_{P} above and using the HMF result that $w_+ = 0$ and that $\int dr \Gamma_\sigma(r) = 1$,

$$\mu_{\mathrm{P}} = 0 + \frac{n_{\mathrm{G}}}{n_{\mathrm{P}}} \chi N_{\mathrm{G}} \phi_{\mathrm{M}}. \qquad \text{(D.30)}$$

In general, the gNP partition function takes the form

$$Q_{\mathrm{P}} = \frac{1}{V} \int dr^{-\mu_{\mathrm{P}}(r)} \qquad \text{(D.31)}$$

$$= e^{-\frac{n_{\mathrm{G}}}{n_{\mathrm{P}}} \chi N_{\mathrm{G}} \phi_{\mathrm{M}}}, \qquad \text{(D.32)}$$

where the second line follows from implementing the HMF approximation.

At this point, we are ready to simplify the terms in Equation D.13. Beginning with the terms of the form $n\log Q$, we have

$$n_{\mathrm{M}} \log Q_{\mathrm{M}} = -\chi n_{\mathrm{M}} N_{\mathrm{M}} \phi_{\mathrm{G}} = -\chi V \rho_0 \phi_{\mathrm{M}} \phi_{\mathrm{G}}, \qquad \text{(D.33)}$$

$$n_{\mathrm{P}} \log Q_{\mathrm{P}} = -\chi n_{\mathrm{G}} N_{\mathrm{G}} \phi_{\mathrm{M}} = -\chi V \rho_0 \phi_{\mathrm{M}} \phi_{\mathrm{G}}, \qquad \text{(D.34)}$$

for the matrix and gNPs, respectively. As a reminder, $n_{\mathrm{G}} = n_{\mathrm{P}} \sigma 4\pi R_{\mathrm{P}}^2$ is the total number of grafted chains, not the number of grafted chains per particle.

In Equation D.14 above, the first two terms on the right-hand side are zero under the HMF approximation. Substituting in for $w_{\mathrm{MG}}^{(\pm)}$ and the two $n\log Q$ terms, we find

$$\mathcal{H} = \frac{\rho_0 V}{\chi}\left\{\left[-\frac{i\chi}{2}(\phi_{\mathrm{M}} + \phi_{\mathrm{G}})\right]^2 + \left[\frac{\chi}{2}(\phi_{\mathrm{M}} - \phi_{\mathrm{G}})\right]^2\right\} + 2\chi V\rho_0\phi_{\mathrm{M}}\phi_{\mathrm{G}} \qquad \text{(D.35)}$$

$$= \frac{\rho_0 V}{\chi}\left\{-\frac{\chi^2}{4}\left[\phi_{\mathrm{M}}^2 + 2\phi_{\mathrm{M}}\phi_{\mathrm{G}} + \phi_G^2\right] + \frac{\chi^2}{4}\left[\phi_{\mathrm{M}}^2 + 2\phi_{\mathrm{M}}\phi_{\mathrm{G}} + \phi_G^2\right]\right\} + 2\chi V\rho_0\phi_{\mathrm{M}}\phi_{\mathrm{G}} \qquad \text{(D.36)}$$

$$= \frac{\rho_0 V\chi}{4}[-4\phi_{\mathrm{M}}\phi_{\mathrm{G}}] + 2\chi V\rho_0\phi_{\mathrm{M}}\phi_{\mathrm{G}} \qquad \text{(D.37)}$$

$$= \chi V\rho_0\phi_{\mathrm{M}}\phi_{\mathrm{G}}. \qquad \text{(D.38)}$$

This provides the enthalpic contribution to the free energy.

The prefactors buried in z_1 in Equation D.13 are needed to obtain the entropy of mixing in the free energy,

$$z_1 = \frac{V^{n_{\mathrm{P}}+n_{\mathrm{M}}}\mathrm{g}^{n_{\mathrm{P}}N_{\mathrm{G}}+n_{\mathrm{M}}N_{\mathrm{M}}}}{\Omega_+\Omega_{\mathrm{AB}}^{(+)}\Omega_{\mathrm{AB}}^{(-)}n_{\mathrm{P}}!n_{\mathrm{M}}!\lambda_{\mathrm{T}}^{n_{\mathrm{P}}+n_{\mathrm{M}}}}. \qquad \text{(D.39)}$$

Here the factors of Ω are the normalization constants from the Hubbard-Stratonovich transformations, λ_{T} is the thermal de Broglie wavelength, and g is the normalization constant from the bond transition probabilities, which are independent of all thermodynamic quantities. The contribution to the free energy is of the form

$$-\log z_1 = n_{\mathrm{P}}\log n_{\mathrm{P}} - n_{\mathrm{P}} + n_{\mathrm{M}}\log n_{\mathrm{M}} - n_{\mathrm{M}} - (n_{\mathrm{P}} + n_{\mathrm{G}})\log V - \log\left[\frac{\mathrm{g}^{n_{\mathrm{P}}N_{\mathrm{G}}+n_{\mathrm{M}}N_{\mathrm{M}}}}{\Omega_+\Omega_{\mathrm{AB}}^{(+)}\Omega_{\mathrm{AB}}^{(-)}}\right]$$

$$\pm n_{\mathrm{P}}\log V_{\mathrm{P}} \pm n_{\mathrm{M}}\log N_{\mathrm{M}} \qquad \text{(D.40)}$$

where the second line contains terms that are added and subtracted to z_1 that are linear in n_{P}, n_{M} and thus do not affect the phase behavior and represent constant shifts in the chemical potentials. Combining those terms with other constants leads to

$$-\log z_1 = n_{\mathrm{P}}\log\frac{n_{\mathrm{P}}V_{\mathrm{P}}}{V} + n_{\mathrm{M}}\log\frac{n_{\mathrm{M}}N_{\mathrm{M}}}{V} + f_0 V\rho_0 \qquad \text{(D.41)}$$

where f_0 is the thermodynamically irrelevant constant shift in the intensive free energy that absorbs the remaining constants.

Bringing everything together, we have for our free energy through its relation to the partition function

$$e^{-\beta F} = \mathcal{Z} \approx z_1 e^{-\mathcal{H}}. \qquad \text{(D.42)}$$

Solving for the free energy, we find

$$\frac{\beta F}{\rho_0 V} = \frac{\phi_P}{V_P}\log\phi_P + \frac{\phi_M}{N_M}\log\phi_M + \chi\phi_M\phi_G + f_0 \qquad \text{(D.43)}$$

We will choose $f_0 = 0$. We can write ϕ_G in terms of ϕ_M and the properties of the nanoparticle by using the definition of the volume fractions

$$\phi_M = \frac{n_M N_M}{n_M N_M + n_P V_P}, \qquad \text{(D.44)}$$

$$\phi_G = \frac{n_P \sigma A_P N_G}{n_M N_M + n_P V_P}. \qquad \text{(D.45)}$$

Here $A_P = 4\pi R_P^2$ is the surface area of the NPs and $n_P\sigma A_P$ is the total number of grafted polymers across all NPs. Solving Equation D.44 for n_P and substituting into Equation D.45 gives

$$\phi_G = (1-\phi_M)\frac{\sigma A_P N_G}{V_P} \qquad \text{(D.46)}$$

$$= (1-\phi_M)\frac{3\sigma N_G}{\rho_0 R_P + 3\sigma N_G}, \qquad \text{(D.47)}$$

where the last line follows from the use of $V_{gNP} = \rho_0 \frac{4}{3}\pi R_P^3 + \sigma A_P N_G$.

The final working expression for the free energy is then

$$\frac{\beta F}{\rho_0 V} = \frac{\phi_P}{V_{gNP}}\log\phi_P + \frac{\phi_M}{N_M}\log\phi_M + \chi\phi_M(1-\phi_M)\frac{3\sigma N_G}{\rho_0 R_P + 3\sigma N_G}. \qquad \text{(D.48)}$$

If we then write the above equation in terms of ϕ_M, we get

$$\frac{\beta F}{\rho_0 V} = \frac{1-\phi_M}{V_{gNP}}\log(1-\phi_M) + \frac{\phi_M}{N_M}\log\phi_M + \chi\phi_M(1-\phi_M)\frac{3\sigma N_G}{\rho_0 R_P + 3\sigma N_G}. \qquad \text{(D.49)}$$

Using this result, we can compare Equation D.49 to the self-consistent field theory (SCFT) results as shown in Figure D.1. Clearly the agreement is nearly quantitative; small differences are likely due to the finite compressibility in the PNC-FT calculations. As in the PNC-FT calculations,

even with an analytic expression, it is difficult to reach a converged solution for the binodal near the critical point, so the full black curve is not drawn in Figure D.1.

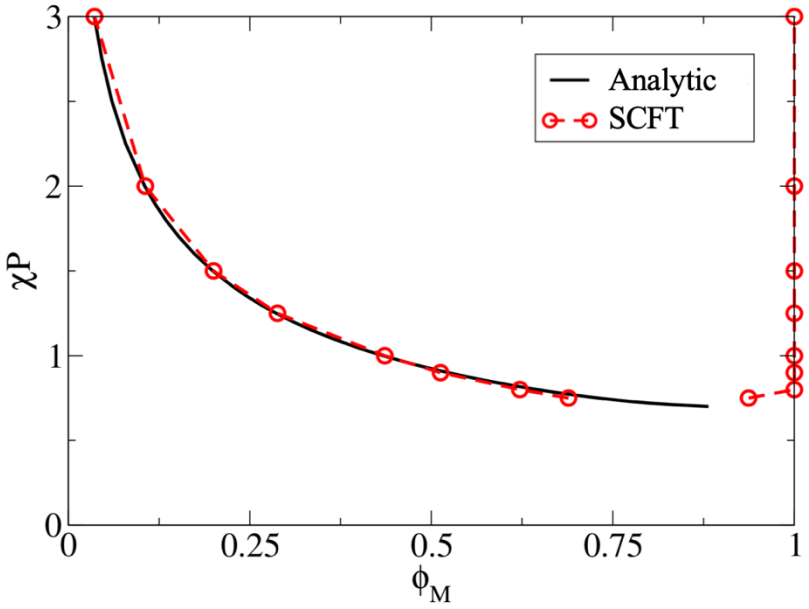

Figure D.1. Binodal plotted as χP as a function of ϕ_M for the analytic expression given by Equation D.49 and by SCFT using our PNC-FT model. Here $P = N = 30$, $\sigma = 0.86$ chains/b^2, $R_P = 3.4113b$, and $\rho_0 = 3.94342$. All units here are in terms of the statistical segment length, b. We vary the bare χ parameter to change the value of χP.

D.4 TILD Name Choice

In our previous publications using the TILD method, we used the name "dynamic mean-field theory" (DMFT) to highlight the close connection to the framework derived by Fredrickson and Orland (FO).[12] Briefly, FO cast the dynamics of polymer chains into the path integral framework of classical dynamics proposed by Martin, Siggia, and Rose,[13] and using a mean-field approximation, they derived the dynamics of polymer chains evolving in a continuous density field, highly reminiscent of the single-chain in mean-field approach by Müller.[14] We have come to realize that our implementation of the method is more closely akin to the theoretically-informed Monte Carlo (TIMC) of de Pablo and coworkers.[15] There are some differences in our implementation of

the method in that we use finite-ranged potentials that are well-behaved when modeled as a field-theoretic simulation or using the TILD method and free of ultraviolet (UV) divergences. These differences are minor technical aspects of the overall framework. To highlight the similarities between the methods and to avoid confusion in the field, we have chosen to refer to our technique as the TILD method.

D.5 TILD Equilibration

Here we briefly discuss our criteria for determining equilibration in the TILD simulations. Figure D.2 shows the density evolution from TILD trajectories as a function of simulation time. We run each system for a minimum of 250,000τ. If after an additional 250,000τ, the density distribution does not change significantly, we consider the system equilibrated. Most systems were run for ≈ 1,500,000τ or longer. Figure D.2 demonstrates that in systems with large χP values the NPs are densely packed, do not diffuse much beyond their initial placement, and thus equilibrate much faster than in systems that have dispersed NPs at equilibrium.

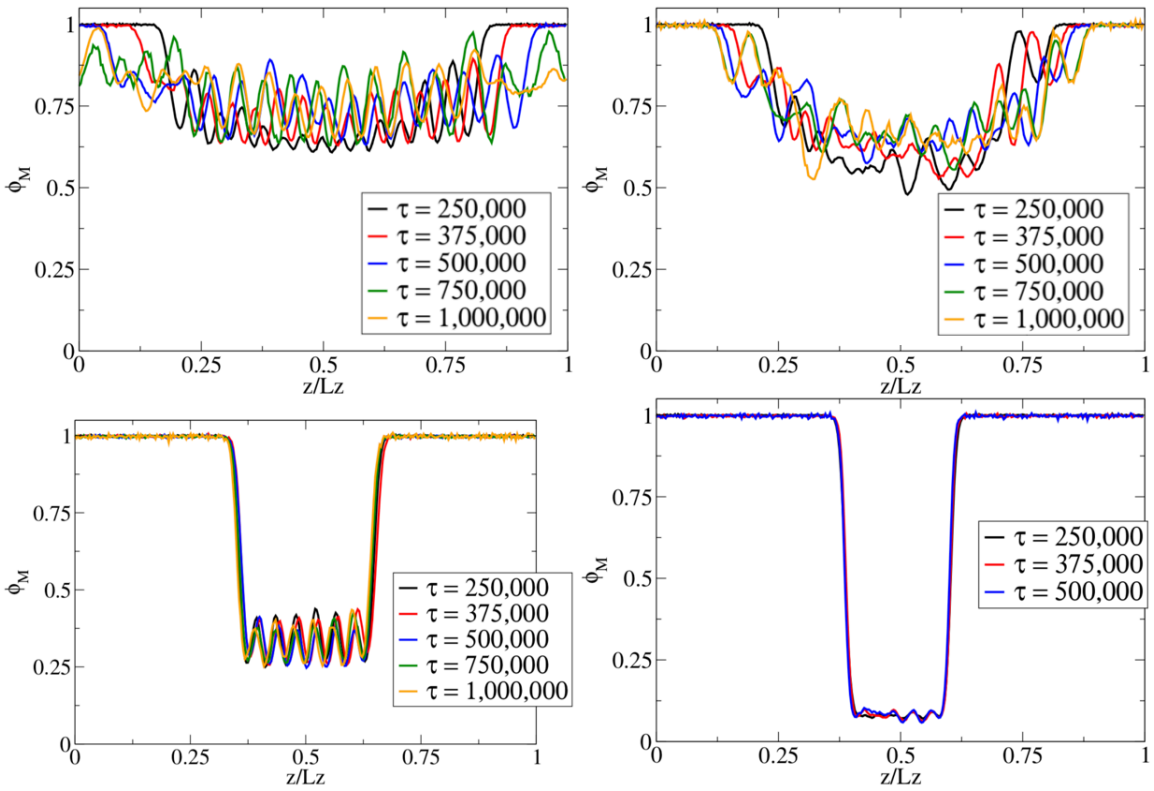

Figure D.2. Matrix volume fraction averaged over the *xy* plane with respect to the *z*-direction for (upper left) $\chi P = 0$, (upper right) $\chi P = 0.5$, (bottom left) $\chi P = 1$, and (bottom right) $\chi P = 2$. Each color represents a matrix volume fraction distribution averaged over $25{,}000\tau$ where the τ reported above is the final τ (e.g. the curves labeled $\tau = 250{,}000$ are ϕ_M averaged from $\tau = 225{,}000$ to $\tau = 250{,}000$). For each system, $P = 15$, $N = 30$, $\sigma = 0.85931$ chains/b^2, $R_P = 3.4113b$, and $\rho_0 = 3.94342$.

D.6 Chain Discretization

Figure D.3 shows how the phase behavior changes as a function of chain discretization. When the number *P* of coarse-grained beads used to model a given molecular weight chain is larger, the macrophase separation is enhanced. This is because the effects of depletion interactions are greater due to the increased conformational entropy of the polymer chains that have more beads. This discretization effect is more pronounced at low molecular weights, and insignificant at ≈ 7.5 kg/mol or greater. We see the change in the phase behavior becomes less pronounced as the *P* is

increased. In other words, the difference in the phase boundary between $2P$ = 1 kg/mol and $4P$ = 1 kg/mol is greater than between $4P$ = 1 kg/mol and $6P$ = 1 kg/mol.

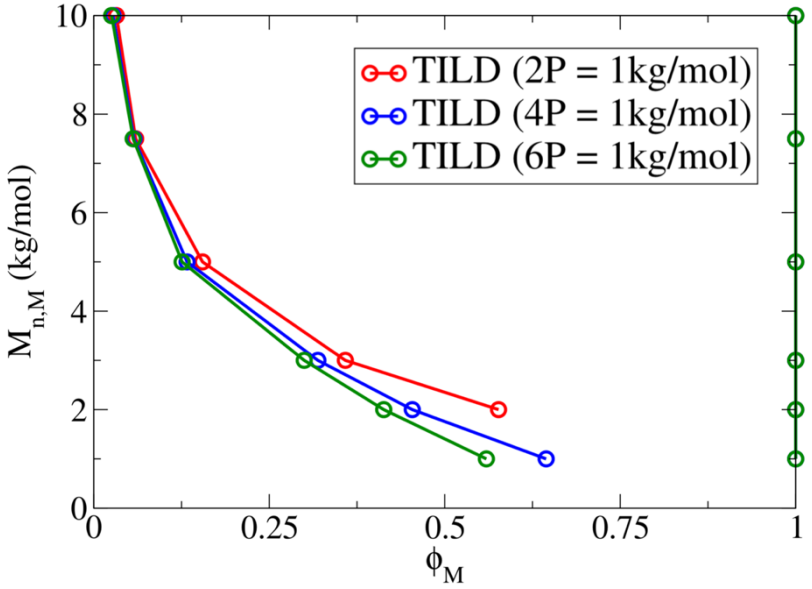

Figure D.3. Binodals for the system shown in Figure 5.3 of the main article using different discretizations of the chains. The green curve is the same curve presented in Figure 5.3 in the main text. The red and blue curves show the effect of the chain discretization in the TILD simulations. We alter the discretization by varying ρ_0 where ρ_0 = 2.276 (red), ρ_0 = 2.788 (blue), and ρ_0 = 3.943 (green).

D.7 Phase Diagrams

Figure D.4 shows the results of Figure 5.5b, but with the y-axis changed to χ instead of χP. This figure shows clearly that the binodals move downward with increasing α for both TILD and mean- field PNC-FT simulations. We can further understand the fact that the binodals move upward for the mean-field results in Figure 5.5b by calculating the spinodal from the free energy in Equation 5.10. Taking the second derivative

$$\frac{\partial^2 F}{\partial \phi_M^2} = \frac{1}{P\phi_M} + \frac{1}{(V_P + (n_G/n_P)N)(1-\phi_M)} - 2\chi \qquad \text{(D.50)}$$

and setting the above equation to 0 determines the spinodal curve. Multiplying through by P gives the spinodal in terms of χP as a function of ϕ_M:

$$2\chi P = \frac{1}{\phi_M} + \frac{P}{(V_P+(n_G/n_P)N)(1-\phi_M)} \qquad \text{(D.51)}$$

Clearly, the value of χP on the spinodal at any given ϕ_M is larger at larger P than at smaller P. In the mean-field results, the changes in the binodals and spinodals are a weaker function of α than in TILD, so they do not shift down as much as a function of χ and when plotted versus χP, as in Figure 5.5b, they actually shift up a bit with increasing α.

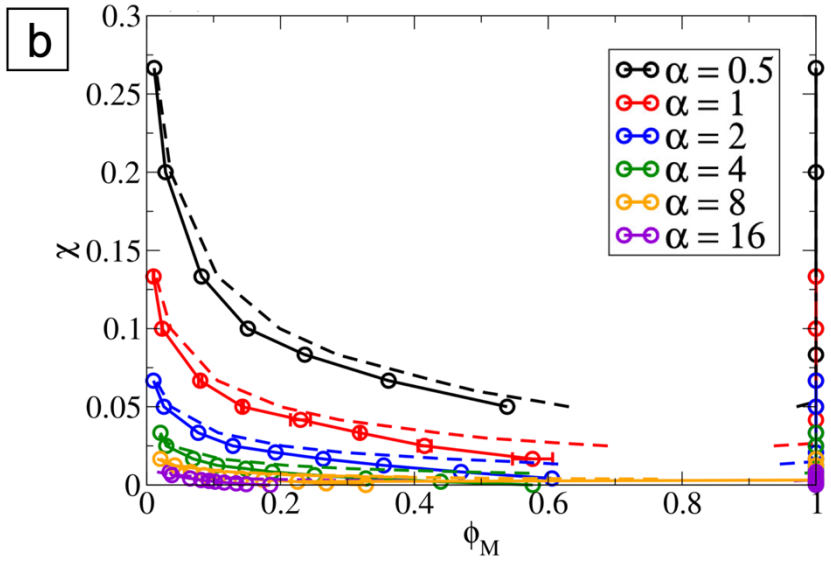

Figure D.4. Data from Figure 5.5b in the main text, plotted with χ on the y-axis instead of χP as a function of ϕ_M for PNC-FT calculations (dashed curves) and TILD simulations (solid curves with points).

D.8 Materials

Unless specified, all chemicals were used as received without further purification. The fixable ATRP-initiator, {[(2-Bromo-2-methylpropionyl)oxy]propyl}triethoxysilane (BPE), was synthesized as described elsewhere.[16,17] Methanol (≥ 99.9%, for HPLC), RP = 7.5 nm silica nanoparticles (SiO_2 NPs, LUDOX® HS-30 colloidal silica), tetrahydrofuran (THF, ≥ 99.0%) used

for making the PNC solutions, and toluene (99.9%, for HPLC) were purchased from Sigma Aldrich. Ammonium hydroxide solution (28% NH_3), anisole (99.5%), chloroform (99%), copper (I) chloride (CuCl, 99.9%), copper (II) chloride ($CuCl_2$, 95%), *N,N*-dimethylformamide (DMF, 99.5%), 4,4'-dinonyl-2,2'-bipyridine (dNbipy, 97%), ethanol (99.5%), ethylenediaminetetraacetic acid disodium salt dihydrate (EDTA-Na_2, 99%), ethylene glycol (99.5%), pentane (98%), and THF (99.5%) used for polymer gNP synthesis were purchased from FUJIFILM Wako Pure Chemicals Corporation, Osaka, Japan. Methyl methacrylate (MMA, 99%) was obtained from Nacalai Tesque Inc., Osaka, Japan and was purified by flash chromatography over activated neutral alumina. Ethyl 2-bromoisobutyrate (EBiB, 98%) was obtained from Tokyo Chemical Industry, Tokyo, Japan. M_n = 0.95 kg/mol (PDI = 1.2) and M_n = 10 kg/mol (PDI = 1.09) polystyrene (PS) were purchased from Polymer Source Inc. and M_n = 2.7 kg/mol (PDI = 1.09) PS was purchased from Pressure Chemical Company. EpoxiCure 2 epoxy hardener and epoxy resin were both obtained from Buehler. N-type, <100> oriented silicon wafers (dopant Ph, 10-20 Ω·cm resistivity, 475-575 μm thickness, single side polished) were purchased from Silicon Quest International. Double coated carbon conductive tape (8 mm W x 20 m L) was purchased from Ted Pella, Inc and Kapton® film was obtained from American Durafilm.

D.9 References

(1) Fredrickson, G. H. *The Equilibrium Theory of Inhomogeneous Polymers*; Oxford University Press: 2006.

(2) Chaikin, P. M.; Lubensky, T. C. *Principles of Condensed Matter Physics*; Cambridge University Press, 2000; Vol. 1.

(3) Lennon, E. M.; Mohler, G. O.; Ceniceros, H. D.; García-Cervera, C. J.; Fredrickson, G. H. Numerical Solutions of the Complex Langevin Equations in Polymer Field Theory. *Multiscale Modeling and Simulation* **2008**, 6, 1347.

(4) Hockney, R. W.; Eastwood, J. W. *Computer Simulation Using Particles*; CRC Press, 1988.

(5) Deserno, M.; Holm, C. How to Mesh Up Ewald Sums. I. A Theoretical and Numerical Comparison of Various Particle Mesh Routines. *J. Chem. Phys.* **1998**, 109, 7678–7693.

(6) Frenkel, D.; Smit, B. *Understanding Molecular Simulations: From Algorithms to Applications*; Academic Press, San Diego, 2002.

(7) Koski, J.; Chao, H.; Riggleman, R. A. Field Theoretic Simulations of Polymer Nanocomposites. *J. Chem. Phys.* **2013**, 139, 244911.

(8) Villet, M. C.; Fredrickson, G. H. Efficient Field-Theoretic Simulation of Polymer Solutions. *J. Chem. Phys.* **2014**, 141, 224115.

(9) Koski, J. P.; Ferrier, R. C., Jr.; Krook, N. M.; Chao, H.; Composto, R. J.; Frischknecht, A. L.; Riggleman, R. A. Comparison of Field-Theoretic Approaches in Predicting Polymer Nanocomposite Phase Behavior. *Macromolecules* **2017**, 50, 8797–8809.

(10) Grønbech-Jensen, N.; Farago, O. A Simple and Effective Verlet-Type Algorithm for Simulating Langevin Dynamics. *Molecular Physics* **2013**, 111, 983–991.

(11) Chao, H.; Koski, J.; Riggleman, R. A. Solvent Vapor Annealing in Block Copolymer Nanocomposite Films: a Dynamic Mean Field Approach. *Soft Matter* **2017**, 13, 239–249.

(12) Fredrickson, G. H.; Orland, H. Dynamics of Polymers: A Mean-Field Theory. *J. Chem. Phys.* **2014**, 140, 084902.

(13) Martin, P. C.; Siggia, E.; Rose, H. Statistical Dynamics of Classical Systems. *Phys. Rev. A* **1973**, 8, 423.

(14) Daoulas, K. C.; Müller, M. Single Chain in Mean Field Simulations: Quasi-Instantaneous Field Approximation and Quantitative Comparison with Monte Carlo Simulations. *J. Chem. Phys.* **2006**, 125, 184904.

(15) Pike, D. Q.; Detcheverry, F. A.; Müller, M.; de Pablo, J. J. Theoretically Informed Coarse Grain Simulations of Polymeric Systems. *J. Chem. Phys.* **2009**, 131, 084903.

(16) Ohno, K.; Morinaga, T.; Koh, K.; Tsujii, Y.; Fukuda, T. Synthesis of Monodisperse Silica Particles Coated with Well-Defined, High-Density Polymer Brushes by Surface-Initiated Atom Transfer Radical Polymerization. *Macromolecules* **2005**, 38, 2137–2142.

(17) Ohno, K.; Akashi, T.; Huang, Y.; Tsujii, Y. Surface-Initiated Living Radical Polymerization from Narrowly Size-Distributed Silica Nanoparticles of Diameters Less than 100 nm. *Macromolecules* **2010**, 43, 8805–8812.